



HAL
open science

Experimental study of the structure and dynamics of cavitating flows

Guangjian Zhang

► **To cite this version:**

Guangjian Zhang. Experimental study of the structure and dynamics of cavitating flows. Electric power. HESAM Université, 2020. English. NNT : 2020HESAE050 . tel-03130085

HAL Id: tel-03130085

<https://pastel.hal.science/tel-03130085>

Submitted on 3 Feb 2021

HAL is a multi-disciplinary open access archive for the deposit and dissemination of scientific research documents, whether they are published or not. The documents may come from teaching and research institutions in France or abroad, or from public or private research centers.

L'archive ouverte pluridisciplinaire **HAL**, est destinée au dépôt et à la diffusion de documents scientifiques de niveau recherche, publiés ou non, émanant des établissements d'enseignement et de recherche français ou étrangers, des laboratoires publics ou privés.

ÉCOLE DOCTORALE SCIENCES DES MÉTIERS DE L'INGÉNIEUR
[Laboratoire de Mécanique des Fluides de Lille – Campus de Lille]

THÈSE

présentée par : **Guangjian ZHANG**

soutenue le : **2 Décembre 2020**

pour obtenir le grade de : **Docteur d'HESAM Université**

préparée à : **École Nationale Supérieure d'Arts et Métiers**

Spécialité : **Génie énergétique**

Etude expérimentale de la structure et de la dynamique des écoulements cavitants

THÈSE dirigée par :
[M. COUTIER-DELGOSHA Olivier]

Jury

M. Todd LOWE, Professeur, Virginia Tech

M. Antoine DUCOIN, Maître de Conférences HDR, Ecole Centrale de Nantes

M. Lionel THOMAS, Maître de conférences HDR, Université de Poitiers

M. Joseph KATZ, Professeur, Johns Hopkins University

M. Matevž DULAR, Professeur, University of Ljubljana

M. Nathanaël MACHICOANE, Maître de conférences,
Université Grenoble Alpes

M. Olivier COUTIER-DELGOSHA, Professeur,
Arts et Métiers Sciences et Technologies

Président

Rapporteur

Rapporteur

Examineur

Examineur

Examineur

Examineur

**T
H
È
S
E**

Acknowledgements

First of all, I would like to express my deepest gratitude to my supervisor Prof. Olivier Coutier-Delgosha for providing me the opportunity to pursue my PhD in his group. His continuous guidance and critical comments have improved this thesis work substantially. His work enthusiasm inspired me to never give up even though with huge frustrations.

I would also like to thank my committee members including Prof. Todd Lowe (Virginia Tech), Prof. Antoine Ducoin (Ecole Centrale de Nantes), Prof. Lionel Thomas (Université de Poitiers), Prof. Joseph Katz (Johns Hopkins University), Prof. Matevž Dular (University of Ljubljana) and Prof. Nathanaël Machicoane (Université Grenoble Alpes) for reviewing my thesis and providing me valuable suggestions.

Sincere thanks are given to Prof. Antoine Dazin and Prof. Annie-Claude Bayeul-Laine for being in my academic follow-up committee. Their rich experience and knowledge always guide me to work in the right direction.

The X-ray imaging experiment was performed at the Advanced Photon Source, and many thanks to Dr. Kamel Fezzaa for his kind help with our experimental setup. I am grateful to Dr. Ilyass Khelifa for his guidance to develop the image-processing method to separate particles from raw X-ray images. I would like to thank my friend, roommate as well as colleague Dr. Xinlei Zhang for his help both in work and life.

The PIV-LIF measurements of cavitating flows were carried out in the Cavitation, Propulsion & Multiphase Flow Laboratory of Virginia Tech. I would like to thank Mr. Mingming Ge, Mr. Navid Nematikourabbasloo and Dr. Merouane Hamdi for aiding me to complete this experiment.

I had an opportunity of visiting Virginia Tech for a number of months. I am grateful to Dr. Zhongshu Ren, Mr. Ben Zhao, Mr. Yuzhi Li and Mr. Mingming Ge for helping me adapt to the new environment quickly. Because of you guys, we managed to go hiking, have hot-pot and visit a lot of interesting places. You guys make my stay in Virginia Tech exciting and memorable.

My sincere appreciation extends to all colleagues at the ENSAM for their help in my work and life, especially to Mr. Alberto Baretter, Mr. Lei Shi, Dr. Yuxin Bai, Mr. Kunpeng Long, Mrs. Naly Ratolojanahary and Mr. Mohamed Ghandour.

Finally and most importantly, I would like to thank my parents for their limitless love and support during my life time. I would also like to thank my girlfriend LR to accompany me in the past 12 years.

Contents

LIST OF SYMBOLS	IV
1. INTRODUCTION	1
1.1. INTRODUCTION TO CAVITATION PHENOMENON	1
1.2. OUTLINE OF THE THESIS.....	2
2. PHYSICAL BACKGROUND AND MEASUREMENT TECHNIQUES	7
2.1. SHEET AND CLOUD CAVITATION.....	7
2.2. MECHANISMS FOR CLOUD SHEDDING	8
2.3. STUDIES ON CAVITATION-TURBULENCE INTERACTIONS	12
2.4. A REVIEW OF MEASUREMENT TECHNIQUES FOR CAVITATING FLOWS	12
2.4.1. <i>Local measurements by intrusive probes</i>	13
2.4.2. <i>Particle Image Velocimetry (PIV)</i>	13
2.4.3. <i>X-ray densitometry based on absorption contrast</i>	14
2.4.4. <i>X-ray velocimetry based on phase contrast</i>	15
3. FAST X-RAY IMAGING TECHNIQUE AND QUANTITATIVE DATA EXTRACTION BASED ON IMAGE POST-PROCESSING	17
3.1. HYDRAULIC TEST RIG.....	17
3.2. X-RAY IMAGING MECHANISMS	19
3.3. X-RAY IMAGING TECHNIQUE	20
3.4. DATA EXTRACTION BASED ON IMAGE PROCESSING	23
3.4.1. <i>Separation of the two phases</i>	23
3.4.2. <i>Void fraction measurement</i>	24
3.4.3. <i>Particle image velocimetry</i>	25
3.5. COMPARISON BETWEEN CONVENTIONAL LASER PIV AND X-RAY PIV	28
3.6. PROCEDURES OF WAVELET-DECOMPOSITION-BASED IMAGE PROCESSING METHOD	29

3.7. IMPROVEMENT OF VOID FRACTION MEASUREMENT ACCURACY	33
3.8. CHAPTER SUMMARY	40
4. STRUCTURE AND DYNAMICS OF DEVELOPED SHEET CAVITATION	42
4.1. GLOBAL BEHAVIOR OF SHEET CAVITATION BASED ON HIGH SPEED PHOTOGRAPHY	42
4.2. MEAN VOID FRACTION AND VELOCITY FIELDS BASED ON X-RAY IMAGING MEASUREMENTS	45
4.3. PROBABILITY OF THE RE-ENTRANT FLOW: DISCUSSION	49
4.4. SPECTRAL ANALYSIS OF VOID FRACTION VARIATION	52
4.5. SUMMARY OF TWO-PHASE FLOW STRUCTURES INSIDE SHEET CAVITY	55
4.6. TURBULENT VELOCITY FLUCTUATIONS INSIDE SHEET CAVITY	58
4.7. VALIDATION OF THE REBOUD EMPIRICAL CORRECTION	61
4.8. CHAPTER SUMMARY	62
5. COMPARISON OF SHEET CAVITY STRUCTURES AND DYNAMICS AT DIFFERENT STAGES 66	
5.1. EXPERIMENTAL MEAN VOID FRACTION	67
5.2. EXPERIMENTAL RESULTS OF MEAN VELOCITY DISTRIBUTIONS	69
5.3. ANALYSIS OF CAVITY INSTABILITY	72
5.4. FREQUENCY ANALYSIS OF VOID FRACTION VARIATION	76
5.5. EFFECT OF CAVITATION ON TURBULENT VELOCITY FLUCTUATIONS	79
5.6. CHAPTER SUMMARY	85
6. TOWARDS THE TRIAL OF INVESTIGATING CLOUD CAVITATION	89
6.1. MULTI-FUNCTIONAL VENTURI-TYPE TEST SECTION	89
6.2. MEASUREMENTS	90
6.2.1. <i>Pressure measurements</i>	91
6.2.2. <i>PIV-LIF measurements</i>	91
6.3. EFFECT OF THE SIDE GAP ON CAVITATION REGIME	94
6.4. MEASUREMENT RESULTS IN THE NEW TEST SECTION	97
6.4.1. <i>Pressure loss versus cavitation number</i>	97
6.4.2. <i>Cavity length versus cavitation number</i>	98
6.4.3. <i>Velocity and pressure fluctuations</i>	100
6.5. CHAPTER SUMMARY	102

7. CLOUD CAVITATION SHEDDING MECHANISMS AND GEOMETRY SCALE EFFECT ON VENTURI CAVITATING FLOW	104
7.1. EXPERIMENTAL SET-UP.....	104
7.2. RESULTS.....	105
7.2.1. <i>The transitional cavitation</i>	105
7.2.2. <i>Re-entrant jet induced cloud cavitation</i>	108
7.2.3. <i>Condensation shock induced cloud cavitation</i>	111
7.2.4. <i>Pressure wave induced cloud shedding</i>	116
7.3. DISCUSSION.....	119
7.3.1. <i>Origin</i>	120
7.3.2. <i>Pressure rise and propagation velocity</i>	122
7.3.3. <i>Cloud shedding processes</i>	123
7.4. SCALE EFFECT ON VENTURI CAVITATING FLOW	123
7.4.1 <i>Problem background</i>	123
7.4.2 <i>Explanations to the observed scale effect</i>	125
7.5. CHAPTER SUMMARY	126
8. OVERALL SUMMARY AND PERSPECTIVES	130
8.1. THE APPLICATION OF X-RAY IMAGING TECHNIQUE TO CAVITATING FLOWS.....	130
8.2. INTERNAL TWO-PHASE FLOW STRUCTURES AND DYNAMICS OF QUASI-STABLE SHEET CAVITATION.....	131
8.3. EFFECT OF CAVITATION ON TURBULENCE.....	132
8.4. CAVITATING FLOWS IN A VENTURI-TYPE TEST SECTION WITH SIDE GAPS	133
8.5. THREE MECHANISMS TO INITIATE CLOUD CAVITATION	134
8.6. GEOMETRY SCALE EFFECT ON THE VENTURI CAVITATING FLOW	134
8.7. PERSPECTIVES	135
REFERENCES	144
LIST OF FIGURES	151

List of Symbols

Latin

f	Frequency, [Hz]
h_{te}	Height at the test section entrance, [m]
h_{th}	Height at the Venturi throat, [m]
h_{ve}	Height at the Venturi entrance, [m]
I_{α}	Local image intensity with cavitation
I_0	Local image intensity with vapor
I_1	Local image intensity with water
k	Turbulent kinetic energy, [m ² /s ²]
L_{cav}	Mean cavity length, [m]
P_{in}	Static pressure at the inlet, [Pa]
P_{out}	Static pressure at the outlet, [Pa]
P'_{in}^*	Nondimensional pressure fluctuations at the inlet
P'_{out}^*	Nondimensional pressure fluctuations at the outlet
P_{vap}	Saturated vapor pressure, [Pa]
Q	Volumetric flow rate, [m ³ /s]
R_1	Source to object distance, [m]
R_2	Object to detector distance, [m]
St	Strouhal number
t	Time, [s]
T_{cav}	Mean cavity thickness, [m]
u	Longitudinal velocity, [m/s]
\bar{u}	Mean longitudinal velocity, [m/s]
u'	Longitudinal velocity fluctuation, [m/s]
u_{in}	Average velocity at the inlet, [m/s]

List of Symbols

u_{ref}	Average velocity at the Venturi throat u_{th} as a reference, [m/s]
u_{re}	Re-entrant jet velocity, [m/s]
u_{sh}	Propagation speed of the condensation shock, [m/s]
u_{wa}	Travelling velocity of the pressure wave, [m/s]
v'	Transversal velocity fluctuation, [m/s]
x	First Cartesian coordinate, [m]
y	Second Cartesian coordinate, [m]
z	Third Cartesian coordinate, [m]

Greek

σ	Inlet cavitation number
ρ	Liquid/vapor mixture density, [kg/m ³]
ρ_l	Liquid density, [kg/m ³]
ρ_v	Vapor density, [kg/m ³]
α	Vapor volume fraction, i.e. void fraction
$\bar{\alpha}$	Mean void fraction
α'	Standard deviation of void fraction
τ	Reynolds shear stress, [m ² /s ²]

Acronyms

APS	Advanced Photon Source
CCD	Charge Coupled Device
CT	Computed Tomography
FFT	Fast Fourier Transform
LES	Large Eddy Simulation
LIF	Laser-Induced Fluorescent
PDF	Probability Density Function
PIV	Particle Image Velocimetry
RANS	Reynolds-Averaged Navier-Stokes

Chapter 1

Introduction

1.1. Introduction to cavitation phenomenon

Cavitation is a unique phase change phenomenon in liquid flows involving processes of the explosive vaporization of liquid in low pressure regions and the subsequent implosions when the pressure increases again. In contrast to boiling where the vaporization of liquid is driven by a temperature change, cavitation could be approximated as an isothermal process starting when the local liquid pressure is reduced below its saturated vapour pressure. Moreover, cavitation inception is also subjected to cavitation nuclei like non-condensable gases or other pollutants in liquid. Their existence weakens cohesion of liquid molecules and thus serves as starting locations for the liquid breakdown with decreasing the ambient pressure. The cavitation nuclei content is also a primary factor determining the difference between the vapour pressure and the actual pressure at cavitation inception (Franc & Michel 2005).

Cavitation can be classified, according to generation mechanisms, into acoustic cavitation, laser-induced cavitation and hydraulic cavitation. The first two types are produced through either ultrasonic waves or lasers depositing high amounts of energy into the liquid locally. The last one is caused by low pressures associated with flow dynamics, such as flow accelerations and strong vortical motions. In the literature and also in the present thesis, cavitation, if there is no specific note, usually refers to hydraulic cavitation since it is the most common and important case encountered in engineering applications.

Hydraulic cavitation can take different forms depending on how the low-pressure regions are generated, and they can be divided into three groups:

- Travelling bubble cavitation. Individual bubbles arise from regions of cavitation inception as a result of rapid growth of cavitation nuclei. They are first transported by the flow and then implode when they reach zones of high pressure.

- Attached cavitation. It appears in a low-pressure separated region close to the solid surface. The typical flow scenarios are cavities forming on the suction side of a hydrofoil or an impeller blade. If the length of the attached cavity exceeds the body upon which it develops, it is called super cavitation, otherwise it is termed as partial cavitation.
- Vortex cavitation. The fluid in the cores of vortices is prone to vaporizing due to low pressures prevailing there. It is commonly observed at the tips of propeller blades or in the free shear layers where Kelvin-Helmholtz vortices can develop.

In most hydraulic applications like turbo-machinery and marine propellers, cavitation is an undesired phenomenon, since the unsteady behavior and violent collapse of cavitation can result in detrimental effects, such as noise, system vibrations, performance decrease, material erosion, etc. However, in some cases, cavitation can have positive consequences. For instance, the torpedoes are enveloped in a stable super-cavity for reducing frictions with water, so that they are able to reach very high speeds (about 400 km/h). The intensive energy released from a collapsing cavity could be utilized to destroy kidney stones for treatment or kill live bacteria for cleaning of waste water.

Although cavitation has been investigated extensively for more than a century, a full understanding of the physical processes underlying the cavitating flows is still far from being realized at the present time. This is mainly due to the lack of quantitative experimental data on two-phase structures and dynamics of cavitation. Therefore, high-fidelity and detailed measurements of cavitating flow fields, especially in the opaque diphasic mixture areas, are extremely desired for a better knowledge of the physical mechanisms governing the cavitation instabilities. This will help to deduce effective means for controlling the negative consequences of cavitation and increasing its positive influence. Furthermore, the quantitative experimental data can be used to validate and improve the numerical simulation models for cavitation. Once reliable predictions are achieved, the costs and time concerning cavitation tests will be reduced substantially.

1.2. Outline of the thesis

Following the previous works in our group (Coutier-Delgosha et al. 2009; Khlifa et al. 2017), partial cavitation developed in small convergent-divergent (Venturi) channels were studied experimentally using an ultra-fast synchrotron X-ray imaging technique aided with

conventional high speed photography as well as particle image velocimetry (PIV). Depending on different operating conditions and geometry dimensions, partial cavitation generally exhibited two regimes with distinct behaviors: quasi-stable sheet cavitation and periodic cloud cavitation with large vapour shedding. The measurement results in the present study provided a detailed description of the two-phase flow structures and dynamics in sheet cavitation. Three mechanisms responsible for the transition of sheet-to-cloud cavitation were revealed and the differences between them were highlighted.

This thesis is composed of the following 7 chapters. Chapter 2 is a literature review on the physical background of sheet/cloud cavitation and the existing experimental techniques applied to cavitating flows. Chapter 3 provides a brief description of the experimental setup and the fast X-ray imaging technique. The emphasis of this chapter is put on the procedures from visualizations to velocity and void fraction field measurements in cavitating flows. In Chapter 4, the complex two-phase flow structures inside the sheet cavity are revealed in detail based on the data from the X-ray measurements. Chapter 5 deals with a comparative study of sheet cavitation at three stages (the early stage, intermediate stage and developed stage). The comparison shows the effect of re-entrant jet behaviors on sheet cavity structures and dynamics. The influence of cavitation on turbulent fluctuations is also discussed. Chapter 6 analyzes the cavitating flows in a Venturi channel with side gaps. It is found that cloud cavitation can be suppressed by altering the propagation path of the re-entrant jet. In Chapter 7, three mechanisms (i.e. re-entrant jet mechanism, condensation shock mechanism and collapse-induced pressure wave mechanism) to initiate cloud cavitation are described in detail, and the reasons causing the scale effect on Venturi cavitating flows are discussed. The thesis is ended with a general conclusion in Chapter 8 summarizing the main contributions of this work and several perspectives for future research are proposed.

1.1. Introduction au phénomène de cavitation

La cavitation est un phénomène de changement de phase unique dans les écoulements de liquide impliquant des processus de vaporisation explosive de liquide dans les régions à basse pression et les implosions ultérieures lorsque la pression augmente à nouveau. Contrairement à l'ébullition où la vaporisation du liquide est entraînée par un changement de température, la cavitation pourrait être approchée comme un processus isotherme commençant lorsque la

pression locale du liquide est réduite en dessous de sa pression de vapeur saturée. De plus, l'amorce de la cavitation est également soumise à des noyaux de cavitation comme des gaz non condensables ou d'autres polluants dans le liquide. Leur existence affaiblit la cohésion des molécules liquides et sert ainsi de points de départ pour la dégradation du liquide avec diminution de la pression ambiante. Le contenu des noyaux de cavitation est également un facteur principal déterminant la différence entre la pression de vapeur et la pression réelle au début de la cavitation (Franc & Michel 2005).

La cavitation peut être classée, selon les mécanismes de génération, en cavitation acoustique, cavitation induite par laser et cavitation hydraulique. Les deux premiers types sont produits soit par des ondes ultrasonores, soit par des lasers déposant localement de grandes quantités d'énergie dans le liquide. Le dernier est causé par les basses pressions associées à la dynamique de l'écoulement, telles que les accélérations de l'écoulement et les forts mouvements tourbillonnaires. Dans la littérature comme dans la présente thèse, la cavitation, s'il n'y a pas de note spécifique, fait généralement référence à la cavitation hydraulique car c'est le cas le plus courant et le plus important rencontré dans les applications d'ingénierie.

La cavitation hydraulique peut prendre différentes formes selon la façon dont les régions à basse pression sont générées, et elles peuvent être divisées en trois groupes:

- Cavitation à bulles itinérantes. Les bulles individuelles proviennent de régions de début de cavitation suite à la croissance rapide des noyaux de cavitation. Ils sont d'abord transportés par le flux puis implosent lorsqu'ils atteignent des zones de haute pression.
- Cavitation attachée. Il apparaît dans une région séparée par basse pression proche de la surface solide. Les scénarios d'écoulement typiques sont des cavités se formant du côté aspiration d'un hydroptère ou d'une aube de turbine. Si la longueur de la cavité attachée dépasse le corps sur lequel elle se développe, on parle de super cavitation, sinon on parle de cavitation partielle.
- Cavitation vortex. Le fluide dans les noyaux des tourbillons a tendance à se vaporiser en raison des basses pressions qui y règnent. Il est couramment observé aux extrémités des pales d'hélices ou dans les couches de cisaillement libre où peuvent se développer des tourbillons de Kelvin-Helmholtz.

Dans la plupart des applications hydrauliques comme les turbomachines et les hélices marines, la cavitation est un phénomène indésirable, car le comportement instable et l'effondrement violent de la cavitation peuvent entraîner des effets néfastes, tels que le bruit,

les vibrations du système, la diminution des performances, l'érosion des matériaux, etc. dans certains cas, la cavitation peut avoir des conséquences positives. Par exemple, les torpilles sont enveloppées dans une super-cavité stable pour réduire les frottements avec l'eau, afin qu'elles puissent atteindre des vitesses très élevées (environ 400 km/h). L'énergie intensive libérée par une cavité qui s'effondre pourrait être utilisée pour détruire les calculs rénaux pour le traitement ou pour tuer les bactéries vivantes pour le nettoyage des eaux usées.

Bien que la cavitation ait été largement étudiée depuis plus d'un siècle, une compréhension complète des processus physiques sous-jacents aux écoulements de cavitation est encore loin d'être réalisée à l'heure actuelle. Ceci est principalement dû au manque de données expérimentales quantitatives sur les structures biphasées et la dynamique de la cavitation. Par conséquent, des mesures haute fidélité et détaillées des champs d'écoulement de cavitation, notamment dans les zones de mélange diphasique opaque, sont extrêmement recherchées pour une meilleure connaissance des mécanismes physiques régissant les instabilités de cavitation. Cela permettra de déduire des moyens efficaces pour contrôler les conséquences négatives de la cavitation et augmenter son influence positive. De plus, les données expérimentales quantitatives peuvent être utilisées pour valider et améliorer les modèles de simulation numérique pour la cavitation. Une fois que des prévisions fiables sont réalisées, les coûts et le temps relatifs aux essais de cavitation seront considérablement réduits.

1.2. Aperçu de la thèse

Suite aux travaux précédents de notre groupe (Coutier-Delgosha et al.2009; Khelifa et al.2017), la cavitation partielle développée dans de petits canaux convergents-divergents (Venturi) a été étudiée expérimentalement à l'aide d'une technique d'imagerie par rayons X synchrotron ultra-rapide assistée. avec la photographie conventionnelle à grande vitesse ainsi que la vélocimétrie d'image de particules (PIV). En fonction des conditions de fonctionnement et des dimensions géométriques différentes, la cavitation partielle présentait généralement deux régimes avec des comportements distincts: la cavitation en nappe quasi-stable et la cavitation nuageuse périodique avec une grande évacuation de vapeur. Les résultats de la mesure dans la présente étude ont fourni une description détaillée des structures et de la dynamique de l'écoulement diphasique dans la cavitation en feuille. Trois mécanismes responsables de la transition de la cavitation feuille à nuage ont été mis en évidence et les différences entre eux ont été mises en évidence.

Cette thèse est composée des 7 chapitres suivants. Le chapitre 2 est une revue de la littérature sur le contexte physique de la cavitation en nappe / nuage et les techniques expérimentales existantes appliquées aux écoulements de cavitation. Le chapitre 3 fournit une brève description de la configuration expérimentale et de la technique d'imagerie rapide par rayons X. L'accent de ce chapitre est mis sur les procédures allant des visualisations aux mesures de vitesse et de champ de fraction de vide dans les écoulements de cavitation. Dans le chapitre 4, les structures d'écoulement diphasiques complexes à l'intérieur de la cavité de la feuille sont révélées en détail sur la base des données des mesures aux rayons X. Le chapitre 5 traite d'une étude comparative de la cavitation des plaques à trois stades (stade précoce, stade intermédiaire et stade développé). La comparaison montre l'effet des comportements des jets rentrants sur les structures et la dynamique des cavités de la feuille. L'influence de la cavitation sur les fluctuations turbulentes est également discutée. Le chapitre 6 analyse les écoulements de cavitation dans un canal Venturi avec des espaces latéraux. On constate que la cavitation des nuages peut être supprimée en modifiant le trajet de propagation du jet rentrant. Dans le chapitre 7, trois mécanismes (à savoir le mécanisme de jet rentrant, le mécanisme de choc de condensation et le mécanisme d'onde de pression induite par l'effondrement) pour initier la cavitation des nuages sont décrits en détail, et les raisons provoquant l'effet d'échelle sur les écoulements de cavitation Venturi sont discutées. La thèse se termine par une conclusion générale au chapitre 8 résumant les principales contributions de ce travail et plusieurs perspectives de recherches futures sont proposées.

Chapter 2

Physical background and measurement techniques

2.1. Sheet and cloud cavitation

Generally speaking, partial cavities have two forms of appearance as well in case of internal flows (in a Venturi) as in case of external flows (on a hydrofoil). For small incident angles (hydrofoil – angle of attack; Venturi – divergent and convergent angles) and high free-stream cavitation numbers, the attached cavity appears to be stationary at a fixed location, and the observed cavity length is rather constant. This situation is referred to as sheet cavitation. A typical sheet cavitation forming on the suction side of a hydrofoil or on the divergent wall of a Venturi channel is presented in Figure 2.1. When the cavitation number is decreased or/and the incident angle is increased to a certain extent, the stable sheet cavity cannot be sustained. A large portion of the cavity is shed periodically from the main cavity forming a cloud-like structure in the cavity wake, and as a result the cavity length undergoes significant oscillations. This phenomenon is commonly called cloud cavitation. Figure 2.2 shows two examples of cloud shedding.

Although cavitation is inherently unsteady, sheet cavitation is usually stated to be stable or quasi-stable since the shedding of small vapour-filled vortices is confined in the cavity closure region, whose characteristic length scale is much smaller than the whole cavity length. Sheet cavitation is sometimes described to be an open cavity due to its frothy appearance at the closure as classified by Laberteaux & Ceccio (2001a). In contrast, cloud cavitation results in large fluctuations of cavity volume and thus is stated to be unstable. The violent collapse of the shed cloud in the downstream wake region can emit pressure waves of high amplitude, which is considered as the main source of noise and erosion (Reisman et al. 1998; Dular et al. 2015). Therefore, cloud cavitation is much more destructive than a stable sheet cavity.

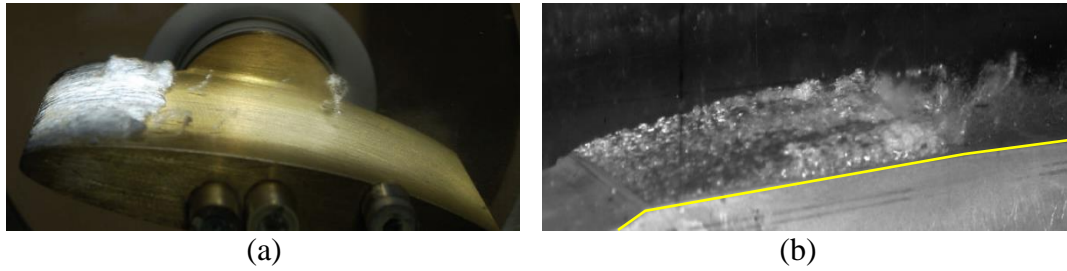


Figure 2.1. (a) Sheet cavitation on the suction side of a hydrofoil from Foeth (2008b); (b) sheet cavitation on the divergent wall of a Venturi channel from Barre et al. (2009).

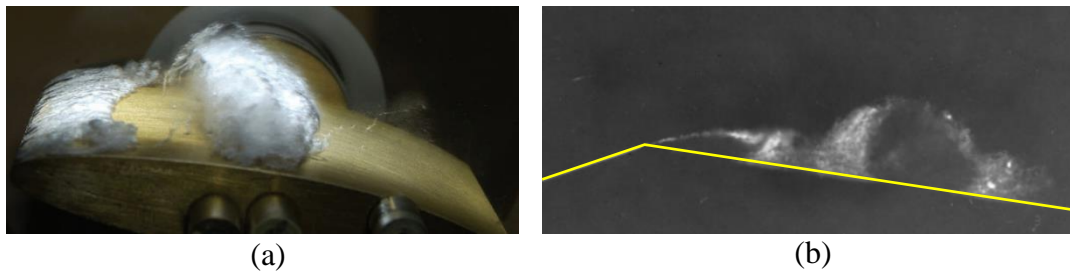


Figure 2.2. (a) Cloud cavitation on the suction side of a hydrofoil from Foeth (2008b); (b) cloud cavitation on the divergent wall of a Venturi channel from Stutz & Reboud (1997a).

2.2. Mechanisms for cloud shedding

In a classical point of view, the different behaviors of a partial cavity depend on the existence or absence of re-entrant flow originating from a stagnation point behind the cavity closure.

As for sheet cavitation (open partial cavities), Gopalan & Katz (2000), Callenaere et al. (2001) and Laberteaux & Ceccio (2001a) concluded that no clear re-entrant jet or only the weak reverse flow existed at the trailing edge of the cavity due to weak adverse pressure gradient. Leroux et al. (2004) did not detect a clear sign of a pressure wave traveling from the cavity closure towards the leading edge inside a stable sheet cavity through ten aligned pressure transducers flush-mounted along the suction side of a hydrofoil, and they attributed it to the absence of the re-entrant jet. Barre et al. (2009) measured a clear re-entrant flow in a globally-steady sheet cavitation using a double optical probe technique. However, in their simultaneous numerical simulation, the re-entrant jet was not predicted, and eventually they did not further clarify the role played by the re-entrant jet in stable sheet cavitation. In general, the absence of re-entrant flow was regarded as the main reason for the stable flow regime of sheet cavitation.

The periodic shedding of large cloud was observed firstly by Knapp (1955) and he proposed a re-entrant jet model to explain the transition from stable sheet cavitation to periodic

cloud cavitation. This re-entrant jet mechanism is presented schematically in Figure 2.3. As the attached cavity grows to a certain length, a thin re-entrant jet, mainly composed of liquid, forms near the cavity closure region and moves upstream beneath the cavity. When this jet reaches the cavity leading edge, the whole cavity is pinched off forming a rolling cavitation cloud that is then convected downstream by the main flow until it collapses. Meanwhile a new cavity begins to grow again and the entire process is repeated.

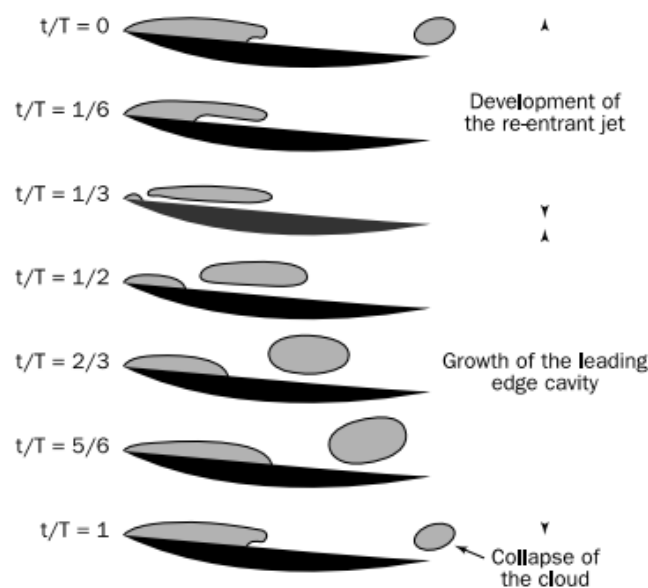


Figure 2.3. Typical unsteady behavior of a partial cavity with the development of a re-entrant jet and the periodic shedding of cavitation clouds from Franc & Michel (2005).

After the establishment of the re-entrant jet model, many studies have been conducted in order to verify the existence, development, the correlation of re-entrant jet with cavitation dynamics. Furness & Hutton (1975) predicted the development of re-entrant jet using a potential flow model. The injection of ink was used by Le et al. (1993) to visualize the re-entrant flow, and the ink was observed near the leading edge, confirming an upstream flow component. Kawanami et al. (1997) placed a small obstacle on the suction side of a hydrofoil to prevent the re-entrant jet from moving upstream, and the large cloud shedding was not observed in the experiment, demonstrating the re-entrant jet was the primary cause of cloud cavitation. Pham et al. (1999) placed a series of six electrical impedance probes spaced equally on the upper flat surface of the hydrofoil to detect the liquid front corresponding to the re-entrant jet. They found that the mean velocity of the re-entrant jet attained a maximum value

near the cavity closure region and was of the same order of magnitude as the free stream velocity. Laberteaux & Ceccio (2001b) observed that a geometry with spanwise variation can sustain stable cavities with re-entrant flow since the re-entrant flow was directed away from the cavity. The conditions necessary for the development of the re-entrant jet has been explored by Callenaere et al. (2001). They confirmed the critical role of the adverse pressure gradient at the cavity closure in the onset of the re-entrant jet instability.

In the numerical simulation of cloud cavitation, the RANS models generally overestimate the turbulent viscosity in the rear part of the cavity. The re-entrant jet is consequently stopped too early and it does not result in any cavity break off. Coutier-Delgosha et al. (2003) reproduced the periodic cloud shedding in a Venturi-type section by using a correction initially proposed in Reboud et al. (1998) on turbulent viscosity which actually reduces the friction losses that the re-entrant jet encounters. Pelz et al. (2017) introduced a physical model of transition from sheet to cloud cavitation based on the criterion that the transition occurs when the re-entrant jet reaches the point of origin of the sheet cavity. A good agreement was found between the model-based calculations and the experimental measurements. Their numerical work could also demonstrate the importance of re-entrant jet to initiate cloud cavitation.

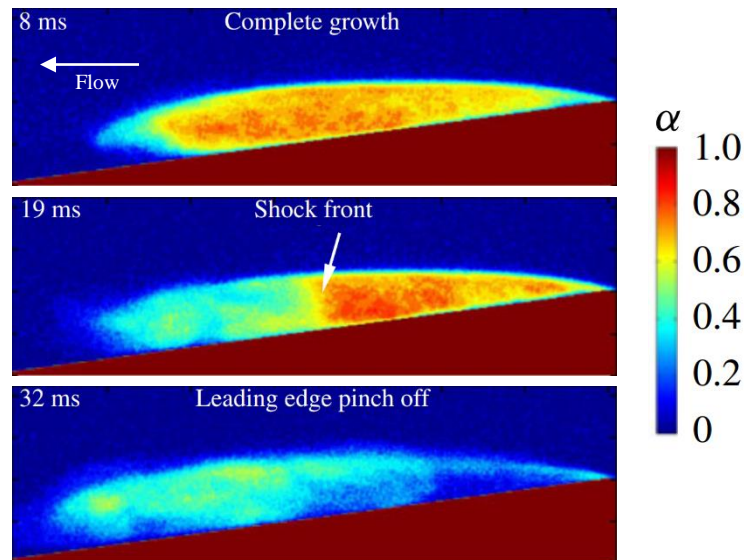


Figure 2.4. Instantaneous void fraction fields illustrating the condensation shock mechanism to cause sheet-to-cloud cavitation from Ganesh et al. (2016).

In addition to the classical re-entrant jet, the mechanism of condensation shock waves dictating sheet-to-cloud shedding has been widely acknowledged in recent years. As early as

1964, the occurrence of condensation shocks in cavitating flows was speculated by Jakobsen (1964) based on the fact that the sound speed in a two-phase mixture is significantly lower than that in either component, i.e. water or water vapour (Brennen 1995). However, the direct experimental observation was made only recently by Ganesh et al. (2016). As shown in Figure 2.4, using X-ray densitometry to visualize the instantaneous distribution of vapour volume fraction in the cavitating flow over a wedge, they found that the leading edge cloud shedding at lower cavitation numbers was resulted from an upstream propagating void fraction discontinuity, i.e. a condensation shock front. In order to demonstrate this new finding different from the classical re-entrant jet mechanism, Ganesh et al. (2017) also placed a small obstacle under the sheet cavity just like what Kawanami et al. (1997) did. The results showed that cloud shedding in the case of condensation shocks cannot be prevented since the condensation front spans the entire cavity height rather than near the wall only.

Motivated by the pioneering work of Ganesh et al. (2016), many interesting numerical and experimental studies were performed later towards revealing the condensation shock mechanism in different configurations (e.g. Wu et al. 2017; Jahangir et al. 2018; Budich et al. 2018; Wu et al. 2019; Trummler et al. 2020; Bhatt & Mahesh 2020). In agreement with the original experiment, all these works found that with a sufficient reduction of the cavitation number, condensation shocks overtaking re-entrant jets became the dominant mechanism for large-scale cloud shedding. Nevertheless, they had divergence on the cause for the onset of condensation shock. In the PhD thesis of Ganesh (2015), it was described that a rapid growth in cavity length and vapour content, hence reduced speed of sound and increased compressibility, resulted in the production of shock waves at the rear of the cavity. Wu et al. (2017), Jahangir et al. (2018) and Bhatt & Mahesh (2020) observed that the propagation of condensation shocks was triggered by the impingement of collapse-induced pressure waves from previously shed clouds. This was also found by Budich et al. (2018), but in addition they also captured the initiation of condensation shocks in the absence of cloud collapsing. It implied that both the rapid cavity growth and the collapse-induced pressure wave could contribute to the formation of overpressure behind the cavity which was sufficient to induce a condensation shock front. It should be noted that a pressure wave with high amplitude emanating from a large cloud collapse might crush the growing cavity suddenly as described by Leroux et al. (2005), which was different from the propagation of condensation shock through the cavity.

2.3. Studies on cavitation-turbulence interactions

The cavitation dynamics is also strongly related to the cavitation / turbulence coupling: the effect of cavitation (including formation and collapse of vapour cavities) on turbulence has been investigated numerically and experimentally.

As for the numerical aspect, Dittakavi et al. (2010) used large eddy simulation (LES) to predict cavitating flows in a Venturi nozzle. By comparison of three cases at different cavitation numbers, they concluded that the vapour formation due to cavitation suppressed turbulent velocity fluctuations and the collapse of vapour structures in the downstream region was a major source of vorticity production, resulting in a substantial increase of turbulent kinetic energy. Xing et al. (2005) observed, in their numerical simulation of vortex cavitation in a submerged jet, that cavitation suppressed jet growth and decreased velocity fluctuations within the vaporous regions of the jet. Gnanaskandan & Mahesh (2016) investigated partial cavitating flows over a wedge and found that the streamwise velocity fluctuations dominated the other two components within the cavity, while all three components of fluctuations were equally significant near the cavity closure and downstream of the cavity,

Regarding the experimental aspect, the acquisition of quantitative velocity fields mainly relied on PIV measurements. Gopalan & Katz (2000) and Laberteaux & Ceccio (2001) observed the largest turbulent fluctuations in the region downstream of the cavity which were regarded as the impact of vapour collapse. Iyer & Ceccio (2002) investigated the effect of developed cavitation on the flow downstream of the cavitating shear layer. They found that the collapse of vapour bubbles led the streamwise velocity fluctuations to be increased but the cross-stream fluctuations and the Reynolds shear stress to be decreased. Aeschlimann et al. (2011b) performed velocity measurements in a 2D cavitating shear layer. They observed that a complex combination of the production of vapour bubbles coupled with their collapse added additional velocity fluctuations, mostly in the main flow direction, while the turbulent shear stresses almost remained constant.

2.4. A review of measurement techniques for cavitating flows

Detailed flow measurements are essential for the understanding of cavitating flows. Due to the existence of non-transparent liquid/vapour mixtures, visual observation by a fast speed camera (high speed photography) is the most straightforward and widely-used method to capture the temporal evolution of cavitation structures, thereby providing insight into the underlying physics (Foeth et al. 2008a; Aeschlimann et al. 2012). Through post-processing of

the high speed video images, it is possible to derive some quantitative data, such as the cloud shedding frequency and the cavity growth rate (Prothin et al. 2016; Jahangir et al. 2018). Synchronized with dynamic pressure measurements, high speed images can also reveal the pressure change associated with the cavity unsteady behaviors (Wang et al. 2017; Wu et al. 2017). On one hand, cavitation visibility helps to obtain its global flow characteristics. On the other hand, cavitation opacity hinders the measurements inside the two-phase region. In order to analyze the internal flow structures of cavitation, other techniques, able to visualize the two-phase morphology as well as measure quantitative data on void fraction and velocity, are required.

2.4.1. Local measurements by intrusive probes

Ceccio & Brennen (1991) detected individual vapour bubbles using a network of silver electrodes mounted on the surface of a hydrofoil, and thus acquired their velocities. Stutz & Reboud (1997a; 1997b; 2000) used a double optical probe to measure the time-averaged void fraction and vapour-phase velocity inside the cavity generated in a two-dimensional Venturi-type section. In this technique, the local velocity was estimated by the time interval of a bubble passing two probe tips successively and the local void fraction was defined as the ratio of the cumulated time of vapour phase at the tip of the probe to a given time of observation. In spite of a relative large measurement uncertainty of about 15%, their work gave a preliminary description of the two-phase flow structure inside a sheet cavity and confirmed the presence of a reverse flow along the solid surface. Coutier-Delgosha et al. (2006) made the first attempt to visualize the two-phase morphology inside the sheet cavity by means of a new endoscopic device. Based on the observation at different stations along the hydrofoil chord, they found that the internal structure close to the leading edge was characterized by large vapour bubbles with a similar critical size and then they were rapidly split into smaller bubbles downstream; most of the bubbles do not have a spherical shape.

2.4.2. Particle Image Velocimetry (PIV)

Different from intrusive and pointwise measurements using probes, PIV enables a whole-field acquisition of instantaneous velocity vectors with little perturbation on the flow. It has thus been applied to a wide range of fluid flows, but in cavitating flows, the strong scattering and reflection from the liquid/vapour mixture will obscure the scattering light from the

surrounding tracer particles. This contaminating effect on the PIV measurements can be avoided by injecting laser-induced fluorescent (LIF) particles which emit light with different wavelength from the laser. The reflected and scattered light, at the wavelength of the laser, is blocked by the optical filter mounted in front of the lens and only the light emitted by the particles is recorded by the camera. However, if there are many vapour bubbles passing between the laser sheet and the camera, the optical paths starting from the fluorescent particles will be deviated severely or blocked completely. As a consequence, most PIV-LIF measurements have focused on the liquid flow regions outside the cavity (Laberteaux & Ceccio 2001; Foeth et al. 2006; Kravtsova et al. 2014) or turbulent cavitating regions with low void fraction (Iyer & Ceccio 2002; Aeschlimann et al. 2011b). Interestingly, the work of Dular et al. (2005) shows that if the position of the laser sheet was close enough to the observation window (~5 mm), the detected particles would be sufficient to evaluate the velocity field inside the sheet cavity. However, the measured velocity field is not representative since it is strongly subjected to the wall effects.

2.4.3. X-ray densitometry based on absorption contrast

Both X-rays and visible light are, in nature, part of the electromagnetic spectrum. However, due to having a much shorter wavelength than visible light, X-rays can penetrate most optically opaque media with weak interactions. This distinct advantage makes X-ray radiography a powerful method to visualize opaque multiphase flows (Heindel 2011).

For cavitating flows, X-ray radiography can be used to measure local void fraction, i.e. density because of the absorption difference between water and vapour. Stutz & Legoupil (2003) applied firstly the X-ray densitometry to cloud cavitation formed in a Venturi-type test section. They found that the mean void fraction varies regularly from 25% at the upstream end of the mean cavity to 10% in the downstream part. Coutier-Delgosha et al. (2007) performed void fraction measurements of cavitation on a plano-convex hydrofoil using the same X-ray attenuation device. They reported that the local mean vapour volume fraction does not exceed 35 % for small sheet cavities, and 60 % for the large ones. Another application of X-ray attenuation measurements can be found in Aeschlimann et al. (2011a) where the main vortex shedding frequency in a turbulent cavitating shear layer was estimated through spectral analysis of the void fraction signal. In recent works (Ganesh et al. 2016; Wu et al. 2019), time-resolved X-ray densitometry was used to measure the instantaneous distribution of void fraction in the

cavitating flow field. A well-defined void-fraction discontinuity spanning the thickness of the cavity was observed to propagate upstream. According to the authors, this discontinuity represented a bubbly shock front which was responsible for periodic shedding of large-scale vapour clouds.

A standard 2D X-ray densitometry system can only provide a projection of the sample's density distribution in the direction of the X-ray beam. This means that the 3D flow information is collapsed onto a single 2D plane. As a remedy, the actual 3D spatial distribution can be retrieved using a tomographic reconstruction. The examples of using X-ray computed tomography (CT) to measure the radial distribution of void fraction in circular nozzle cavitating flows can be found in Bauer et al. (2018) and Jahangir et al. (2019).

2.4.4. X-ray velocimetry based on phase contrast

X-ray phase-contrast imaging enables clear visualization of boundaries between phases with different refractive index (Kastengren & Powell 2014). Aside from detailed illustration of two-phase morphology (Karathanassis et al. 2018), X-ray phase-contrast images can also be used to perform velocimetry by tracking either seeded particles or phase interfaces. Early applications of X-ray velocimetry are for solving the so-called optical access issue. For example, Lee & Kim (2003) employed a low-energy synchrotron X-ray beam instead of a laser sheet to illuminate the seeded particles in the flow in an opaque tube. The instantaneous velocity field was extracted by cross-correction similar to the conventional PIV analysis. For opaque flows with a very low speed (a few millimeters per second), they also developed a compact X-ray-based PIV system employing a medical X-ray tube as a light source (Lee et al. 2009).

For high speed fluid flows, a short exposure time is needed to freeze the fluid motion. The third-generation synchrotron radiation sources such as the advanced photon source (APS) at Argonne National Lab can produce a high-energy and coherent X-ray beam which satisfies the requirements of ultra-fast X-ray phase-contrast imaging. Im et al. (2007) used the APS X-ray source to greatly improve the particle image quality making single-particle tracking velocimetry possible in an optically opaque vessel. Wang et al. (2008) revealed for the first time the internal structures of high-speed (order of 60 m/s) optically dense sprays near the nozzle exit using the ultrafast APS X-ray phase-contrast imaging technique. The velocity fields were measured by tracking the movements of the phase enhanced liquid–gas boundaries. A

similar application of synchrotron X-ray phase-contrast imaging in fuel injector nozzles was presented by Moon (2016) for comparing the dynamic structure of biodiesel and conventional fuel sprays.

The first attempt to measure velocity field inside cavitating regions by means of fast X-ray image was described by Coutier-Delgosha et al. (2009). Later Khelifa et al. (2017) also used the similar method to measure high speed cavitating flows in a small size Venturi-type test section. In the experiment, the flows were seeded with silver-coated hollow glass sphere particles which were visualized clearly along with the bubbly structures of cavitation by combined effects of X-ray absorption and phase contrast enhancement. Cross-correlation algorithms were applied on the particles and the bubble structures to evaluate the liquid-phase and the vapor-phase velocities respectively. Furthermore, the distribution of vapour volume fraction was determined from X-ray absorption difference in vapour and liquid. Based on the experimental results, the presence of significant slip velocities between the liquid and vapour phase was demonstrated quantitatively for the first time. Their work laid a foundation for the present study on flow structures and dynamics inside sheet cavities.

Chapter 3

Fast X-ray imaging technique and quantitative data extraction based on image post-processing

The time-resolved, whole-field measurements inside a partial cavity have always been challenging due to the opaqueness of the liquid/vapour mixture. The lack of experimental data on the internal two-phase flow structures and dynamics has been a major issue for the understanding of the cavitation physics and the validation of the numerical models. Motivated by solving this problem, our group has developed in the last 13 years an ultra-fast X-ray imaging technique applied to situations of cavitating flows in a 2D Venturi-type section. Such a technique enables to obtain by image processing i) the liquid velocity field (tracking the motion of the seeding particles), ii) the vapour velocity field (tracking the motion of the vapour bubbles), and iii) the distribution of the vapor volume fraction (based on the difference of X-ray absorption in vapour and water). In this chapter, a brief description of the fast X-ray imaging technique will be given, and the emphasis will be put on the procedures to obtain the velocity and void fraction fields, from the flow visualizations.

3.1. Hydraulic test rig

The studied sheet cavitation is generated in a small size Venturi-type test section installed in a closed hydraulic loop designed by Coutier-Delgosha et al. (2009) as shown in Figure 3.1. During the experiments, the test loop is filled with water driven by a circulating pump. The flow rate measured by a turbine flow meter is regulated by a frequency inverter varying the pump rotation speed. A secondary recirculation loop is added to attain small flow rates while avoiding the pump operating in off-design conditions. Different extent of cavitation could be set properly by adjusting the pressure on the free surface of the tank with the aid of a vacuum

pump or a pressurizer. A heater combined with a cooling system is employed enabling the flow temperature to stabilize at a given value that is measured by a thermocouple located upstream of the test section.

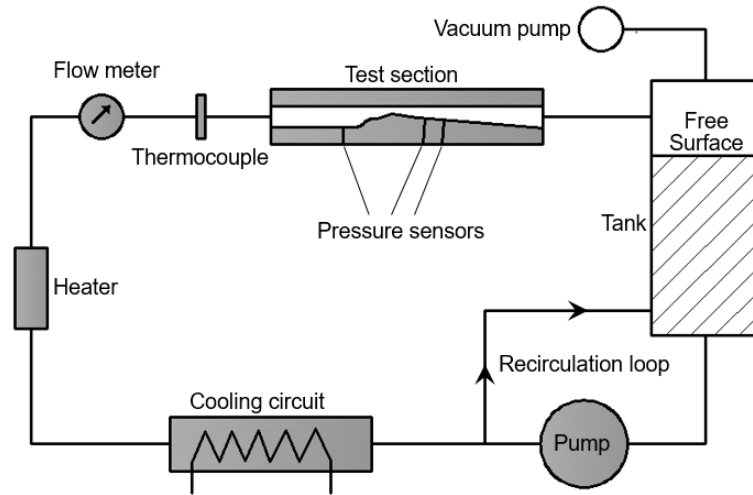


Figure 3.1. Schematic of the cavitation tunnel.

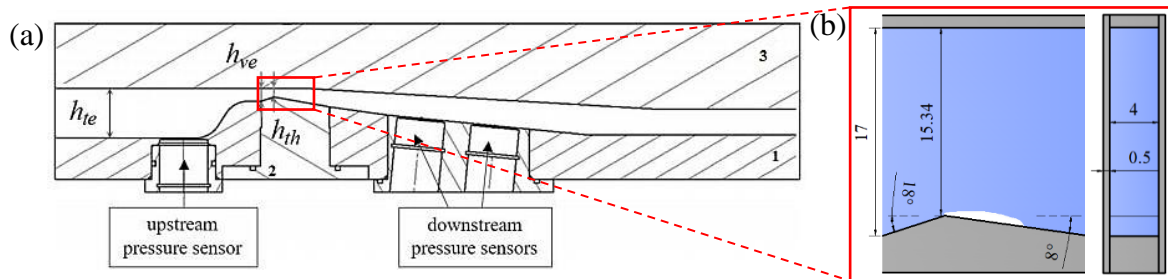


Figure 3.2. (a) Profile of Venturi-type test section; the convergent-divergent channel is formed by the lower insert part (2) with the confinement of the top wall (3); flow direction is from left to right, (b) detailed dimensions of the convergent-divergent section (in mm).

The overall test section 30 cm long is presented in Figure 3.2. The lower part (2) is inserted into the bottom wall (1) forming the convergent-divergent flow channel with the confinement of the top wall (3). The Venturi has a rectangular cross section and is characterized by a convergent angle of 18° and a divergent angle of 8° . The width of the flow passage is 4 mm. The height h_{ve} at the Venturi entrance is 17 mm with $h_{th} = 15.34$ mm at the throat producing a small contraction ratio of 1.1. The height h_{te} of the test section entrance is 31 mm. The thickness of each Plexiglas side wall is reduced as less as 0.5 mm in order to decrease X-ray energy absorbed by non-fluid parts. Three pressure transducers are flush mounted on the bottom wall

of the test section. The upstream one is used to determine the inlet pressure P_{in} for calculating the cavitation number σ :

$$\sigma = \frac{P_{in} - P_{vap}}{\frac{1}{2} \rho_l u_{in}^2} \quad (3.1)$$

where P_{vap} is the vapour pressure at the flow temperature, u_{in} is the average velocity at the cross section of upstream pressure sensor and ρ_l is the liquid density. The average velocity is computed according to the volume flow rate measured by a flow meter with a 2% reading uncertainty. The pressure sensors are calibrated in a range of 0–3 bar with a full scale uncertainty of 0.25%. The accuracy of the pressure and velocity measurements leads to an uncertainty of 3.5% in the cavitation number. The two downstream ones are used to detect possible oscillations of the sheet cavity formed at the throat.

3.2. X-ray imaging mechanisms

The X-ray imaging in this work is based on two different mechanisms: absorption contrast and phase contrast. The arrangement of in-line X-ray imaging system is depicted in Figure 3.3(a). The radiograph will be projected onto the x-y plane perpendicular to the optic axis z. R_1 and R_2 are the source to object distance and object to detector distance, respectively. Considering a sample of a spherical vapour bubble in water, the working principle of absorption-based X-ray imaging is illustrated in Figure 3.3(b). In this method, the detector is placed at the object exit surface $z = 0$. The contrast in the resulting image comes from the difference in the attenuation of X-ray energy since vapour has a smaller absorption coefficient than water. In phase-contrast X-ray imaging via free-space propagation as shown in Figure 3.3(c), the sharp contrast at the periphery of the recorded image results from Fresnel diffraction and the interference between neighboring points of the wavefront at a certain distance from the sample. To make phase effects detectable an appropriate propagation distance R_2 between the object and the detector is required and the X-ray beam must be (at least partially) spatially coherent. Note that absorption contrast still contributes to the intensity image acquired by the propagation-based phase contrast technique.

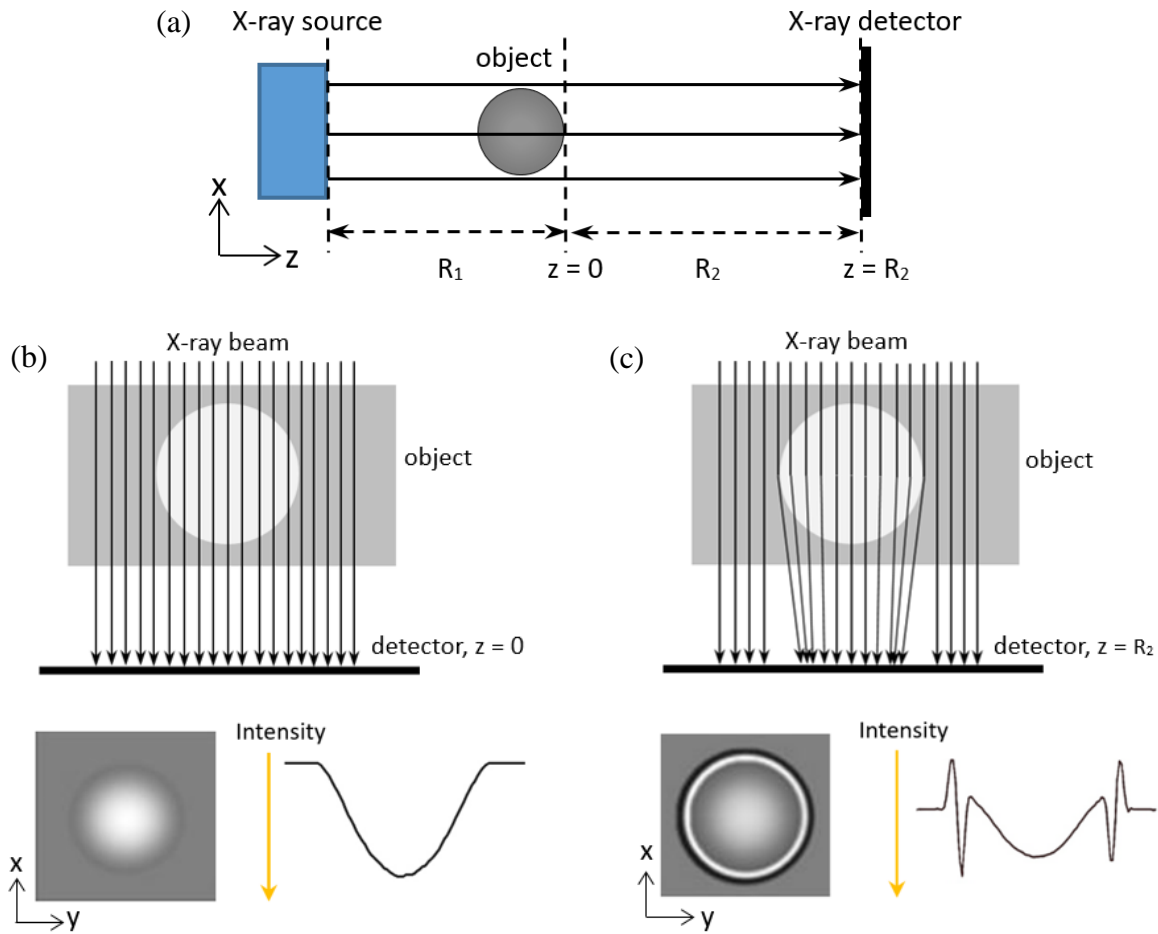


Figure 3.3. (a) Schematic of in-line X-ray imaging system; R_1 and R_2 are the source to object distance and object to detector distance, respectively. (b) Simple model for absorption contrast of X-ray imaging; the resulting image recorded at the exit-surface $z = 0$ is a two dimensional distribution of intensity. (c) Simple model for free-space propagation-based phase contrast of X-ray imaging; the resulting image recorded at a certain distance downstream $z = R_2$ is a two dimensional distribution of intensity.

3.3. X-ray imaging technique

The experiments were performed using the third generation synchrotron radiation at the Advanced Photon Source (APS) in USA where a high-energy and spatially coherent X-ray source is available. A complete description of the experimental method can be found in Khelifa (2014). Here a brief description is provided.

As illustrated in Figure 3.4(a), the X-ray source is aligned with the test section on one side and the X-ray detector (a scintillator) on the other side converting X-ray beam into visible light which is then recorded by the high speed CCD camera. The X-ray source emits two types of

pulses with a cross section of $1.7 \times 1.3 \text{ mm}^2$: a primary pulse with a duration of 500 ns and a secondary pulse with a duration of 100 ps. The time interval between two primary or secondary X-ray pulses is $3.68 \text{ }\mu\text{s}$. The source-to-object distance is about 60 m, and the object-to-detector distance is optimized to 50 cm for phase contrast enhancement.

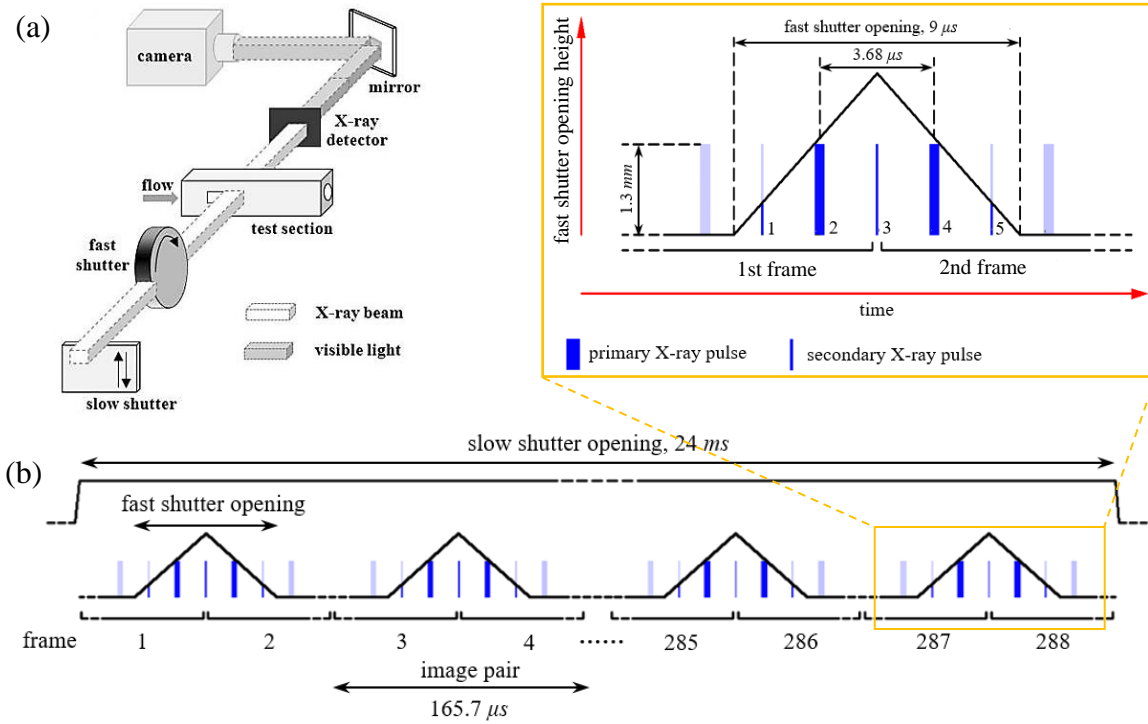


Figure 3.4. (a) Diagram showing light path of X-ray imaging system at the APS (from Khelifa et al. 2017). (b) Synchronization of the shutters, the X-ray pulses and the camera frames to acquire image pairs for PIV analysis.

In the beamline, the slow shutter, operating at a frequency of 1 Hz with an opening time of 24 ms, is equipped to protect the test section and the detector by reducing heat load on them. The fast shutter used is a mechanical rotating chopper which operates at a frequency of 6035 Hz with an opening time of $9 \text{ }\mu\text{s}$ (Gembicky et al. 2005). Figure 3.4(b) shows the synchronization scheme of the X-ray flashes, the two shutters, and the camera frames, to obtain appropriate pairs of images for PIV analysis. The camera frame transfer is triggered by the secondary pulse 3, so that each image in the same pair could obtain nearly identical illumination. The acquisition frequency of the camera is set to 12 070 fps (twice the fast shutter operating frequency), which enables a spatial resolution of 704×688 pixels with a pixel size of $2 \text{ }\mu\text{m}$. It should be noted that only a packet of 144 image pairs is recorded during the opening period of the slow shutter (24 ms per second).

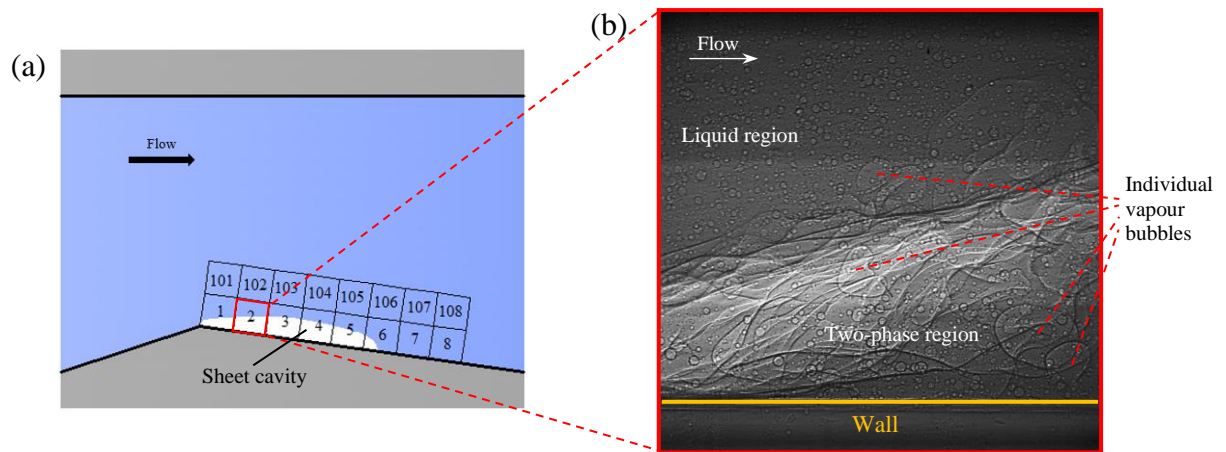


Figure 3.5. (a) Schematic of X-ray beam scanning positions; position 1 corresponds to the beginning of the cavity. The test section was moved to different positions enabling X-ray beam to scan the complete flow field of interest. (b) A representative raw X-ray image of cavitation recorded at the scanning window 2.

Silver-coated hollow glass spheres with nominal mean diameters of 10 and 17 μm were injected into the flow as tracers of the liquid phase. Because of the small cross section of the X-ray beam, successive but not simultaneous acquisitions at different positions are necessary to obtain the complete image for the flow field of interest as shown in Figure 3.5(a). To that end, the test section was moved parallel to the divergent floor of Venturi in front of the X-ray beamline by a motorized platform. At each position, 1872 pairs of images are recorded, which are actually divided equally into 13 packets (corresponding to the slow shutter opening 13 times), and thus the time between packets is not continuous.

Figure 3.5(b) presents a typical raw X-ray image of cavitation recorded at the second position. The bright band at the center results from extra partial exposure to a secondary X-ray pulse as indicated in Figure 3.4(b). In addition to absorption contrast, the X-ray phase contrast leads to a fringe pattern with sharp intensity variation along the phase interface, which allows a better visualization of the two-phase flow morphology and the seeded particles. As can be found in the raw radiograph, the vapour structures in the position close to the cavity leading edge are generally coherent except a few individual vapour bubbles identified. The seeded particles both inside and outside the cavity are also visualized clearly. They are much smaller and have relatively regular round shape, compared to individual vapour bubbles.

3.4. Data extraction based on image processing

Although the two-phase information is contained simultaneously in the X-ray images, the transition from visualization to quantitative measurement (e.g. velocity and void fraction fields) is not easy. In the conventional PIV images, a high signal-to-noise ratio (hence a distinct cross correlation peak) is achieved by large contrast in gray levels between particles and liquid background as the liquid can rarely scatter laser light. However, due to the relatively bright background associated with X-ray imaging mechanisms, the signal-to-noise ratio would drop greatly if the background is not removed from the X-ray image. In order to analyze the dynamics of each phase, image processing is required to extract the tracer particles from the liquid background and vapour structures so that velocimetry algorithms can be applied to each phase separately.

3.4.1. Separation of the two phases

The first attempt to separate the seeding particles and the vapour bubbles could be found in Khelifa et al. (2017) where the liquid background was eliminated based on the vapour volume fraction measurements and large areas of vapour structures were removed using a high-pass filter. This image processing method was greatly dependent on the accuracy of void fraction while the error could be $\pm 15\%$ according to their description if measurements of void fraction were performed using each individual image without pair averaging. In the present work, we employed a new wavelet-decomposition-based image processing method to separate the seeding particles from the non-uniform background of the liquid and the vapour structures. For a smooth narrative, the detailed description of procedures of this new method is provided in Section 3.6. The final result is presented in Figure 3.6. The particle image (Figure 3.6(b)) extracted from the raw X-ray image (Figure 3.6(a)) will be used for the measurements of liquid phase velocities. Figure 3.6(c) shows the remaining vapour structures which will be used for calculating the instantaneous velocity field of vapour phase. It should be pointed out that compared to the first attempt the same raw X-ray images were also used in the present study, nevertheless this new method is not dependent on the void fraction accuracy and is much less time-consuming (approximately 1/3 processing time with the same computing resources).

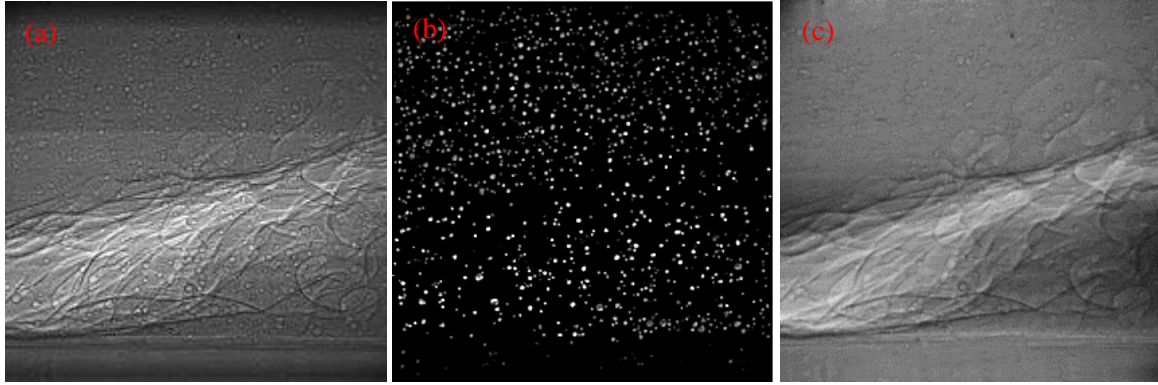


Figure 3.6. Result of image processing for separation of two phases. (a) Raw X-ray image of cavitation; (b) particle image for measurements of liquid phase velocities; (c) vapour structure image for measurements of gaseous phase velocities.

3.4.2. Void fraction measurement

The local void fraction α is defined as the ratio of the vapour volume to the total volume along any given beam path crossing the test section. The value represents the averaged void fraction in the spanwise direction. Since the vapour has a different X-ray attenuation coefficient from the liquid, the local vapour volume fraction α could be estimated quantitatively using Equation 3.2, derived from Lambert–Beer’s law,

$$\alpha = 1 - \frac{\ln\left(\frac{I_0}{I_\alpha}\right)}{\ln\left(\frac{I_0}{I_1}\right)} \quad (3.2)$$

where I_0 is the local intensity measured when the test section is completely filled with vapor (for convenience, vapour is replaced here with air as they almost have an identical absorption coefficient), I_1 is the local intensity measured when the test section is full of water, and I_α is the local intensity measured when cavitation occurs in the test section. For computing α , it is thus necessary to take the calibration images of air and water under the same acquisition conditions as the cavitation tests. Figure 3.7(a) and (b) show the calibration images for gaseous phase and liquid phase, respectively. They were obtained by averaging a large number of reference images corresponding to each phase. Figure 3.7(c) presents a processed image for the computation of void fraction. The aim of processing the raw image is to reduce the effect of imperfect synchronization and fringes due to X-ray phase contrast mechanism on void fraction measurements. The detailed processing procedures are provided in Section 3.7. The final result of instantaneous vapour volume fraction field is illustrated in Figure 3.7(d).

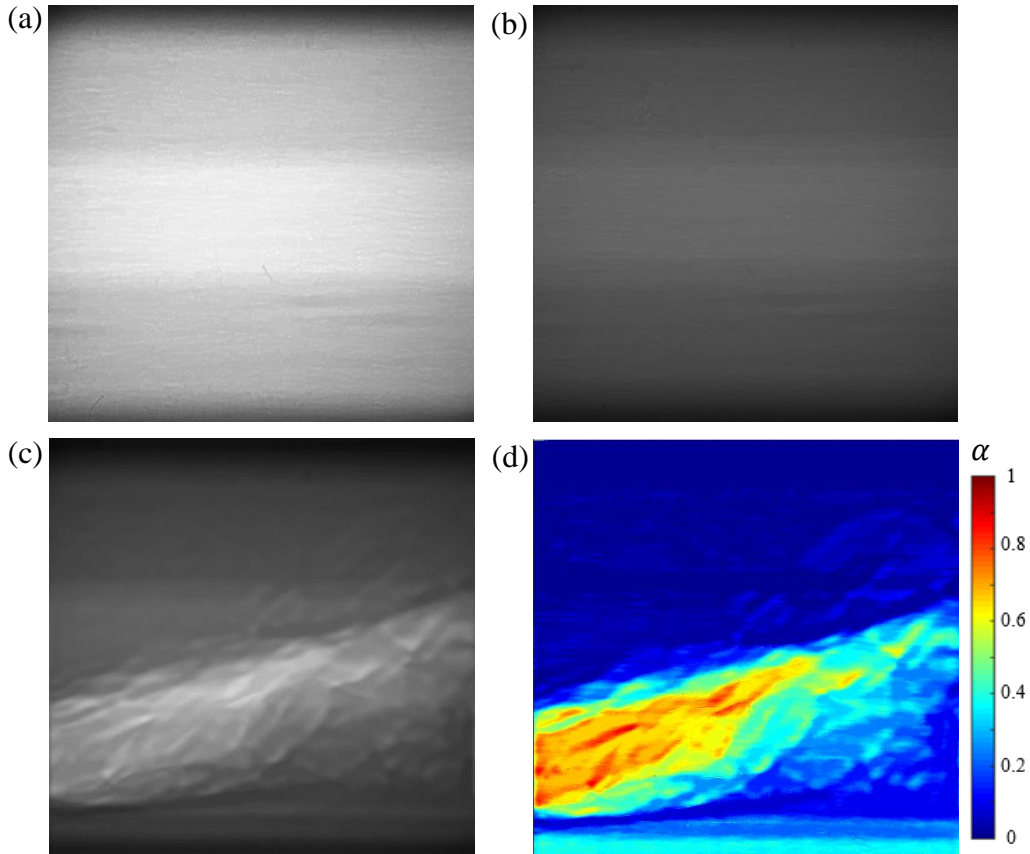


Figure 3.7. Measurements of vapour volume fractions, (a) calibration image of air; (b) calibration image of water; (c) processed image for computation of void fraction; (d) vapour volume fraction field.

3.4.3. Particle image velocimetry

Based on the MatPIV.1.6.1 open source toolbox, cross-correlation algorithm was applied on each pair of consecutive particle images obtained by the aforementioned image processing procedures to determine the corresponding liquid phase displacements. The time delay between the two pictures was $3.68 \mu\text{s}$. Four interrogation passes with window offset were carried out and the interrogation window size was progressively decreased in order to increase the spatial resolution.

In the first pass the interrogation window size was set to comply with the one quarter rule to limit in-plane loss of particle pairs. For instance, in the present case where the largest displacement estimated from the flow rate is 20 pixels, a window dimension of 80×70 pixels was chosen with a larger size in the streamwise direction. It should be noted that the correlation coefficient is computed directly in the spatial domain rather than using an FFT-based approach.

In spite of its low efficiency, this direct computation allows to eliminate the constraint of equal window size with the power of 2 (32×32 pixels, 64×64 pixels, etc.) required by FFT implementation, and it can be useful to reduce the velocity gradient effect in the direction perpendicular to the flow.

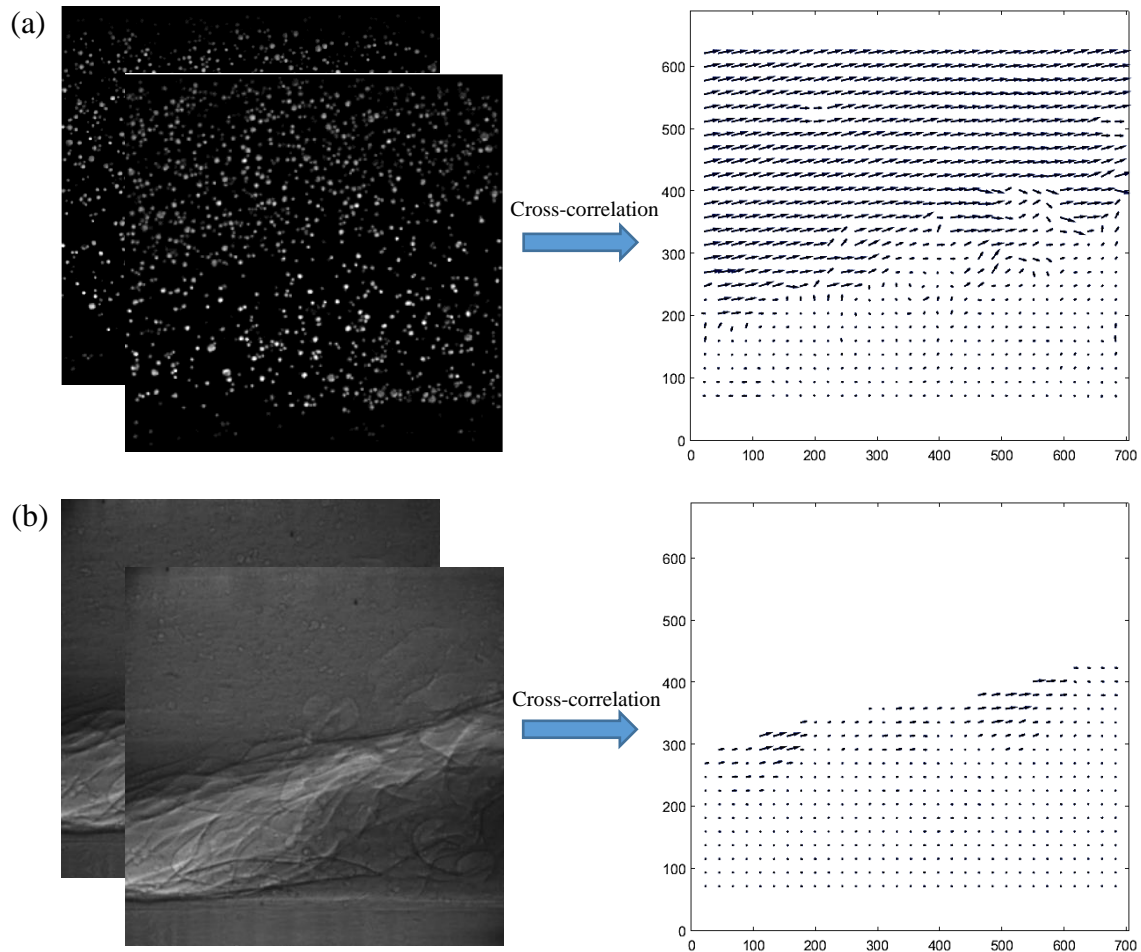


Figure 3.8. Instantaneous velocity vector field evaluated from an image pair, (a) liquid phase; (b) vapour phase.

In the next pass, the refined interrogation windows were shifted locally according to the integer displacement field evaluated from the first pass such that the proportion of matched particle pairs is increased. The final interrogation window size should be made sufficiently small to reduce velocity differences within the interrogation area, meanwhile it is also limited by the particle concentration. To ensure a good signal-to-noise ratio, at least 4 matched particle pairs are required in the last interrogation window. Thanks to the method we use to extract particles from vapour structures, it is easy to know the mean number of particles

(approximately 1200) in an X-ray image. Therefore, the minimum window size is estimated to be 40×40 pixels. Considering that the particle distribution is not strictly homogeneous, the last window size was enlarged slightly in the main flow direction into 50×40 pixels. This final window size determines the actual spatial resolution in the PIV data which implies that the turbulent structures with scales smaller than this size cannot be resolved.

In the studied cavitating flows, the local velocity field exhibits a strong shear even within the smallest interrogation window. It would make the signal-to-noise ratio decrease drastically and cause a large uncertainty in velocity measurements. In order to solve this problem in regions with high velocity gradient, an image deformation scheme (Raffel et al. 2007) was utilized in the last pass. The correlation peak was estimated with a sub-pixel accuracy by using the three-point Gaussian fitting scheme in two directions.

Figure 3.8(a) shows an instantaneous velocity vector field of the liquid phase evaluated through the above cross-correlation algorithm, in which the aberrant vectors detected by median test were rejected and then replaced by bilinear interpolation from their valid neighboring vectors. The two ends where illumination is not sufficient were excluded. Each pair of processed particle images produced 26×31 local velocity vectors spaced equally by 22 pixels ($44 \mu\text{m}$).

The same cross-correlation algorithms used for the liquid phase were also applied to each pair of vapour images. Since there are no seeding particles to trace the vapour phase, the cross-correlation is based on the variations of gray levels related to the presence of vapour bubble interfaces and the void ratio difference. Thanks to the calculated vapour volume fraction field, the liquid region was masked out. In practice the measurements of vapour velocities were activated only when the spatially-averaged void fraction within the final interrogation window is greater than 7%. Figure 3.8(b) presents the computed velocity field of the vapour phase.

The uncertainty of the velocity measurements for both phases were discussed in Khelifa et al. (2017). The cross-correlation accuracy of tracer particles was estimated by generating synthetic images of a cavitating flow with imposed particle displacements. The comparison between imposed and measured values shows that the mean error of the liquid phase velocity measurements is around ± 0.24 m/s (approximately 3% of the reference velocity of the studied flow). The uncertainty in vapour phase velocity measurements was also estimated by imposing known displacements on vapour structures of a cavitating flow. The results indicated an error of around ± 0.46 m/s (approximately 5% of the reference velocity) for the vapour phase.

3.5. Comparison between conventional laser PIV and X-ray PIV

Unlike the standard PIV measurements where only the particles in a given plane are illuminated with a thin laser sheet, all particles and bubbles along the beam path are projected into the X-ray image due to the line-of-sight nature associated with the X-ray imaging method. Therefore, the standard PIV result represents the 2D velocity field in the illuminated plane while the X-ray PIV result is the span-averaged velocity field containing amassed flow information in the spanwise direction. Lee & Kim (2003) reports the velocity profile in an opaque circular pipe measured by the X-ray PIV method, where the measured velocity at the pipe center is only two-thirds of the theoretical value. This discrepancy is attributed to the three-dimensionality of the laminar flow boundary layer given a mean velocity of 0.5 mm/s in an opaque Teflon tube with an inner diameter of 750 μm .

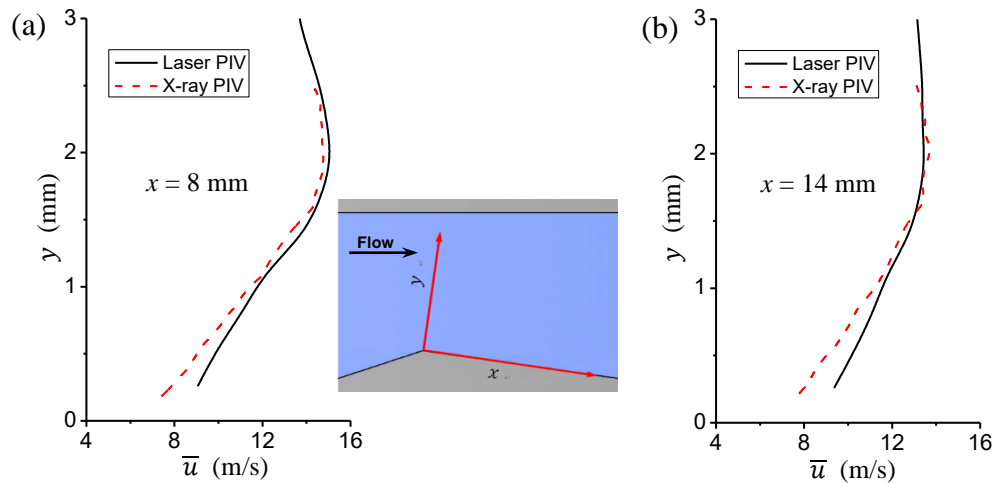


Figure 3.9. Comparison of mean streamwise velocity (\bar{u}) profiles at two locations measured by the standard PIV and the X-ray PIV in the non-cavitating condition, (a) $x=8 \text{ mm}$; (b) $x=14 \text{ mm}$.

The standard PIV measurements under the non-cavitating condition was also carried out in the Venturi-type test section in order to examine the two-dimensionality of the flow. The central plane of the Venturi channel was illuminated by a thin laser sheet of 1 mm thickness, thus allowing 2D velocity measurements less affected by the two side walls. As shown in Figure 3.9, the mean streamwise velocity profiles measured by the standard PIV and the X-ray PIV are compared quantitatively with each other at two different distances from the Venturi throat ($x=8 \text{ mm}$ and $x=14 \text{ mm}$). Note that the x -axis is along the Venturi divergent floor and the origin is located at the apex of the Venturi throat (indicated in the inset of Figure 3.9). As

can be seen, the velocity profile acquired by X-ray agrees well with the standard PIV result away from the bottom wall, which indicates that the flow is almost two dimensional in this region. Nevertheless, the velocity difference adjacent to the bottom wall is relatively high indicating a certain extent of three dimensionality of the flow in this region, which might be caused by corner flows and relatively thick boundary layers on the two side walls.

3.6. Procedures of wavelet-decomposition-based image processing method

A raw X-ray image of cavitation shown in Figure 3.6(a) is taken here as an example to illustrate the procedures of extracting the particles from the raw image. As mentioned before, the imaging is based on a combination of absorption contrast and phase contrast. The identification of particles also relies on the traits of these two mechanisms.

A two-dimensional signal (an image for instance) can be decomposed into approximation components and detail components at different levels by the discrete wavelet transform. As shown in Figure 3.10(a), it is accomplished by convolving the original signal s with a low-pass filter and a high-pass filter simultaneously resulting in an approximation component a_1 and a detail component d_1 respectively. Note that the two filters are quadrature mirror filters associated with the selected wavelet function. This decomposition is repeated until the desired level to further increase the resolution scale using the same scheme, replacing the original signal s by a_1 and producing a_2 and d_2 , and so on. The level N corresponds to the scale of 2^N in the wavelet function.

Figure 3.10(c) presents the decomposition results by performing a 4-level discrete wavelet transform with the db5 wavelet function in the Matlab software. As shown in Figure 3.10(b), the part delimited by the red frame in the raw image is zoomed up for clarity. The reason of choosing db5 wavelet is that its shape matches quit well with the sharp fringe intensity variations due to the phase contrast mechanism. Observing the approximation component a_4 , we can know that there is no useful signals included in it (all particles are filtered out), so further decomposition is not necessary. The level of wavelet decomposition is therefore determined as 4. Observing the detail components from d_1 to d_4 , it is found that the different scales of signals are separately stored in detail components at different levels: the background high-frequency noise is primarily contained in d_1 ; most edge information of particles and vapour bubbles is contained in d_2 ; the interiors of particles are mainly contained in d_3 while only a small portion of particles of largest scales are contained in d_4 .

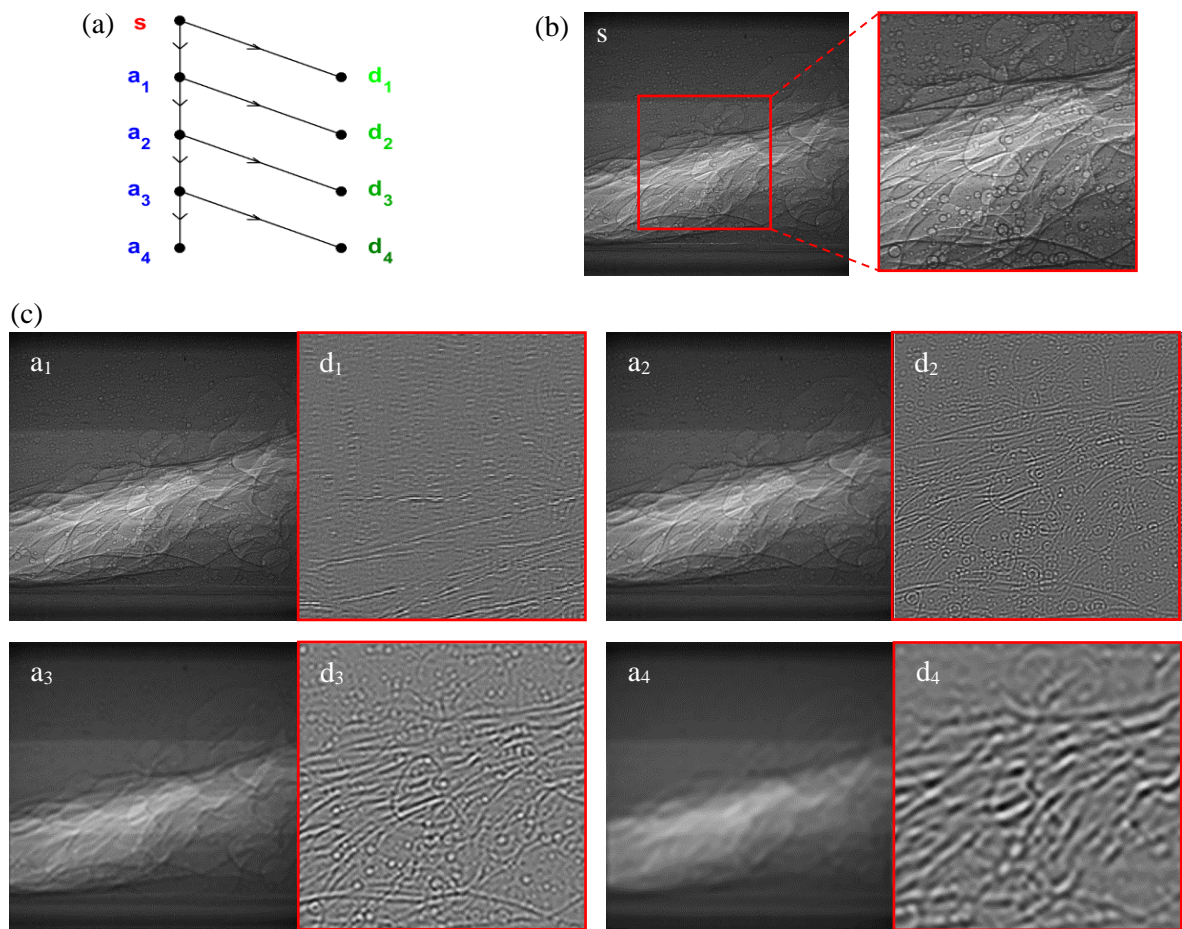


Figure 3.10. Discrete wavelet transform. (a) A binary tree of 4-level discrete wavelet transform; (b) raw X-ray image and the enlarged part; (c) wavelet decomposition results corresponding to the binary tree of 4-level discrete wavelet transform.

The phase contrast enhances the visibility of the edge. Therefore the first identification of particles is based on the detection of the edges with sharp contrast (i.e. large intensity gradient). In this case, we wish to highlight the boundaries of the particles rather than their interiors. This can be realized by choosing appropriate threshold values for each level from 1 to 4. In general, a relatively large threshold value is set for level 2 with small threshold values for the other levels since most edge information is contained in the detail component d_2 . In practice these threshold values were determined empirically in the Matlab graphical user interface tool – Wavemenu where it is convenient to adjust threshold values to obtain a subjectively optimal result. Figure 3.11(a) and (b) show the decomposition results using the threshold values determined from Wavemenu. It can be seen that the boundaries of the particles and the vapour

bubbles are separated out while leaving the particle interiors and the large-area vapour structures in the approximation component. In addition, the non-uniformities of image intensities caused by the beam's secondary pulse are solved, which would make the edge detection more effective.

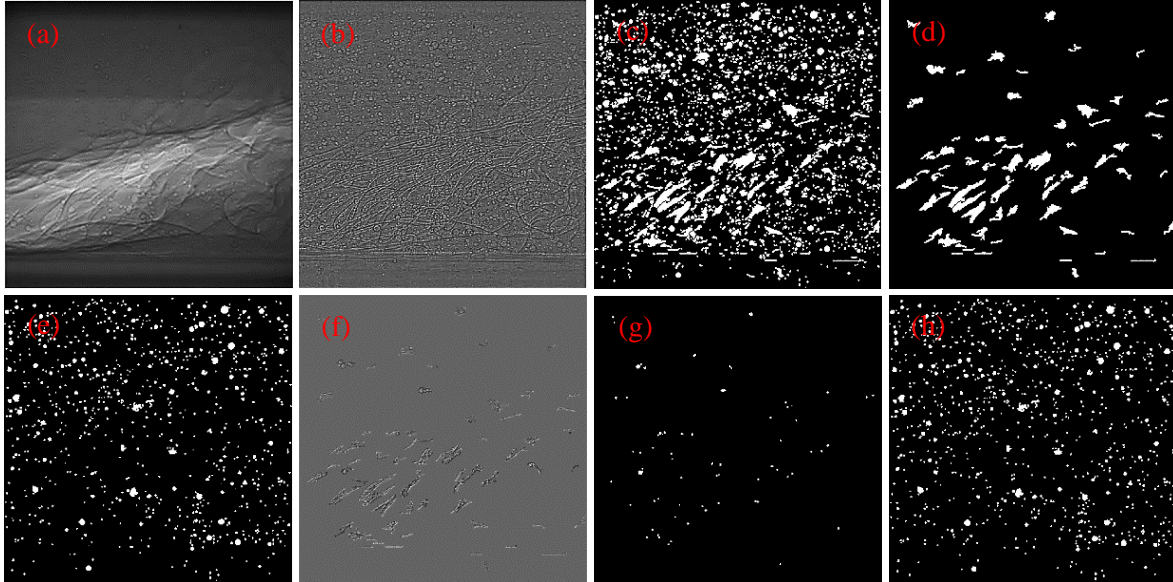


Figure 3.11. Particle detection based on the phase contrast imaging mechanism, (a) reconstructed approximation component; (b) reconstructed detail component; (c) preliminary particle detection by Canny edge detector; (d) removed objects by prescribed criteria; (e) remaining particles; (f) removed region shown in grey level mode; (g) hidden particles in the removed regions; (h) final result of the first identification of particles.

The Canny edge detector (Canny 1986) based on image intensity gradients was then used, because of its ability to derive clean, thin edges that are well connected to nearby edges. In order to facilitate the following morphological operations, the enclosed areas by the detected edges are filled and presented as a binary image where the pixels with value 1 represent the locations occupied by particles. The remaining thin edges were removed via the morphological opening operation. Figure 3.11(c) shows the result of the preliminary detection, which is not satisfactory due to the presence of vapour bubble edges. Criteria based on the size of the tracer particles and their shapes were applied to remove these spurious objects caused by vapour bubble edges: (1) the largest diameter of an object must not exceed 20 pixels ($40\ \mu\text{m}$); (2) the eccentricity of an object must be less than 0.4 to ensure its roundness. The removed objects and the remaining particles are shown in Figure 3.11(d) and (e), respectively. In fact, there are

some particles hiding in the removed region (Figure 3.11(f)), so the Canny edge detector and the criteria with slightly more strict thresholds were reapplied on the removed region to identify the hidden particles as shown in Figure 3.11(g). The final result of the first identification of particles is shown in Figure 3.11(h) and the number of objects recognized is 870.

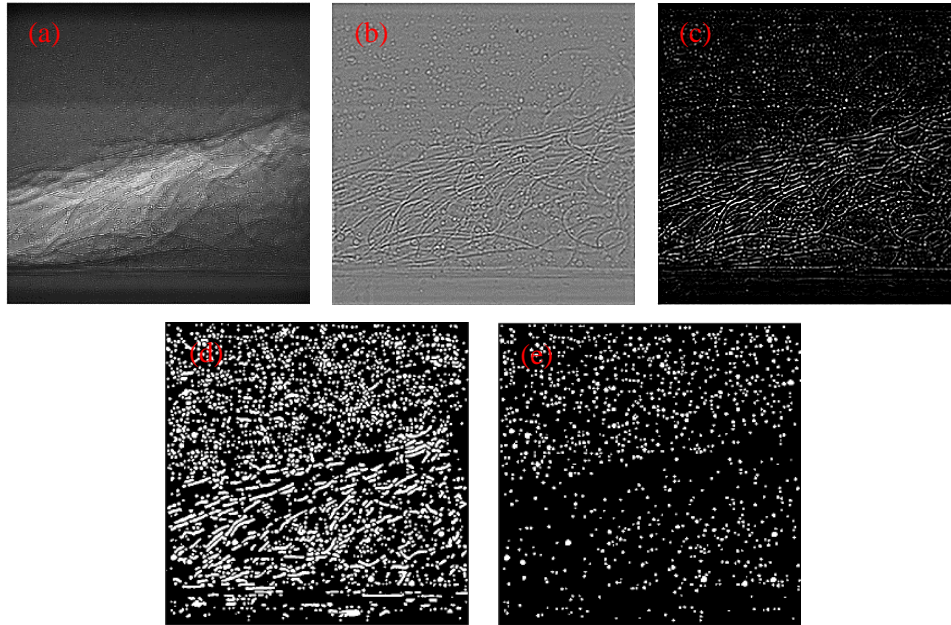


Figure 3.12. Particle detection based on the absorption contrast imaging mechanism, (a) reconstructed approximation component; (b) reconstructed detail component; (c) background suppression; (d) binary image of identified particles with the presence of vapour structures; (e) final result of the second identification of particles.

On the other hand, we can take advantage of absorption contrast to identify particles since the hollow glass spheres reduce the X-ray attenuation. In this second identification, we wish to highlight the interiors of the particles instead of their edges. Figure 3.12(a) and (b) show the decomposition results using a relatively large threshold value at decomposition level 3 since the interiors of particles are mainly concentrated in the detail component d_3 . Figure 3.12(c) presents the background suppression with a constant threshold value given that the background is almost homogeneous. This processing increases the contrast of particle interiors. Then the same procedures as the first identification were implemented to obtain the binary image of particles identified based on local attenuation difference as shown in Figure 3.12(d) and (e). The number of objects in the second identification is 1060.

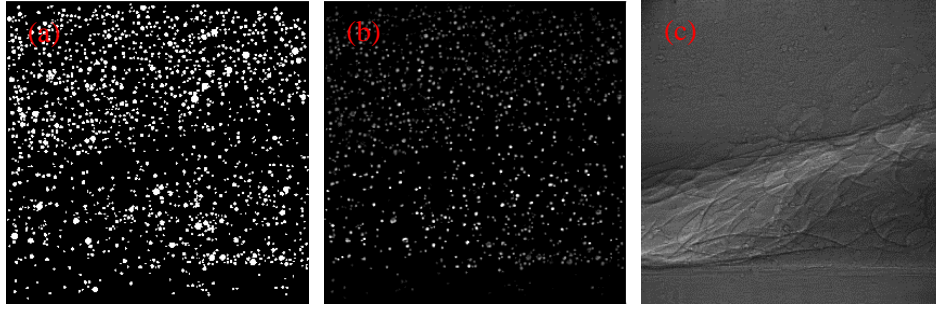


Figure 3.13. (a) Combination of particles identified by the two methods; (b) particle gray level restoration; (c) vapour structures after filtering particles out.

Figure 3.13(a) displays a combination of particles identified by the above two methods. The total number of objects recognized is 1230. This number is important for determining the interrogation window size in PIV evaluation. All tracer particles are finally restored according to their detected locations. Figure 3.13(b) illustrates the final image of particles which is used for the measurements of liquid phase velocities. It should be noted that the gray levels of particles were restored from the image shown in Figure 3.12(c) instead of the raw X-ray image because the non-uniform exposure to X-ray beam would affect the PIV calculation, given that the cross-correlation peak is dominated by brighter particle images and the bright background might remain in the particle image due to the imperfect detection of particle locations. In order to obtain vapour tracers, the identified particles were removed from the raw X-ray image after intensity equalization and then replaced by the local average intensity of their neighborhood. Figure 3.13(c) presents the final image of vapour structures which is used for calculating the instantaneous velocity field of vapour phase.

3.7. Improvement of void fraction measurement accuracy

Theoretically, every reference image of air or water in a sequence has the same intensity at the corresponding pixels if the synchronization scheme (Figure 3.4(b)) is realized perfectly. Then any reference image of air or water can be used to calibrate void fraction. However, when we observe a sequence of air reference images, it is found that the global intensity and the width of the bright band in the center vary with the images. This suggests the ideal synchronization scheme is difficult to be achieved. In fact the fast shutter, the camera and the X-ray pulses are synchronized in three different ways which are responsible for the image-to-image difference. Figure 3.14 illustrates the three synchronization schemes and their corresponding image pairs.

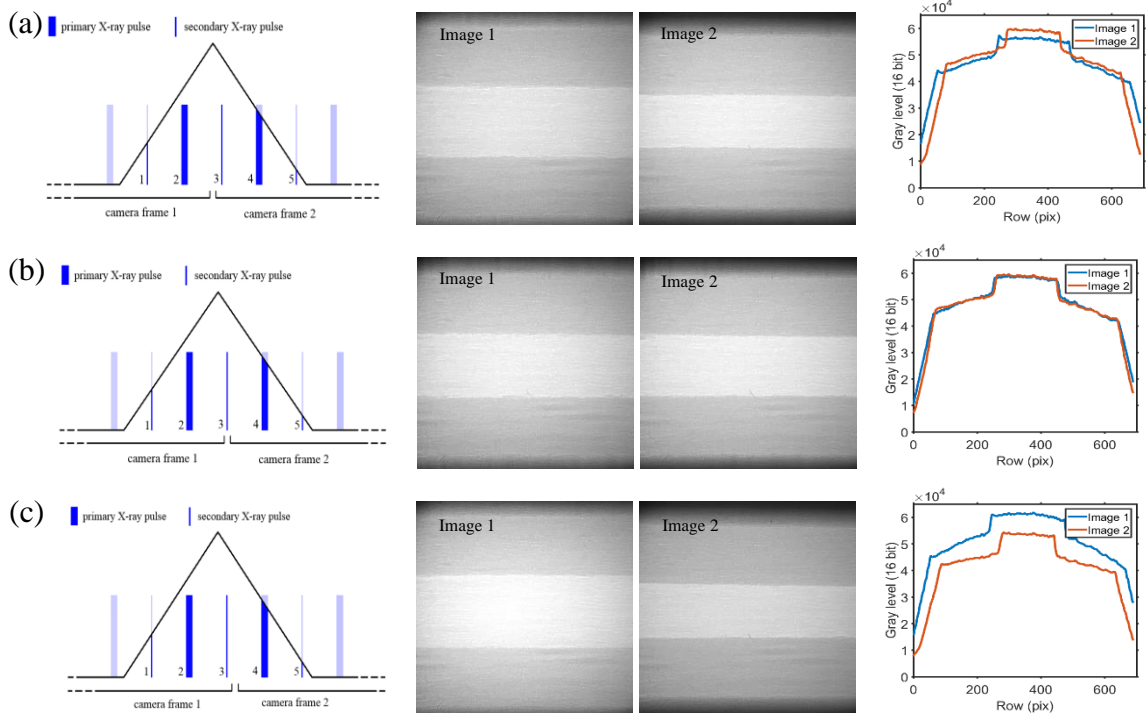


Figure 3.14. Three actual synchronization schemes, (a) Image 1 exposed to one primary pulse and one secondary pulse, Image 2 exposed to one primary pulse and two secondary pulses; (b) both Image 1 and Image 2 exposed to one primary pulse and one secondary pulse; (c) Image 1 exposed to one primary pulse and two secondary pulses, Image 2 exposed to one primary pulse and one secondary pulse. The image row-averaged intensity is plotted for a quantitative comparison between Image 1 and Image 2 in the same pair.

The image row-averaged intensity is also plotted for a quantitative comparison between the first frame (Image 1) and the second frame (Image 2) in the same pair. The maximum opening of the fast shutter is slightly offset to the left relative to the middle secondary pulse 3 in all three schemes since it is observed that the first image of each pair has a wider bright band compared to the second one. The camera frame transfer determines the secondary pulse 3 to illuminate Image 1 (scheme c) or Image 2 (scheme a) or neither (scheme b) resulting in additional intensity to them.

Due to the application of the slow shutter to reduce the risk of damage to the Plexiglas windows by the X-rays, only a packet of 144 pairs of images were recorded per opening of the slow shutter (13 packets in total). Figure 3.15(a) illustrates the global intensity variation of the air reference images in a packet of 144 image pairs. The green solid line denotes the mean intensity of the first image of each pair. The blue solid line denotes the mean intensity of the

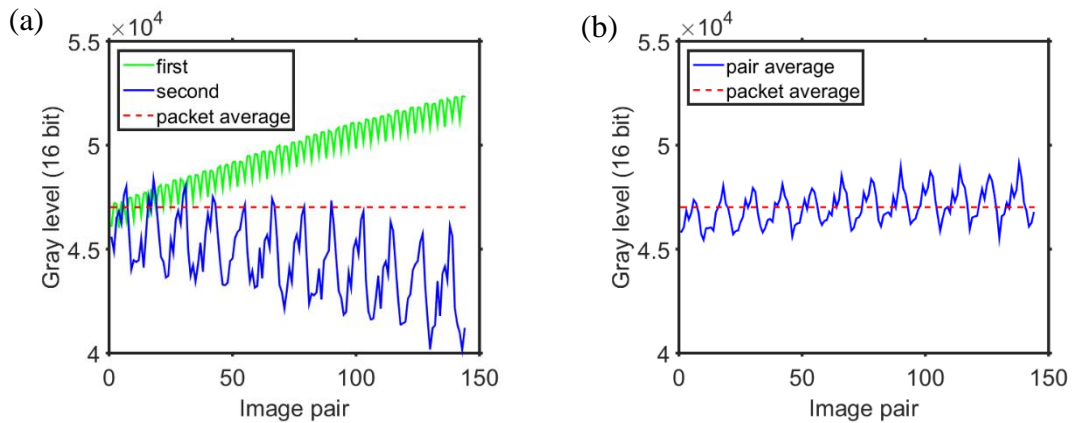


Figure 3.15. Variation of global intensity of air reference images in a packet of 144 image pairs. (a) Intensity variations of the first image and the second image; the green solid line denotes the mean intensity of the first image of each pair; the blue solid line denotes the mean intensity of the second image of each pair; the red dashed line signifies the average intensity of all images in the packet; (b) variation of the average intensity of the two images belonging to the same pair (the blue solid line) relative to the packet average value (the red dashed line).

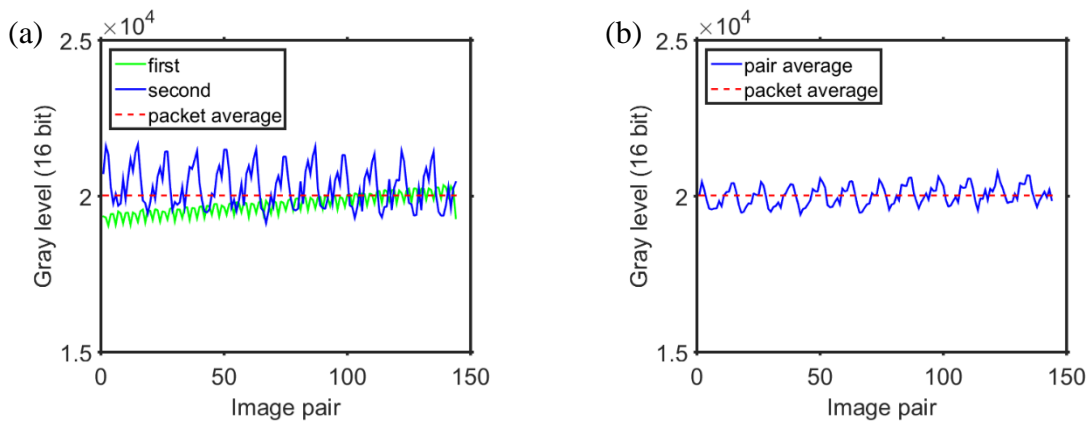


Figure 3.16. Variation of global intensity of water reference images in a packet of 144 image pairs. (a) Intensity variations of the first image and the second image; the green solid line denotes the mean intensity of the first image of each pair; the blue solid line denotes the mean intensity of the second image of each pair; the red dashed line signifies the average intensity of all images in the packet; (b) variation of the average intensity of the two images belonging to the same pair (the blue solid line) relative to the packet average value (the red dashed line).

second image of each pair. The red dashed line indicates the average intensity of all images in the packet. It can be seen that the global intensity of the first image is different from the second

image in the same pair, and both intensity variations diverge with the image pairs in an oscillating way which seemingly poses a convergence problem if the average image of a packet is used as the calibration image for gaseous phase. However, let us observe the variation of the average intensity of the two images belonging to the same pair shown in Figure 3.15(b), it is noted that the quasi-periodic oscillation is steady in a statistical sense, relative to the average intensity of the packet. In addition, the other 12 packets of air reference images have the same tendency (not presented). The reference images of water were also examined and the results in a packet are illustrated in Figure 3.16. Although the image-to-image variation pattern is different, the variation of the pair average intensity is still consistent with the air reference images. Therefore, the calibration image of air (or water) for calculating vapour volume fraction can be obtained through averaging all the images in a packet.

Taking into account the slight packet-to-packet difference, the calibration images for gaseous phase and liquid phase were finally obtained by averaging all the images in the thirteen packets of each phase (as shown in Figure 3.7(a) and (b), respectively). Accordingly, the local void ratio measurements in the cavitating flow cases were performed using the average of the two X-ray images belonging to the same pair as well. In this way, the non-uniform illumination caused by the synchronization problems will have a better correspondence with the reference images than the individual images, and each velocity field will correspond to only one vapour volume fraction field.

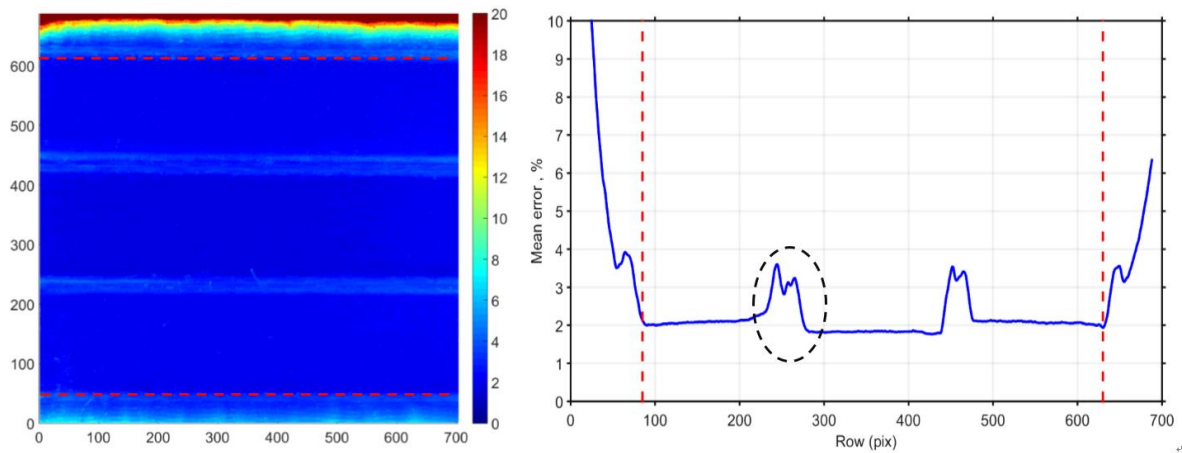


Figure 3.17. Mean vapour volume fraction error estimated from pure air images.

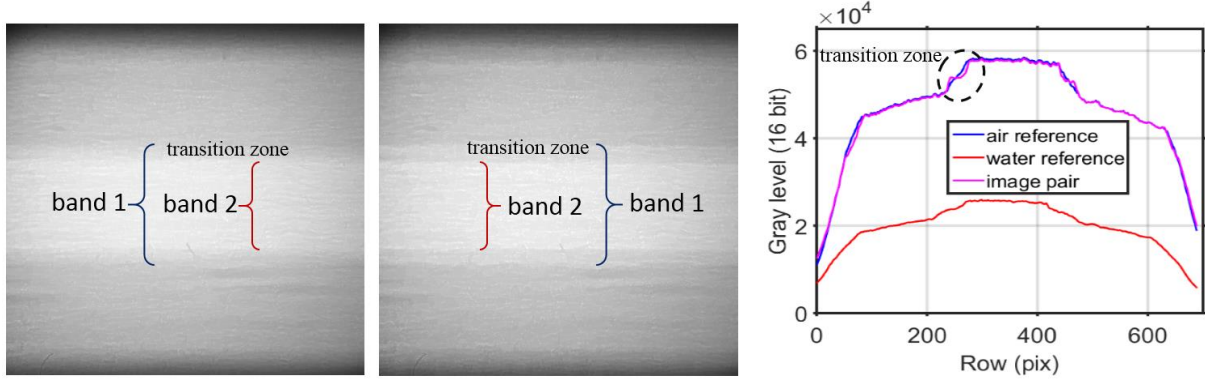


Figure 3.18. Comparison between the air calibration image (left) and the averaged image of a typical air image pair (middle); their row-averaged intensity is plotted for a quantitative comparison (right).

Images of pure air and images of pure water can be used to estimate the accuracy of the aforementioned method for calculating vapour volume fraction since the errors are represented by the discrepancies between the calculated values and the theoretical values (100% for the vapour phase, 0% for the liquid phase). Figure 3.17 indicates the mean vapour volume fraction errors estimated from 1872 (i.e. 144×13) pairs of air images. The big errors (exceeding $\pm 20\%$) are found at two ends, which is attributed to the insufficient exposure. Consequently, for a reliable result only the domain ranging from the 90th row to the 630th row (limited by the red dashed lines) is considered in the following analysis. Thanks to averaging image pairs, the mean error within the middle band is as small as outside the band attaining $\pm 2\%$. However, the relatively large error (around $\pm 4\%$) is observed clearly in the vicinity of the middle band edges. The explanation for this error is illustrated in Figure 3.18 by comparison between the air calibration image and the averaged image of a typical pair of air images. As mentioned previously, the middle band of the first image (band 1) is wider than the second one (band 2). So in the pair averaged image there must be a narrow transition zone between the edges of these two bands with abrupt intensity change. However, due to averaging sufficient number of image pairs, the intensity variation within the transition zone of the air calibration image becomes relatively smooth, since the middle band width varies with images. The different intensity transition from the air calibration image results in the relatively large errors.

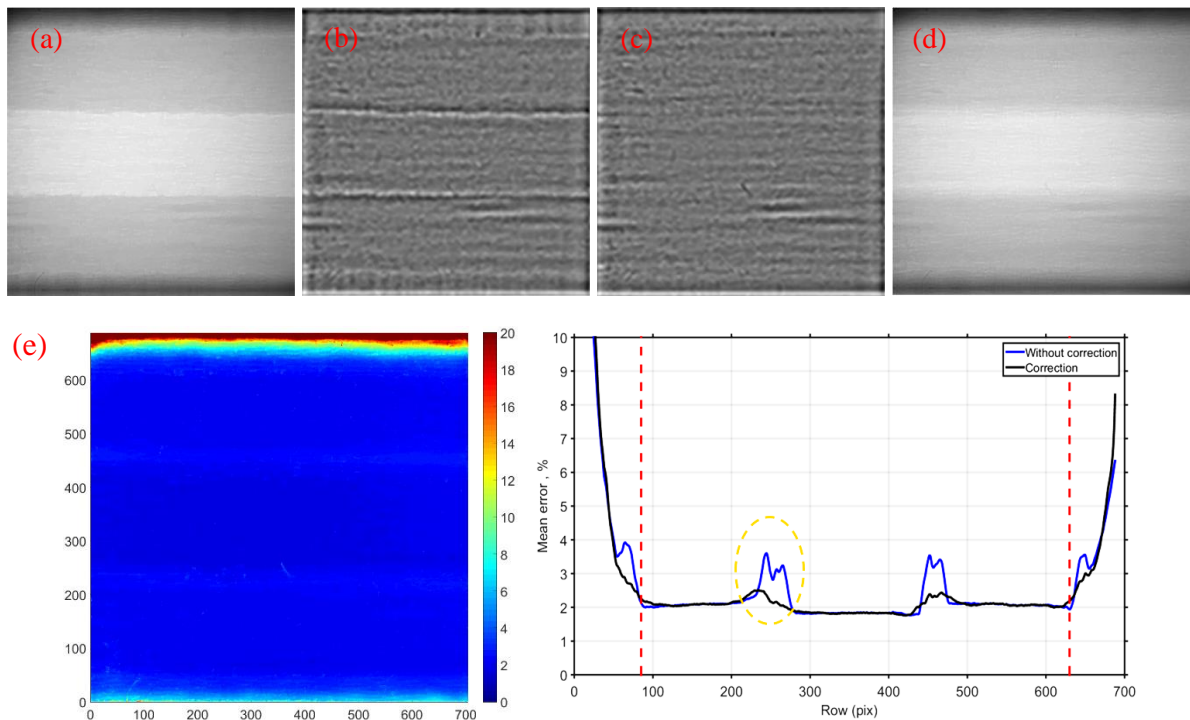


Figure 3.19. Smooth the band edges to reduce vapour volume fraction errors within the transition zone. (a) An original X-ray image of air with sharp intensity change at the middle band edges; (b) separated detail component of band edges; (c) smoothing the intensity change at the band edges; (d) reconstructed air image with smooth intensity change at the band edges; (e) mean vapour volume fraction error estimated from processed air images, compared to the mean error estimated from air images without band edge intensity correction.

In order to improve the accuracy within the transition zone, the band edges with sharp intensity change need to be smoothed to make them closer to the air calibration image. In an original X-ray image of air (Figure 3.19(a)), wavelet decomposition was used to separate the band edges out (Figure 3.19(b)) as the local discontinuities can be described better with wavelets. A 2D averaging filter was then applied on the detected band edges to smooth the intensity change as shown in Figure 3.19(c). The processed detail component was combined with the approximation component of the wavelet transform to reconstruct the final result as shown in Figure 3.19(d). All the other air images were treated according to the above steps as well. Figure 3.19(e) depicts the mean vapour volume fraction errors obtained from 1872 pairs of processed air images. It is obvious that thanks to the band edge smoothing the error within the transition zone is reduced to the same order of magnitude (around $\pm 2\%$) as the rest area.

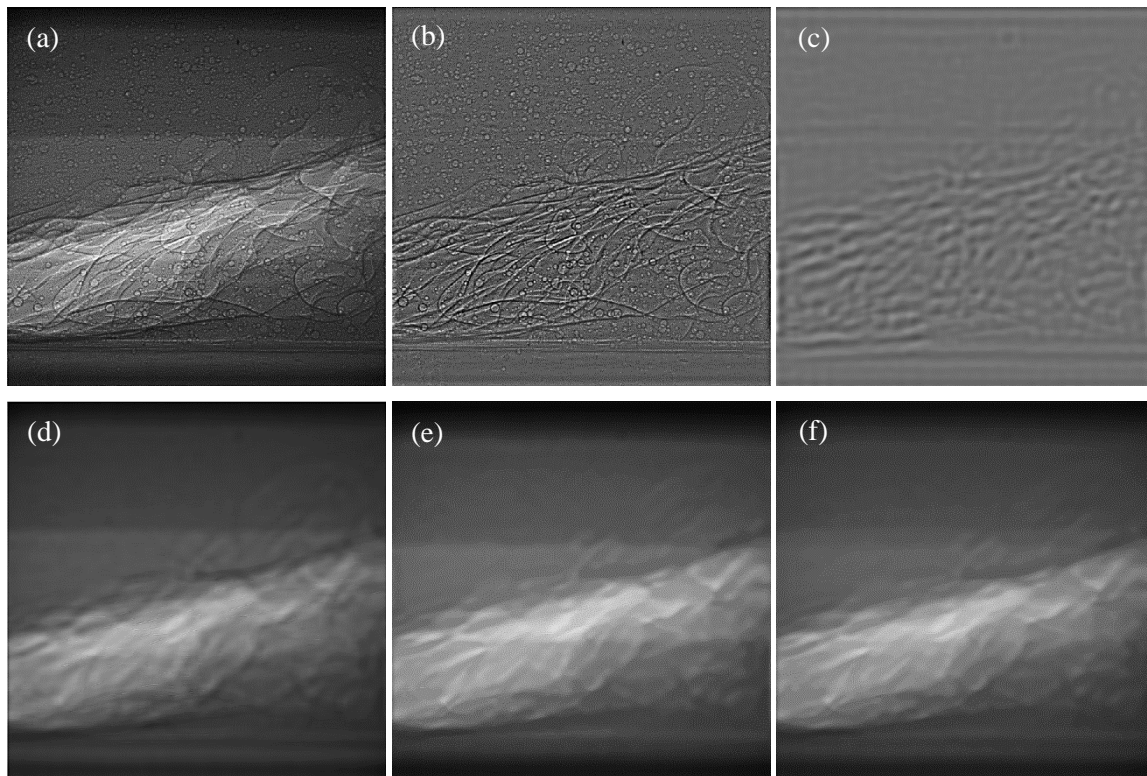


Figure 3.20. Image processing for vapour volume fraction measurements, (a) unprocessed X-ray image of cavitation; (b) detail component of wavelet decomposition; (c) detail component processed by averaging filter; (d) first processed image in a pair; (e) second processed image in a pair; (f) pair averaged image for estimating vapour volume fraction.

The fringe patterns due to phase contrast in the unprocessed X-ray image of cavitation (Figure 3.20(a)), although important for identifying particles and vapour bubbles, have a negative influence on the computation of void fraction. The diffracted dark edge lines coupled with bright ones at phase interfaces result in a local underestimation or overestimation of the vapour volume fraction. In order to reduce this detrimental effect of phase contrast, the same wavelet transform as in the processing of particle identification was employed to decompose the original X-ray image but with different threshold values aiming to make the particle and vapour interfaces contained completely in the detail component. Figure 3.20(b) presents the detail component where the two edges of the middle band are also included. A low pass averaging filter was applied on the image of detail component, after which the diffraction traits of black lines and white lines are neutralized; the high frequency particles are filtered out, and the middle band edges are smoothed. The processed detail component (Figure 3.20(c)) was subsequently added to the image of approximation component reconstructing the image of

vapour structures without particles nor vapour bubble interfaces as shown in Figure 3.20(d). The other X-ray image in the same pair was treated using the same procedure (Figure 3.20(e)). The average image of the pair is indicated in Figure 3.20(f): this is the one used for the calculation of the vapour volume fraction, rather than the individual one.

3.8. Chapter summary

Cavitating flow is inherently opaque due to high reflections and multiple scatterings of visible light on vapour/liquid interfaces. Conventional experimental studies of cavitation are often limited to the determination of the global flow characteristics (like geometrical description of cavity shape and cloud shedding frequencies), and/or sometimes some measurements in the surrounding liquid flow area. However, an accurate description of cavitation physics strongly relies on the visualizations of two-phase morphology and the measurements of characteristic quantities (like velocity and void fraction) inside the volume of liquid/vapor mixture.

Dedicated to the measurement of the internal flow fields of cavitation, an ultra-fast X-ray imaging technique was developed in consideration of X-rays high penetrability and weak interaction with matter. In addition to the absorption contrast mechanism, the X-ray phase contrast leads to a sharp intensity variation at the phase interface, which allows a better visualization of the two-phase flow structures. Silver-coated hollow particles were injected into the cavitating flow as the liquid phase tracers, and they were visualized simultaneously with the vaporous structures based on the combination of absorption and phase contrast. Although the two-phase information of structures and dynamics is contained in the X-ray images, the extraction of desired data is not easy. In the present work, a wavelet-decomposition-based image processing method was introduced to separate the seeding particles from the vapour structures. In this way, image cross-correlations could be applied on both seeding particles and vapour bubbles to evaluate the instantaneous velocity field of the liquid and the gaseous phase, respectively. The local vapour volume fraction could also be derived simultaneously from the difference of X-ray attenuation. Thanks to the unprecedented acquisition of these data, the detailed experimental study of the cavitating flow structure and dynamics is made possible for the first time.

3.8. Résumé du chapitre

L'écoulement de cavitation est intrinsèquement opaque en raison de réflexions élevées et de multiples diffusions de lumière visible sur les interfaces vapeur/liquide. Les études expérimentales conventionnelles de la cavitation se limitent souvent à la détermination des caractéristiques d'écoulement global (comme la description géométrique de la forme de la cavité et des fréquences de dispersion des nuages) e/ou parfois à certaines mesures dans la zone d'écoulement du liquide environnant. Cependant, une description précise de la physique de la cavitation repose fortement sur les visualisations de la morphologie à deux phases et les mesures de grandeurs caractéristiques (comme la vitesse et la fraction de vide) à l'intérieur du volume de mélange liquide / vapeur.

Dédiée à la mesure des champs de flux internes de cavitation, une technique d'imagerie ultra-rapide aux rayons X a été développée en tenant compte de la haute pénétrabilité des rayons X et de la faible interaction avec la matière. En plus du mécanisme de contraste d'absorption, le contraste de phase des rayons X conduit à une forte variation d'intensité à l'interface de phase, ce qui permet une meilleure visualisation des structures d'écoulement diphasique. Des particules creuses recouvertes d'argent ont été injectées dans le flux de cavitation en tant que traceurs de phase liquide, et elles ont été visualisées simultanément avec les structures vaporeuses basées sur la combinaison de l'absorption et du contraste de phase. Bien que les informations en deux phases des structures et de la dynamique soient contenues dans les images radiographiques, l'extraction des données souhaitées n'est pas facile. Dans le présent travail, une méthode de traitement d'image basée sur la décomposition en ondelettes a été introduite pour séparer les particules d'ensemencement des structures de vapeur. De cette manière, des corrélations croisées d'image pourraient être appliquées à la fois aux particules d'ensemencement et aux bulles de vapeur pour évaluer le champ de vitesse instantané du liquide et de la phase gazeuse, respectivement. La fraction volumique locale de vapeur pourrait également être dérivée simultanément de la différence d'atténuation des rayons X. Grâce à l'acquisition sans précédent de ces données, l'étude expérimentale détaillée de la structure et de la dynamique des écoulements de cavitation est rendue possible pour la première fois.

Chapter 4

Structure and dynamics of developed sheet cavitation

In the present experiments, the flow temperature was kept constant at 17 ± 0.5 °C and the flow rate Q was set to 35.09 l/min leading to a reference velocity $u_{\text{ref}} = 9.53$ m/s at the Venturi throat. The Reynolds number based on the throat height is $Re = 1.45 \times 10^5$. Three cases with different cavitation numbers ($\sigma = 7.54, 8.0$ and 9.13) were tested. They correspond to the developed stage, the intermediate stage and the early stage of sheet cavitation, respectively. Note that periodic cloud cavitation is not observed in the studied geometry due to the scale effect on Venturi cavitating flows (which will be discussed in detail in Chapter 7). In this chapter, we analyze the structure and dynamics of sheet cavitation at the developed stage. The comparison of sheet cavitation at different stages will be presented in the next chapter.

4.1. Global behavior of sheet cavitation based on high speed photography

The cavitating flow in the convergent-divergent channel was captured from side view using a high-speed Photron Fastcam SA 1.1 camera with a Tokina 100 mm lens. The flow was illuminated by a high-power LED in two ways: back-lighting and top-lighting. In the back-lighting mode, the opaque two-phase structures blocked most of the light from the back source resulting in lower grayscale intensities in the recorded photograph. The frame rate in this mode was set to 8000 fps with a very short exposure time ($1/1000000$ s) to freeze the fast-moving vapour structures. In the top-lighting mode, the cavitation structures reflected light from the top LED into the camera sensor on the side resulting in higher intensities in the recorded photograph. The frame rate in this mode was set to 8000 fps with a $1/50000$ s exposure time. In both modes, the field of view was 1024×512 pixels with a resolution of $24 \mu\text{m}/\text{pixel}$.

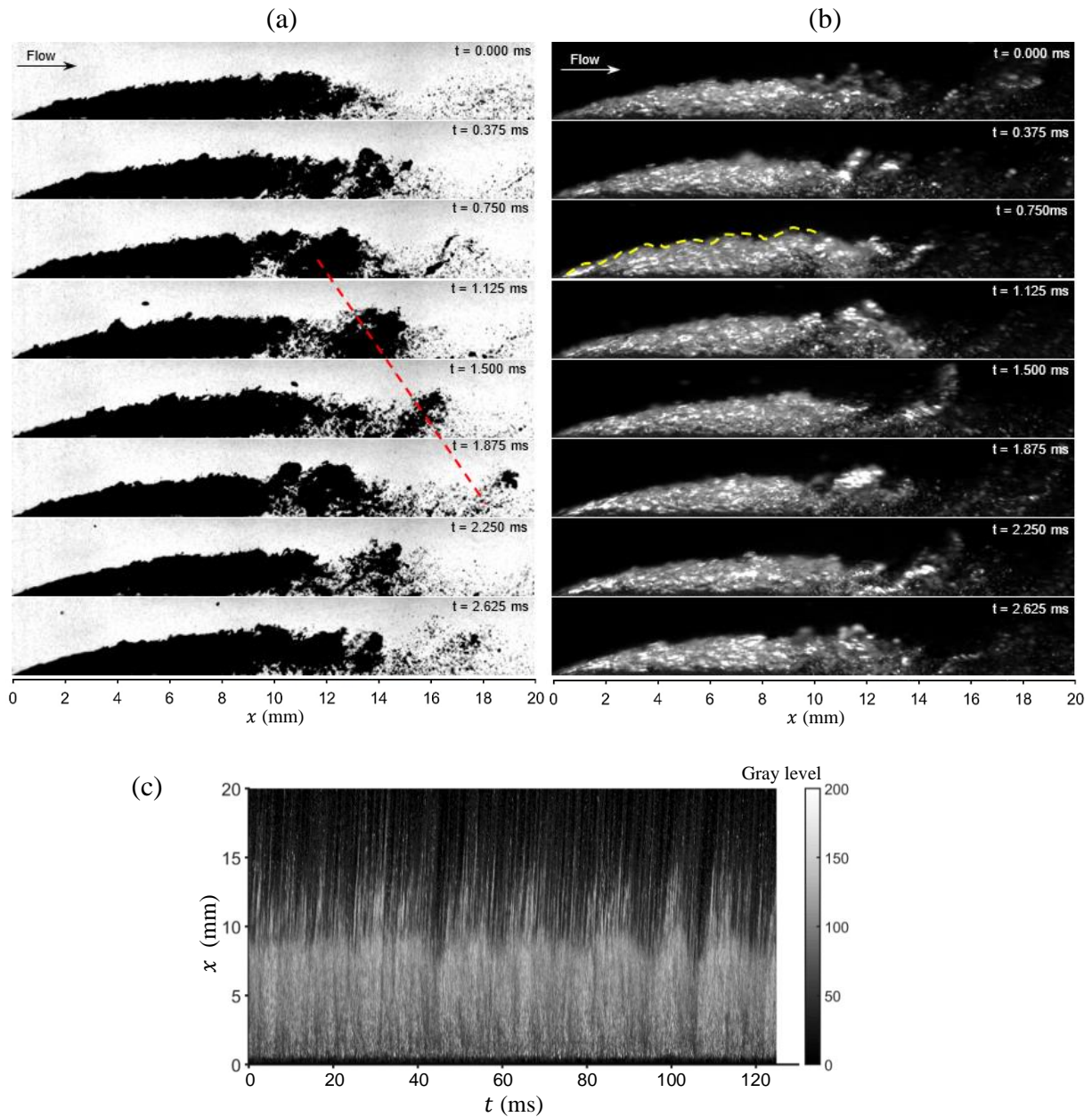


Figure 4.1. Time series of high-speed photographs for the cavitating case of $\sigma = 7.54$, (a) back-lighting mode; (b) top-lighting mode; (c) time-space (t-x) diagram derived from 1000 consecutive cavitation snapshots in top-lighting mode.

As the cavitation number decreases, the cavitating region grows and the liquid-vapour interface becomes increasingly wavy and unstable. Figure 4.1(a) and (b) show a sequence of side-view images for the developed cavitating case of $\sigma = 7.54$ recorded in back-lighting and top-lighting modes, respectively. From these images, an open partial cavity is observed with a turbulent frothy closure. The beginning of the cavity is located close to the throat of the Venturi

channel ($x = 0$). The upstream part ($x = 0-10$ mm) with interfacial waves (indicated by the yellow dashed line) appears to attach to the solid surface steadily. Small-scale vapour structures are rolled up and detached continuously from the cavity closure region ($x = 10-12$ mm). As these vapour structures are entrained by the flow and convected downstream, they rapidly split and/or collapse into a large number of very small bubbles in the cavity wake region ($x > 12$ mm). This process is also indicated by the red dashed line in Figure 4.1(a). The temporal-spatial ($t-x$) diagram is a useful data processing method to illustrate unsteady cavitation behaviors. Gray levels in each high speed photograph is averaged along the y axis generating a column of the $t-x$ diagram. Figure 4.1(c) presents the $t-x$ diagram for $\sigma = 7.54$ which is obtained by stacking 1000 consecutive snapshots in top-lighting mode. It is clear that the upstream part ($x = 0-10$ mm) of the cavity is fairly stable with slight length oscillations, while vapour structures are shed after $x = 10$ mm in an irregular fashion.

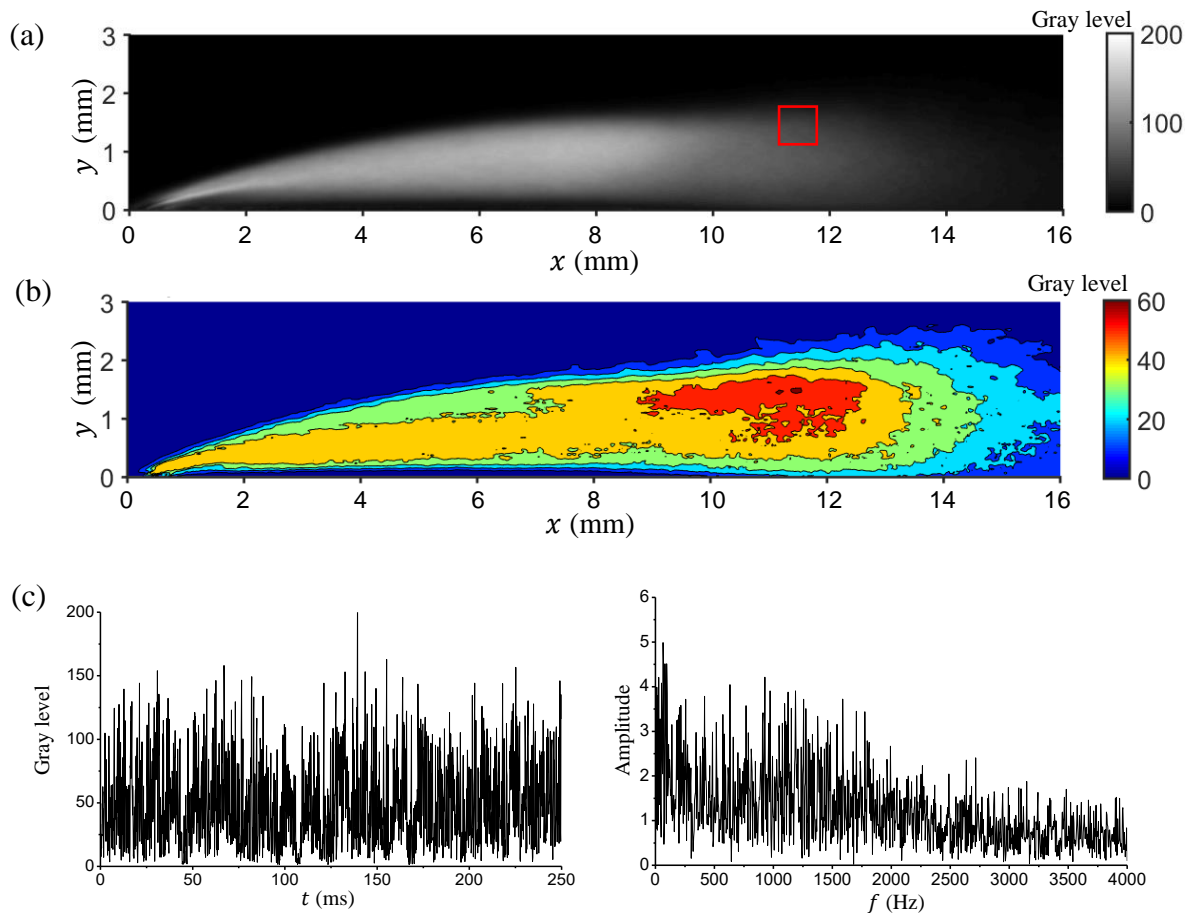


Figure 4.2. (a) Mean gray level values of 2000 high speed images; (b) standard deviations of gray levels; (c) time evolution of gray level in the probing window (indicated by the red frame in (a)) and its FFT result.

As shown in Figure 4.2(a) and (b), mean values and standard deviations of gray levels of 2000 images were calculated in order to determine the cavity length and the shedding frequency information. The method of estimating the cavity length from the mean gray level image is not accurate since it is too subjective to the selection of the threshold value. Dular et al. (2004) found that the position of the maximum standard deviation of gray level is correlated well with the position of maximal cavitation structure oscillation. Therefore, one can consider the location of the maximum standard deviation as the sheet cavity termination. In recent years, this method has been widely used as could be found in Danlos et al. (2014), Prothin et al. (2016), Long et al. (2017) and Zhang et al. (2019).

In our case, the maximum standard deviation is identified at the point of $x = 11.5$ mm, $y = 1.5$ mm and thus the mean cavity length is determined to be 11.5 mm. Another reliable method is to use the contour line of $\bar{\alpha} = 0.1$ in the time-averaged void-fraction field to designate the mean cavity length. As shown in Figure 4.3(a), the cavity length is also around 11.5 mm. This good agreement demonstrates that it is reasonable to use the standard deviation method to determine the cavity length. Moreover, the maximum standard deviation is also an objective way to select the probing window for estimating the cavity shedding frequency. The time evolution of gray level in Figure 4.2(c) is obtained by averaging all gray level values in a 50×50 pixel probing window with its center at the position of the maximum standard deviation. From its Fast Fourier Transform (FFT) result, no characteristic frequency is detected implying that the small vapour shedding from the cavity closure occurs in an irregular way.

So far the mainstream explanation to the relatively stable sheet cavitation is that no re-entrant jet exists underneath the cavity or the re-entrant jet only exists near the cavity closure region, thereby producing intermittent shedding of small vapour structures. The conjecture of lacking re-entrant jet is considered as the primary mechanism causing the main part of the sheet cavity attaching to the wall steadily. In the next sections, we will challenge the current theory of sheet cavitation by X-ray imaging measurements and illustrate how the seemingly stable sheet cavitation is linked to a clear re-entrant jet penetrating the entire sheet cavity.

4.2. Mean void fraction and velocity fields based on X-ray imaging measurements

Since the time-resolved acquisitions by X-ray imaging are not simultaneous at different positions, it is impossible to analyze the complete instantaneous flow field. Nevertheless, the time-averaged flow field at each position can be connected well with each other except some

slight mismatching which is caused by the inaccurate movement of the motorized platform clamping the test section. Figure 4.3(a) presents the distribution of the mean void fraction $\bar{\alpha}$ assembled from 22 scanning windows (10 in the upper row and 12 in the lower row). The averaged void fraction profiles at different distances from the throat are overlaid on the mean cavity shape in gray scale as shown in Figure 4.3(b), in order to indicate the location of the profiles in the cavity visually. The maximum mean void fraction is found to be at the point close to the cavity origin with a value of 75%, while the maximum instantaneous void fraction can be up to 100% implying that a pure vapour pocket is likely to exist in the leading edge of the cavity. A drastic decrease of void fraction down to nearly 0 is detected towards the solid surface, which is not revealed well by the gray level variation from high speed photographs.

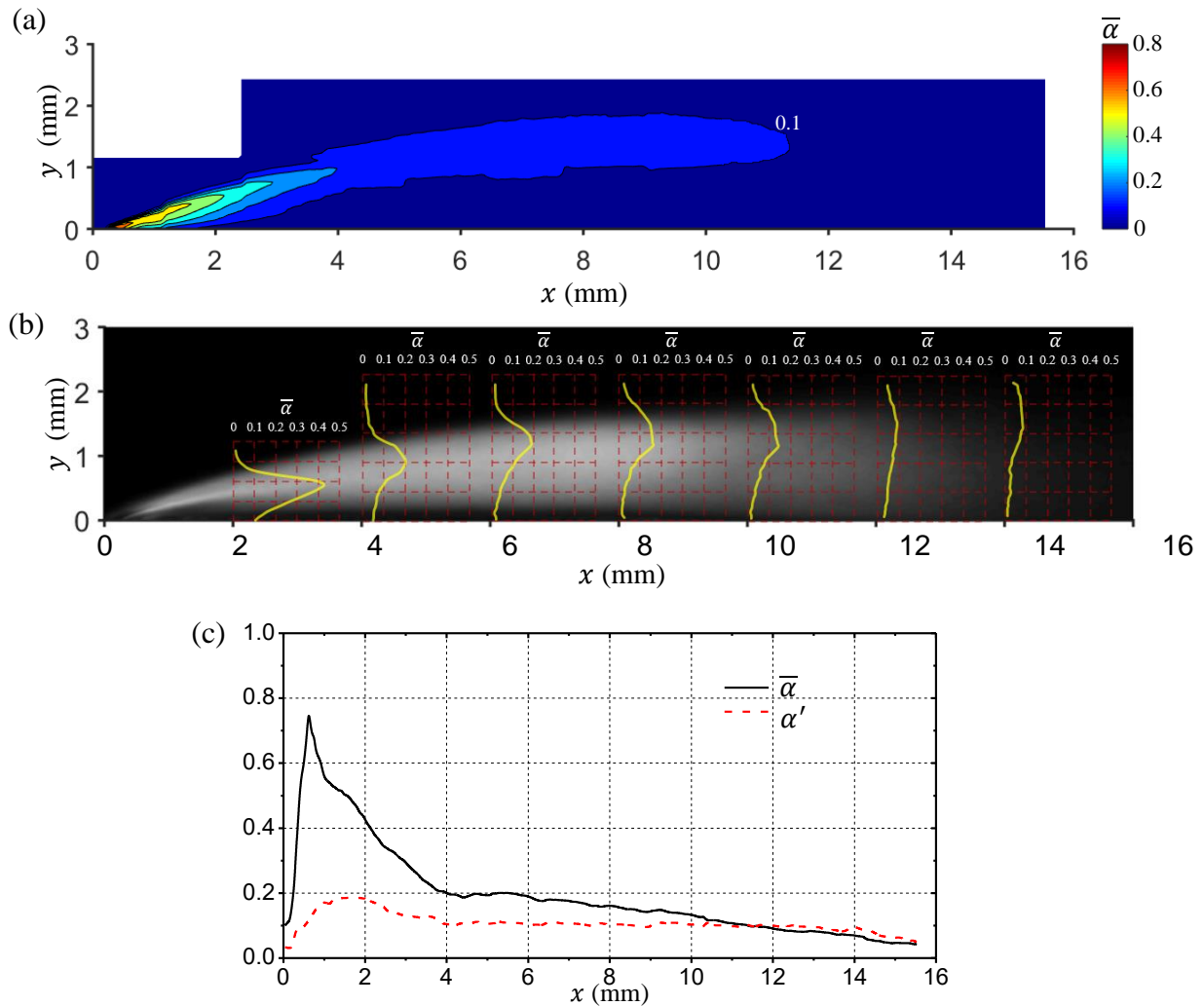


Figure 4.3. (a) Distribution of the mean void fraction $\bar{\alpha}$; (b) mean void fraction profiles overlaid on the mean cavity shape; (c) evolution of the mean void fraction $\bar{\alpha}$ and the standard deviation of void fraction α' along the streamwise direction.

The maximum mean void fraction in the transverse direction is plotted in Figure 4.3(c), and it illustrates clearly the spatial evolution of the mean void fraction along the flow direction. The evolution of the standard deviation of void fraction α' is also plotted in the same way. In the region of $x = 0-4$ mm, the mean void fraction is rapidly decreased from the maximum value 75% to 20%. Thereafter, it reduces progressively from 20% to 0 in the cavity wake at a much slower rate. The distinction suggests that different two-phase flow structures exist in these two regions. The void fraction evolution along the streamwise direction in the present sheet cavity is quite different from the one reported by Coutier-Delgosha et al. (2006) for cloud cavitation on a plano-convex hydrofoil: in their configuration, the void fraction is rather constant in the entire attached cavity.

With regard to the evolution of the standard deviation of void fraction, the maximum value is found to be in the range of $x = 1-2$ mm, which is far away from the location of maximum standard deviation of gray level ($x = 11.5$ mm). The explanation to this great disparity is the fact that the gray level of high speed images can only indicate the presence of cavitation structures, whereas it does not directly give any indication about the void fraction. For instance, the shedding cloud appears very bright in high speed photos while its vapour volume fraction is only around 20% as reported by Ganesh et al. (2016). Surprisingly, the standard deviation of void fraction remains nearly constant at the value of 0.1 in a wide range of $x = 4-12$ mm before it begins to decrease. The standard deviation is observed to be greater than the mean void fraction from $x = 11.5$ mm to the wake, which is attributed to the rapid collapse of shedding vapour structures causing a relatively large void fraction fluctuation.

Figure 4.4(a) shows the spatial distribution of the time-averaged longitudinal velocity normalized by the reference velocity \bar{u}/u_{ref} for the case of $\sigma = 7.54$. The contour lines 0 and 1 of \bar{u}/u_{ref} are superimposed with the mean void fraction field as shown in Figure 4.4(b), in order to illustrate the relationship between them. Based on the two figures, the following results can be obtained in a statistical sense. In this seemingly steady sheet cavitation, an obvious reverse flow (under the contour line of 0) is observed beneath the cavity along the wall. It is commonly referred to as the re-entrant jet. A strong velocity shear layer is formed between the reverse flow and the outer main flow, and it extends to the cavity wake region. The vapour is mainly contained within the shear layer. The thickness of the re-entrant jet remains quite constant in the region of $x = 4-12$ mm, and the ratio of the re-entrant jet thickness to the cavity thickness is around 0.4, which is out of the range of 15% and 35% measured by Callenaere et

al. (2001) in cloud cavitation. The downstream end of the re-entrant jet is located about 4 mm downstream of the cavity closure rather than exactly at the cavity closure reported by previous research. The upstream stagnation point of the re-entrant jet is located at $x = 1.5$ mm, which corresponds to the position of the maximum standard deviation of void fraction. The good agreement suggests that the re-entrant jet plays a crucial role in the void fraction variation, which can be summarized as follows: when the pure vapour pocket at the leading edge interacts with the re-entrant jet, it breaks up into a low-void-ratio bubbly mixture. The bubbly mixture is then convected downstream in the shear layer with a very slow decrease of void fraction along the streamwise direction. This might result from the coherent vortical structures in the shear layer, which limits the collapse of the bubbly mixture.

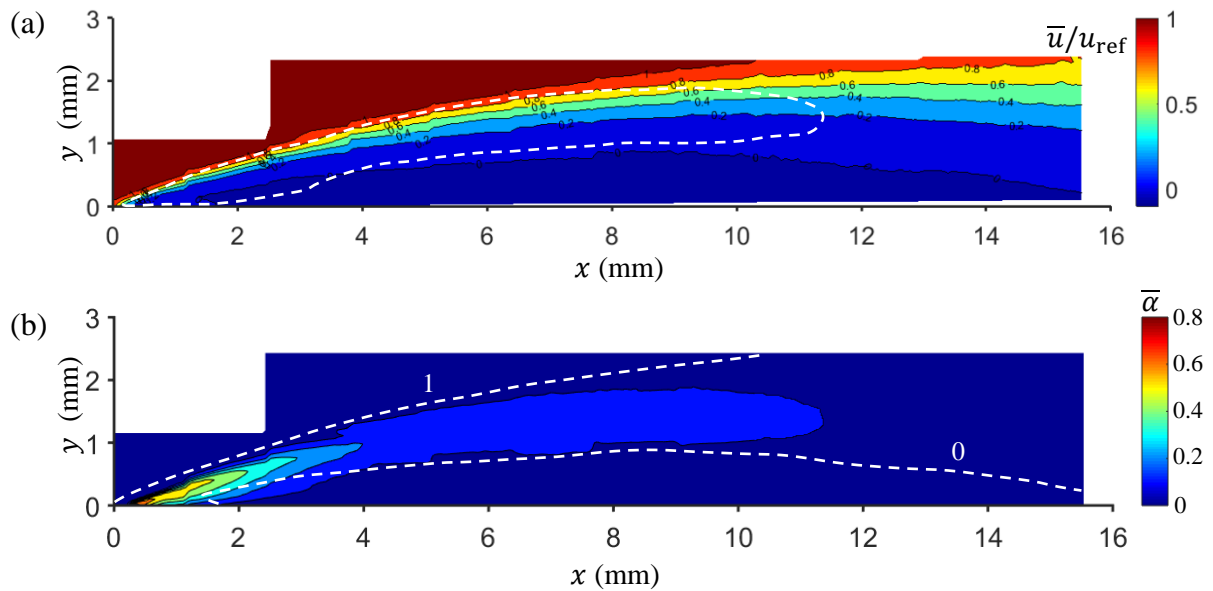


Figure 4.4. (a) Distribution of the time-averaged longitudinal velocity normalized by the reference velocity, \bar{u}/u_{ref} . The white dashed line denotes the contour line of $\bar{\alpha} = 0.1$. (b) Mean void fraction field on which the contour lines of $\bar{u}/u_{\text{ref}} = 0$ and 1 are overlaid to indicate the mean reverse flow and the external main flow.

The profiles of the mean void fraction (red dashed line) and the mean longitudinal velocity are compared in Figure 4.5 at different distances from the throat for the case $\sigma = 7.54$. The maximum void fraction is found to be located in the shear layer between the re-entrant jet and the main flow. More specifically, it corresponds generally to the location of the maximum velocity gradient. The vapour content in the reverse flow region is almost 0, which confirms

the existing knowledge that the re-entrant jet is mostly a liquid film entraining some cavitation bubbles. The velocity in the re-entrant jet is fairly uniform spanning the whole thickness. The time-averaged flow field is not sufficient to characterize this complex phenomenon since cavitation is unsteady in nature. So the next two sections will be focused on the investigation of the transient characteristics of the re-entrant jet and the void fraction.

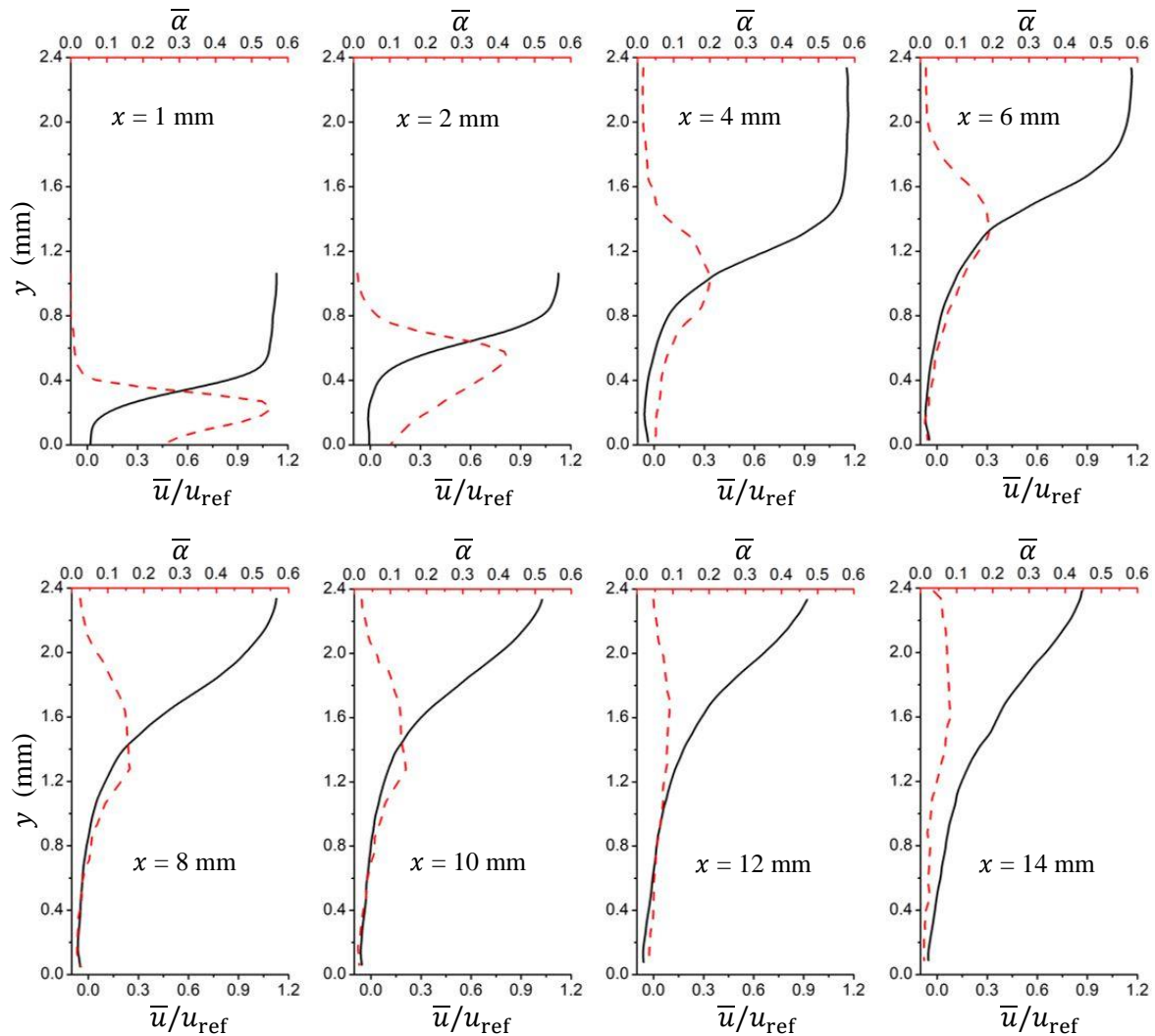


Figure 4.5. Comparison of the mean void fraction profiles (red dashed line) and the mean longitudinal velocity profiles (black solid line) at different distances from the throat.

4.3. Probability of the re-entrant flow: discussion

The time-varying streamwise velocities at four positions ($x = 1, 2, 8$ and 15 mm) along the horizontal line of $y = 0.1$ mm (adjacent to the Venturi wall) are shown in Figure 4.6. It should be clarified that due to the application of the slow shutter for reducing X-ray dose received by

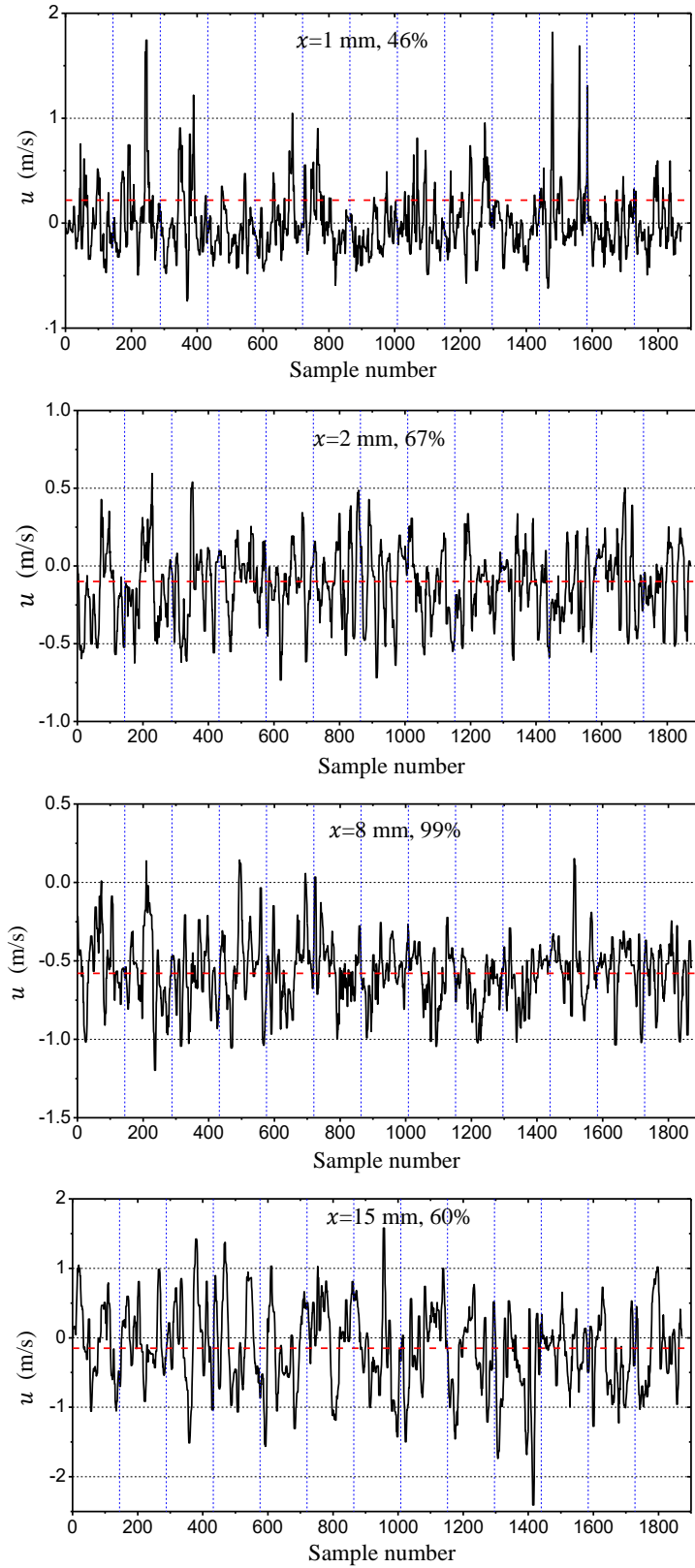


Figure 4.6. Time-varying streamwise velocities at four positions along the line of $y = 0.1$ mm. The percentage represents the probability of re-entrant jet occurrence. The red dashed line denotes the averaged velocity. The vertical blue dashed lines separate different packets.

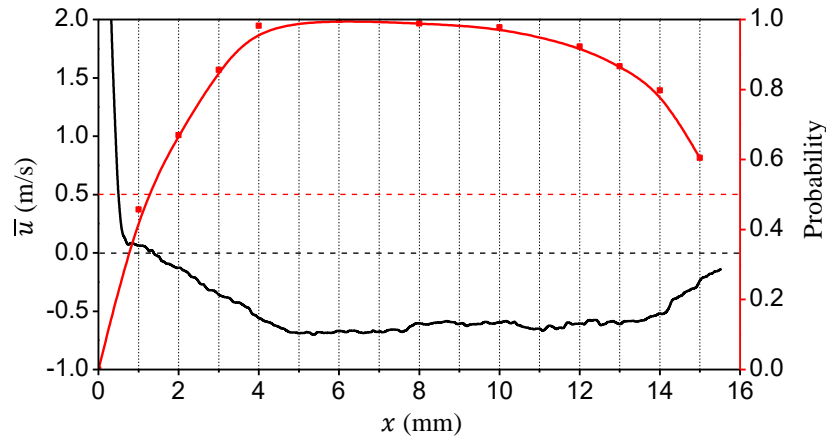


Figure 4.7. Evolution of the probability of re-entrant jet occurrence (red line with squares) and the time-averaged longitudinal velocity (black line) along the horizontal line of $y = 0.1$ mm.

the Plexiglas windows, only a packet of 144 pairs of images was recorded successively during each opening of the slow shutter (13 packets in total). Considering the time discontinuity between different packets, sample number is thus used in the time trace of streamwise velocities. Different packets are also highlighted with the vertical blue dashed lines. The percentage in each subfigure represents the time fraction of the negative velocity, i. e. the probability of re-entrant jet occurrence and the red dashed line denotes the averaged velocity. At $x = 1$ mm where the average velocity is positive, the probability of re-entrant jet occurrence is less than 50%. As expected, in the mean reverse flow region, the probability of re-entrant jet occurrence is more than 50%. A continuous presence of re-entrant jet is identified at $x = 8$ mm as the probability there is nearly 100%.

In order to highlight the near-wall upstream moving flow, Figure 4.7 provides the evolution of the probability of re-entrant flow along the line of $y = 0.1$ mm. Also shown is the time-averaged longitudinal velocity. The re-entrant flow probability of 50% occurs at around $x = 1.5$ mm, which corresponds to the location of maximum standard deviation of void fraction. It suggests that the most frequent switch between positive and negative velocity leads to the largest void fraction fluctuation. The probability reaches nearly 100% at $x = 4$ mm. This is the ultimate location the vapour pocket can grow to as the re-entrant jet can make it shrink and break up. In the range of $x = 4$ -12 mm, the velocity magnitude of the mean reverse flow remains almost constant at its maximum value of approximately 0.6 m/s ($7\% u_{ref}$). The persistence of the re-entrant flow with a constant mean velocity in this wide range of streamwise positions results, when combined with the outer main flow, in a relatively steady shear layer.

Based on the above analysis, we can infer that the upstream vapour pocket oscillates within a limited range of $x = 0-4$ mm and under the action of re-entrant jet it detaches from the wall, transforming into a low-void-fraction bubbly mixture that is afterwards transported downstream in the relatively steady shear layer. This explains why the mean void fraction is rapidly decreased from the maximum value 75% to 20% in the region of $x = 0-4$ mm and then reduced progressively from 20% to 0 at a much slower rate. It should be pointed out that the re-entrant jet in the studied sheet cavitation is quite weak (the maximum mean value is only 7% u_{ref}), in contrast to the measured velocity of re-entrant jet in periodic cloud cavitation, which is generally of the same order of magnitude as the free-stream velocity (Le et al. 1993; Pham et al. 1999; Callenaere et al. 2001). This might be the primary mechanism for sheet cavitation to remain in a quasi-stable state.

4.4. Spectral analysis of void fraction variation

In this section we will determine whether the upstream vapour pocket is oscillating randomly or regularly. To that end, two probe locations close to the cavity leading edge are selected for examining the time-varying void fraction. The first probe location is indicated in Figure 4.8(c) by a red frame which is actually included in the X-ray beam scanning position 1 (the numbering system for scanning positions can be found in Figure 3.5 and 4.11). Figure 4.8(a) shows the time history of spatially averaged void fraction at the position of the first probe. Due to the reason mentioned above, only the first packet of 144 samples (corresponding to a duration of 24 ms) is presented here. Taking the packet-to-packet difference into account, all the 13 packets of spectra are averaged and the mean spectrum is shown in Figure 4.8(b). As can be seen, there exists a single spectral peak at approximately 167 Hz indicating that the void fraction at the first probe location varies in a quasi-periodic pattern rather than randomly. Then, let us examine the second probe location which is indicated in Figure 4.9(c) by a red frame (in the scanning position 2). Just like for the first probe, only the first packet of void fraction variation is presented in Figure 4.9(a), and the average of the 13 spectra obtained from the 13 packets is shown in Figure 4.9(b). A dominant frequency is also identified at 167 Hz which is consistent with the one obtained at the first location. Since the void fraction in both probe locations varies regularly at the same dominant frequency, it is reasonable to speculate that the upstream vapour pocket oscillates quasi-periodically at about 167 Hz. The corresponding Strouhal number ($St = f * L_{cav}/u_{ref}$) based on the mean cavity length and the reference velocity is calculated to be 0.18.

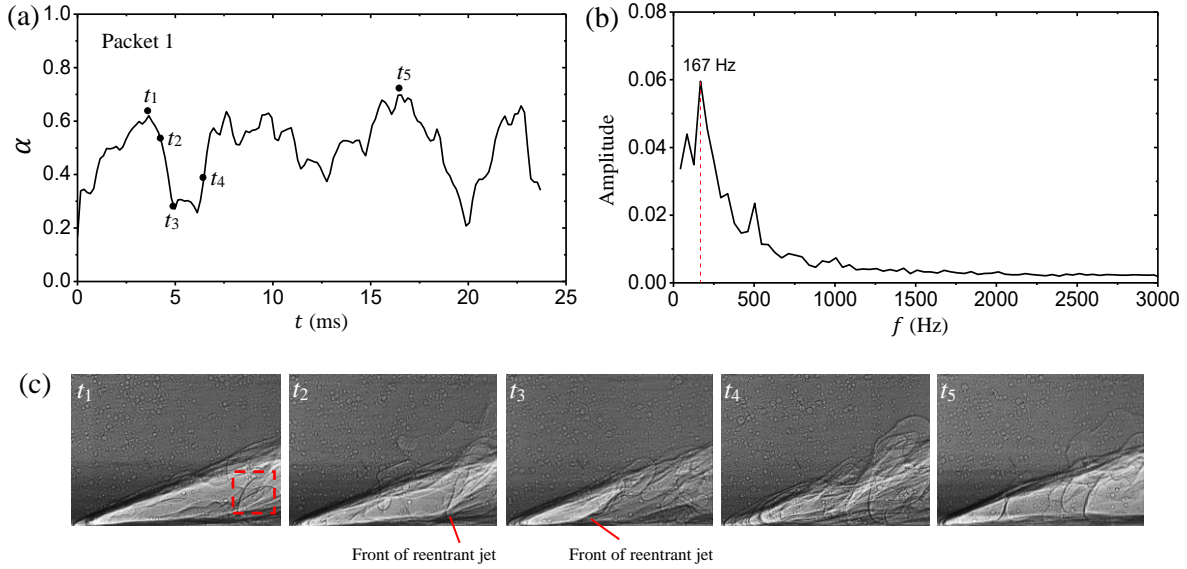


Figure 4.8. Examination of void fraction in the X-ray scanning position 1, (a) time-varying void fraction in the first probe location indicated by the red dashed frame in (c); (b) average of all the spectra of 13 packets; (c) X-ray images at five typical time instants.

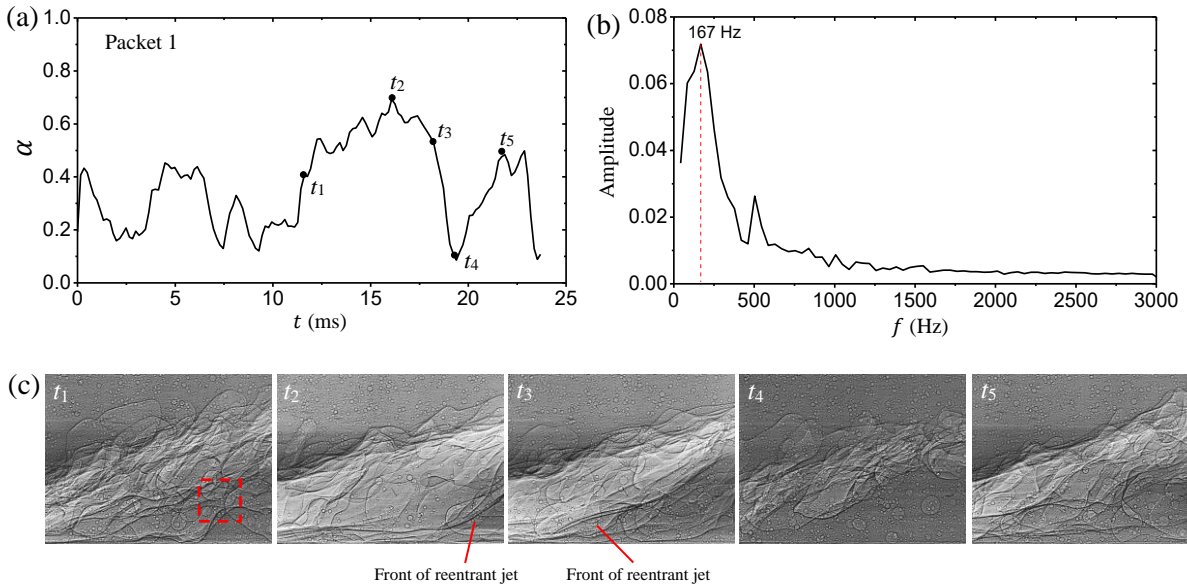


Figure 4.9. Examination of void fraction in the X-ray scanning position 2, (a) time-varying void fraction in the second probe location indicated by the red dashed frame in (c); (b) average of all the spectra of 13 packets; (c) X-ray images at five typical time instants.

X-ray images at five typical time instants are shown in Figure 4.8 (c) for the scanning position 1 and in Figure 4.9 (c) for the scanning position 2. It is clear that the very upstream part of the cavity is characterized by an attached vapour pocket which is fed by intense

vaporization at its upper interface with the liquid flow. Through the deformation of the vapour pocket boundary, one can identify the front of the re-entrant jet, whose appearance is different from the condensation shock front described in detail by Ganesh et al. (2016) and Budich et al. (2018). The vapour pocket shrinks and transitions into a low-void-ratio bubbly mixture under the action of condensation and break-up brought by the re-entrant jet. As shown in Figure 4.8 (c), the re-entrant jet has already reached the vicinity of the throat at the instant t_3 leading the vapour pocket to almost disappear. It is interesting to note that the re-entrant jet in the studied sheet cavitation can almost penetrate the entire cavity, but it never pinches off the cavity forming the shedding of large vapour clouds. This might be attributed to the re-entrant jet having insufficient momentum.

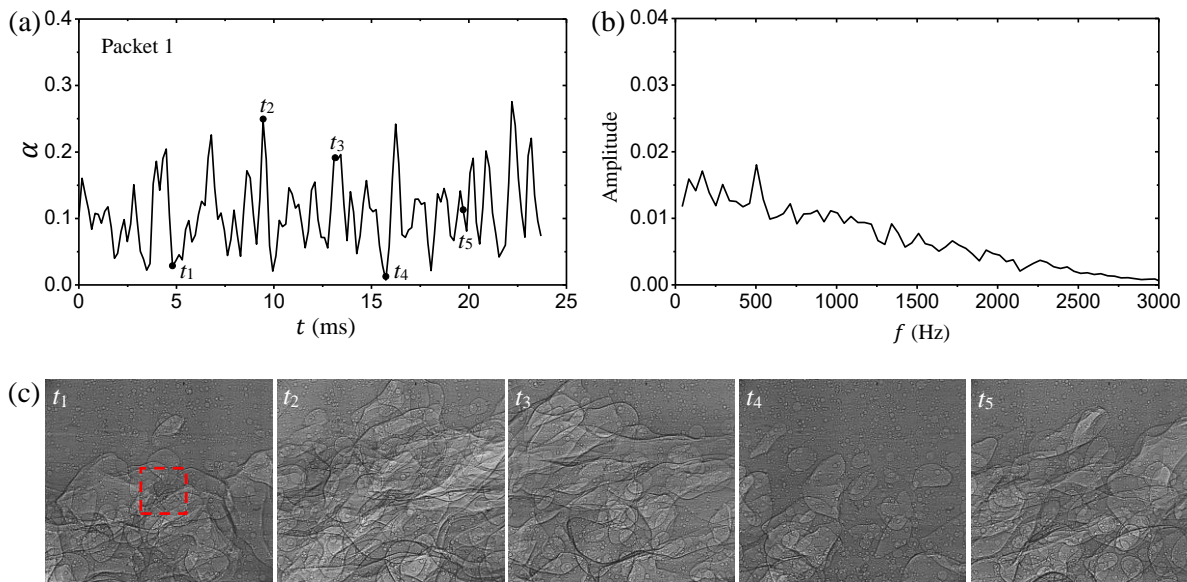


Figure 4.10. Examination of void fraction in the X-ray scanning position 107, (a) time-varying void fraction in the third probe location indicated by the red dashed frame in (c); (b) average of all the spectra of 13 packets; (c) X-ray images at five typical time instants.

The void fraction variation with time in the shear layer is also investigated. Figure 4.10(a) shows the time trace of void fraction at the third probe location, which is included in the scanning position 107. The average of all the spectra of 13 packets is shown in Figure 4.10(b). Multiple spectral peaks with comparable amplitude can be recognized and the high-frequency content of the void fraction fluctuations increases considerably in comparison with the spectra obtained in the upstream region, which implies that the cavitation structure within the shear layer varies fast in a chaotic manner. The X-ray images at five typical instants in Figure 4.10(c)

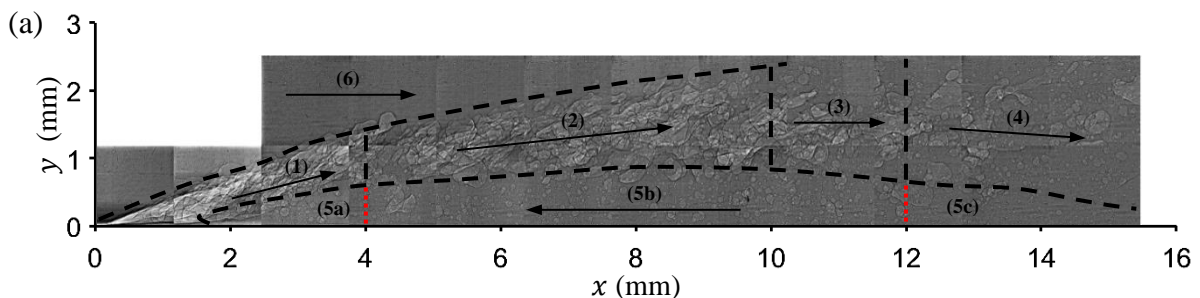
reveal the constant presence of the bubbly mixture at the probe position. Due to the high velocity gradient in the shear layer, the coherent vapour bubbles are twisted into a large variety of shapes and sizes.

4.5. Summary of two-phase flow structures inside sheet cavity

Based on the above analysis, the sheet cavity in the present flow conditions is essentially divided into 6 parts as shown in Figure 4.11(a). The complete flow field is reconstructed by assembling 22 instantaneous X-ray images in the corresponding scanning positions. In each position one X-ray image is selected manually to represent the local flow characteristics. In order to display the internal structures clearly, this giant reconstructed picture (7887×1326 pixels) is equally split into 3 sections which are enlarged and presented in Figure 4.11(b-d) with the scanning position numbers.

The upstream part (1) of the sheet cavity is characterized by an attached vapour pocket which is sustained due to intense vaporization at its upper interface with the liquid flow. Under the influence of the re-entrant jet, the vapour pocket grows and retracts quasi-periodically in the range of $x = 0-4$ mm at a frequency of 167 Hz, and consequently the mean void fraction in this region decreases rapidly from 75% to 20%.

The re-entrant jet region (5) can be divided into 3 sub-regions (5a), (5b) and (5c), namely the upstream part, the main part and the downstream part. The upstream part (5a) of the re-entrant jet ends on average at $x = 1.5$ mm where the probability of reverse flow is about 50% and corresponds to the location of maximum standard deviation of void fraction. When the attached vapour pocket interacts with the front of the re-entrant jet, it detaches from the wall and transitions into a low-void-fraction bubbly mixture. The upstream part (5a) of the re-entrant jet is likely to reach the vicinity of the throat, thereby making the vapour pocket almost disappear. But it does not cut the sheet cavity completely into two parts forming large vapour cloud shedding. The main part (5b) of the re-entrant jet is characterized by the continuous



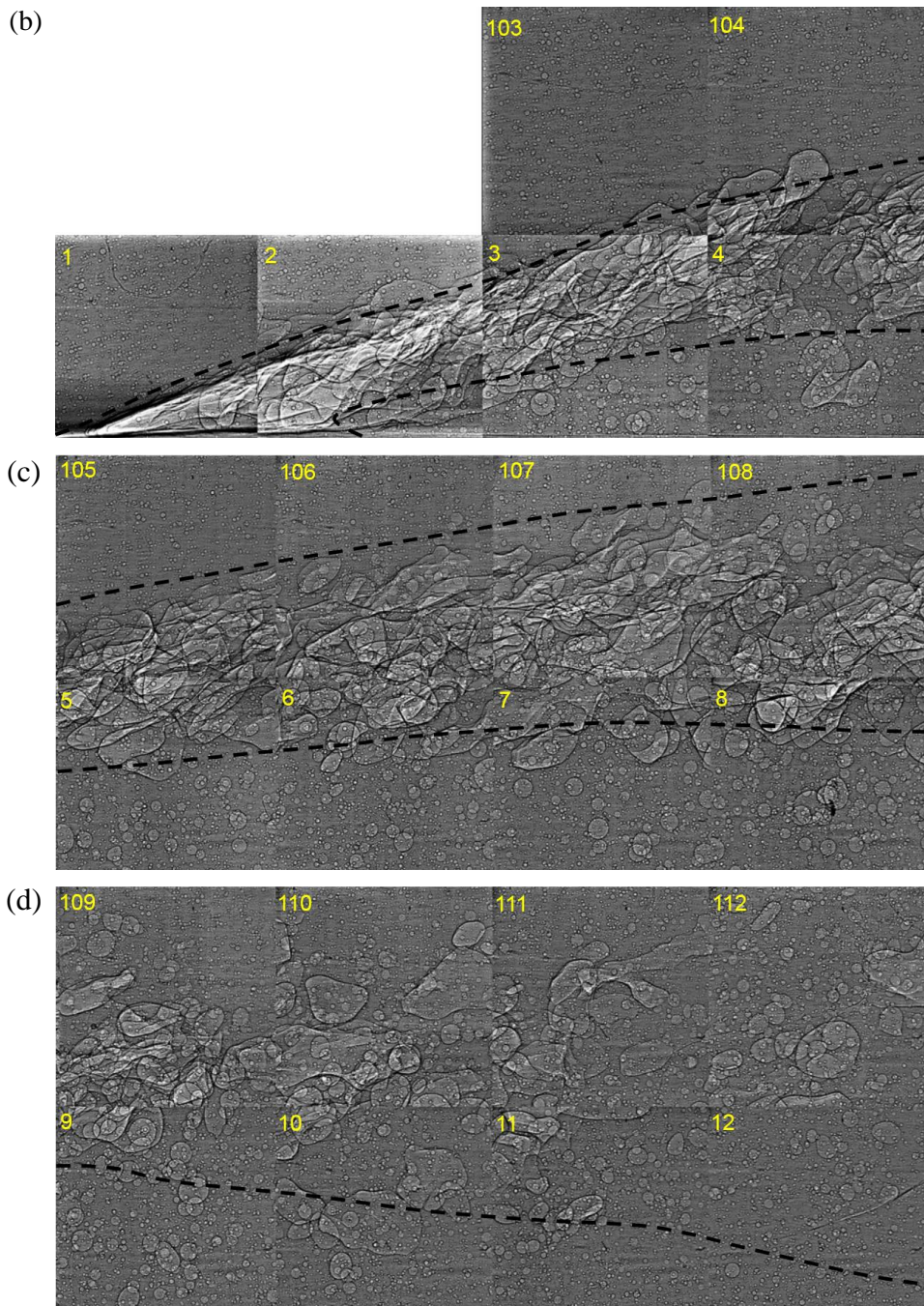


Figure 4.11. Two-phase flow structures inside sheet cavity, (a) a reconstructed image from 22 scanning positions showing the internal structures of sheet cavity. The arrows indicate the mean flow directions in each sub-regions; the image is equally split into 3 sections which are zoomed and shown in (b-d).

presence of reverse flow. In this region, the thickness of the re-entrant jet remains quite constant, and the mean velocity is fairly uniform spanning the whole thickness. The magnitude of the mean reverse flow velocity also remains quite constant along the streamwise direction at its

maximum value of approximately 0.6 m/s (7% u_{ref}). The downstream part (5c) is the region where the re-entrant jet originates from. The whole re-entrant jet can be considered as a liquid film moving upstream with dispersed cavitation bubbles, since the mean void fraction in this region is close to 0. The sparse bubbles entrained by the reverse flow tend to be of spherical shape as the velocity gradient is relatively small. The mean diameter of bubbles is estimated to be of the order of 100 microns.

The re-entrant jet (especially the main part (5b)) exists persistently in the studied sheet cavitation with a relatively constant thickness and velocity. The driving force acting on the re-entrant jet is the adverse pressure gradient which is related to the test section geometry and the occurrence of cavitation. The primary resistance to the re-entrant jet is the shear stresses imposed by the main flow. The re-entrant flow in the sheet cavitation oscillates only in a small size region, while the main part is characterized by a statistically steady state, which suggests the competition between the driving and drag forces, so the re-entrant jet generally reaches an equilibrium.

A strong velocity shear layer (2) exists steadily between the re-entrant jet (5) and the main flow (6) outside the cavity. In this region, the mean void fraction decreases along the flow direction at a very slow rate, and the standard deviation of void fraction is almost constant. No characteristic frequency is detected in the time variations of the void fraction. The low-void-fraction bubbly mixtures originated from the upstream vapour pocket are convected in the shear layer (2) without significant morphological and phase changes as their collapse might be limited by the low pressure in the cores of vortical structures. The coherent bubbles are deformed into a large variety of shapes and sizes as a consequence of high velocity gradient in the shear layer. The mean diameter of the bubbles cannot be estimated because they are highly coherent and non-spherical.

In the range of $x = 0-10$ mm, the quasi-steady re-entrant jet does not lead to any clear vapour shedding from the main cavity although a large portion of the cavity has already detached from the Venturi wall. This is the reason why the main part of the sheet cavity appears to be stable but with a wavy interface in the high speed photographs.

In the cavity closure region (3), small-scale vapour structures are shed continuously from the main cavity under the entrainment of the main flow and/or the action of horseshoe vortices. The mean sheet cavity is also terminated in this region (the mean cavity length is 11.5 mm in the present flow conditions). The part (4) is the cavity wake region where the shedding vapour

structures collapse into a large number of small bubbles. The mean void fraction in the wake is basically below 5%.

4.6. Turbulent velocity fluctuations inside sheet cavity

The acquisition of time-resolved velocity fields inside the sheet cavity allows us to obtain Reynold stresses as well. It should be clarified that what will be presented in the following is different from the classical Reynold stresses, since the instantaneous velocity was integrated along the flow passage thickness. Figure 4.12(a-c) show the distributions of streamwise velocity fluctuations $\overline{u'u'}/u_{\text{ref}}^2$, transversal velocity fluctuations $\overline{v'v'}/u_{\text{ref}}^2$ and shear stress $|\overline{u'v'}|/u_{\text{ref}}^2$, respectively, with the evolution of velocity gradient $\partial\overline{u}/\partial y$ along the flow direction shown in (d). The velocity fluctuations in longitudinal and transversal directions have the similar distributions and both of their domains of high-velocity fluctuations correspond pretty well to the shear area (indicated by the two dashed lines). The turbulence level in the reverse flow region is quite low due to the relatively steady state of the re-entrant jet in sheet cavitation. With the growth of shear layer thickness, the velocity gradient decreases along the streamwise direction. The longitudinal and transversal velocity fluctuations are observed to decrease gradually along the flow direction, which is consistent with the trend of velocity gradient. In the cavity wake ($x > 12$ mm) where the shedding vapour structures collapse, the longitudinal and transversal fluctuations do not increase compared with the upstream region. One possible explanation for this is that the decrease of fluctuations caused by the velocity gradient reduction is dominant, compared with the effect of vapour collapse, since the collapse is relatively mild in sheet cavitation. Let us recall the PIV measurements by Laberteaux & Ceccio (2001) in which they conclude that vapour collapses increase the turbulence level, leading the velocity fluctuations to be the largest in the wake of the cavity. It appears to be inconsistent with what is found in the present X-ray measurement results, while the fact is that they could not measure the internal velocity field of the sheet cavity and consequently draw that conclusion based on the comparison only outside the cavity.

With regard to the distribution of shear stress $|\overline{u'v'}|/u_{\text{ref}}^2$, it appears to be weakly correlated with the velocity gradient. The most intense area of shear stress is located in the range of $x = 12-16$ mm, which is exactly where the vapour collapse occurs. It implies that the collapse of vapour phase substantially increases the coupling between the streamwise and cross-stream velocity fluctuations. The second area of intense shear stress is located in a narrow

strip area ($x = 0-4$ mm) corresponding to the interface between the upstream vapour pocket and the liquid main flow. This interface is also the position where the sheet cavity is fed from the liquid through intense vaporization. Therefore, it is reasonable to conjecture that the phase change of vaporization also contributes to the coupling between the streamwise and cross-stream velocity fluctuations. In the range of $x = 4-10$ mm, the vapour bubbles are convected without significant phase change and accordingly the correlation between the streamwise and cross-stream velocity fluctuations reaches the lowest level.

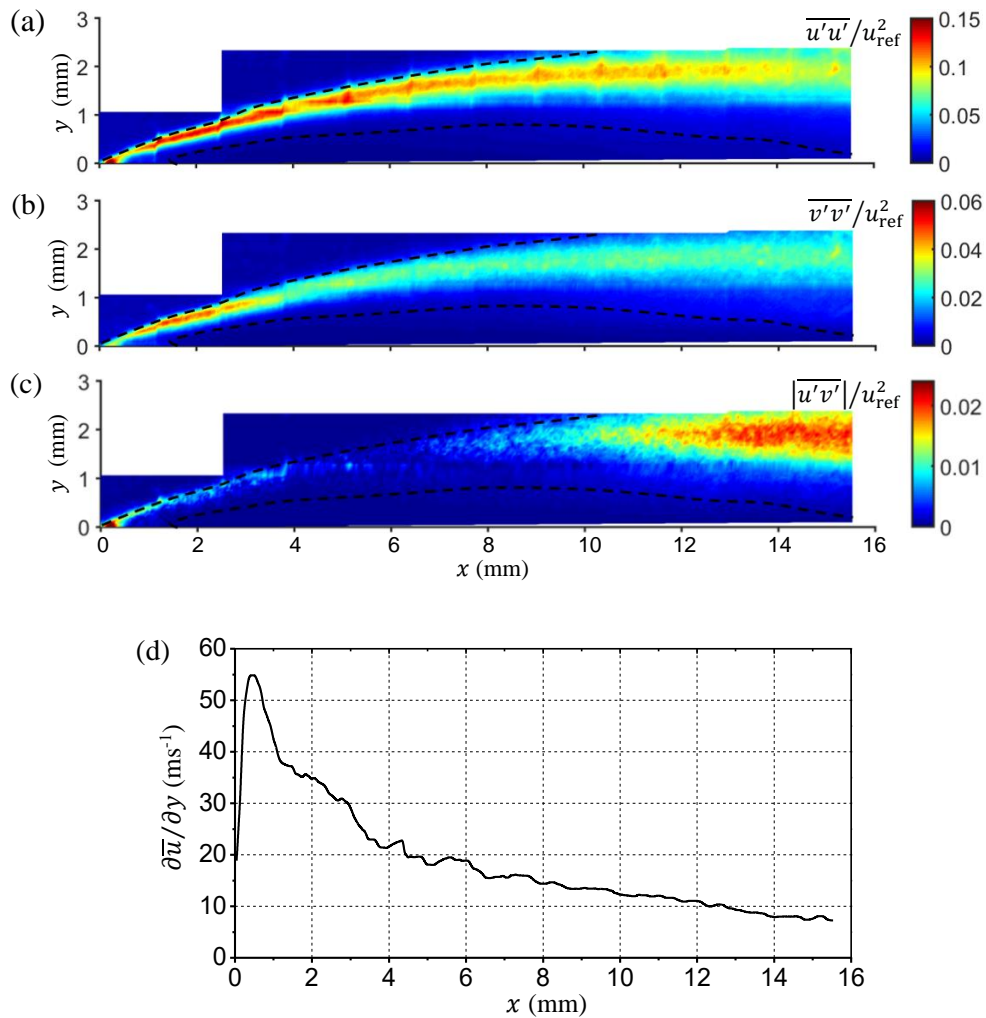


Figure 4.12. (a) Distribution of streamwise velocity fluctuations $\overline{u'u'}/u_{\text{ref}}^2$, (b) distribution of transversal velocity fluctuations $\overline{v'v'}/u_{\text{ref}}^2$, (c) distribution of shear stress $|\overline{u'v'}|/u_{\text{ref}}^2$, (d) evolution of velocity gradient $\partial\overline{u}/\partial y$ along the flow direction. The two dashed lines indicate the shear area between the re-entrant jet and the main flow.

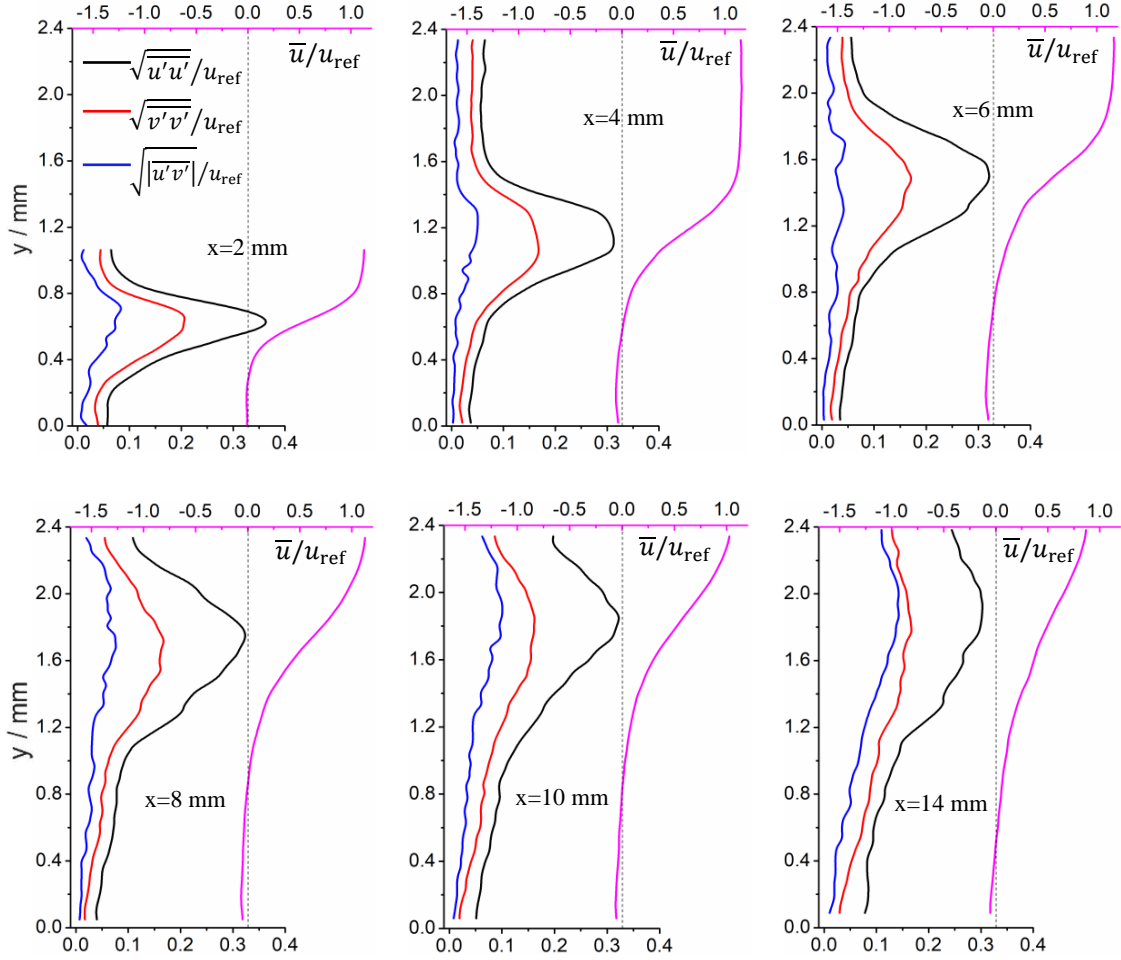


Figure 4.13. Profiles of streamwise velocity fluctuations $\sqrt{u'u'}/u_{\text{ref}}$ (black line), transversal velocity fluctuations $\sqrt{v'v'}/u_{\text{ref}}$ (red line), and shear stress $\sqrt{|u'v'|}/u_{\text{ref}}$ (blue line) with mean streamwise velocity \bar{u}/u_{ref} (pink line) at different streamwise locations.

Figure 4.13 shows the profiles of streamwise velocity fluctuations, transversal velocity fluctuations, and shear stress compared with the profiles of mean streamwise velocity at different distances from the throat. It is observed that the peaks of velocity fluctuations in the streamwise and cross-stream directions, as expected, correspond approximately to the location of maximum velocity gradient. The turbulence level in the reverse flow region is of the same order of magnitude as in the outer main flow. The streamwise fluctuations are much larger than the cross-stream ones within the shear layer, while in the other regions they just have a slight disparity. That means the turbulence in the shear layer is anisotropic and is dominated by the streamwise velocity fluctuations. The isotropic hypothesis of turbulence modelling may thus require special corrections for the shear layer in cavitating flows.

4.7. Validation of the Reboud empirical correction

The simultaneous acquisition of instantaneous velocity field and density field enables us to validate the Reboud correction experimentally. In this section, we will firstly make a brief introduction of the Reboud empirical correction (Reboud et al. 1998, Coutier-Delgosha et al. 2003) and then demonstrate its rationality based on the present experimental data.

The local speed of sound in the liquid/vapour mixture is strongly related to the void fraction (Shamsborhan et al. 2010) and in some flow conditions it may decrease drastically to a few meters per second. This implies that the cavitating flow is highly compressible in the two-phase region where the Mach number is expected to exceed 1. The mixture density in cavitating flows is defined as

$$\rho = \alpha\rho_v + (1 - \alpha)\rho_l = \rho_v + (1 - \alpha)(\rho_l - \rho_v) \quad (4.1)$$

where α is the vapour volume fraction; ρ_l is the water density and ρ_v is the vapour density.

The standard k- ω SST model (Menter 1994) is superior to the other two-equation models in predicting turbulent flows with adverse pressure gradient since it accounts for the transport of the principle Reynolds shear stress τ based on the well-known Bradshaw hypothesis: the Reynolds shear stress τ in a boundary layer is proportional to the turbulent kinetic energy k , written as,

$$\tau/k = \rho a_1, \text{ with } a_1 \text{ being a constant.} \quad (4.2)$$

Although the standard k- ω SST model is well applied to single-phase flows, it fails to predict cavity sizes and shedding frequencies in unsteady cavitating flows. Taking into account the effect of cavitation compressibility on turbulent fluctuations, the Reboud correction is to replace the mixture density used in Bradshaw hypothesis by a function of density,

$$\tau/k = f(\rho)a_1 \quad (4.3)$$

$$f(\rho) = \rho_v + (1 - \alpha)^n(\rho_l - \rho_v) = \rho_v + \left(\frac{\rho - \rho_v}{\rho_l - \rho_v}\right)^n (\rho_l - \rho_v) \quad (4.4)$$

The correction is based on the void fraction and leads to a fast artificial decrease of the turbulent viscosity and thus the local shear stress when the vapour starts to appear.

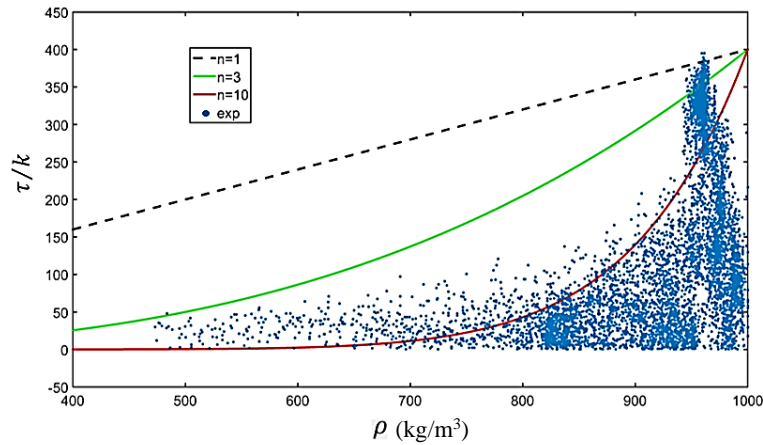


Figure 4.14. Comparison between the experimental data and the Reboud empirical modification with $n=1$, 3 and 10 ($n=1$ is the Bradshaw hypothesis).

In order to evaluate the validity of the Reboud correction, the ratio of the Reynolds shear stress to the turbulent kinetic energy τ/k within the boundary layer is plotted in Figure 4.14 as a function of the mixture density ρ . The experimental results are then compared with the Bradshaw assumption ($n=1$) and the Reboud empirical correction with $n=3$ or 10. We can observe that the ratio τ/k derived from the experimental data is not a linear function of the mixture density ρ within the boundary layer; the evolution of τ/k is close to the Reboud correction with $n=10$ although a part of the data still deviates from the correction curve. It explains why the Reboud correction has been widely used in the past two decades and provides significant improvements in the RANS simulations of cavitating flows.

4.8. Chapter summary

The sheet cavitation generated in a small size Venturi channel was at first studied by means of high speed photography. The main part of the sheet cavity was observed to attach to the solid surface steadily with a wavy interface. Small vapour structures were rolled up and detached continuously from the cavity closure region at multiple high frequencies. These global behaviors of sheet cavitation observed from high speed images are consistent with the previous research about this cavitation pattern. So far for the stable character of the sheet cavitation was usually related to an absence of re-entrant jet or a re-entrant jet existing only in the rear part of the cavity, leading to a relatively stable fore part with a turbulent frothy closure. However, this conjecture was supported by very limited experimental data on the two-phase structures and velocity fields inside the sheet cavity.

Based on the present data from the X-ray measurements, the complex two-phase flow structures inside the sheet cavity were revealed in detail for the first time. As shown in Figure 4.11, the sheet cavity in the present flow conditions is essentially divided into 6 parts. An oscillating vapour pocket exists in the upstream part (1) of the cavity and the mean void fraction in this region decreases from the maximum value 75% to 20% rapidly. The main part of the re-entrant jet (5) exists persistently near the wall with a relatively constant thickness and velocity. When the vapour pocket interacts with the front of the re-entrant jet, it shrinks and transforms into a low-void-ratio bubbly mixture under the action of condensation and break-up. The whole re-entrant jet can be regarded as a liquid film moving upstream since the mean void fraction in this region is close to 0. The sparse bubbles entrained by the reverse flow tend to be of spherical shape and the mean diameter is estimated to be of the order of 100 microns. A strong velocity shear layer (2) exists steadily between the re-entrant jet (5) and the main flow (6) outside the cavity. In this region, the mean void fraction decreases along the flow direction at a very slow rate, and the low-void-fraction bubbly mixtures originated from the upstream vapour pocket are convected downstream without significant morphological and phase changes as their collapse might be limited by low pressure in the cores of coherent vortical structures. In the part (3), small-scale vapour structures are detached continuously from the main cavity under the entrainment of the main flow and/or the action of horseshoe vortices. The part (4) is the cavity wake region where the shedding vapour structures collapse into a large number of small bubbles. The mean void fraction in the wake is basically below 5%.

The turbulent velocity fluctuations inside the sheet cavity were also investigated. The domains of high-velocity fluctuations in the streamwise and cross-stream direction were found to correspond to the shear area. Both of them decrease gradually along the flow direction, which is consistent with the trend of velocity gradient. The turbulence level in the reverse flow region is as low as in the main flow, demonstrating the relatively steady status of the re-entrant jet in the sheet cavitation. Unlike the streamwise and cross-stream fluctuations, the shear stress appears to be weakly correlated with the velocity gradient. The collapse of vapour phase was found to be the main cause of the larger shear stress in the cavity wake. The phase change of vaporization at the upstream interface was also found to increase the coupling between the streamwise and cross-stream velocity fluctuations. The lowest shear stress was identified in the shear layer where vapour bubbles are convected without significant phase change.

Thanks to the simultaneous acquisition of instantaneous velocity field and density field,

the well-known Reboud empirical correction was examined experimentally for the first time. Compared with the original Bradshaw hypothesis, the Reboud correction with $n=10$ was found to agree much better with the X-ray experimental data. It explains why the Reboud correction has provided significant improvements in the RANS simulations of cavitating flows in the past two decades.

4.8. Résumé du chapitre

La cavitation de la feuille générée dans un canal Venturi de petite taille a d'abord été étudiée au moyen d'une photographie à grande vitesse. On a observé que la partie principale de la cavité de la feuille se fixait à la surface solide de manière constante avec une interface ondulée. De petites structures de vapeur ont été enroulées et détachées en continu de la région de fermeture de la cavité à de multiples hautes fréquences. Ces comportements globaux de cavitation de feuille observés à partir d'images à grande vitesse sont cohérents avec les recherches précédentes sur ce modèle de cavitation. Jusqu'à présent pour le caractère stable de la feuille, la cavitation était généralement liée à une absence de jet rentrant ou à un jet rentrant existant uniquement dans la partie arrière de la cavité, conduisant à une partie antérieure relativement stable avec une fermeture mousseuse turbulente. Cependant, cette conjecture était soutenue par des données expérimentales très limitées sur les structures à deux phases et les champs de vitesse à l'intérieur de la cavité de la feuille.

Sur la base des données actuelles des mesures aux rayons X, les structures d'écoulement diphasiques complexes à l'intérieur de la cavité de la feuille ont été révélées en détail pour la première fois. Comme le montre la figure 4.11, la cavité de feuille dans les présentes conditions d'écoulement est essentiellement divisée en 6 parties. Une poche de vapeur oscillante existe dans la partie amont (1) de la cavité et la fraction de vide moyenne dans cette zone décroît rapidement de la valeur maximale 75% à 20%. La partie principale du jet rentrant (5) existe en permanence à proximité de la paroi avec une épaisseur et une vitesse relativement constantes. Lorsque la poche de vapeur interagit avec l'avant du jet rentrant, elle se rétracte et se transforme en un mélange bouillonnant à faible taux de vide sous l'action de la condensation et de la rupture. L'ensemble du jet rentrant peut être considéré comme un film liquide se déplaçant vers l'amont puisque la fraction de vide moyenne dans cette région est proche de 0. Les bulles clairsemées entraînées par le flux inverse ont tendance à être de forme sphérique et le diamètre moyen est estimé à être de l'ordre de 100 microns. Une couche de cisaillement à forte vitesse (2) existe

régulièrement entre le jet rentrant (5) et le flux principal (6) à l'extérieur de la cavité. Dans cette région, la fraction de vide moyenne diminue le long de la direction d'écoulement à une vitesse très lente, et les mélanges bouillonnants à faible fraction de vide provenant de la poche de vapeur en amont sont convectés en aval sans changements morphologiques et de phase significatifs car leur effondrement pourrait être limité par basse pression dans les noyaux de structures vorticales cohérentes. Dans la pièce (3), des structures de vapeur à petite échelle se détachent en continu de la cavité principale sous l'entraînement du flux principal et / ou sous l'action de tourbillons en fer à cheval. La partie (4) est la région de sillage de la cavité où les structures de vapeur qui s'échappent s'effondrent en un grand nombre de petites bulles. La fraction de vide moyenne dans le sillage est essentiellement inférieure à 5%.

Les fluctuations de vitesse turbulente à l'intérieur de la cavité de la feuille ont également été étudiées. On a trouvé que les domaines de fluctuations à haute vitesse dans la direction du courant et du courant transversal correspondent à la zone de cisaillement. Les deux diminuent progressivement le long de la direction d'écoulement, ce qui est cohérent avec la tendance du gradient de vitesse. Le niveau de turbulence dans la région d'écoulement inverse est aussi bas que dans l'écoulement principal, démontrant l'état relativement stable du jet rentrant dans la cavitation de la feuille. Contrairement aux fluctuations fluviales et transversales, la contrainte de cisaillement semble être faiblement corrélée avec le gradient de vitesse. L'effondrement de la phase vapeur s'est avéré être la principale cause de la contrainte de cisaillement plus importante dans le sillage de la cavité. Le changement de phase de vaporisation à l'interface amont s'est également avéré augmenter le couplage entre les fluctuations de vitesse dans le sens du courant et transversales. La contrainte de cisaillement la plus faible a été identifiée dans la couche de cisaillement où les bulles de vapeur sont convectées sans changement de phase significatif.

Grâce à l'acquisition simultanée du champ de vitesse instantanée et du champ de densité, la correction empirique bien connue de Reboud a été examinée expérimentalement pour la première fois. Par rapport à l'hypothèse originale de Bradshaw, la correction Reboud avec $n = 10$ s'est avérée bien mieux en accord avec les données expérimentales radiographiques. Cela explique pourquoi la correction Reboud a apporté des améliorations significatives dans les simulations RANS des écoulements cavitants au cours des deux dernières décennies.

Chapter 5

Comparison of sheet cavity structures and dynamics at different stages

The cavitation number and the geometrical layout are the two principal parameters to control the partial cavity regime forming on the Venturi divergent wall. The former parameter is responsible for the low pressure condition and the latter one determines the underlying pressure distribution which is crucial to the onset of the re-entrant jet. In the Venturi channel with appropriate geometry dimensions, the cavity regime can range from the relatively stable sheet cavitation to the periodic cloud shedding as the cavitation number decreases. However, this transition process is likely to be modified or even inhibited through changing the geometrical parameters. As shown in the work of Callenaere et al. (2001), when the height of the upper confinement plate was increased to a certain extent, the cloud cavitation would disappear. In the present Venturi channel, the contraction ratio of the height from the inlet to the throat is small, which yields a similar effect as increasing the confinement height. As a consequence, it is possible for the cavitating flow to sustain a relatively steady regime of sheet cavitation in a wide range of cavitating conditions.

The variation of cavitation number in the present experiment was achieved by adjusting the inlet pressure while keeping the flow rate constant (the reference velocity u_{ref} at the Venturi throat remains at 9.53 m/s). The cavitation pattern observed does not exhibit a significant change with the reduction of cavitation number. In other words, the cavitating flow in this specific geometric configuration is characterized by a quasi-stable sheet cavitation with irregular shedding of small vapour structures near the cavity closure and the classic periodic cloud cavitation is not observed. Chapter 4 was dedicated to the analysis of the internal structure and dynamics for the sheet cavitation at the developed stage ($\sigma = 7.54$) which features

a low-speed reverse flow region existing continuously underneath the cavity. In this chapter, a comparative study of sheet cavitation at three stages ($\sigma = 7.54$ corresponding to the developed stage, $\sigma = 8.0$ corresponding to the intermediate stage and $\sigma = 9.13$ corresponding to the early stage) is performed. The effect of cavitation on the turbulent fluctuations is also presented.

5.1. Experimental mean void fraction

Figure 5.1 shows the measured distributions of time-averaged void fraction $\bar{\alpha}$ at different cavitation numbers. Also indicated are the mean cavity length L_{cav} and thickness T_{cav} determined from the contour of $\bar{\alpha} = 0.1$. Note that the number of X-ray scanning positions varies according to the extent of cavitation. In practice, only the positions where vaporous structures dominate were recorded due to the limitation of available beam time. It can be seen that the cavitating area grows significantly both in length and thickness with decreasing the cavitation number σ . The highest local mean void fraction is obtained immediately

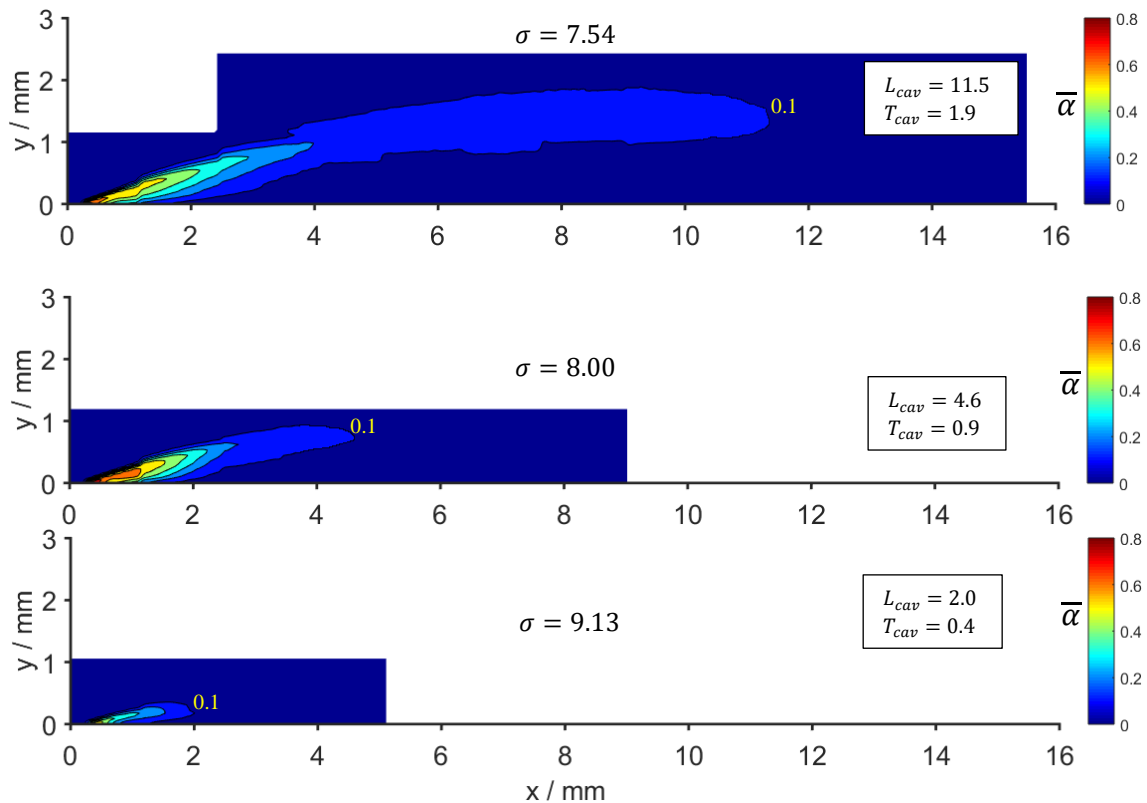


Figure 5.1. Distribution of the mean void fraction $\bar{\alpha}$ at different cavitation numbers. The mean cavity length L_{cav} and thickness T_{cav} (in mm) are obtained based on the contour line of $\bar{\alpha} = 0.1$.

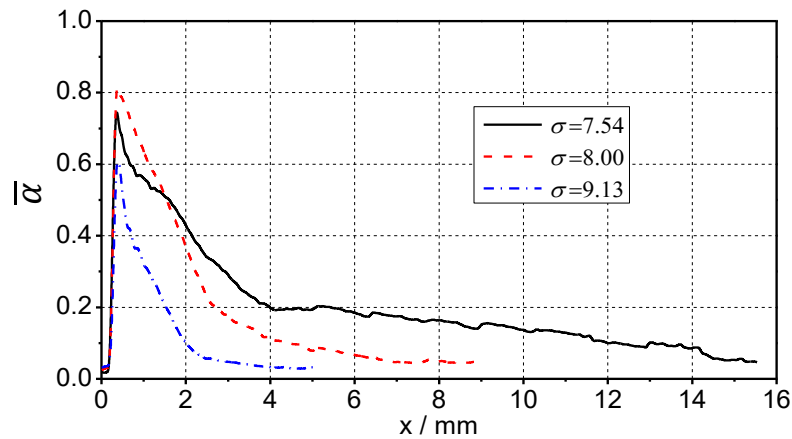


Figure 5.2. Evolution of the mean void fraction (maximum value in the y direction) along the flow direction.

downstream of the Venturi throat in the three cases. Similar to the already developed cavity ($\sigma = 7.54$), the rear portion of the intermediate cavity ($\sigma = 8.0$) presents an obvious trend to detach from the divergent wall as well, illustrating the influence of reverse flow beneath the cavity. For the sheet cavity at early stage ($\sigma = 9.13$), it appears to attach to the wall without any evident flow separation.

The maximum mean void fraction in the transverse direction is plotted in Figure 5.2, and it illustrates clearly the spatial evolution of the mean void fraction along the flow direction for the three cases. Within the cavity at early stage, the mean void fraction decreases regularly from 60% to 10% at the closure of the mean cavity ($x = 2$ mm). For the developed and intermediate cavities, the mean void fraction shows a rapid decrease from their respective maximum value to 20%, after which the void fraction further reduces at a relatively slower rate until the downstream end of the mean cavity ($x = 11.5$ mm and $x = 4.6$ mm, respectively). Based on an overall comparison of the three cases, the void fraction inside the cavities increases with the extent of cavitation. Nevertheless, it is interesting to note that the mean vapour volume fraction of the intermediate cavity is higher than that of the developed cavity in the region close to the leading edge, which will be interpreted in Section 5.3.

The averaged void fraction profiles at six stations in the flow direction are shown in Figure 5.3 for the three cases. The maximum void fraction on each vertical station seems to be shifted towards the upper interface of the cavity as we move downstream along the cavity, while a noticeable decrease of the void fraction in the near wall region can be discerned clearly. Again,

at the location $x = 1$ mm, the mean void fraction of the intermediate cavity is the highest, compared to the other two cases.

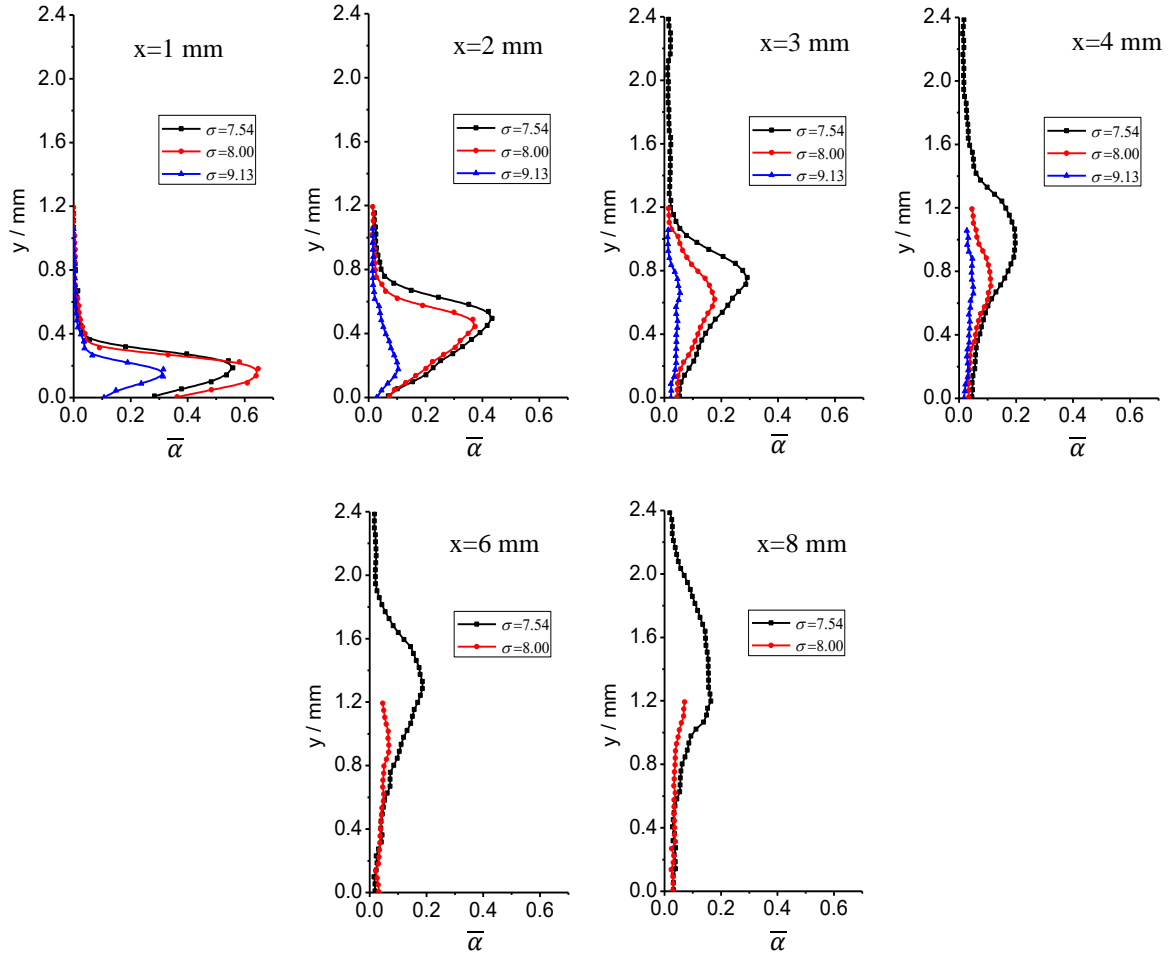


Figure 5.3. Comparison of mean void fraction profiles at different streamwise locations.

5.2. Experimental results of mean velocity distributions

Figure 5.4 indicates a comparison of three cases for the time-averaged longitudinal velocity fields in which the mean velocity \bar{u} is normalized by the reference velocity u_{ref} . The mean cavity profile represented by the isoline of $\bar{\alpha} = 0.1$ is also overlaid on the corresponding velocity field using the white dotted line. It is clear that the averaged velocity flow field is significantly altered by the development of cavitation. In the case of early cavity, no reverse flow is observed in the mean velocity field, which is consistent with the observation of the cavity attaching to the wall. With the expansion of cavitation area, the adverse pressure gradient at the cavity closure is supposed to increase. It results in higher probability for the onset of a reverse flow. It is clear that a reverse flow region (under the contour line of 0) is formed along

the wall beneath the rear part of the intermediate cavity as well as the developed cavity, and the reduction of cavitation number leads to a pronounced increase of the mean reverse flow size in terms of length and thickness. As can be seen, the re-entrant flow, mainly composed of liquid (very low void fraction), tends to displace the cavity away from the wall, which contributes to the thickening of the sheet cavity. Although the downstream end of the mean reverse flow region is significantly different in the two cases, their upstream ends are almost located at the same distance from the throat, exactly $x = 1.5$ mm for $\sigma = 7.54$ and $x = 2.1$ mm for $\sigma = 8.0$. It should be pointed out that in the two cases, the rear ends of the mean reverse flow are both positioned more downstream than their mean cavity closure.

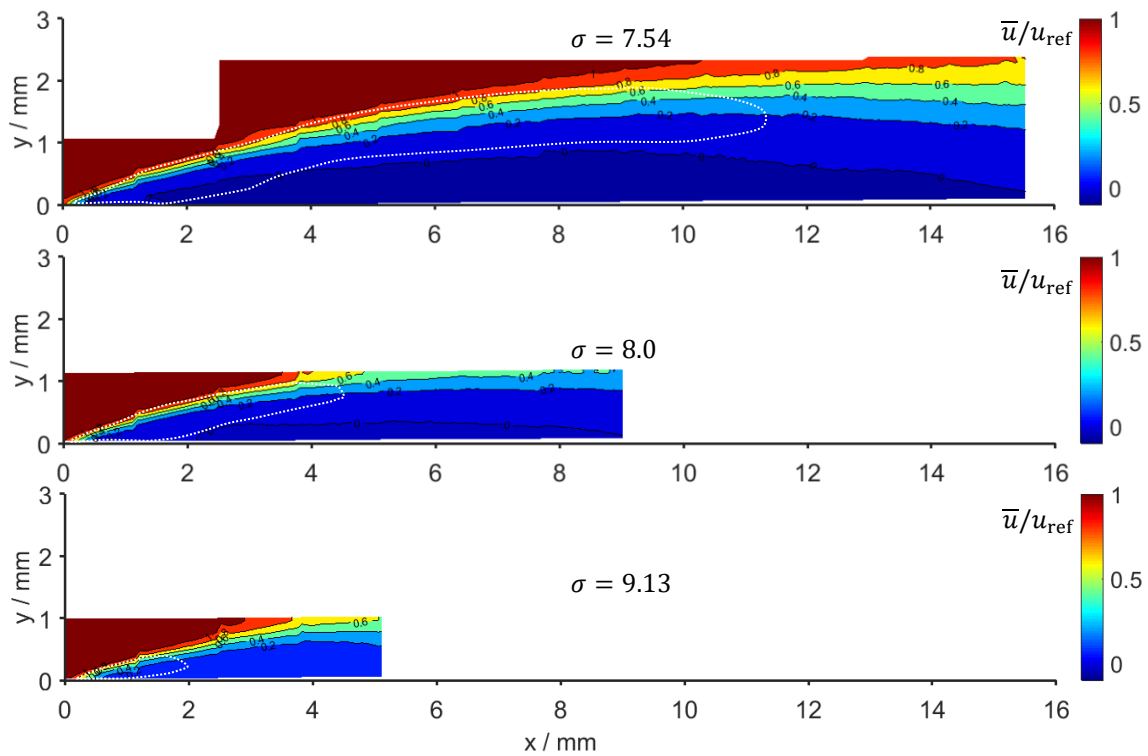


Figure 5.4. Contours of the time-averaged longitudinal velocity normalized by the reference velocity \bar{u}/u_{ref} at different cavitation numbers. The white dotted line depicts the mean cavity profile.

In order to highlight the near-wall upstream moving flow, the variation of time-averaged longitudinal velocity along the horizontal line located at $y=0.1$ mm (parallel to the Venturi wall) is shown in Figure 5.5 for the three cavitation numbers. For the case $\sigma = 9.13$, the average streamwise velocity reaches its minimum at approximately $x=2$ mm, which corresponds to the mean cavity closure. For the two other cases with re-entrant jet, the overall variation trend is

qualitatively similar: the near-wall flow in the cavity wake begins to be reversed due to the augmented adverse pressure gradient; as it propagates upstream, the magnitude of the mean reverse flow increases until attaining a maximum value that remains constant in a relatively wide region; then it is halted under the action of shear stress imposed by the main flow as it becomes closer to the leading edge of the cavity. Although the re-entrant jet is strengthened with decreasing σ (from 4% u_{ref} to 7% u_{ref}), it is still quite weak compared to the measured velocity of re-entrant jet in periodic cloud cavitation, which is generally of the same order of magnitude as the free-stream velocity (Le et al. 1993; Pham et al. 1999; Callenaere et al. 2001). Therefore the re-entrant jet region in the studied flow conditions may be regarded as a nearly stagnant liquid layer that separates the cavity from the solid wall.

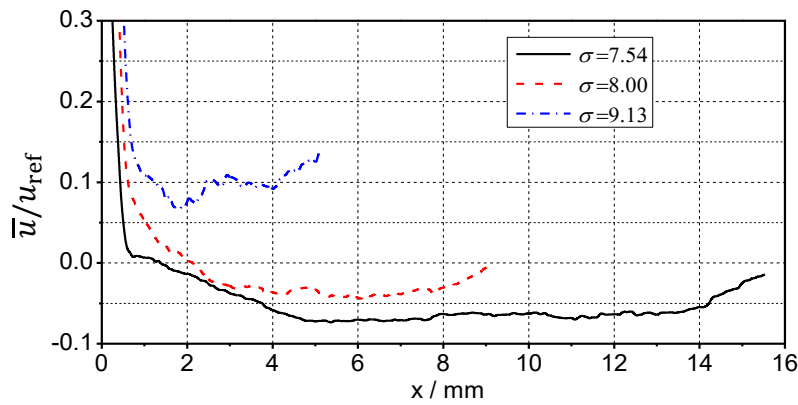


Figure 5.5. Evolution of the time-averaged longitudinal velocity \bar{u}/u_{ref} along the horizontal line of $y=0.1$ mm (adjacent to the Venturi wall).

A quantitative comparison of mean streamwise velocity profiles for the three cavitation numbers at six stations is shown in Figure 5.6. All velocity profiles are apparently influenced to some extent by the adverse pressure gradient, and thus do not exhibit a typical turbulent boundary layer type. Although the mean near-wall flow at $\sigma = 9.13$ is always directed downstream, it still shows a clear evidence of separation. In the three cases a free shear layer can be observed between the low-velocity (negative or positive) near-wall region and the external high-speed main flow. With the reduction of cavitation number, the mean velocity distribution along the re-entrant jet thickness tends to be more uniform, which consequently reduces the shear-induced flow instability.

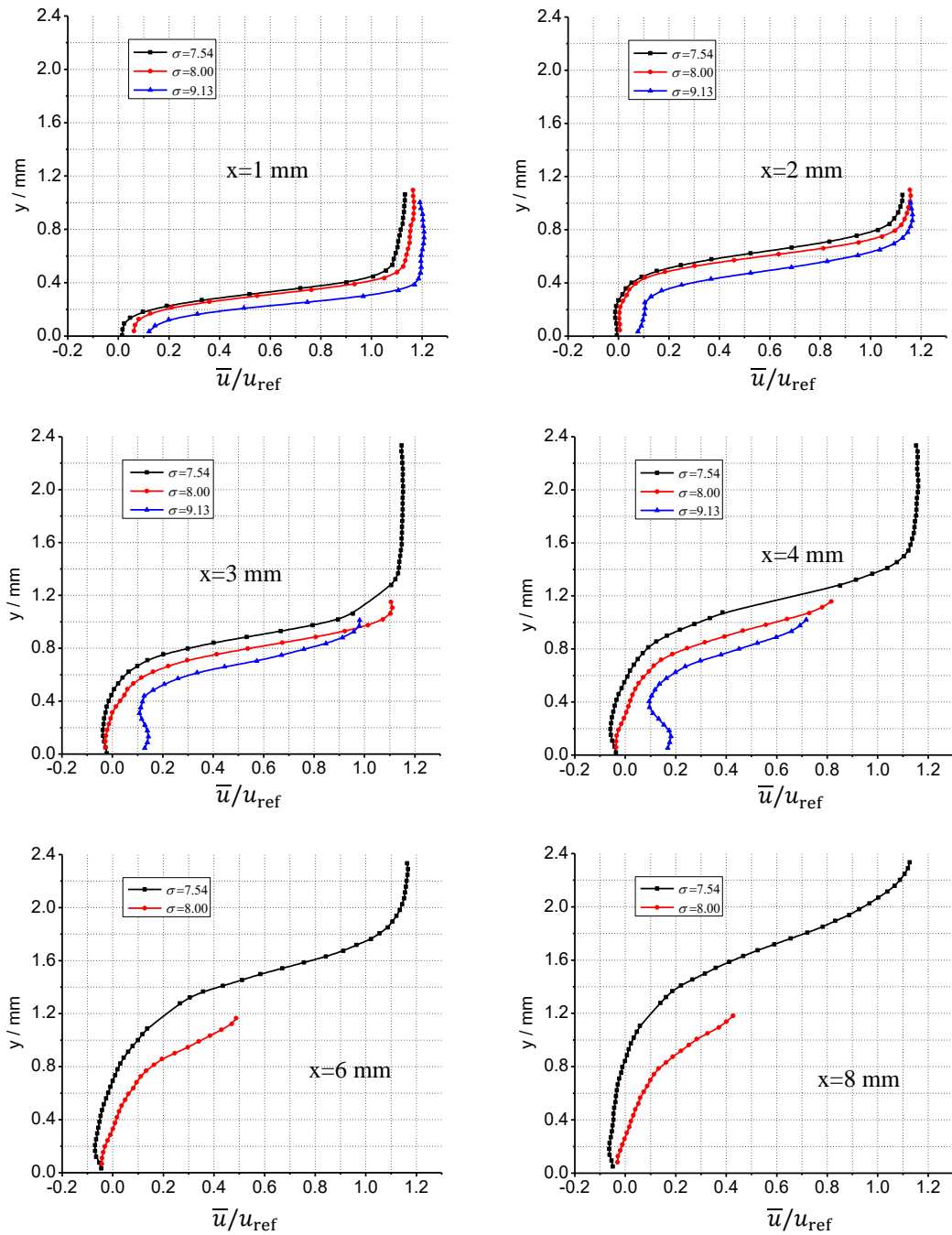


Figure 5.6. Comparison of mean longitudinal velocity profiles at different streamwise locations.

5.3. Analysis of cavity instability

Figure 5.7 shows the internal structure of the sheet cavity using the reconstructed X-ray image, on which the mean velocity vectors and the boundary of the mean reverse flow (indicated by the red dashed line) are overlaid. At $\sigma = 7.54$ and 8.0 , the very upstream part of the cavity is characterized by an attached vapour pocket which is fed by intense vaporization

at its upper interface with the liquid main flow. With the cavity expansion towards downstream, the quasi-pure vapour pocket cannot be sustained, and it starts to break up into a bubbly mixture. The intensity of this breakup process can be described by the standard deviation of void fraction α' shown in Figure 5.8. It can be seen that the location of the maximum α' is close to $x=1.5$ mm for $\sigma = 7.54$ and $x=2$ mm for $\sigma = 8.0$, which corresponds roughly to the upstream end position of the mean reverse flow, suggesting the predominant effect of the re-entrant jet on the cavity breakup. It should be also noted that in these two cases the weak re-entrant jet is able to reach the leading edge of the cavity, like in cloud cavitation, but it has insufficient momentum to break the cavity completely into two parts, let alone roll up the cavity into a

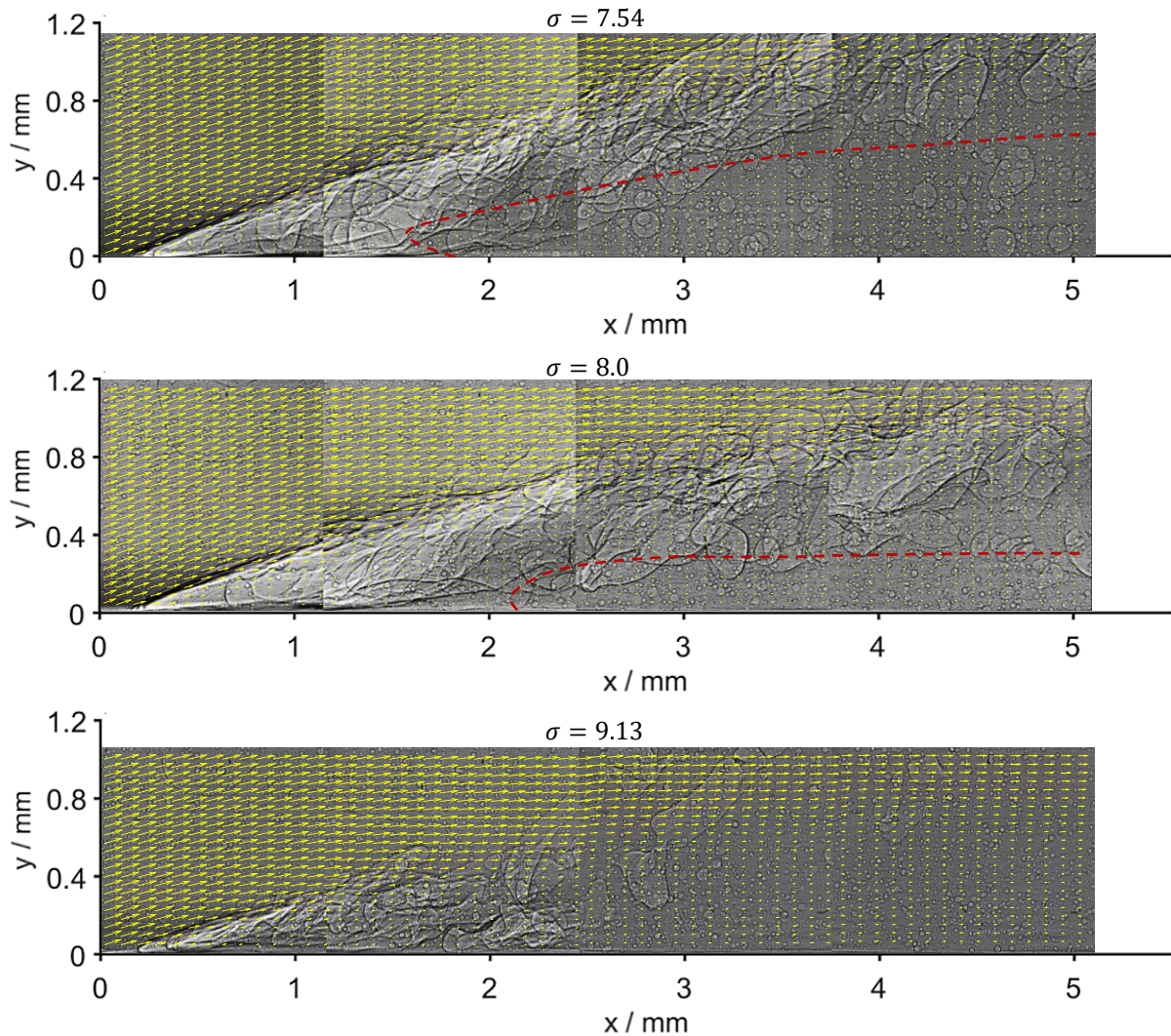


Figure 5.7. Reconstructed X-ray image from the first four positions showing the characteristic structures of the cavity in the upstream region. The mean velocity vectors are overlaid on the corresponding area. The red dashed line indicates the boundary of the mean reverse flow.

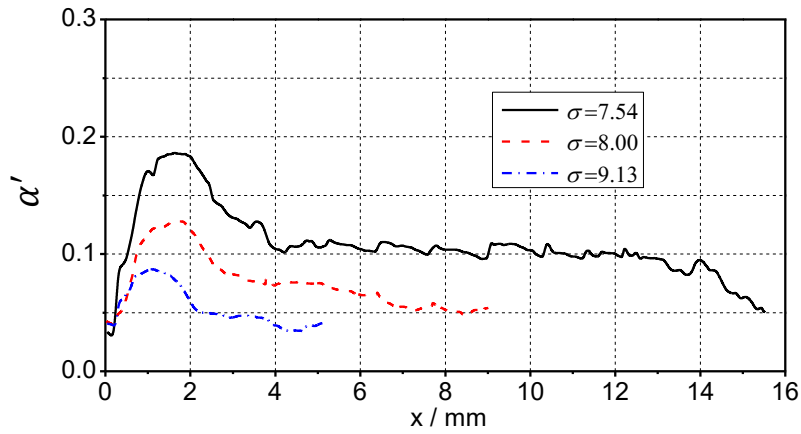


Figure 5.8. Evolution of the standard deviation of void fraction α' along the streamwise direction.

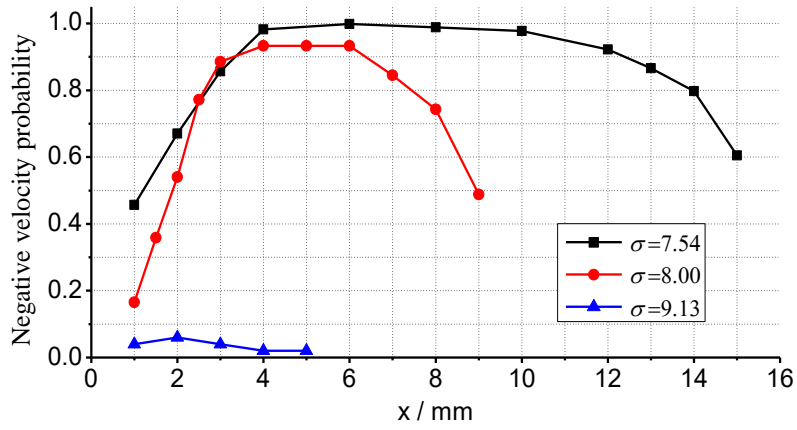


Figure 5.9. Evolution of the occurrence probability of negative velocity along the line of $y = 0.1$ mm.

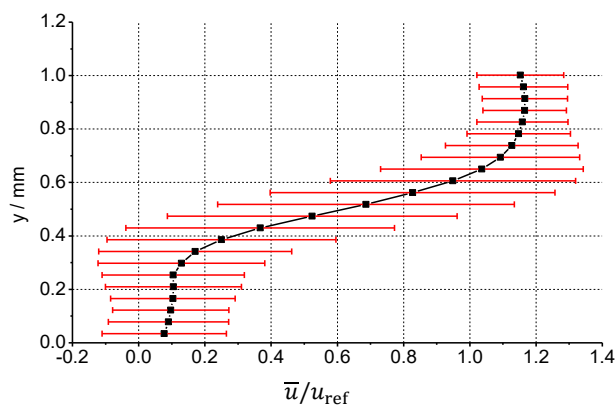


Figure 5.10. The mean longitudinal velocity profile at station of $x=2$ mm for $\sigma = 9.13$. The error bars denote the standard deviation of the velocity.

large-scale cloud structure. At $\sigma = 9.13$, it is less possible to sustain a vapour pocket since the slow vapour production rate is not able to support the vapour filling process after it is partially transported downstream. The position of the maximum α' is close to $x=1$ mm, where there is no re-entrant jet. This largest void fraction perturbation may be attributed to the shear-induced unsteadiness.

In order to have a better understanding of the unsteady behavior of the re-entrant jet, the probability of negative velocity in the near-wall region is presented in Figure 5.9. Although the mean velocity at $\sigma = 9.13$ is always positive, the turbulent fluctuations are enough for the instantaneous velocity to become negative. One example of negative velocity is given in Figure 5.10. However, we can generally say that there is no re-entrant jet in the sheet cavitation at early stage. The two other cases exhibit a region where the reverse flow is present quite constantly, but the primary distinction between them consists in the size of this region. The relatively steady reverse flow, combined with the outer main flow, results in a strong shear area between them, especially in the developed cavity case. The local low pressure induced by large turbulent fluctuations in this area prevents the bubbly mixture from collapsing immediately after detaching from the wall, and thus contributes to the formation of a long tail-like cavitation structure, i.e. the significant increase in cavity length.

As aforementioned, the mean vapour content in the upstream part of the cavity is higher at $\sigma = 8.0$ than at $\sigma = 7.54$. This interesting finding may be ascribed to the different behavior of re-entrant jet in these two cases since the re-entrant jet is strongly associated with the condensation of the upstream part of the cavity. Let us look at the position $x=1$ mm where the probability of negative velocity is 46% for $\sigma = 7.54$ and only 17% for $\sigma = 8.0$. This difference implies that the vapour structure for $\sigma = 8.0$ is less influenced by the pressure rise brought by the re-entrant jet (which results in less vapour destruction) at the position $x=1$ mm. Considering that the mean void fraction depends on the combined effects of the vapour production and destruction rates, it is possible for the flow at $\sigma = 8.0$ to exhibit a higher mean void fraction at this position, even with less vapour production than at $\sigma = 7.54$. In addition, the different behaviors of the re-entrant jet in these two cases are also reflected on the distribution of α' in Figure 5.8. The α' at $\sigma = 7.54$ is much larger than that at $\sigma = 8.0$ even though the mean void fraction at $\sigma = 7.54$ is lower before $x=1.5$ mm. This implies that the re-entrant jet plays an important role to make the void fraction vary in a wider range. A more detailed description of

the void fraction variations and the corresponding frequency spectrum will be presented in the next section.

5.4. Frequency analysis of void fraction variation

As described in Chapter 4, the time history of void fraction within the front part of the cavity at $\sigma = 7.54$ reveals the presence of a clear dominant frequency, which is assumed to be controlled by the unsteady behavior of the re-entrant jet. In this section, the spatially averaged

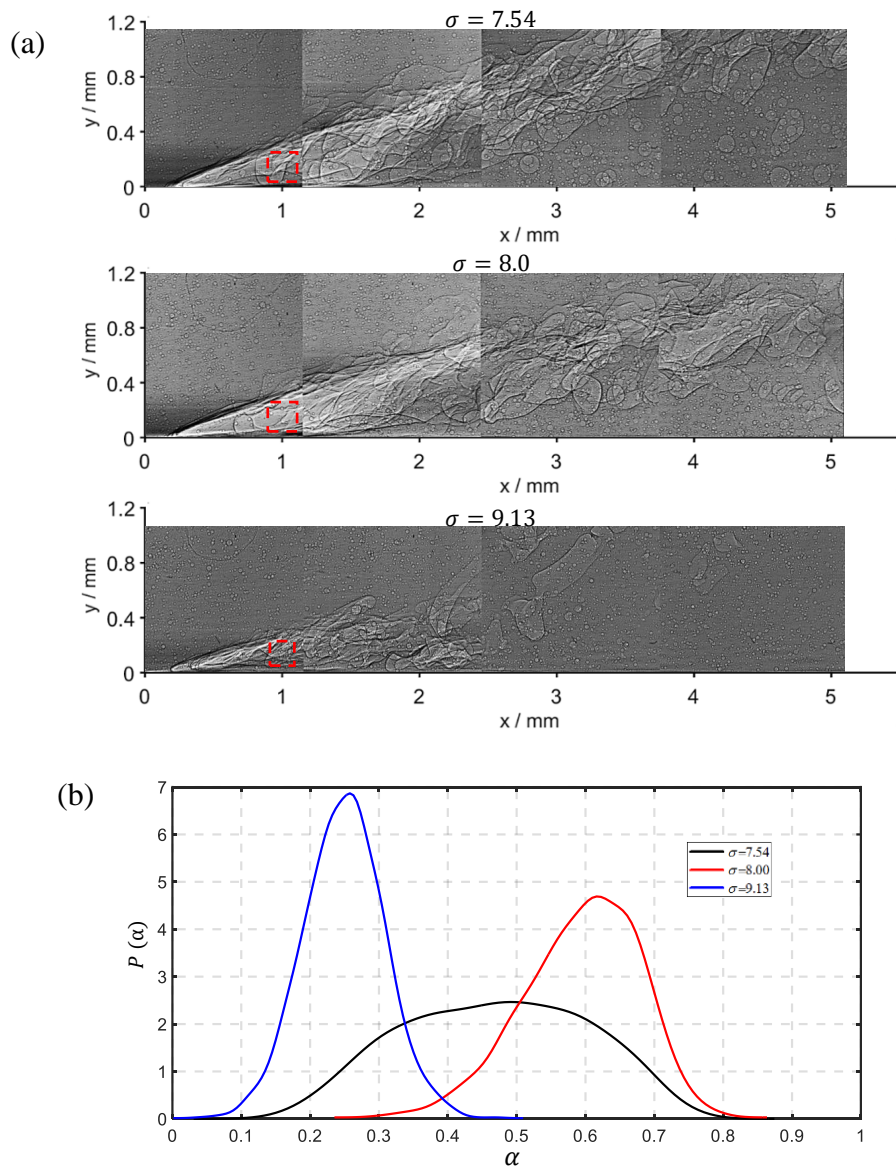


Figure 5.11. (a) The location and size of the probe window chosen to examine the void fraction variation for three cases; (b) PDF of void fraction $P(\alpha)$ within the selected probe window.

void fraction variation within a chosen probe window is examined for the three cases in order to unveil the underlying mechanisms of the cavity unsteadiness. Figure 5.11(a) illustrates the location and size of this probe window for three cavitation numbers, and the corresponding probability density function (PDF) of void fraction is shown in Figure 5.11(b). The PDF of void fraction at $\sigma = 7.54$ has a wider distribution with finite probability for a large range of void fraction. Larger values of void fraction are more probable when the probe location is free of re-entrant jet and smaller values when the re-entrant is present. Since the probability of re-entrant jet occurring at the probe position is 46% (close to 50%), the PDF at $\sigma = 7.54$ shows a quasi-symmetric distribution with respect to the most probable value. Conversely, the PDF at $\sigma = 8.0$ presents an asymmetric distribution where the larger void fraction values are much more probable than the smaller ones. This is in accordance with the small probability (17%) of re-entrant jet occurring at the probe position. Furthermore, the lower limit of void fraction (~ 0.3) for $\sigma = 8.0$ is higher than that (~ 0.1) for $\sigma = 7.54$. This indicates that the re-entrant jet for $\sigma = 8.0$ is weaker and thus leads to less destruction of vapour at the probe location. The PDF at $\sigma = 9.13$ has a Gaussian type distribution where the mean void fraction is close to the most probable value. It may result from the shear induced instability given that the flow does not see any re-entrant jet.

Due to the use of slow shutter in the experiments, only a packet of 144 pairs of images was recorded per opening of the shutter. Here we only present the time-varying void fraction within the probe window in a representative packet (out of 13 in total) as shown in Figure 5.12(a). The corresponding spectra by means of FFT are shown in Figure 5.12(b-d). Moreover, taking into account the remaining 12 packets, all spectra of the 13 packets are averaged in one figure to give a more general description of the cavity instability as shown in Figure 5.13. By comparison of all spectra, we can find that only a single dominant spectral peak is obtained for $\sigma = 7.54$ at a lower frequency denoted as f_1 , suggesting that the void fraction at the probe position varies in a quite regular mode. The time history of void fraction in Figure 5.12(a) also evidently presents an observable periodicity. For $\sigma = 8.0$, two peaks of similar amplitude can be detected at a lower frequency f_1 and a higher one f_2 . For $\sigma = 9.13$, only a higher frequency f_2 is dominant on the spectrum. With the reduction of probability of the re-entrant jet reaching the probe position (i.e. increasing cavitation number), the frequency f_1 shifts towards small values and its amplitude becomes lower. For $\sigma = 9.13$ without re-entrant jet, f_1 cannot even be identified. These results confirm the strong correlation between the re-entrant jet and the lower

frequency f_1 , i.e. the re-entrant jet is responsible for the quasi-periodic variation of void fraction at $\sigma = 7.54$.

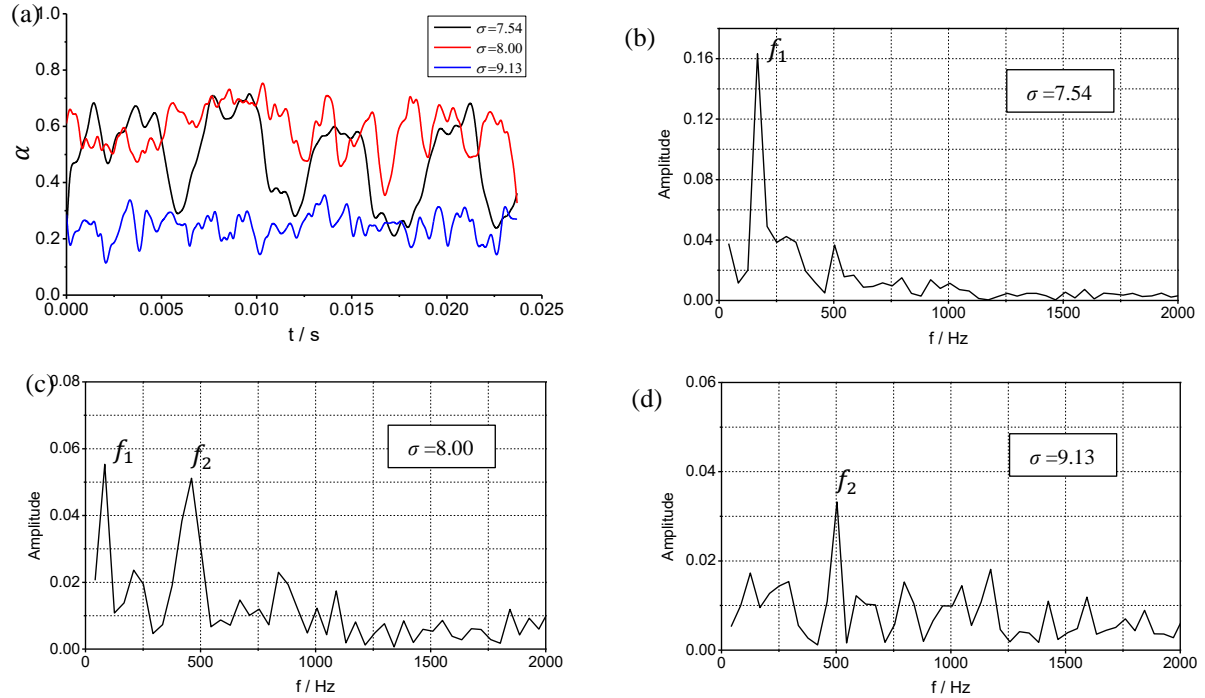


Figure 5.12. (a) Time-varying void fraction in a representative packet corresponding to a duration of 0.024 s; (b-d) FFT of the time-varying void fraction for three cavitation numbers.

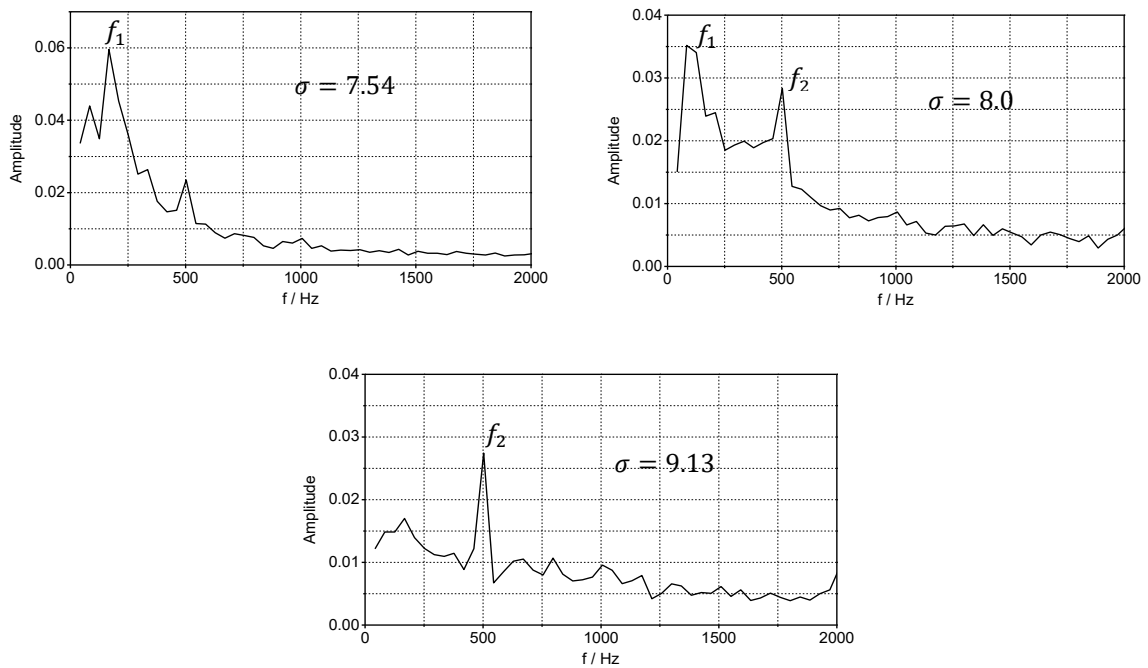


Figure 5.13. Average of 13 packets of spectra for three cavitation numbers.

In this section, we discuss the phenomena possibly responsible for the higher frequency f_2 . The preliminary conjecture is that f_2 corresponds to the shear-induced flow instability, based on the fact that the re-entrant jet is absent at $\sigma = 9.13$. However, it is interesting to note that the frequency f_2 seems rather fixed at about 500 Hz, and it does not shift with different packets or flow conditions. According to this observation, it is reasonable to suspect that f_2 results from an external factor rather than the flow itself. The suspicion is verified by testing the temporal evolution of effective X-ray intensity for imaging as shown in Figure 5.14 where the dominant frequency is exactly coincident with f_2 . Therefore, we can conclude that the void fraction variation due to shear-induced flow instability is random rather than controlled by a dominant frequency. It should be pointed out that the imaging brightness fluctuations are not caused by the X-ray source itself: they actually come from the errors of synchronization between the X-ray flashes, the fast shutter and the camera frames as mentioned in Chapter 3.

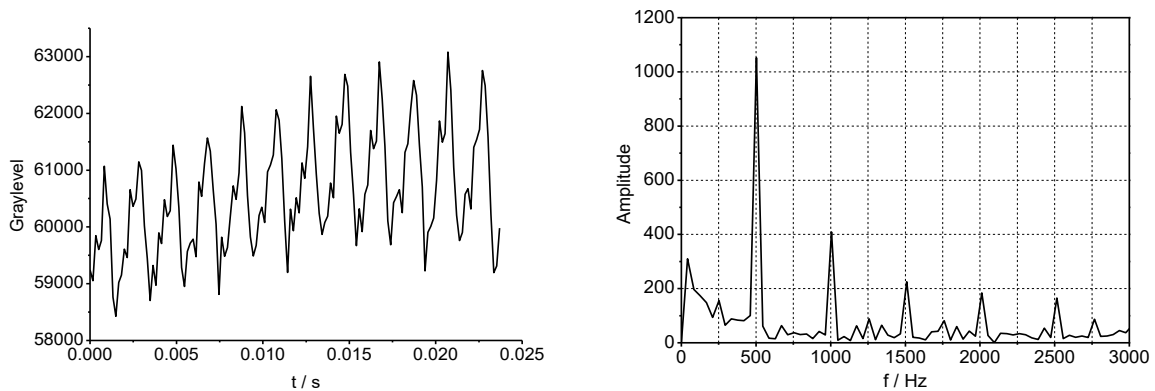
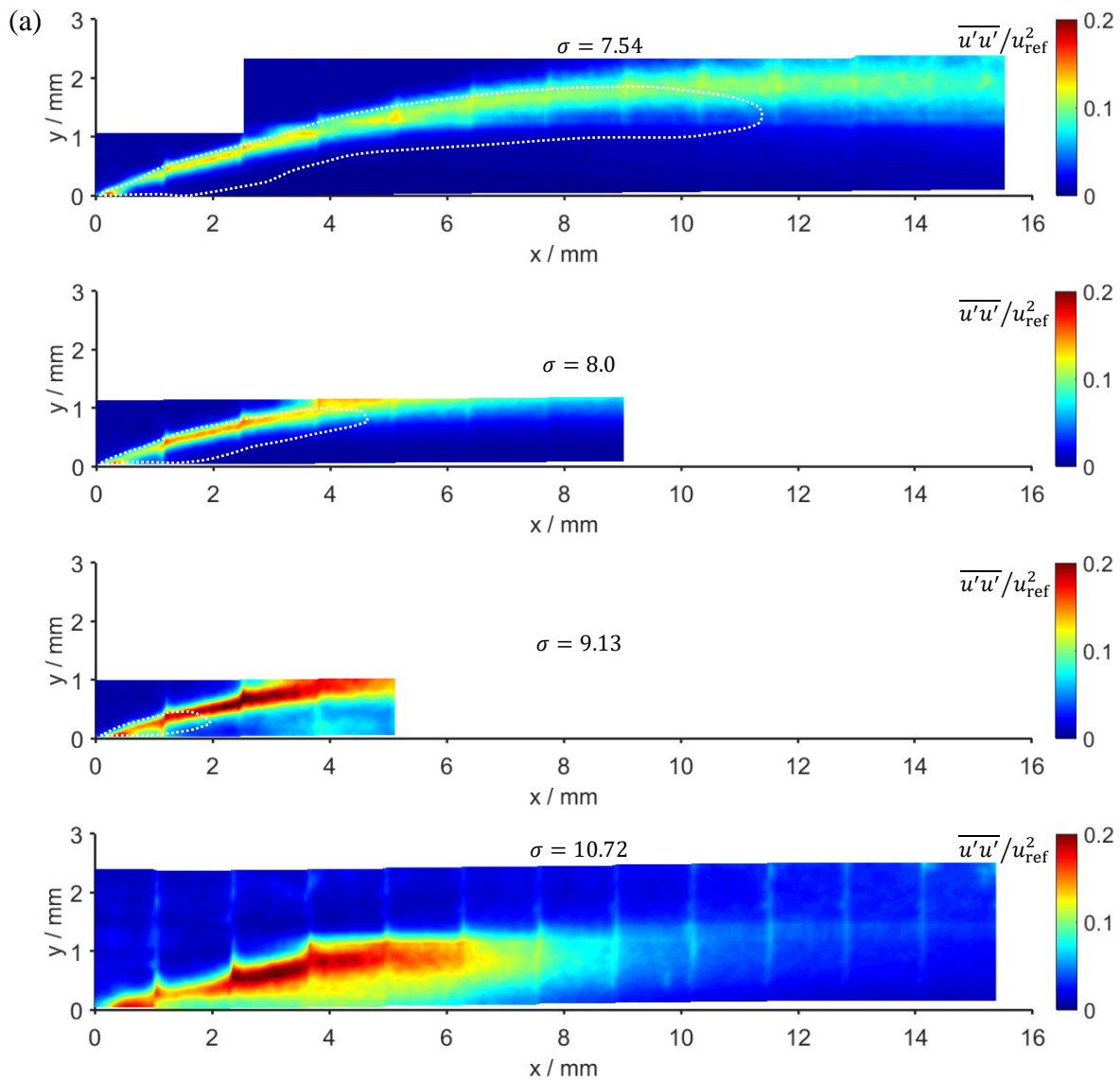


Figure 5.14. Brightness fluctuations when the test section is empty (full of air) and the corresponding spectrum.

5.5. Effect of cavitation on turbulent velocity fluctuations

It is impossible to generally conclude that cavitation promotes or depresses turbulence since the cavitation-related phenomena may have different effects on turbulent fluctuations including velocity field modification, phase change and the presence of vapour phase. In addition, cavitation may influence the Reynolds normal stresses and the shear stresses differently. The large difference in the mean cavity length also makes the comparison of different cases quite complicated. In spite of the difficulties mentioned, some conclusions can still be drawn, as discussed in the following part.

Figure 5.15(a) shows the distributions of non-dimensional longitudinal velocity fluctuations $\overline{u'u'}/u_{\text{ref}}^2$ for four different cavitation numbers. Note that $\sigma = 10.72$ corresponds to the non-cavitating flow which is considered as a reference case. The transversal velocity fluctuations are similar as those in the streamwise direction, so they are not presented here. It is evident that the longitudinal turbulent fluctuations in the three cavitating flows are mainly concentrated in the shear layer with high velocity gradient, implying that the influence of cavitation on turbulence level is highly correlated with the modification of velocity field. The distribution of longitudinal velocity fluctuations in the non-cavitating case looks different from the cavitating cases. This can be interpreted from the mean streamwise velocity field at $\sigma = 10.72$ as shown in Figure 5.15(b). Although the mean flow velocity is always positive, a region



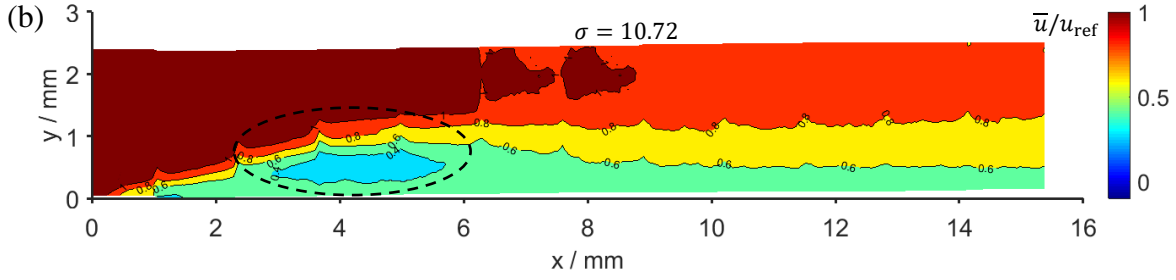


Figure 5.15. (a) Distributions of normalized longitudinal velocity fluctuations $\overline{u'u'}/u_{ref}^2$ at four different cavitation numbers. The white dashed line depicts the mean cavity profile. (b) Mean streamwise velocity field in the non-cavitating case.

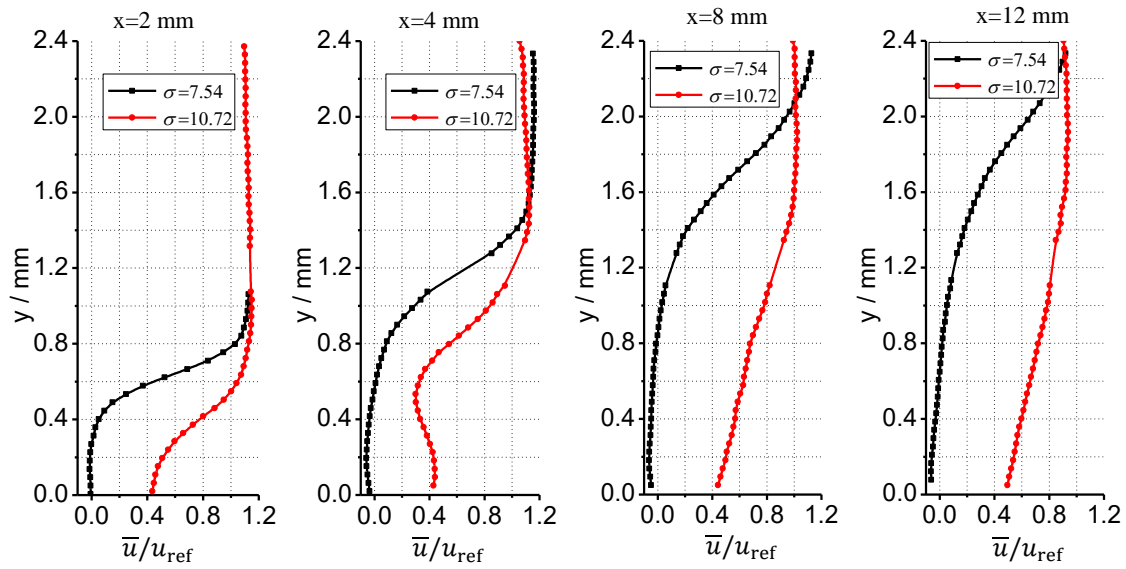


Figure 5.16. Comparison of mean streamwise velocity \bar{u}/u_{ref} profiles between the non-cavitating case $\sigma = 10.72$ and the cavitating case $\sigma = 7.54$.

(indicated by a dashed ellipse) similar to a recirculation zone is still formed just downstream of the throat under the influence of adverse pressure gradient in the divergent section. The intense velocity fluctuations exactly occur in this recirculation-resembling zone and then decrease rapidly towards downstream.

In order to further study the influence of cavitation on the velocity field, the comparison of mean streamwise velocity profiles at different locations is performed between the non-cavitating case $\sigma = 10.72$ and the cavitating case $\sigma = 7.54$ as shown in Figure 5.16. It can be seen that cavitation leads the mean velocity gradient to decrease in the near-wall region, whereas, in turn, it increases the velocity gradient in the shear layer. In the non-cavitating case, the effect of adverse pressure gradient on the velocity field appears to be limited to a relatively

small size region compared to the cavitating flow because the velocity profile at $x=12$ mm for the non-cavitating case has already recovered to a shape close to a turbulent boundary layer type while the cavitating flow still undergoes a reverse flow at the same location.

Let us look back at Figure 5.15 and make a qualitative comparison between the cavitating case of $\sigma = 7.54$ and the non-cavitating case. The noticeable difference can be identified in the near-wall region where the longitudinal velocity fluctuations are attenuated substantially in the cavitating case. This observation is consistent with the relatively steady state of the re-entrant jet in this region. The reduction of velocity gradient due to cavitation also explains the decrease of velocity fluctuations. In contrast, the cavitating flow in the downstream region exhibits higher velocity fluctuations than those in the non-cavitating case. This can be attributed to the impact of larger velocity gradient and vapour structure collapse. But one cannot tell which mechanism is predominant in the augmentation of velocity fluctuations. It is interesting to compare the two cavitating flows at $\sigma = 7.54$ and $\sigma = 9.13$ in their wake region ($x > 12$ mm and $x > 2$ mm, respectively). As the cavitation number decreases, the vapour collapse in the cavity wake becomes more intense. Nevertheless, the velocity fluctuations at $\sigma = 7.54$ are not higher than at $\sigma = 9.13$ since the velocity gradient is also an important factor for the velocity fluctuations. Therefore it can be inferred that the collapse of small vapour structures in sheet cavitation do not result in evident velocity perturbations and the degree of velocity shear plays a more important role in the turbulent fluctuations.

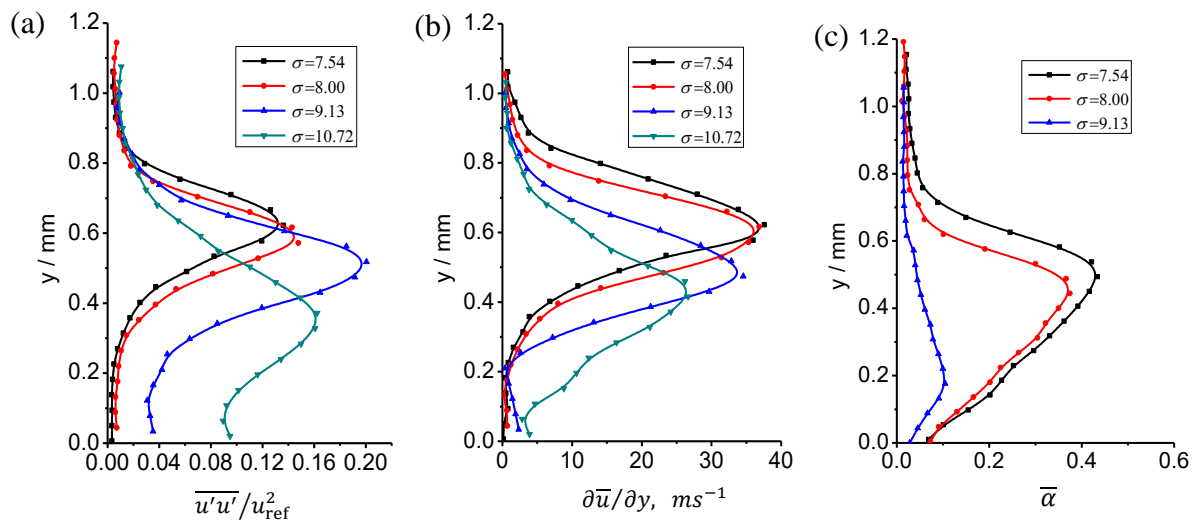


Figure 5.17. Profiles of (a) longitudinal velocity fluctuations $\overline{u'u'}/u_{\text{ref}}^2$, (b) mean velocity gradient $\partial\bar{u}/\partial y$ and (c) mean void fraction $\bar{\alpha}$ at $x=2$ mm.

The occurrence of cavitation causes the presence of vapour phase, which may also have an influence on the turbulent fluctuations. Figure 5.17(a) depicts the profiles of longitudinal velocity fluctuations for different cavitation numbers at the station of $x=2$ mm where the flow is scarcely affected by cavitation collapse. The degree of flow shear is quantified by the magnitude of velocity gradient as shown in Figure 5.17(b), and the presence of vapour phase is described via the average void fraction as illustrated in Figure 5.17(c). In general, one can observe that the maximum intensity of longitudinal velocity fluctuations occurs at the location of the largest velocity gradient, which indicates the strong positive correlation between these two quantities. When decreasing the cavitation number, the peak value of velocity gradient, i.e. the shear intensity, increases. However, the longitudinal velocity fluctuations show a different trend: first increasing and then decreasing as cavitation develops. First, let us merely compare the three cavitating cases ($\sigma = 7.54, 8.0$ and 9.13). An increase in the extent of cavitation is found to reduce the longitudinal velocity fluctuations in the shear layer although the shear degree is increased. This result suggests that the presence of vapour phase due to cavitation should be responsible for reversing the positive correlation between the velocity gradient and the fluctuations. In other words, more vapour tends to suppress the streamwise turbulent fluctuations. Then the comparison between the non-cavitating case ($\sigma = 10.72$) and the small-cavity case of $\sigma = 9.13$ reveals that the occurrence of cavitation leads to a rise in $\overline{u'u'}/u_{\text{ref}}^2$, which differs from the preceding trend observed. This is actually another consequence of the competition between the damping effect imposed by the presence of vapour phase and the promoting effect caused by the flow shear. Indeed, as presented in Figure 5.17(c), the small amount of vapour at $\sigma = 9.13$ is not expected to yield a prominent damping on the velocity fluctuations.

The fact that vapour suppresses the turbulent fluctuations is in agreement with the numerical results of Dittakavi et al. (2010) in a similar Venturi channel. They attribute it to a modification of the vortex-stretching process, due to the presence of vapor. As a non-cavitating vortex is stretched, its diameter reduces. In order to satisfy the conservation of angular momentum, the rotation rate increases and consequently the pressure at the vortex core decreases. However, the core of a cavitating vortex has to maintain a constant pressure, which limits the vorticity production due to vortex stretching. Therefore the formation of vapour results in suppression of turbulent fluctuations. In addition, the local speed of sound in vapour/liquid mixtures could be reduced to a few meters per second, which makes the

cavitation structures highly compressible. The compressibility of the two-phase mixture may also damp out the velocity fluctuations, as suggested by Barre et al. (1994).

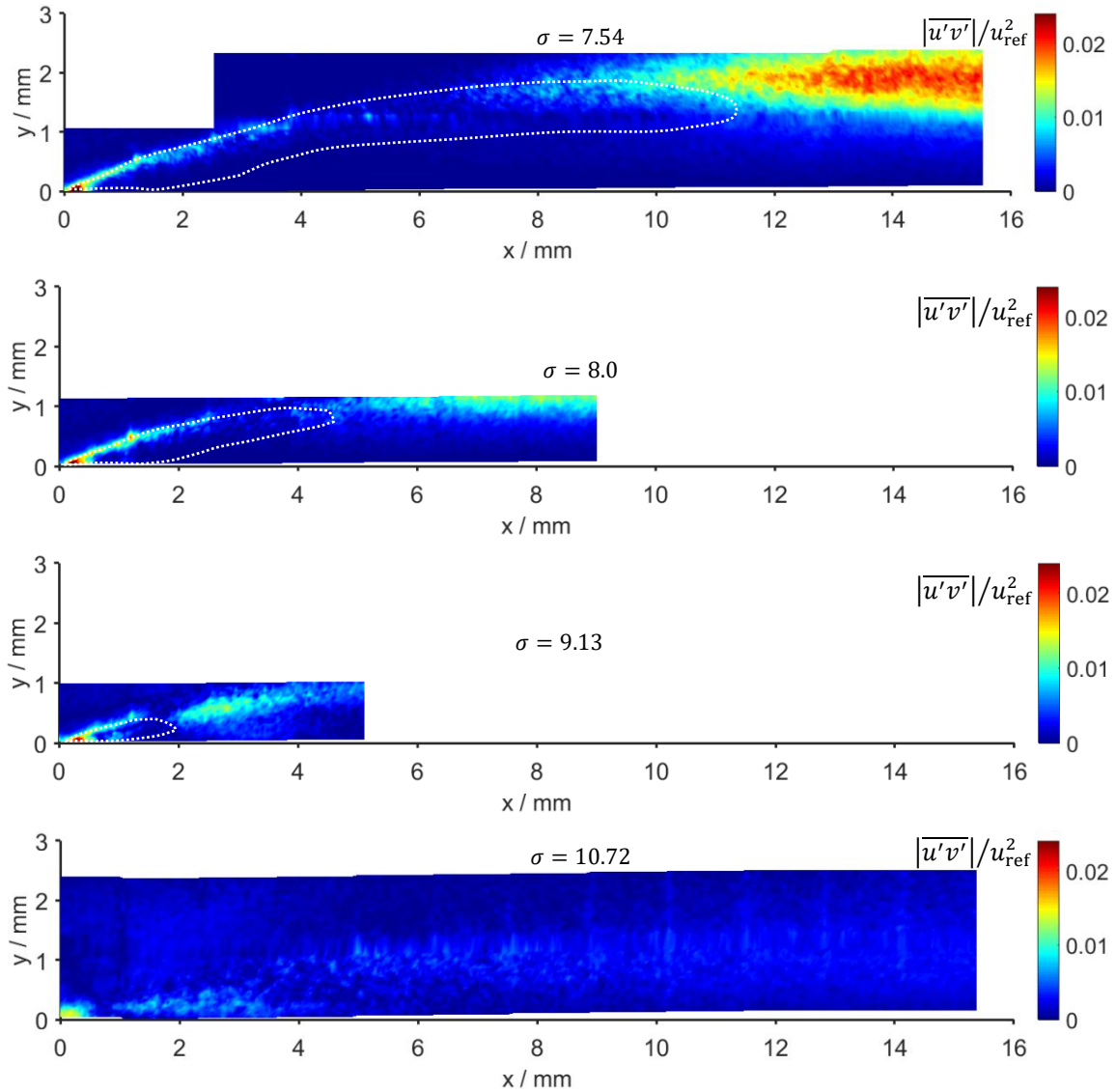


Figure 5.18. Distributions of normalized Reynolds shear stress $|\overline{u'v'}|/u_{\text{ref}}^2$ at four different cavitation numbers. The white dashed line depicts the mean cavity profile.

The distributions of non-dimensional Reynolds shear stress $|\overline{u'v'}|/u_{\text{ref}}^2$ at the four different cavitation numbers are shown in Figure 5.18. Unlike the streamwise velocity fluctuations, the shear stress seems to be weakly dependent on the velocity gradient. Compared to the non-cavitating case, two regions of high shear stress can be identified in all three cavitating cases. One is a slender strip area along the cavity interface where the liquid

evaporates to feed the sheet cavity. The development of cavitation does not cause any significant variation in the magnitude of the shear stress, but the strip area becomes longer. Another one corresponds well to the cavity wake region where the shed vapour structure collapses, and the magnitude of the shear stress increases considerably with the extent of cavitation. In the region where the vapour bubbles are transported without significant phase change, the shear stress remains at a low level. Based on the above observations, one may infer that the vapour collapse and the vaporization are the two dominant mechanisms to increase the correlation between the streamwise and cross-stream velocity fluctuations.

5.6. Chapter summary

In this chapter, the sheet cavitation produced in a convergent-divergent channel is studied systematically by a detailed comparison of the cavities at three representative stages ($\sigma = 7.54$ corresponding to the developed stage, $\sigma = 8.0$ corresponding to the intermediate stage as well as $\sigma = 9.13$ corresponding to the early stage). The measurements based on the X-ray imaging indicate that the structure and dynamics of sheet cavitation are highly associated with the behavior of the re-entrant jet.

The sheet cavity grows significantly both in length and thickness when the cavitation number is decreased. At the early stage of sheet cavitation, no reverse flow is observed and accordingly the cavity attaches to the wall without evident flow separation. When cavitation develops to an intermediate stage, a reverse flow is initiated in the near-wall region. It tends to displace the rear part of the cavity away from the wall, and hence contributes to the thickening of the sheet cavity. With a further reduction in cavitation number, the size of the reverse flow region increases; the re-entrant jet is strengthened in terms of the magnitude of negative velocity, and the presence of the re-entrant jet becomes more continuous. The enhanced reverse flow combined with the outer main flow generates a stronger shear layer between them where the local low pressure induced by larger turbulent fluctuations prevents the bubbly mixture from collapsing immediately after detaching from the wall, and thus contributes to the significant increase in the cavity length. As in periodic cloud cavitation, the re-entrant jet in the studied sheet cavitation, especially at the developed stage, can almost penetrate the entire cavity, but it never pinches off the cavity into two parts due to insufficient momentum.

When cavitation develops from the intermediate stage to the developed stage, the mean void fraction measured in the very upstream part of the cavity becomes smaller. This

unexpected phenomenon can be explained from a net effect of two competing mechanisms: vapour production and destruction. With the reduction of cavitation number, the vapour production rate is increased due to more intense vaporization, but in the same time the probability and intensity of the re-entrant jet reaching the cavity leading edge is also increased. Considering the strong destruction effect of the re-entrant jet on the vapour phase, it is therefore possible for the mean void fraction to decrease with the reduction of cavitation number. By comparing the void fraction variation in the three cases, the re-entrant jet is confirmed to be responsible for the quasi-periodic variation of void fraction. In addition, the shear-induced flow instability is another mechanism leading the void fraction to oscillate but in an irregular manner without a dominant frequency.

With respect to the influence of cavitation on the longitudinal velocity fluctuations, it is highly correlated with the modification of velocity field. The longitudinal turbulent fluctuations are mainly concentrated in the shear layer with a high velocity gradient, and they are attenuated substantially in the near-wall low-velocity region. The collapse of small vapour structures in the studied sheet cavitating flows does not result in an evident perturbation of the velocity field, while the presence of vapour phase due to cavitation is observed to strongly suppress the streamwise turbulent fluctuations, which might be attributed to two mechanisms: (1) the presence of the vapor phase modifies the vortex-stretching process, and (2) the cavitation compressibility damps out the turbulent fluctuations. Regarding the effect of cavitation on the Reynolds shear stress, the vapour collapse and the vaporization are the two dominant mechanisms to increase the correlation between the streamwise and cross-stream velocity fluctuations.

5.6. Résumé du chapitre

Dans ce chapitre, la cavitation tôle réalisée dans un canal convergent-divergent est étudiée systématiquement par une comparaison détaillée des cavités à trois étages représentatifs ($\sigma = 7,54$ correspondant à l'étage développé, $\sigma = 8,0$ correspondant à l'étage intermédiaire ainsi que $\sigma = 9,13$ correspondant au stade précoce). Les mesures basées sur l'imagerie aux rayons X indiquent que la structure et la dynamique de la cavitation de la feuille sont fortement associées au comportement du jet rentrant.

La cavité en feuille croît de manière significative à la fois en longueur et en épaisseur lorsque le nombre de cavitation est diminué. Au stade précoce de la cavitation de la feuille,

aucun écoulement inverse n'est observé et, par conséquent, la cavité se fixe à la paroi sans séparation évidente de l'écoulement. Lorsque la cavitation se développe à un stade intermédiaire, un écoulement inverse est initié dans la région proche de la paroi. Il a tendance à écarter la partie arrière de la cavité de la paroi, et contribue ainsi à l'épaississement de la cavité en feuille. Avec une réduction supplémentaire du nombre de cavitation, la taille de la région d'écoulement inverse augmente; le jet rentrant est renforcé en termes de grandeur de vitesse négative, et la présence du jet rentrant devient plus continue. L'écoulement inversé amélioré combiné à l'écoulement principal externe génère une couche de cisaillement plus forte entre eux où la basse pression locale induite par des fluctuations turbulentes plus importantes empêche le mélange bouillonnant de s'effondrer immédiatement après le détachement de la paroi, et contribue ainsi à l'augmentation significative de la cavité. longueur. Comme dans la cavitation nuageuse périodique, le jet rentrant dans la cavitation de la feuille étudiée, en particulier au stade développé, peut presque pénétrer dans toute la cavité, mais il ne pince jamais la cavité en deux parties en raison d'une impulsion insuffisante.

Lorsque la cavitation se développe de l'étage intermédiaire à l'étage développé, la fraction de vide moyenne mesurée dans la partie très amont de la cavité devient plus petite. Ce phénomène inattendu peut s'expliquer par un effet net de deux mécanismes concurrents: la production de vapeur et la destruction. Avec la réduction du nombre de cavitation, la vitesse de production de vapeur est augmentée en raison d'une vaporisation plus intense, mais dans le même temps, la probabilité et l'intensité du jet rentrant atteignant le bord d'attaque de la cavité sont également augmentées. Compte tenu du fort effet de destruction du jet rentrant sur la phase vapeur, il est donc possible que la fraction de vide moyenne diminue avec la réduction du nombre de cavitation. En comparant la variation de la fraction de vide dans les trois cas, le jet rentrant est confirmé comme étant responsable de la variation quasi-périodique de la fraction de vide. De plus, l'instabilité de l'écoulement induite par le cisaillement est un autre mécanisme conduisant la fraction de vide à osciller mais de manière irrégulière sans fréquence dominante.

En ce qui concerne l'influence de la cavitation sur les fluctuations de vitesse longitudinales, elle est fortement corrélée à la modification du champ de vitesse. Les fluctuations turbulentes longitudinales sont principalement concentrées dans la couche de cisaillement avec un gradient de vitesse élevé, et elles sont atténuées sensiblement dans la région de basse vitesse proche de la paroi. L'effondrement de petites structures de vapeur dans les écoulements de cavitation en feuille étudiés n'entraîne pas une perturbation évidente du champ de vitesse, tandis que la

présence de phase vapeur due à la cavitation supprime fortement les fluctuations turbulentes dans le sens du courant, qui pourraient être attribuées à deux mécanismes : (1) la présence de la phase vapeur modifie le processus d'étirement du vortex, et (2) la compressibilité de la cavitation amortit les fluctuations turbulentes. En ce qui concerne l'effet de la cavitation sur la contrainte de cisaillement de Reynolds, l'effondrement de la vapeur et la vaporisation sont les deux mécanismes dominants pour augmenter la corrélation entre les fluctuations de vitesse de flux et transversales.

Chapter 6

Towards the trial of investigating cloud cavitation

Compared to the relatively stable sheet cavitation, another form of partial cavitation, i.e. cloud cavitation, has attracted more attention since the violent cloud shedding and subsequent collapse have a high potential to damage material and produce noise and vibration in practical applications. However, in the present convergent-divergent channel with a small contraction ratio, the transition from sheet to cloud cavitation is not observed with decreasing cavitation number. This was actually unexpected before manufacturing such a test section. In order to investigate cloud cavitation by X-ray imaging as well as other measurement techniques, we decided to make another Venturi-type test section according to an existing geometry in our lab which is proven to be able to produce a well-defined periodic cloud cavitation.

6.1. Multi-functional Venturi-type test section

The side view of the new test section is shown in Figure 6.1(a). It was specially designed to be applicable in the experiments of high-speed visualization, particle image velocimetry (PIV) and in-line X-ray imaging. The part indicated by the dashed rectangle is zoomed and shown in Figure 6.1(b). The base (1) and the lid (2) were made of non-transparent hard plastic through the 3D printing technique. Both of them constitute the main body of the test section. The bottom insert (3) acts as the convergent-divergent floor of the Venturi section. The top insert (4) forms the ceiling of the Venturi. The inserts (3) and (4) were both manufactured in glass rather than plexiglass since the former one has a better light transmittance and is less likely to be burned by intense laser. The Venturi profile is depicted by the dashed lines. The heights at the inlet and the outlet are both 20 mm, and the height at the throat is 10 mm. The convergent and divergent angles of the Venturi are 18° and 8° , respectively. The pressure sensor (5) was flush mounted at the inlet with another one (6) at the outlet.

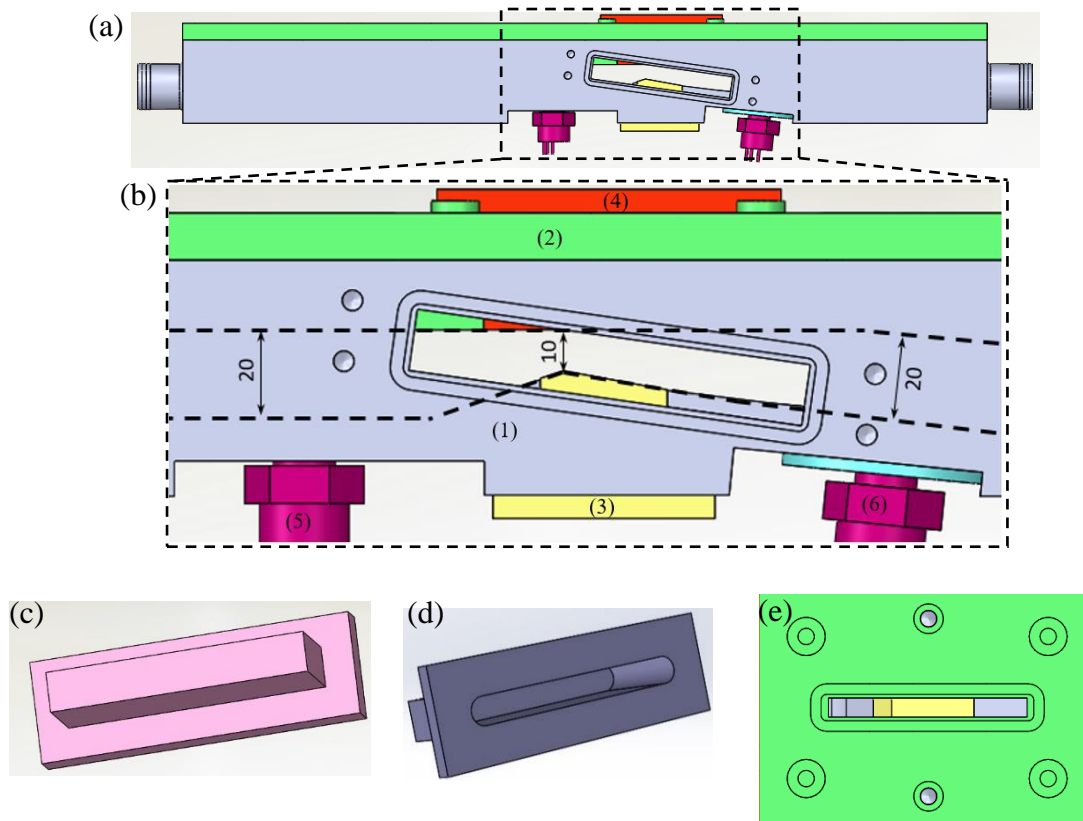


Figure 6.1. Test section - flow direction from left to right, (a) side view of the overall test section; (b) the zoomed convergent-divergent section, dimensions in mm; (c) side wall insert; (d) hollow side wall insert for X-ray imaging; (e) top view of the convergent-divergent section.

Two identical parts as shown in Figure 6.1(c) were inserted into the slots in the base (1) from front and back forming the observation window and also serving as the side walls of the Venturi channel. It should be noted that the two side inserts were made of plexiglass as its refractive index is close to water. In the X-ray imaging experiment, the side insert was replaced by a hollow one with a thickness of only 0.5 mm at the tip, as shown in Figure 6.1(d). Figure 6.1(e) shows the top view after removing the top insert (4). The slot here is important for the PIV experiments as it allows the calibration plate to be placed into the Venturi channel. The channel width is only 5 mm in order to minimize the 3D effect of cavitation.

6.2. Measurements

The high speed visualization of cavitation was performed in back-lighting and top-lighting modes as described in Section 4.1. Apart from this, the other measurements were also carried out in the new test section.

6.2.1. Pressure measurements

The transient pressure at the inlet and the outlet was measured using two piezoresistive pressure sensors (Keller 10L series) calibrated in a range of 0–3bar. Signals from the pressure sensors were collected synchronously through a NI USB-6216 data acquisition card and exported to a computer by the Labview software. The sampling frequency was set to be 10 kHz and the sample size was 10,000 (corresponding to a recording time of 1 s) for all flow conditions. Figure 6.2 shows an example of pressure signals recorded by the inlet and outlet sensors. The averaged inlet pressure P_{in} was used to determine the cavitation number σ :

$$\sigma = \frac{P_{in} - P_{vap}}{\frac{1}{2}\rho_l u_{in}^2} \quad (6.1)$$

where P_{vap} is the vapour pressure at the flow temperature, u_{in} is the bulk velocity at the inlet computed according to the volumetric flow rate, and ρ_l is the liquid density. It can be seen qualitatively from Figure 6.2 that the pressure fluctuation at the outlet is much more intense than that at the inlet due to the occurrence of cavitation.

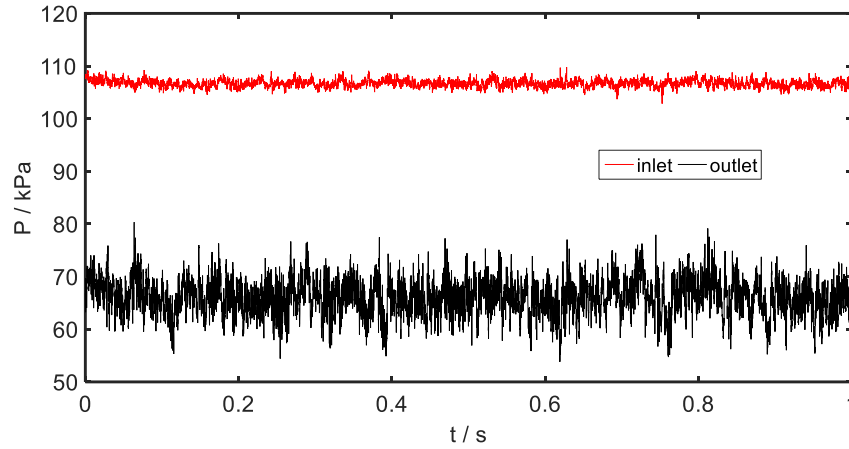


Figure 6.2. An example of pressure signals recorded by the inlet and outlet sensors ($\sigma=2.08$, $u_{in}=10$ m/s).

6.2.2. PIV-LIF measurements

The velocity fields in the cavitating flows were measured using the LaVision PIV system. The light source was a double-pulsed Nd:YAG laser with the pulse duration of 10 ns. The laser beam was expanded by a cylindrical lens into a light sheet with thickness of about 1mm for illuminating the center plane of the Venturi channel. The energy density in the laser sheet could

be adjusted to sufficiently high as it goes through the replaceable glass inserts which are less likely to be damaged.

Before starting the circulating pump, a calibration plate shown in Figure 6.3 was placed in the center plane of the Venturi channel filled with water touching the divergent floor. The purpose of this step was to define the scale (mm/pixel), and eliminate perspective and refraction errors. The coordinate system used was also defined during the calibration process. The x-axis is along the Venturi divergent floor and the origin is located at the apex of the Venturi throat.

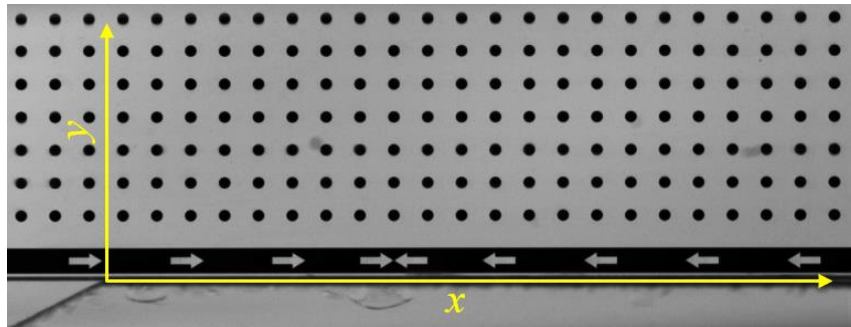


Figure 6.3. Calibration plate with regular distribution of marks. The dot diameter is 0.33 mm and the distance between dots is 1 mm. The coordinate system used is also defined.

The fluorescent particles (Rhodamin B, diameter of around 20 μm) were added to the cavitating flow as the liquid phase tracers. They absorb the laser light with the wavelength of 532 nm and emit light at 584 nm. An optical notch filter at 532 nm from EO Edmund was mounted in front of the camera lens. In this way, the reflected laser light (remaining at the wavelength of 532 nm) from the two-phase structures is blocked by the notch filter, and only the light emitted by the fluorescent particles is recorded. For each operating condition, 2000 pairs of particle images were acquired by the high-speed Photron Fastcam SA 1.1 camera at frequency 2000Hz. The spatial resolution of the raw image was 1024×512 pixels. The time delay between the two images of the same pair varied from 8 to 12 μs depending on the flow velocity for achieving a particle shift of about 5 pixels.

A raw particle image in the area of interest is presented in Figure 6.4(a). As can be seen, the cavitation structure is still visible in the image, as it reflects the light emitted from the fluorescent particles. Its contaminating effect on the particle image could be reduced through performing a high-pass Gaussian filter and the processed image is shown in Figure 6.4(b). On the other side, the number of detected particles is indeed influenced by the presence of the vapour/liquid mixture. It is attributed to two reasons: (a) vapour structures between the laser

sheet and the side wall block the fluorescent particles in the illuminated plane; this problem is not the primary cause for less detected particles in the present experiments since the measurement plane is close enough to the front observation window (only 2 mm), (b) the cavity of higher vapour content can carry fewer particles, as a consequence, few particles are distinguished in the upstream attached cavity while the particle density in the detached vapour clouds is less decreased.

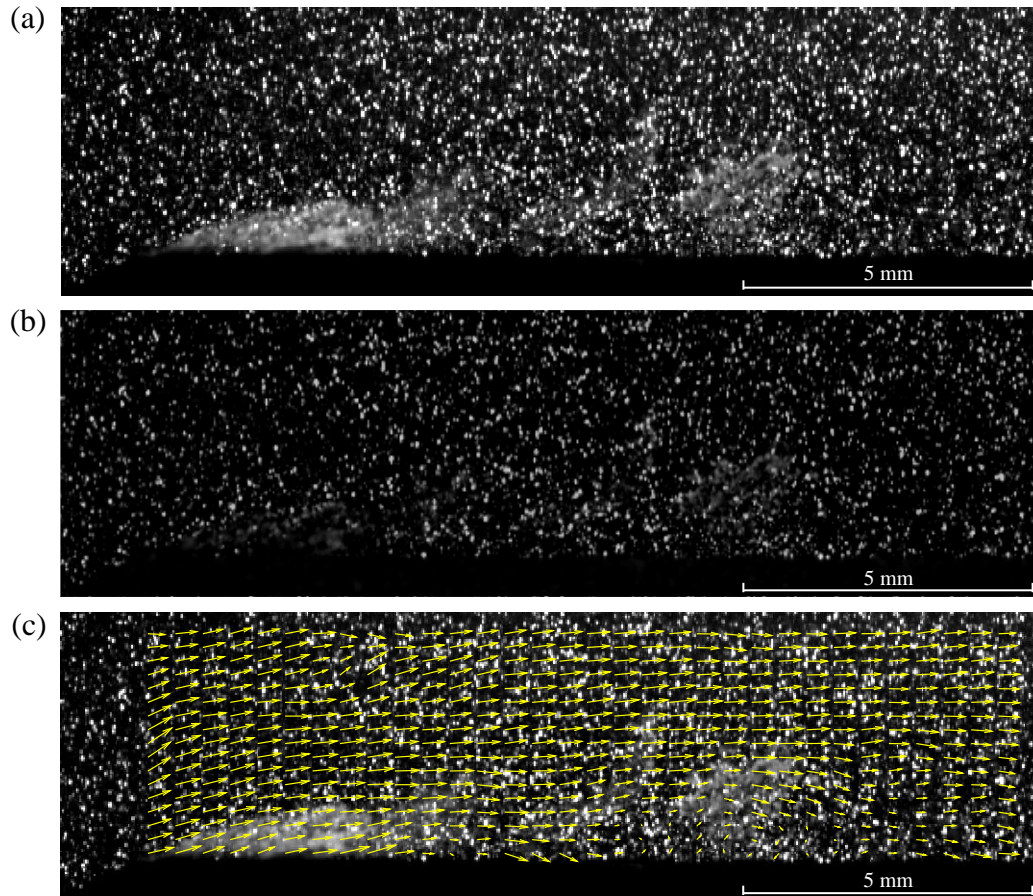


Figure 6.4. An example of evaluating the instantaneous velocity field in the cavitating flow ($\sigma=2.49$, $u_{in}=8.75$ m/s), flow direction from left to right. (a) Raw PIV image; (b) processed image with a high-pass Gaussian filter; (c) instantaneous velocity vector field (every second vector is displayed in the horizontal direction for clarity).

The instantaneous velocity fields were evaluated using the iterative cross-correlation algorithm in the software Davis 8.1 from LaVision. The interrogation window for the first pass was 64×64 pixels followed by 2 passes with interrogation windows of 16×16 pixels and the

overlap of 50% was used. The correlation peak was determined with a sub-pixel accuracy by using the three-point Gaussian fitting scheme in two directions. The particle density was taken into account in the final pass where the vectors in the interrogation windows with less than 4 particles were rejected and replaced by a bilinear interpolation from their valid neighboring vectors. This implied that the calculated velocities in the attached cavity had a higher uncertainty as the particle concentration there was not sufficient.

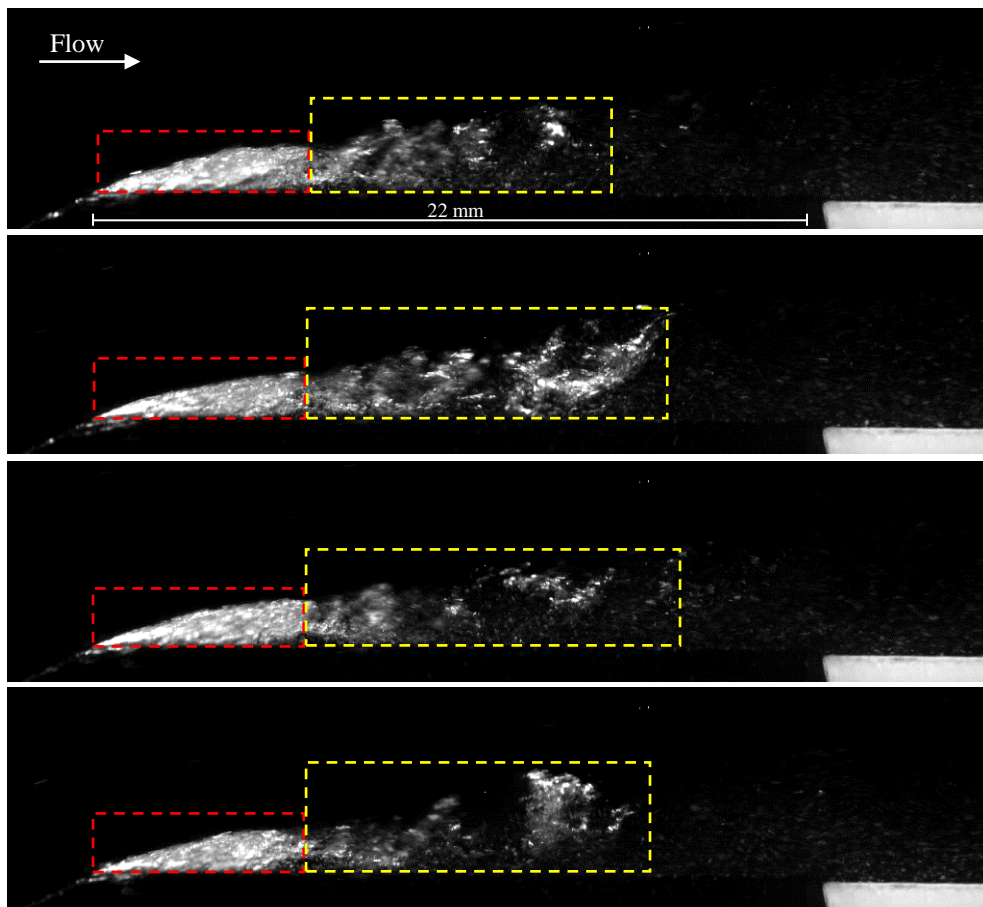


Figure 6.5. A sequence of high speed images showing a typical cavitation regime obtained in the new test section ($\sigma=2.34$, $u_{in}=10$ m/s). The time interval between two images is 0.5 ms.

6.3. Effect of the side gap on cavitation regime

Neither a relatively stable sheet cavitation nor a periodic shedding of large scale vapour clouds is observed from the high speed visualizations of cavitating flows in the new test section. This is unexpected since a clear cloud cavitation has been obtained in another test section with the same geometry. Figure 6.5 shows the representative cavitation regime observed in the new test section. It is clear that the cavity consists of two distinct parts. The fore part (as shown by

the red frame) is characterized by an attached sheet cavity with nearly constant length, and the rear part (indicated by the yellow frame) is a long region where the cavity seems to break up into numerous vapour bubble clusters.

This ‘strange’ cavitation behavior is attributed to the influence of a gap between the bottom insert and the side wall insert, which is revealed in the high speed images using back illumination as shown in Figure 6.6. An evident reverse flow can be identified in the region indicated by the yellow frame in Figure 6.6(a) through tracking individual vapour bubbles. An example of tracking a single bubble in a sequence of high speed images is also shown in Figure 6.6(a). Figure 6.6(b) illustrates the schematic of flow paths in the side gap. As can be seen, the re-entrant jet (indicated by the red line with arrow) is directed into the gap instead of moving upstream along the wall due to smaller resistance in the gap. When it encounters the flow towards downstream (indicated by the yellow line with arrow), the re-entrant jet is forced to deflect upwards and then impinges on the cavity at several points. In this way, the rear part of the cavity is pinched off into a number of small vapour clouds, while the front portion remains relatively stable due to the weak interaction with the re-entrant jet.

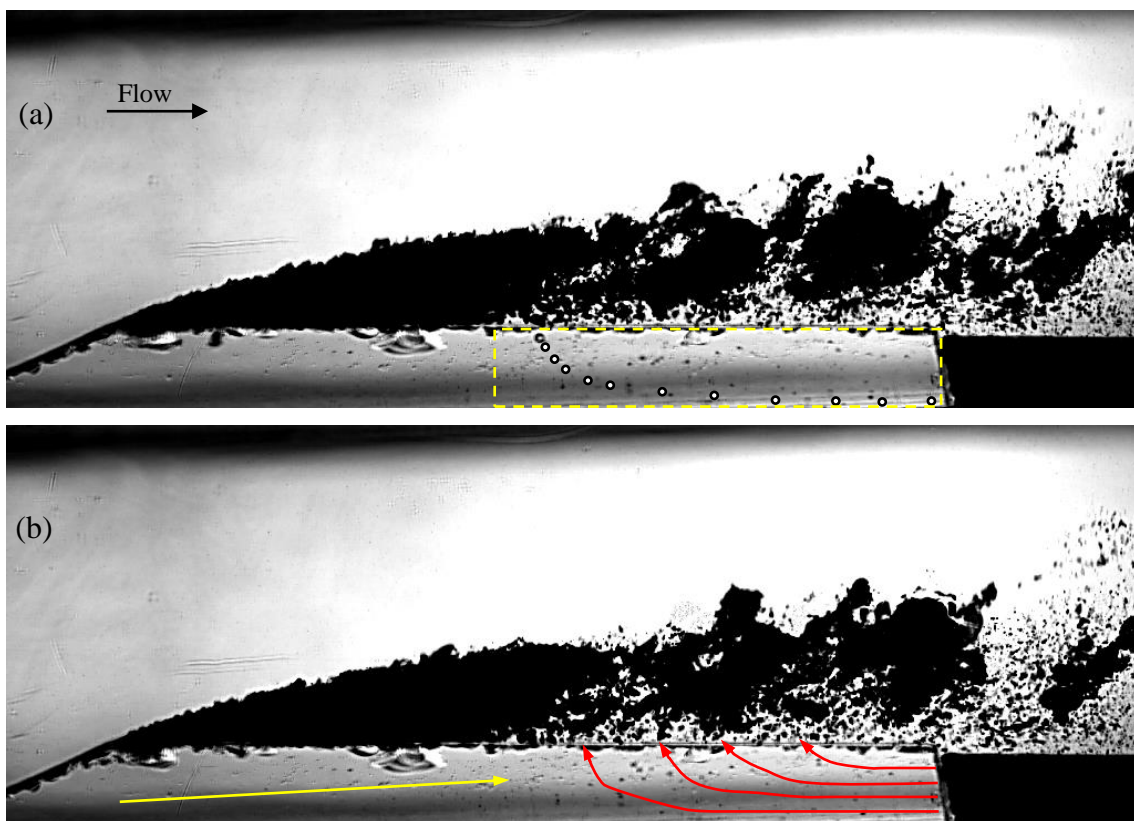


Figure 6.6. High speed images in back-lighting mode showing the flow paths in the gap between the bottom insert and the side wall insert ($\sigma=2.08$, $u_{in}=10$ m/s).

The effect of the gap could also be checked by the flow velocity field. As shown in Figure 6.7, we compare the mean streamwise velocity profiles at two vertical stations ($x=5$ mm and $x=10$ mm) in two test sections: one is the newly-made test section with a gap; the other is the non-detached test section without a gap. The flow is free of cavitation with a nominal velocity of 15 m/s at the throat, and the velocity is measured using the PIV technique. It can be observed that the gap alters the flow field significantly: the existence of the gap increases the flow channel width, and thus makes the velocity decreased.

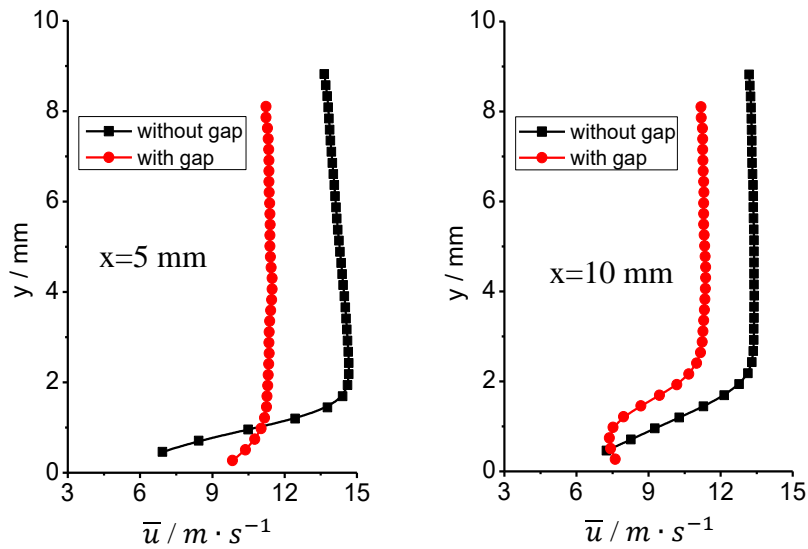


Figure 6.7. Comparison of mean streamwise velocity profiles in two test sections: one with a gap and the other without a gap.

The 3D printing technique was employed to make the main body of the new test section considering its advantages of time-saving and low cost. However, it is beyond our expectation that the large assembly error between the printed parts and the machined glass inserts leads to the presence of a gap, which actually suppresses the cloud cavitation, and hence delayed our plan to perform fast X-ray imaging measurements in cloud cavitating flows.

On the other hand, as a positive side effect, the influence of the gap on the cloud cavitation could be a passive control to this destructive form of cavitation. Danlos et al. (2014) grooved the Venturi divergent wall and found this geometrical change suppressed the shedding of large-scale vapour clouds as shown in Figure 6.8. In the case of smooth divergent wall, the re-entrant jet moves upstream along the wall and pinches off the cavity as it reaches the leading edge, thereby generating a detached cloud. However, in the case of grooved wall, the behavior of the

re-entrant jet is supposed to be similar to that described in Figure 6.6, and thus leads to a similar cavitation regime as in the test section with a gap. Compared to the violent collapse of a large shed cloud in a short duration, the continuous shedding and collapse of small vapour structures emit pressure pulses with a much lower amplitude, thus reducing the risk of damage to the surrounding material surface. In addition, this effective means of passive control to cloud cavitation also demonstrates that the re-entrant jet is an important driving mechanism to initiate cloud cavitation.

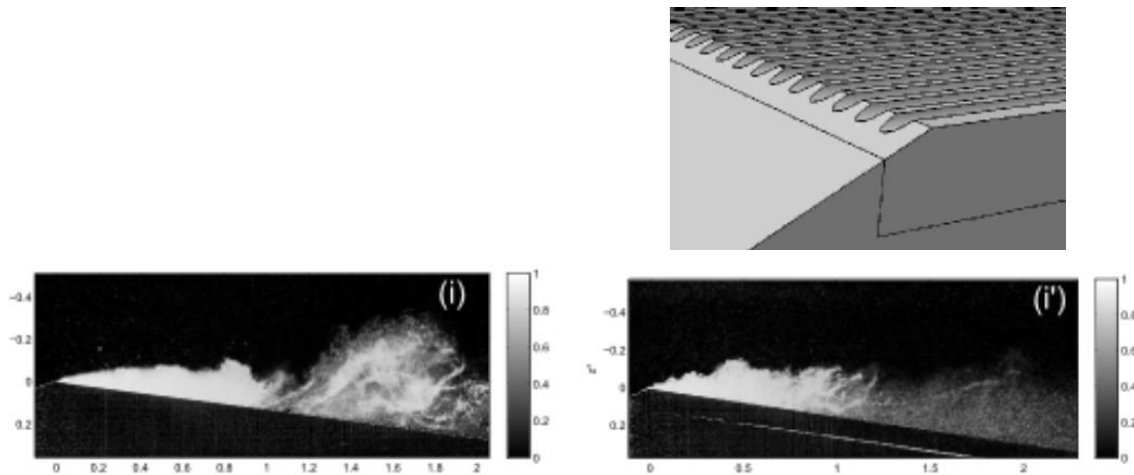


Figure 6.8. Cloud cavitation regime on the smooth divergent wall (left) versus sheet cavity without large cloud shedding on the grooved wall (right) from Danlos et al. (2014).

6.4. Measurement results in the new test section

Although the desired cloud cavitation is not observed in the new test section, we still obtain some interesting results, which are presented in this section.

6.4.1. Pressure loss versus cavitation number

The extent of cavitation is described primarily by the cavitation number which can be varied through adjusting the inflow velocity and inlet pressure in the experiments. The absolute pressure loss $P_l = P_{in} - P_{out}$, defined as the difference between the average inlet and outlet pressure, is evidently related to the degree of the cavitation. As shown in Figure 6.9(a), decreasing the cavitation number results in an increase of the cavitation volume and consequently the absolute pressure loss is increased over the convergent-divergent channel due to the flow blockage effect. In addition, the absolute pressure loss is positively correlated with the inflow velocity u_{in} . Figure 6.9(b) presents the relationship between the cavitation number

and the pressure loss $P_{L_c} = (P_{in} - P_{out})/0.5\rho u_{in}^2$ normalized by the inlet dynamic pressure. It can be seen that all experimental points collapse well around one curve, suggesting that the normalized pressure loss is only a function of the cavitation number, independent of the inflow velocity. Another parameter of the pressure ratio $P_r = P_{out}/P_{in}$ is also plotted as a function of the cavitation number as shown in Figure 6.9(c), and it is observed to be also independent of the inflow velocity.

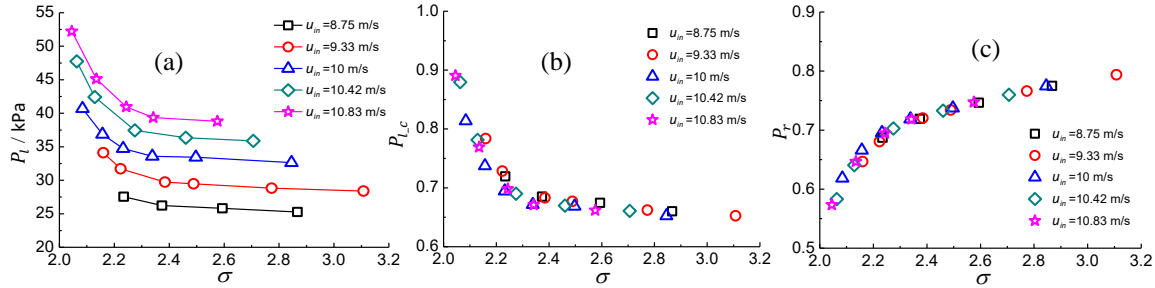


Figure 6.9. The pressure loss as a function of the cavitation number σ , (a) absolute pressure loss P_L ; (b) pressure loss coefficient $P_{L,c}$; (c) outlet-to-inlet pressure ratio P_r .

6.4.2. Cavity length versus cavitation number

In the present work, the mean cavity length was evaluated based on the distribution of the standard deviation of gray levels in a sequence of high speed images. The location of the maximum standard deviation was used to define the position of the mean cavity closure and consequently the mean cavity length was determined as the distance from the Venturi throat to the location of the maximum standard deviation. This criterion has been applied to all the measured flow conditions regardless of the cavitation regime with small oscillation or large scale shedding. For each operating point, 2000 high speed images were recorded to estimate the mean cavity length. Figure 6.10 shows an example of the influence of the number of the images used to calculate the mean value and the standard deviation of gray levels. The convergence test was performed exactly at the position of the maximum standard deviation determined from 2000 images. As can be seen that when the image number is greater than 1500, the mean value and the standard deviation of gray levels tend to stabilize in a small range of ± 0.5 . Therefore, 2000 images would be sufficient to evaluate the mean cavity length.

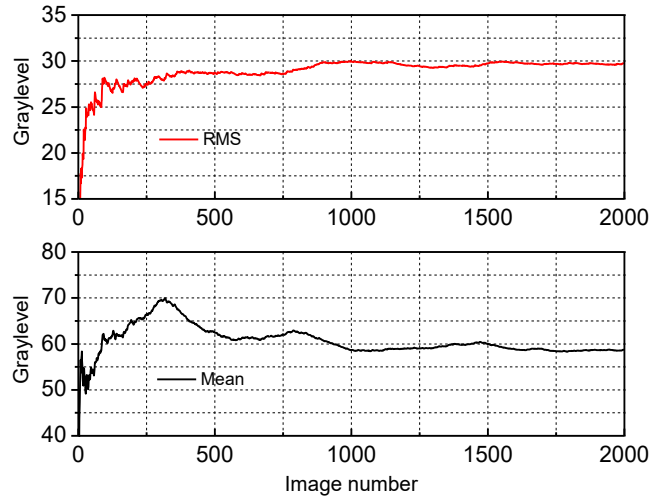


Figure 6.10. Convergence test of the mean value and the standard deviation of gray levels ($\sigma=2.23$, $u_{in}=10$ m/s).

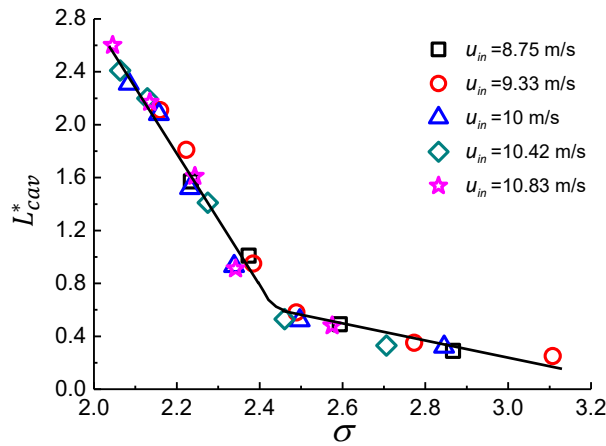


Figure 6.11. The nondimensional mean cavity length as a function of the cavitation number. The curve fits through the measurement points.

The nondimensional mean cavity length $L_{cav}^* = L_{cav}/h_{th}$ is illustrated in Figure 6.11 as a function of the cavitation number for different inflow velocities. Here L_{cav} is the mean cavity length and h_{th} is the height at the Venturi throat. It can be found that similar to the pressure loss coefficient all the measurement points of the mean cavity length collapse on one curve again, indicating that the mean cavity length is only dependent on the cavitation number irrespective of the inflow velocity. With the reduction of cavitation number, the mean cavity length is as expected increased. But a critical cavitation number at around 2.4 could be identified, on the two sides of which the ratio of the cavity length variation is quite different. For the flow conditions with the cavitation number greater than the critical value, the attached

cavity appears to be relatively steady whereas when the cavitation number is lower than the critical value, the slight change could lead to a strong influence on the extent of cavitation. This phenomenon was also reported by Long et al. (2017).

6.4.3. Velocity and pressure fluctuations

Based on 2000 instantaneous velocity fields evaluated from the PIV measurements, we could obtain the statistical turbulence properties: the streamwise velocity fluctuation u'^* , the cross-stream velocity fluctuation v'^* and the primary Reynolds shear stress $u'v'^*$. Their definitions are given as follows,

$$u'^* = \sqrt{\overline{u'u'}}/u_{\text{ref}} \quad (6.2)$$

$$v'^* = \sqrt{\overline{v'v'}}/u_{\text{ref}} \quad (6.3)$$

$$u'v'^* = \sqrt{\overline{|u'v'|}}/u_{\text{ref}} \quad (6.4)$$

where u_{ref} is the bulk velocity at the Venturi throat. In order to investigate the effect of cavitation on turbulent velocity fluctuations, the mean cavity length should be of slight difference for the measured cavitation numbers to ensure the similar dynamics. In the present work, four relatively high cavitation numbers ($\sigma = 2.63, 2.55, 2.49$ and 2.42) were selected according to the relationship between cavity length and cavitation number in Figure 6.11. These four flow conditions yield a similar cavitation regime which is characterized by a relatively stable cavity with small vapour shedding in the rear part. The vapour volume fraction in the attached cavities is relatively low such that more tracer particles can be carried and detected for the cross-correlation operation. Since the mean cavity length is around 6 mm for the studied cases, two vertical stations were identified: $x=3$ mm, within the attached cavity and $x=12$ mm, in the cavity wake where the detached vapour clouds collapse.

The profiles of u'^* , v'^* and $u'v'^*$ for the different cavitation numbers at $x=3$ mm and $x=12$ mm are presented in Figure 6.12(a) and (b), respectively. It is clear that the decrease of cavitation number leads to a rise in the turbulent fluctuations for all the three components in the wake region due to the impact of cavitation collapse. This is in a good agreement with the experimental results reported by Gopalan & Katz (2000) and Laberteaux & Ceccio (2001). On the other hand, the presence of vapour phase is observed to reduce the streamwise and cross-stream velocity fluctuations in the attached cavity. This finding is consistent with the

measurements by fast X-ray imaging described in Chapter 5. The effect of the presence of vapor on the Reynolds shear stress $u'v'^*$ is not clear since the correlation between the streamwise and cross-stream velocity fluctuations is not dependent on the variation of the cavitation number.

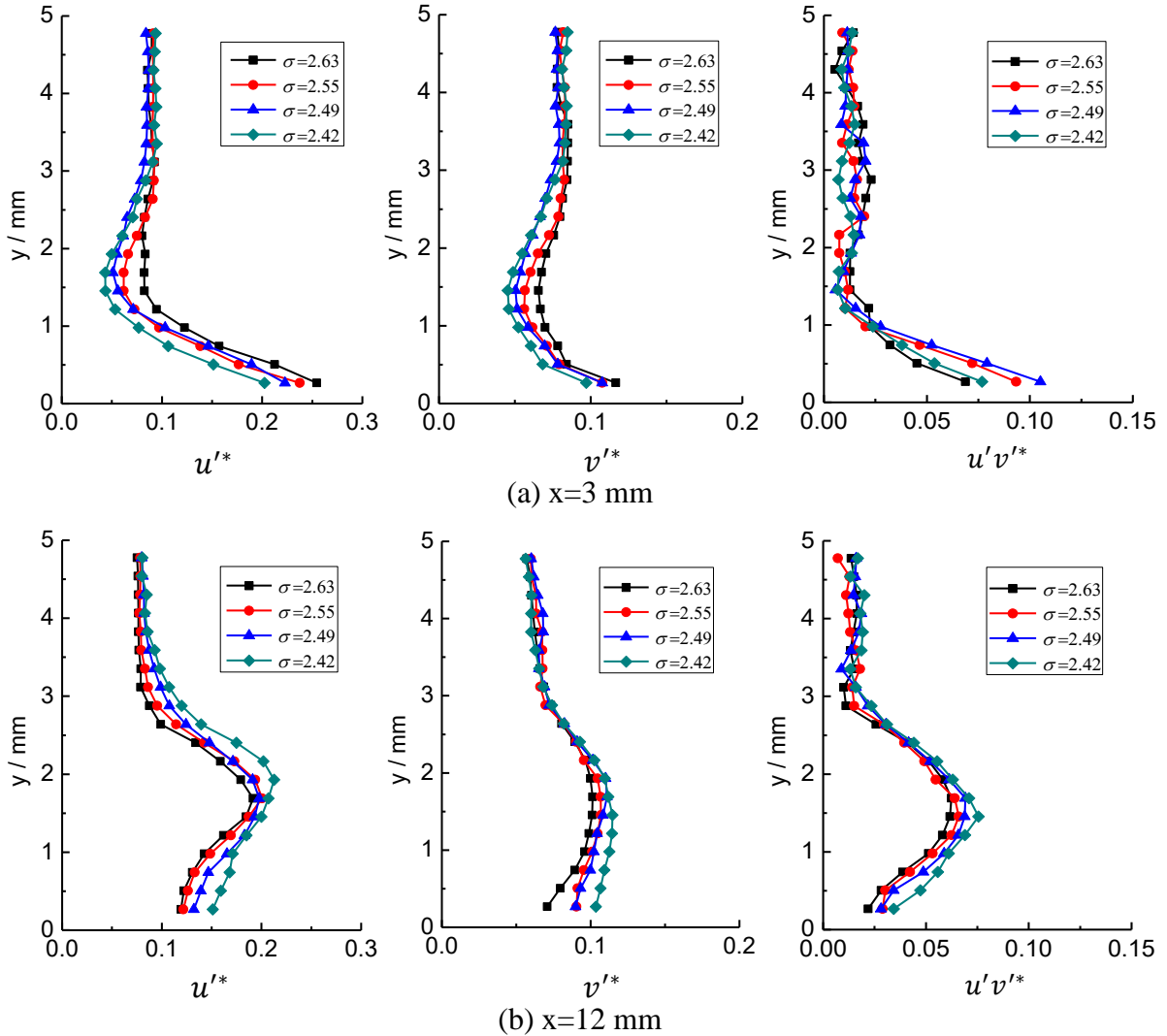


Figure 6.12. (a) Profiles of u' , v' and $u'v'^*$ for the different cavitation numbers at $x=3$ mm; (b) profiles of u' , v' and $u'v'^*$ for the different cavitation numbers at $x=12$ mm.

The average pressure fluctuation intensity was derived from the standard deviation of the pressure signal recorded by the sensors. Figure 6.13(a) and (b) illustrate the intensity of pressure fluctuations ($P_{in}'^*$, $P_{out}'^*$) normalized by the inlet dynamic pressure at the inlet and outlet, respectively. As expected, with decreasing the cavitation number the collapse of vapour bubbles leads to an increase in pressure fluctuations at the Venturi outlet. This trend is more

pronounced in the flow conditions with lower cavitation numbers. On the contrary, the pressure fluctuations at the inlet present a global trend of decrease with the extent of cavitation, suggesting that the pressure fluctuations upstream of the cavity are suppressed due to the presence of the two-phase cavitation structures. This is consistent with the effect on the velocity fluctuations. However, a different trend is observed at higher cavitation numbers: an increase in the extent of cavitation results in a rise of pressure fluctuations at the inlet. One possible interpretation is that the small amount of vapour presence at higher cavitation numbers does not yield a significant damping on the pressure fluctuations while the cavitation collapse plays a major role.

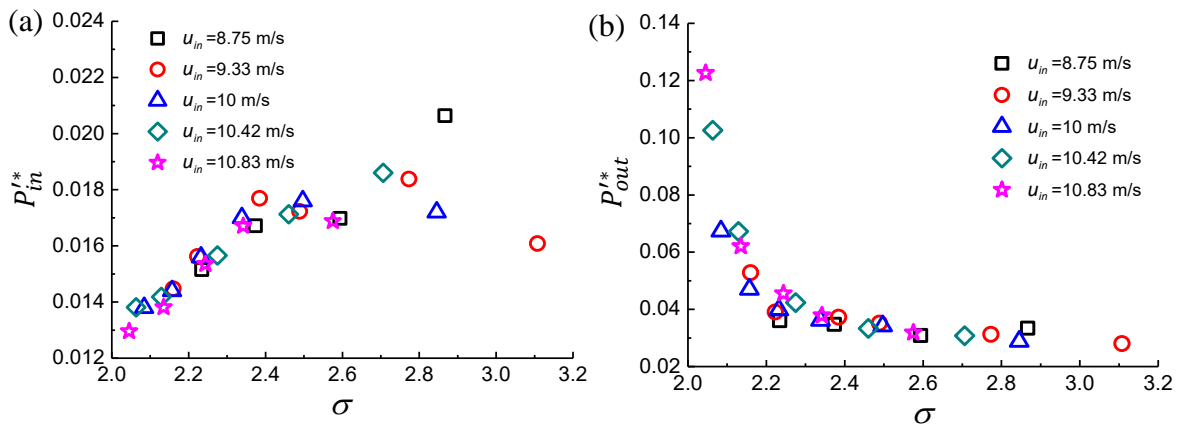


Figure 6.13. Nondimensional pressure fluctuation intensity with respect to the cavitation number, (a) P'_{in} at the Venturi inlet; (b) P'_{out} at the Venturi outlet.

6.5. Chapter summary

In this chapter we describe the attempt to produce a classic cloud cavitation in a newly-made test section which can be used in the X-ray imaging experiment. However, the large assembly error between the printed parts and the machined glass inserts leads to the presence of a gap, which actually alters the propagation path of the re-entrant jet, thereby preventing the periodic shedding of large vapour clouds. As a positive side effect, the influence of the gap on the cloud cavitation could be a passive control to this destructive form of cavitation.

Based on the experimental results in the new test section, the global parameters of the pressure loss coefficient, pressure ratio and mean cavity length were plotted with respect to the cavitation number. It was found that these parameters were only a function of the cavitation number, independent of the inflow velocity. In order to investigate the effect of cavitation on

turbulent velocity fluctuations, two vertical stations were selected: one within the attached cavity and another in the cavity wake. It was observed that the collapse of vapour clouds resulted in a rise of turbulence level while the presence of the attached cavity suppressed the velocity fluctuations. The effect of cavitation on the intensity of pressure fluctuations was found to be consistent with the effect on the velocity fluctuations.

6.5. Résumé du chapitre

Dans ce chapitre, nous décrivons la tentative de produire une cavitation nuageuse classique dans une nouvelle section de test qui peut être utilisée dans l'expérience d'imagerie aux rayons X. Cependant, la grande erreur d'assemblage entre les pièces imprimées et les inserts en verre usinés conduit à la présence d'un interstice, qui modifie en fait le trajet de propagation du jet rentrant, évitant ainsi le rejet périodique de gros nuages de vapeur. En tant qu'effet secondaire positif, l'influence de l'écart sur la cavitation des nuages pourrait être un contrôle passif de cette forme destructrice de cavitation.

Sur la base des résultats expérimentaux de la nouvelle section d'essai, les paramètres globaux du coefficient de perte de charge, du rapport de pression et de la longueur moyenne de la cavité ont été tracés par rapport au nombre de cavitation. Il a été constaté que ces paramètres étaient uniquement fonction du nombre de cavitation, indépendant de la vitesse d'entrée. Afin d'étudier l'effet de la cavitation sur les fluctuations de vitesse turbulentes, deux stations verticales ont été sélectionnées: une dans la cavité attachée et une autre dans le sillage de la cavité. On a observé que l'effondrement des nuages de vapeur entraînait une augmentation du niveau de turbulence tandis que la présence de la cavité attachée supprimait les fluctuations de vitesse. L'effet de la cavitation sur l'intensité des fluctuations de pression s'est avéré cohérent avec l'effet sur les fluctuations de vitesse.

Chapter 7

Cloud cavitation shedding mechanisms and geometry scale effect on Venturi cavitating flow

The transition from sheet to cloud cavitation is, in the classic view, related to the presence of a strong re-entrant jet which has sufficient momentum to break off the original sheet cavity from the leading edge, thereby producing periodic shedding of large clouds. In addition to the classic re-entrant jet mechanism, the recent experimental work of Ganesh et al. (2016) demonstrates that the condensation shock propagating upstream within the bubbly mixture is also an important driving mechanism for periodic cloud cavitation. It should be noted that the pressure wave emitted from the collapse of the downstream vapour clouds may favor the formation of the condensation shock, but it can also cause cloud shedding in a different manner, which is regarded as the third mechanism for cloud cavitation.

In this chapter, the three mechanisms (i.e. re-entrant jet mechanism, condensation shock mechanism and clouds-collapse-induced pressure wave mechanism) to initiate periodic cloud cavitation are illustrated in detail through high speed visualization of cavitating flows in a convergent-divergent channel. Moreover, the distinction between the condensation shock and clouds-collapse-induced pressure wave mechanism is highlighted with the help of a set of X-ray images from the team of Prof. Matevž Dular and Dr. Martin Petkovšek at University of Ljubljana. Also, we apply these three mechanisms to explain the observed geometry scale effect on Venturi cavitating flows.

7.1. Experimental set-up

As mentioned in the previous chapters, the cavitating flow regime in the Venturi channel with a small contraction ratio is characterized by a quasi-stable sheet cavitation. In order to

produce well-defined periodic cloud cavitation, we use a new Venturi test section without any gap considering the small contraction ratio might limit the cavitation dynamic range, whose schematic is shown in Figure 7.1. The convergent and divergent angles are 18° and 8° , same as the old test section, while it has a 21 mm inlet height and a 10 mm throat height producing a larger contraction ratio of 2.1. The channel width is 5 mm. The static pressure at the inlet is measured at the position of 40 mm before the Venturi throat for determining the inlet cavitation number. The entire section was made with transparent Plexiglas in order to enable clear visualization of cavitation. The high speed photography experiments were performed in the cavitation tunnel described in Section 3.1. The cavitating flow was illuminated by the high-power LED from top, and the high speed camera recorded the side view images at a frame rate of 16000 fps.

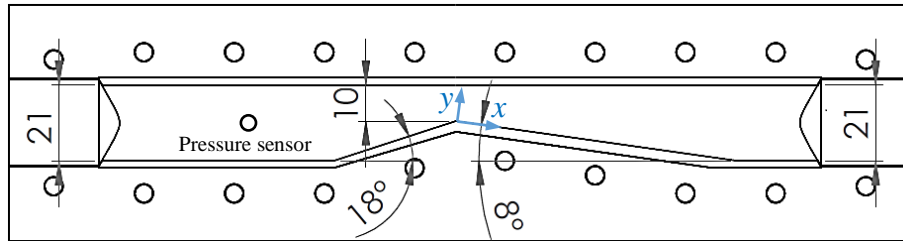


Figure 7.1. Schematic of the Venturi section with dimensions in mm, flow from right to left.

7.2. Results

7.2.1. The transitional cavitation

In the previous chapters, the X-ray imaging measurements reveal the continuous existence of a weak re-entrant flow underneath the quasi-stable sheet cavity. Compared to the old Venturi geometry, an increase in the contraction ratio of the new test section results in an augmentation of the adverse pressure gradient behind the throat, which favors the formation of a stronger re-entrant jet. Under the action of a re-entrant jet with more momentum, the sheet cavity is expected to exhibit a larger scale instability.

Figure 7.2 shows a time-space ($t-x$) diagram for $\sigma = 5.76$ corresponding to the intermediate regime between stable sheet cavitation and periodic cloud cavitation. In contrast to the continuous shedding of small vapour structures in sheet cavitation, the tendency of larger cloud shedding becomes more apparent and the location where the clouds separate from the main cavity tends to be more upstream. Based on preliminary visual inspection, no clear periodicity can be discerned. Therefore, it is referred to as the transitional cavitation regime.

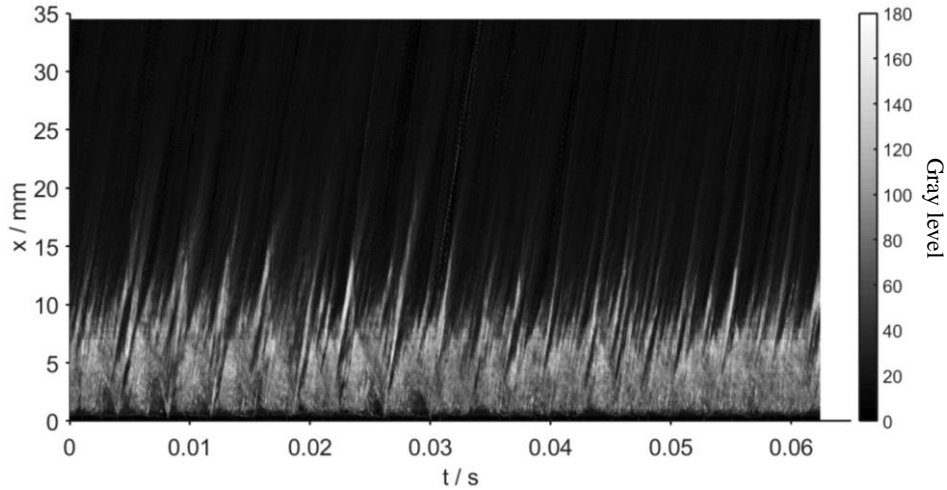


Figure 7.2. T-x diagram obtained by stacking 1000 successive high speed images of cavitation (inlet cavitation number $\sigma = 5.76$, bulk flow velocity at the throat $u_{th} = 11.17$ m/s). These flow conditions produce the transitional cavitation regime.

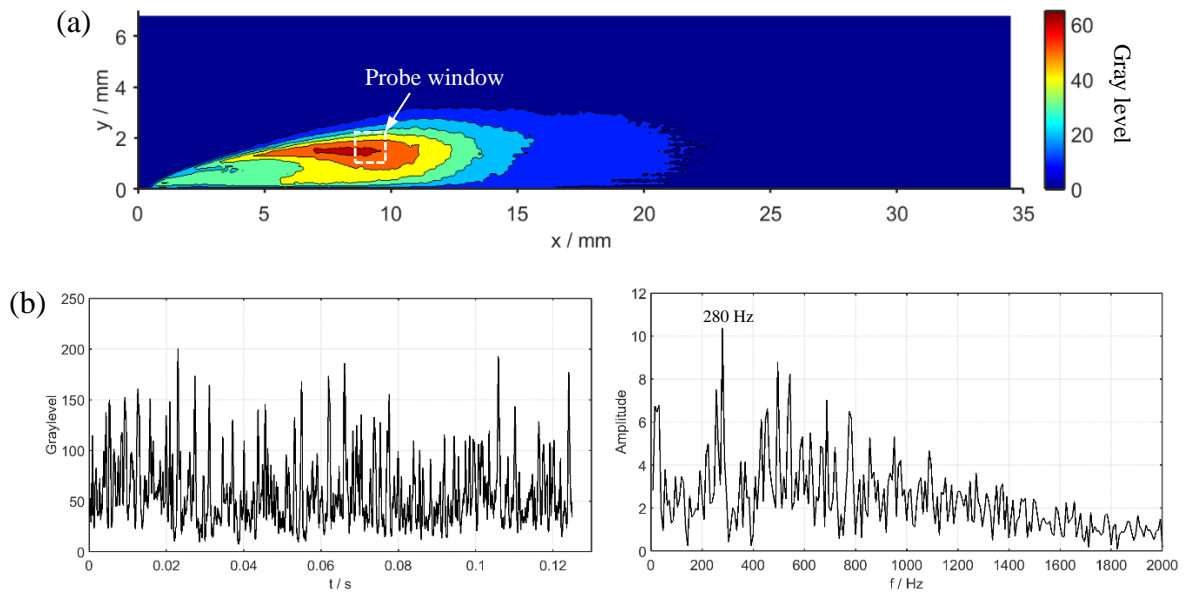


Figure 7.3. Spectral analysis of the transitional cavity shedding for $\sigma = 5.76$ and $u_{th} = 11.17$ m/s. (a) Distribution of the standard deviation of gray level. The probe window for tracing gray level variation is located at the maximum standard deviation. (b) Time-varying spatially averaged gray level within the probe window and the corresponding FFT result.

In order to analyze the spectral content of the cavitation cloud shedding, we trace the gray level variation in the mean cavity closure region. The probe window is indicated in Figure 7.3(a) by a rectangular frame with its center at the position of the maximum standard deviation of gray level. In line with the previous analysis, the mean cavity length is also determined by the

position of the maximum standard deviation, i. e. $L_{cav} = 9.2$ mm in the current case. Figure 7.3(b) presents the time history of spatially averaged gray level within the probe area during 125 ms (2000 images) and its spectrum calculated by FFT. A maximum peak can be found at the frequency of 280 Hz, but with the presence of other higher frequency peaks with similar magnitudes. This suggests that the main cloud shedding is accompanied by several secondary sheddings that have a comparable contribution to the cavity oscillations. In the present transitional cavitation, the Strouhal number based on L_{cav} and u_{th} is $St = 0.23$.

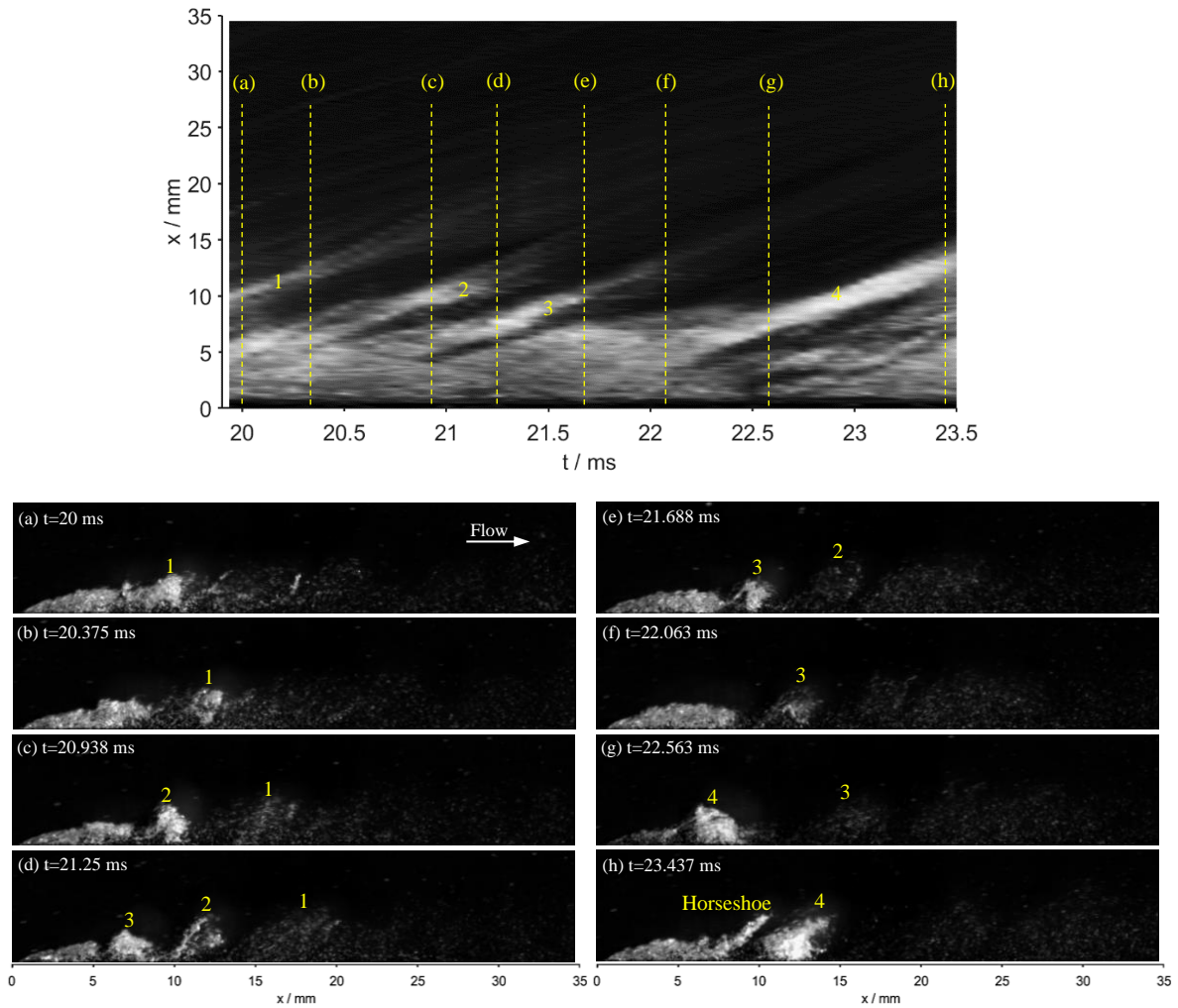


Figure 7.4. High speed photography images showing the main and secondary cloud sheddings of a transitional cavity for $\sigma = 5.76$ and $u_{th} = 11.17$ m/s. The numbers 1-3 denote the secondary clouds, and 4 denotes the main cloud. The corresponding time instants are indicated in the above t-x diagram that is a small portion of the one in Figure 7.2.

Figure 7.4 shows a series of high speed images of the transitional cavity in a typical shedding cycle. The corresponding time instants are indicated in the above t-x diagram with the same alphabetic markings. At higher cavitation numbers, the cavity thickness is relatively thin in comparison with the re-entrant jet. As described by Callenaere et al. (2001), a significant interaction exists between the cavity interface and the re-entrant jet along its upstream movement, thereby producing many smaller clouds shed within a cycle. This process is illustrated in Figure 7.4(a-f) where the smaller clouds numbered 1-3 can be observed to shed in the aft portion of the cavity. The occurrence of the spectral peaks at higher frequencies in Figure 7.3(b) is also attributed to these secondary cloud sheddings. As shown in Figure 7.4(g), a larger vapour cloud numbered 4 separates from the main cavity, which is regarded as the primary shedding within a cycle, and it is responsible for the strongest frequency peak in Figure 7.3(b). It can be seen in Figure 7.4(h) that a horseshoe vortex develops at the sheet cavity closure, which is a typical structure of cavitating flow due to the three dimensionality of the flow.

7.2.2. Re-entrant jet induced cloud cavitation

With a reduction in cavitation number, the sheet cavity increases both in length and thickness, which favors a stronger re-entrant jet propagating upstream underneath the cavity without significant interactions with the cavity upper interface. When the re-entrant jet reaches the leading edge, it breaks completely the cavity into two parts, and the rear part is rolled up forming large-scale cloud shedding. The time evolution of such a process over multiple cycles is presented in the t-x diagram of Figure 7.5 for $\sigma = 4.95$ and $u_{th} = 14.6$ m/s. Compared to the transitional cavity, a well-defined periodicity can be identified visually in this classic cloud cavitation.

In Figure 7.5, the yellow solid line depicts the cavity growth process; the red solid line denotes the progression of the re-entrant jet, and the blue dashed lines indicate the shed cloud. It can be seen that the cavity grows at a nearly constant velocity until an instant when the re-entrant jet is initiated, and afterwards, the cavity growth slows down. At the instant of the re-entrant jet travelling to the origin point, the cavity length attains maximum (~25 mm). The characteristic velocity of the re-entrant jet is estimated to be 4.2 m/s on average according to the slope of the red solid line. It is interesting to note that the re-entrant jet is slightly accelerated

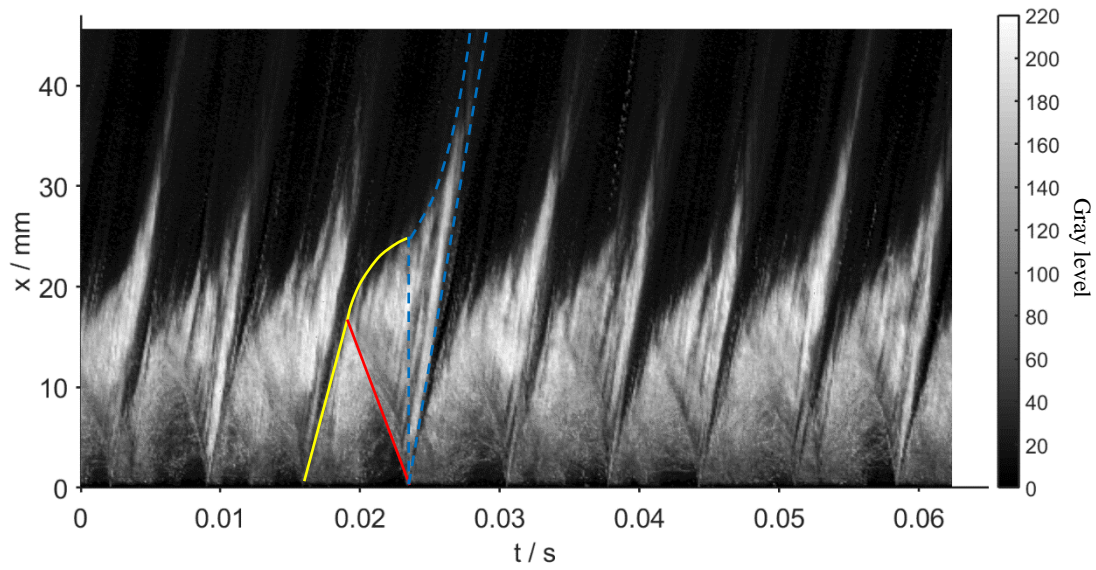


Figure 7.5. T-x diagram obtained by stacking 1000 successive high speed images of re-entrant jet induced cloud cavitation ($\sigma=4.95$, $u_{th}=14.6$ m/s). The yellow solid line depicts the cavity growth process. The red solid line denotes the progression of the re-entrant jet, and the blue dashed lines indicate the shed cloud.

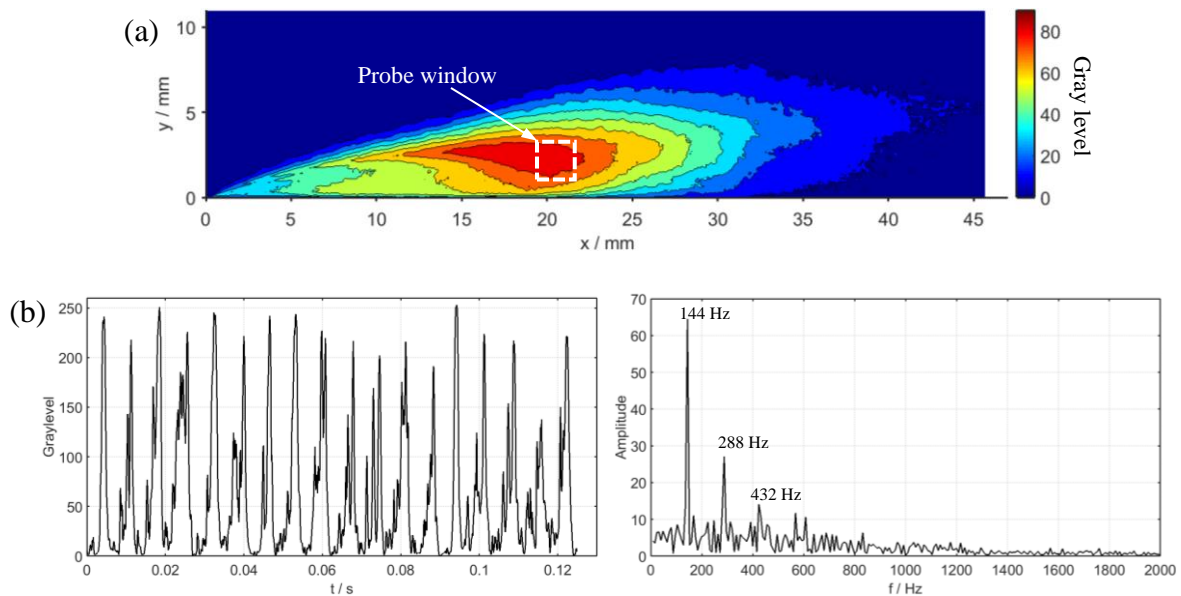


Figure 7.6. Spectral analysis of re-entrant jet induced cloud cavitation for $\sigma=4.95$ and $u_{th}=14.6$ m/s. (a) Distribution of the standard deviation of gray level. The probe window for tracing gray level variation is located at the maximum standard deviation. (b) Time-varying spatially averaged gray level within the probe window and the corresponding FFT result.

during its upstream motion. This implies that the driving force (i.e. adverse pressure gradient) and resistance (i. e. shear stress) acting on the reentrant jet are not statistically balanced: to be more specific, the former force prevails over the latter one. Just because of this acceleration process during the cavity growth phase, the re-entrant jet gains sufficient momentum to pinch off the cavity.

The cloud shedding frequency is determined based on the time-varying gray level at the cavity closure whose location is indicated in Figure 7.6 (a). The transient gray level signal at the probe position and the corresponding spectrum are shown in Figure 7.6 (b). The spectrum at the cavity closure reveals that the periodic cloud shedding occurs at a dominant frequency of 144 Hz, which corresponds to a period of 6.95 ms. The smaller peaks at 288 Hz and 432 Hz are not caused by secondary cloud shedding and they are just the harmonics of the dominant frequency. This is in accordance with the well-defined periodicity observed in Figure 7.5. In this case, the mean cavity length is $L_{cav}=20.5$ mm, also determined by the position of the maximum standard deviation of gray level. The Strouhal number based on L_{cav} and u_{th} is computed to be $St = 0.20$.

Figure 7.7 shows a sequence of high speed images for the re-entrant jet induced cloud cavitation. The corresponding time instants are indicated in the above t-x diagram with the same alphabetic markings. Figure 7.7(a, b) depict the growth of an attached sheet cavity, with a vapour cloud detached from the previous cavity being transported downstream. Figure 7.7(c-f) show a re-entrant jet forms at the cavity closure and then moves towards the leading edge. During the growth phase of the sheet cavity, the upstream part is increasingly occupied by vapour phase, making it appear nearly transparent. Although it is difficult to recognize the exact location of the re-entrant jet, its upstream motion can be inferred from the shrinkage of the cavity transparent portion, as indicated by the yellow arrows in Figure 7.7 (d-f). This is because the pressure rise brought by the re-entrant jet can cause the transparent vapour condensing into the opaque mixture. When the re-entrant jet reaches the throat, the entire cavity is peeled off forming the detached cloud and a new cavity appearing at the leading edge begins to grow. Due to the counter-directional velocity of the main flow and the re-entrant jet, the multiple smaller clouds coalesce into a larger cavitating spanwise vortex denoted by the red curve with arrow, as shown in Figure 7.7 (g-i). During the same period, the new cavity grows slower than the cloud roll-up, thereby generating a clear spatial separation between them. As the shed cloud

is convected downstream in a rolling motion, it collapses in the high pressure wake region and the new sheet cavity continues to grow, as shown in Figure 7.7 (j).

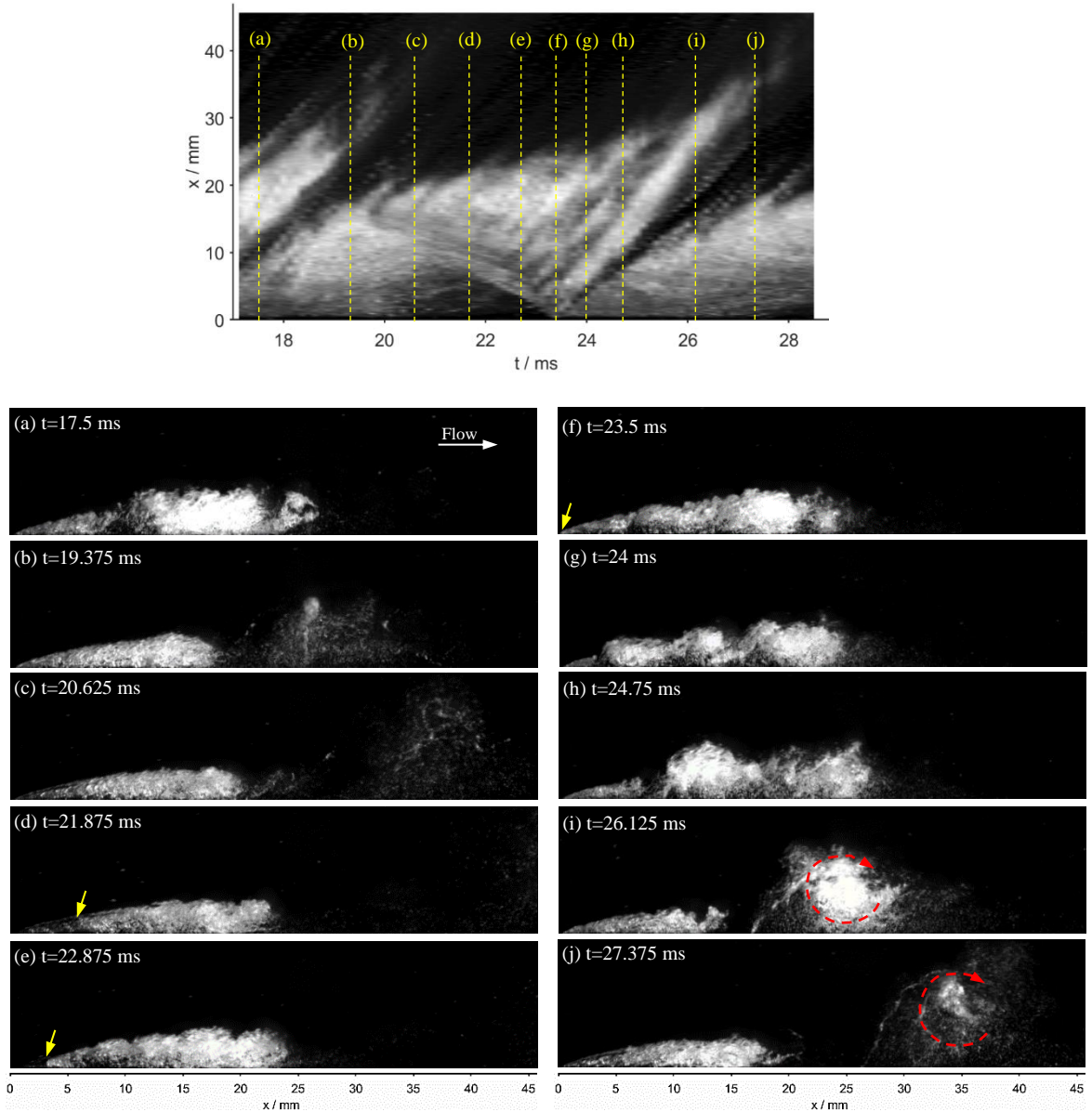


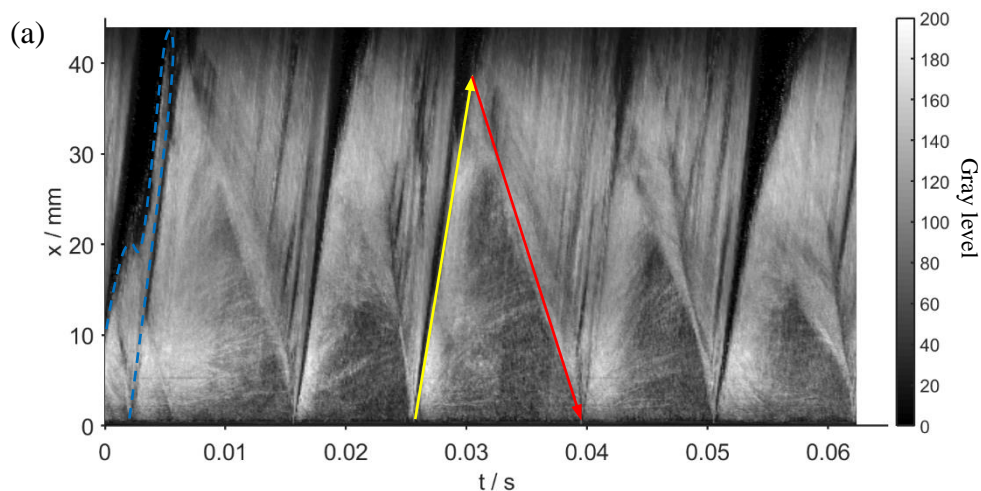
Figure 7.7. High speed photography images showing re-entrant jet induced cloud shedding for $\sigma = 4.95$ and $u_{th} = 14.6$ m/s. The corresponding time instants are indicated in the above t-x diagram that is a portion of the one in Figure 7.5.

7.2.3. Condensation shock induced cloud cavitation

As the cavitation number further decreases, high vapour production rate leads to a fast change in the cavity length and density, which favors the formation of a condensation shock at

the cavity closure. In cavitating cases with lower cavitation numbers, the large-scale cloud shedding is mainly associated with the propagation of the condensation shock rather than the classically-described re-entrant jet. Figure 7.8(a) shows the cloud cavitation dynamics driven by condensation shocks in the form of a t-x diagram for $\sigma = 4.31$ and $u_{th} = 20.83$ m/s. Compared to the re-entrant jet induced cloud shedding processes, a more noticeable cycle-to-cycle variation can be observed in the present studied case. A typical cycle is composed of processes of the cavity growth (indicated by the yellow arrow) and the cavity retraction caused by the condensation shock (indicated by the red arrow) both at nearly constant rates. The propagating velocity of the condensation shock can also be estimated by the slope of the red arrow. It is averaged over 10 shedding cycles and calculated to be 6.5 m/s considering large cycle-to-cycle variations. Interestingly, the t-x diagram also depicts a small cloud shedding event (as indicated by the blue dashed lines) which occurs irregularly. This is attributed to a classic re-entrant jet instability.

Similar to the previous procedures of spectral analysis, we trace the time-varying gray level at the cavity closure and the corresponding FFT result is shown in Figure 7.8(b). The mean cavity length for the present case is $L_{cav} = 34.9$ mm, also determined by the position of the maximum standard deviation of gray level. The spectrum reveals the presence of a single dominant frequency at 80 Hz (i.e. a period of 12.5 ms), which is associated with the primary cloud shedding induced by the condensation shock. The corresponding Strouhal number based on L_{cav} and u_{th} is computed to be $St = 0.13$, which is smaller than the re-entrant jet associated Strouhal numbers. A decline trend in Strouhal number is also reported by Jahangir et al. (2018) when the periodic cloud shedding mechanism transforms from re-entrant jets to shock waves.



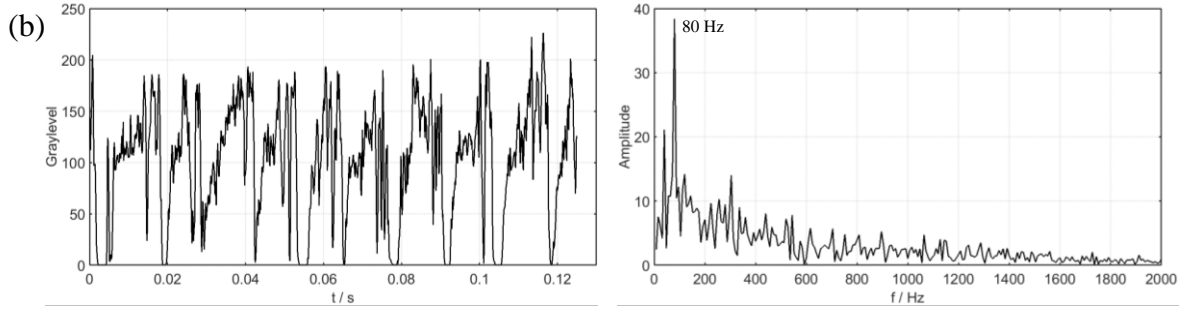
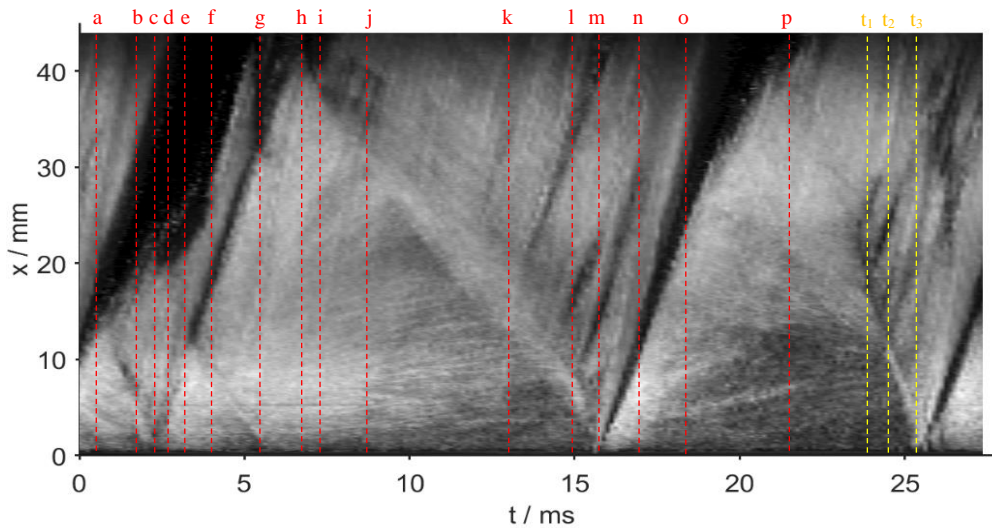


Figure 7.8. (a) Temporal evolution of the cloud shedding processes mainly induced by condensation shocks for $\sigma = 4.31$ and $u_{th} = 20.83$ m/s. (b) Time-varying gray level signal and the corresponding FFT result probed at the cavity closure.

Although in the present cavitation regime, the prevalent mechanism governing the periodic cloud shedding is the upstream propagating shock wave, the re-entrant jet induced cavity instability can still appear occasionally. Figure 7.9 shows the high speed images of a re-entrant jet induced cloud shedding event and the following cycle of large cloud shedding induced by condensation shock. Figure 7.9 (a, b) presents the incomplete cavity growth under the influence of the re-entrant jet. Meanwhile the previously shed vapour cloud is rolled up and advected downstream. When the re-entrant jet reaches the vicinity of the leading edge, it pinches off the sheet cavity forming the detached cloud, as shown Figure 7.9 (c). With the cloud being convected downstream, a new sheet cavity starts to grow, as shown Figure 7.9 (d-f). Different from the shedding process described in Figure 7.7, the so-called detached cloud is still connected to the sheet during its most period of moving downstream. This is due to the fast cavity growth since the vapour production rate is relatively high in the present flow conditions.



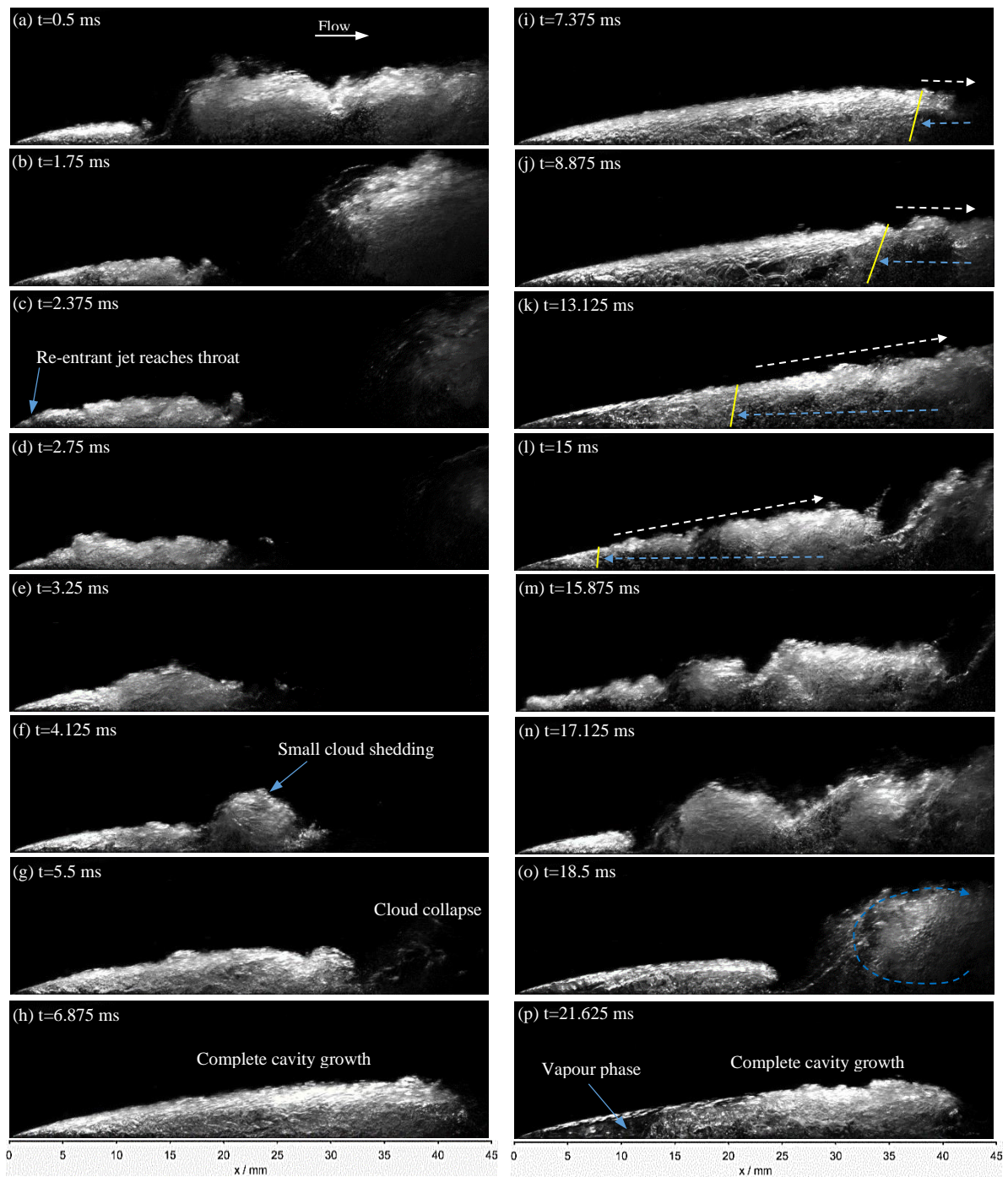


Figure 7.9. High speed photography images showing processes of a small cloud shedding induced by re-entrant jet and a large cloud shedding induced by condensation shock for $\sigma = 4.31$ and $u_{th} = 20.83$ m/s. The corresponding time instants are indicated in the above t-x diagram that is a portion of the one in Figure 7.8(a).

Figure 7.9 (g) depicts the instant of the cloud collapse, which seems to have no significant impact on the cavity growth. In Figure 7.9 (h), the sheet cavity has grown completely to its maximum length (~ 42 mm) with a well-defined closure line. Shortly after, a condensation shock forms at the trailing edge of the cavity, as can be observed in Figure 7.9 (i). The yellow solid line indicates roughly the location of the shock front. Distinct from the thin re-entrant jet beneath the cavity, the condensation shock spans almost the entire cavity height. Following the simulation results of Budich et al. (2018), the flow behind the shock front is directed upstream, as indicated by the blue dashed arrow. With the condensation shock propagating upstream through the cavity, the cavity retracts towards the leading edge. This process is illustrated in Figure 7.9 (j-l). During the same period, a shear layer develops between the outer main flow (indicated by the white dashed arrow) and the reversed flow across the shock, exhibiting classical Kelvin–Helmholtz instabilities. The coherent vortical motions within the shear layer

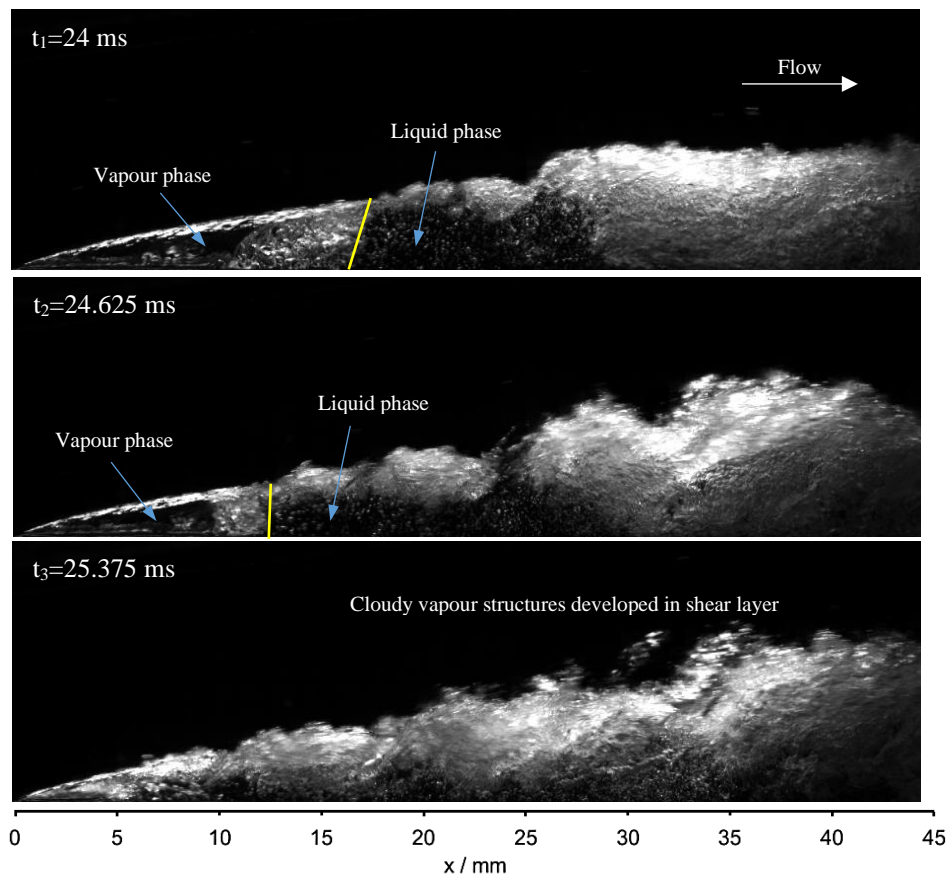


Figure 7.10. High speed images at three representative time instants showing the cavity collapse caused by condensation shock for $\sigma = 4.31$ and $u_{th} = 20.83$ m/s. The corresponding time instants are indicated in the t-x diagram of Figure 7.9.

enhance the formation of new cloudy structures behind the shock. Once the shock wave reaches the leading edge, the cavity collapses completely, while the downstream cloud is further fed by the shear layer evaporation, as shown in Figure 7.9 (m). After a momentary cessation of vapour production, another new cavity begins to grow from the Venturi throat, and the shed cloudy structures merge as they move downstream in a spanwise rotating way (Figure 7.9 (n, o)).

In Figure 7.9 (p), the cavity grows again to its maximum length, and its internal void fraction is higher than the preceding cavity shown in Figure 7.9 (h) as evidenced by the fore part of the cavity being nearly filled with pure vapour. The lower pressure within the cavity associated with lower density is expected to initiate a stronger condensation shock. Three representative time instants are selected in Figure 7.10, illustrating a more evident propagation of condensation shock. At the time instant t_1 , the shock front (indicated by the yellow line) can be identified clearly, across which, the opaque two-phase mixture transforms to the transparent liquid phase by condensation, thereby generating a discontinuity in void fraction. Just behind the shock front, a thin cavitating shear layer can be observed. At the subsequent time instant t_2 , the condensation shock continues to travel upstream further collapsing the sheet cavity. At the final time instant t_3 , the sheet cavity disappears totally, and subsequently the cloudy vortical structures are rolled up into a large cloud moving downstream.

7.2.4. Pressure wave induced cloud shedding

In the above examined cavitation cases, the collapse of the shed clouds does not appear to noticeably disturb the growing cavity. This implies that the collapse-induced pressure wave may attenuate fast with propagation distance to a low intensity when it impinges on the trailing edge of the sheet cavity, and thus its influence on the overall cavity dynamics is negligible. However, we can conceive that with further reduction in cavitation number, the collapse of a larger amount of vapour may emit a pressure wave strong enough to stop the cavity growth or even make it disappear abruptly. This phenomenon is clearly observed in a set of X-ray images provided by our collaborative team. Interestingly, the condensation shock mechanism is also observed in the same images, i.e. the two mechanisms trigger cloud shedding alternately in the same flow conditions. Compared to the conventional high speed images, X-ray phase contrast imaging enables a more detailed visualization of two-phase structures, and thus to distinguish these two mechanisms clearly.

Firstly, the processes of the condensation shock induced cavity retraction are presented in Figure 7.11. The test section is also a Venturi-type channel with the same convergent and divergent angle as the above-mentioned one. The throat height is 0.25 mm and the channel width is 0.5 mm. The free-stream velocity at the throat is $u_{th}=10$ m/s. The cavitating flow was illuminated by the synchrotron X-ray beam at APS and recorded at 67890 frames per second, i.e. $14.73 \mu\text{s}$ of time interval between two consecutive frames. Due to the limitation of the beam size, only the upstream portion of the whole flow field is captured.

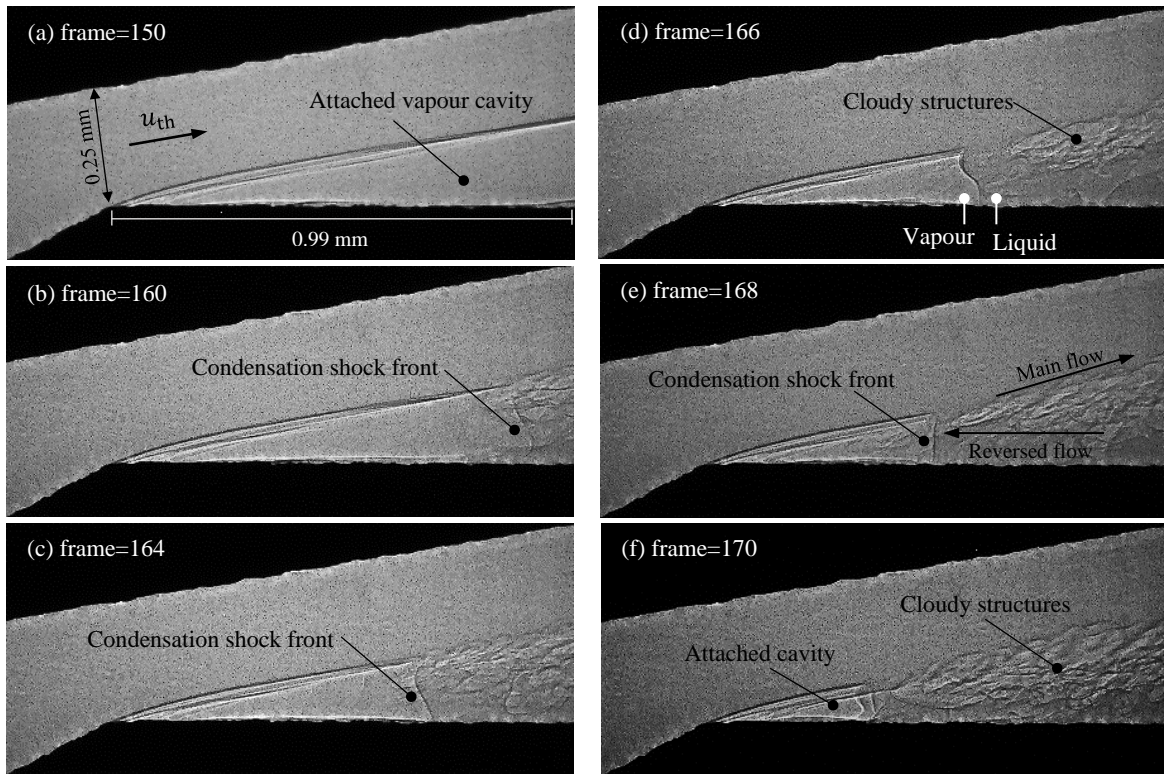


Figure 7.11. A sequence of X-ray images showing the upstream progression of the condensation shock through the attached sheet cavity.

As a supplementary material to the conventional high speed images, Figure 7.11 provides further evidence to support the condensation shock mechanism distinct from the classic re-entrant jet mechanism. In this case, the void fraction in the attached sheet cavity is 100%, i.e. pure vapour cavity. It is clear that the shock front spans the entire cavity height, across which, the vapour phase is condensed completely into the liquid phase. It also confirms that the downstream cloudy vapour structures are not separated from the main cavity, instead they are newly generated in the shear layer between the main flow and the post-shock reverse flow.

Moreover, the propagation speed of the shock wave is estimated to be 3.2 m/s through tracking the shock front in the frame series.

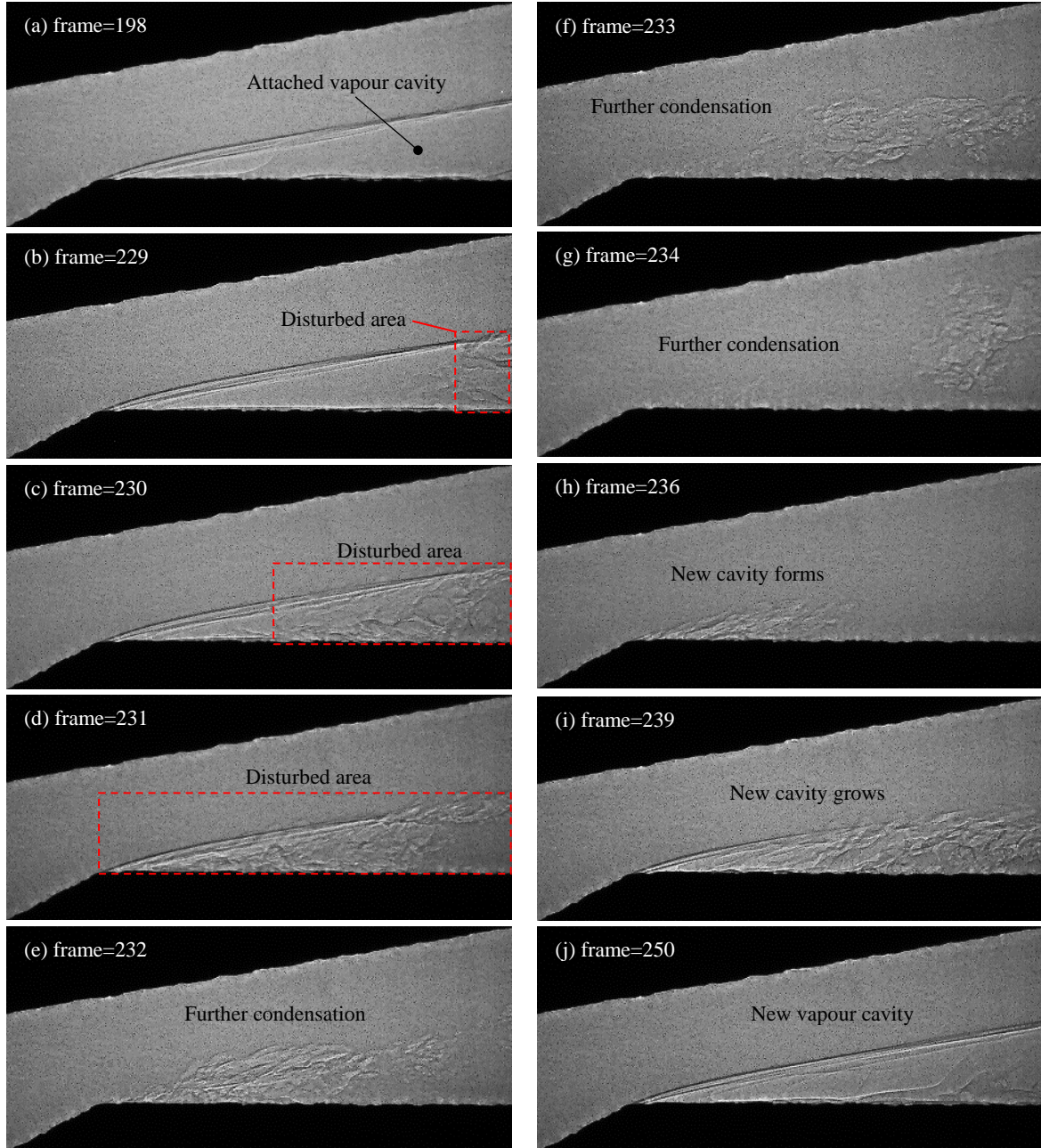


Figure 7.12. A sequence of X-ray images showing a cavity shedding cycle induced by pressure wave emitted from cloud collapse.

The next shedding cycle just after the one presented in Figure 7.11 is shown in Figure 7.12, where the dominant mechanism of cavity detachment is found to be pressure wave emanating

from the cloud collapse. Although we cannot see the cloud collapse in the downstream wake, the position of the pressure wave can be roughly inferred via its impact on the pure vapour cavity. In Figure 7.12(b), the rear part of the cavity has been perturbed, which is believed to be caused by the collapse-induced pressure wave. In the subsequent two frames Figure 7.12(c) and (d), the disturbed area has extended to the whole cavity, which is believed to be related to the pressure wave spreading within the cavity. After the passage of the pressure wave, the pressure rise will continue to condense the disturbed vapour/liquid mixture. In Figure 7.12(g), the vapour volume attains the minimum value. The attached sheet cavity has disappeared totally from the Venturi wall, and the main flow entrains the residual vapour downstream. As the throat region recovers to the original low-pressure status, a new cavity starts to grow, as can be observed in Figure 7.12(h). Figure 7.12(i, j) illustrate the further cavity growth until a vapour sheet is formed.

Comparing the two shedding mechanisms revealed in the X-ray images, we can find that the propagation of the pressure wave front does not result in an obvious discontinuity in the flow field as is the case for the condensation shock, which allows us to distinguish these two mechanisms easily. In addition, the propagation velocity of the pressure wave within the cavity is estimated, based on the position of the perturbations, to be 23 m/s at least, which travels much faster than the condensation shock front.

As mentioned above, the flow behind the condensation shock front is oriented upstream, and hence a shear layer between the main flow and the reversed flow is developed. Due to low pressure induced by large turbulent fluctuations in the shear layer, a large amount of vapour volume is newly produced there. In contrast, the flow does not show any signature of reversal after the passage of the pressure wave, and therefore no new vapour is generated. Different amounts of vapour collapsing downstream of the cavity emit pressure waves with distinct magnitude. This might lead the two mechanisms to alternate in the same flow conditions.

7.3. Discussion

In the literature, two mechanisms are well acknowledged to initiate the periodic cloud cavitation. One is the classical re-entrant jet mechanism, and another is the condensation shock mechanism which is experimentally demonstrated by Ganesh et al. (2016) only recently. The third independent mechanism of collapse-induced pressure wave is neglected as it is generally categorized into the condensation shock mechanism. This inappropriate classification may be

caused by the fact that pressure waves emitted from cloud collapse are called shock waves in many published papers, and some researchers tend to support the condensation shock is initiated by the collapse-induced pressure wave of the previously shed cloud, e.g. Stanley et al. (2014), Wu et al. (2017), Jahangir et al. (2018), Bhatt & Mahesh (2020). In this section, we will give a detailed discussion on the differences of the three mechanisms based on the present experimental results and the data reported in the literature.

7.3.1. Origin

As shown in Figure 7.13, the flow which originally moves over the cavity is forced to deflect towards the Venturi wall due to the pressure difference inside and outside of the sheet cavity. Subsequently it reattaches to the wall establishing a local stagnation point just downstream of the cavity. On the upstream side of the stagnation point, conservation of mass forces the liquid to flow underneath the cavity, which is referred to as re-entrant jet. The above description indicates that the upstream movement of the re-entrant jet is a pressure driven phenomenon and the magnitude of adverse pressure gradient at the cavity closure is directly related to the re-entrant flow strength.

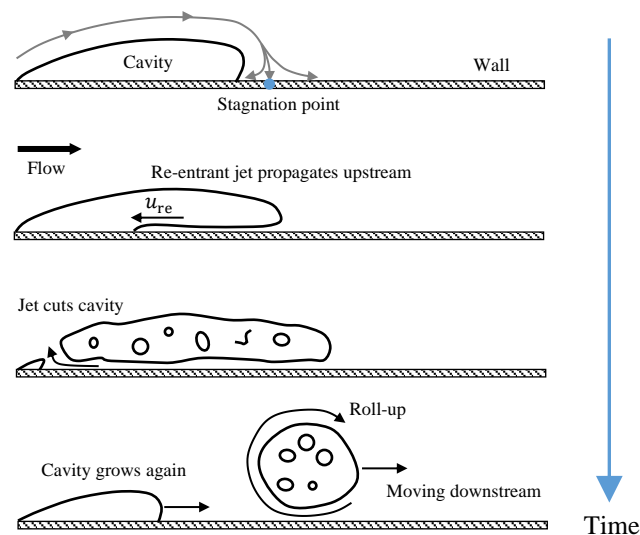


Figure 7.13. Schematic illustration of cloud shedding processes initiated by re-entrant jet.

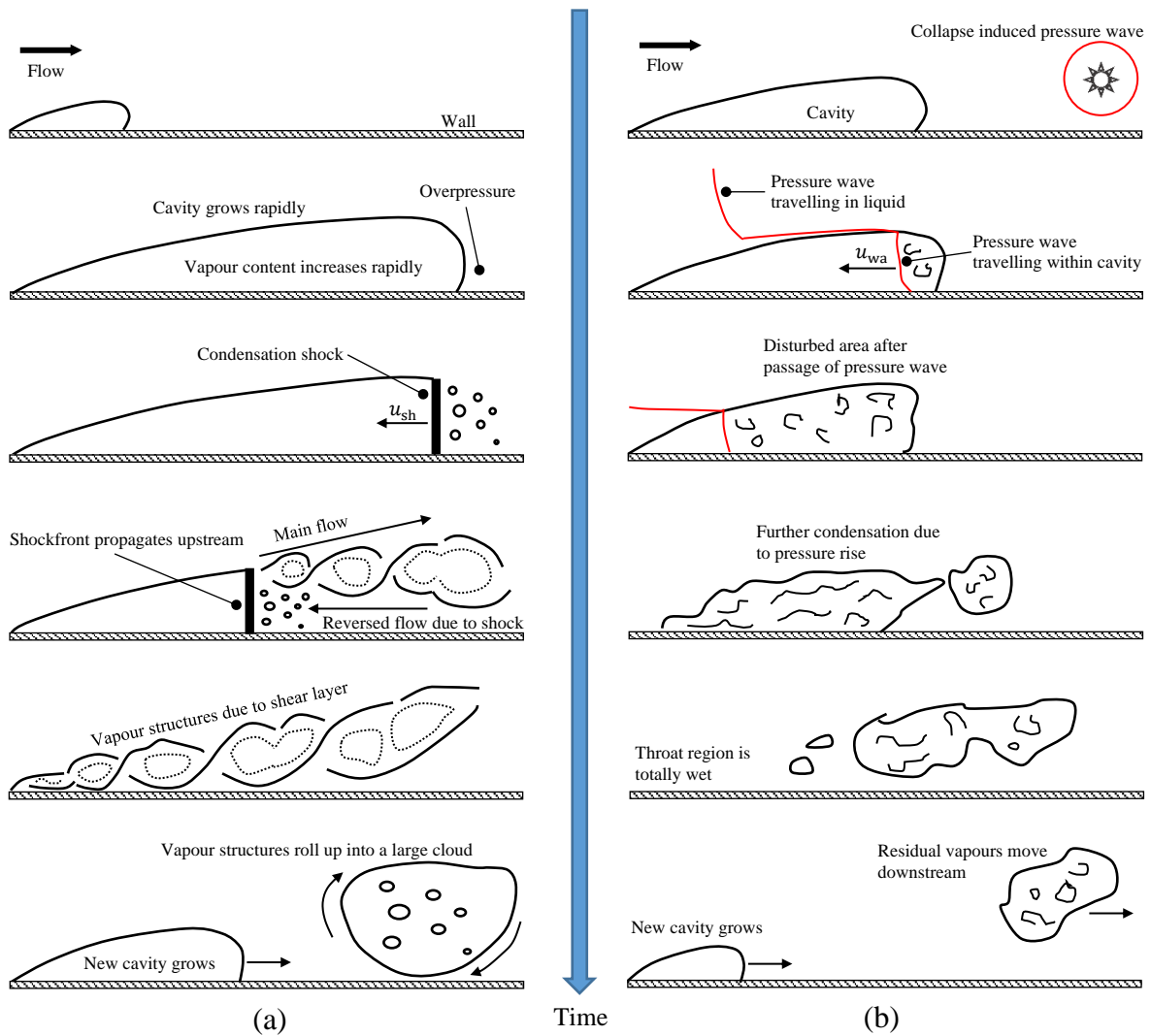


Figure 7.14. Schematic illustration of cloud shedding processes initiated by condensation shock (a) and collapse-induced pressure wave (b).

The origin of condensation shock waves forming at the rear of the cavity is not yet well understood. The first explanation for this phenomenon is provided by Ganesh (2015) where it is suggested that a rapid increase in the cavity length and vapour content associated with higher vapour production rate results in the generation of shock waves at lower cavitation numbers. As sketched in Figure 7.14(a), an overpressure region downstream of the cavity causes an abrupt and intense condensation of the vapour phase. This process releases a large amount of latent heat initiating further condensation towards the cavity leading edge. When the characteristic speed based on the condensation rate exceeds the local speed of sound, a void fraction discontinuity is eventually formed. The quantities across this discontinuity have been

proven to satisfy the Rankine–Hugoniot jump conditions numerically (Budich et al. 2018) and experimentally (Ganesh et al. 2016), and thus it represents a compressible shock wave phenomenon. On the other hand, the pressure wave emitted by the downstream cloud collapse can also contribute to initiating the condensation shock, as suggested by some researchers. However, we have observed the formation of a condensation front in the absence of cloud collapse from Figure 7.9(i), implying that the collapse-induced pressure wave is not the necessary condition for initiating the condensation shock. This is consistent with the conclusion of Budich et al. (2018).

As illustrated in Figure 7.14(b), a large vapour cloud collapses abruptly in the downstream high pressure region, which creates a void and surrounding liquid rushes into the void producing a water hammer effect. This causes a large amount of pressure to be concentrated locally resulting in compression waves that travel in all directions. Although the pressure waves are named as shock waves in the literature, there is no strong evidence to show they propagate supersonically, and therefore they are more accurately termed as pressure waves rather than shock waves.

7.3.2. Pressure rise and propagation velocity

The measurements of Ganesh et al. (2016) show that the order of magnitude of the pressure increase across the condensation shock front is only a few kPa, indicating the front is a weak discontinuity in pressure. The subsequent numerical simulations of Budich et al. (2018) and Bhatt & Mahesh (2020) in the same geometry and flow conditions also predict the same order of pressure rise. In contrast, Wu et al. (2017) have measured a large rise of pressure (as high as 690 kPa) when the collapse-emitted pressure wave passes over the transducer. The great difference of pressure rises caused by the condensation shock and pressure wave indicates they are distinct mechanisms for cloud shedding. Wu et al. (2017) also reported the pressure change associated with the re-entrant jet propagation is not significant.

The re-entrant jet velocity is estimated to be $u_{re} = 4.2$ m/s ($0.29 u_{th}$) according to the t-x diagram in Figure 7.5. The propagation speed of the condensation shock is estimated to be $u_{sh} = 6.5$ m/s ($0.31 u_{th}$) and $u_{sh} = 3.2$ m/s ($0.32 u_{th}$) through analyzing the t-x diagram in Figure 7.8 and tracking the shock front in Figure 7.11, respectively. Since the shock speed is supersonic, we can infer that the local speed of sound drops to the order of a few meters per second, which is possible in bubbly mixtures. However, the condensation shock can also

propagate through a pure vapour cavity as shown in Figure 7.11. This might be attributed to that the intense phase change concentrated at the shock front reduces the local sonic speed drastically. The travelling velocity of the collapse-induced pressure wave within the cavity is estimated to be $u_{wa} > 23$ m/s ($2.3 u_{th}$) based on the position of perturbations in Figure 7.12. In general, the measured condensation shock speed is comparable to the re-entrant jet velocity, but it is much lower than the propagation speed of the pressure wave. The great difference between the condensation shock and pressure wave speed further supports that they are distinct mechanisms.

7.3.3. Cloud shedding processes

The cloud shedding processes initiated by the re-entrant jet, condensation shock and collapse-induced pressure wave are illustrated schematically in Figure 7.13, Figure 7.14(a) and Figure 7.14(b) respectively. For the re-entrant jet mechanism, the cloud shedding is caused by the physical re-entrant jet pinching off the sheet cavity. This process does not involve significant phase change. For the condensation shock mechanism, the original sheet cavity collapses completely due to the upstream-propagating condensation shock while the vapour content in the shed cloud is originated from the post-shock cavitating shear layer. For the collapse-induced pressure wave mechanism, it represents an external forcing of the cavity. In addition to traveling within the cavity, the pressure wave also spreads in the liquid main flow at a higher velocity that is expected to be the speed of sound in the liquid phase. Unlike the condensation shock front with concentrated phase change, the pressure wave does not result in a discontinuity in void fraction. After the passage of the pressure wave, the condensation continues to take place within the cavity until the remaining vapour structures are transported downstream as a cloud.

7.4. Scale effect on Venturi cavitating flow

7.4.1 Problem background

The issue of scale effect was raised when a small Venturi-type section was used for X-ray imaging experiments. Limited by the small size of the X-ray beam cross section (see Section 3.3), the test section had to be designed with very small dimensions. As a consequence, a test section was manufactured with a geometry scaled down 10 times from the original one used by Stutz & Legoupil (2003). Figure 7.15(a) shows the main dimensions of the scaled test

section (referred to as Venturi 1). The convergent and divergent angles of 18° and 8° stay the same as the original test section. The channel width is 4 mm, and the height at the entrance of the Venturi profile is 5 mm with the throat height of 3.34 mm.

Unexpectedly, the cavitating flow in Venturi 1 is characterized by a quasi-stable sheet cavitation although the original geometry can produce periodic shedding of large vapour clouds. In order to understand the reason for this flow stabilization, an experimental study was performed in six geometrically similar Venturi sections where either width or height or both were scaled, as can be found in Dular et al. (2012). The results reveal that small geometry dimensions, especially small throat heights, influence the occurrence of unsteady cloud shedding. In order to obtain classic cloud cavitation, a 12 mm spacer insert was added to Venturi 1 such that a new geometry (Venturi 2) with increased heights was produced. Figure 7.15(a) shows also the main dimensions of Venturi 2. The entrance and throat heights were increased to 17 mm and 15.34 mm respectively. Other geometrical parameters were not changed. Nevertheless, as described in Chapter 4 and 5, we find that partial cavities developed in Venturi 2 exhibit the similar behaviors as in Venturi 1, i. e. remaining in a relatively steady regime without noticeable shedding in a wide range of cavitating conditions.

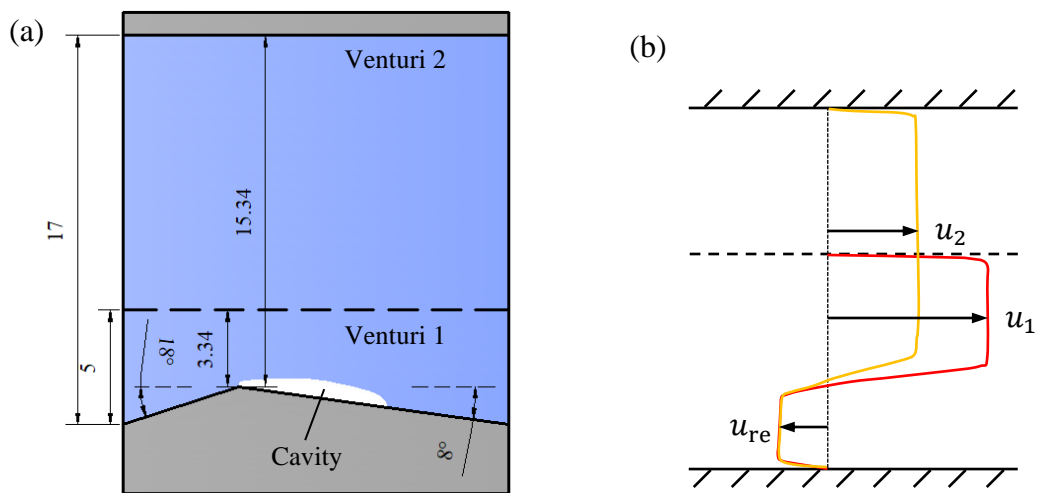


Figure 7.15. (a) Main dimensions (in mm) of two Venturi-type test section. (b) Schematic showing the effect of throat height on shear velocity gradient.

7.4.2 Explanations to the observed scale effect

Although Venturi 1 and Venturi 2 are largely different in geometrical parameters, especially in throat height, they are both characterized with a quasi-stable sheet cavitation. For Venturi 1 with a smaller throat height, the occurrence of a reverse flow (u_{re}) will lead the outer main flow to move at a higher speed ($u_1 > u_2$), hence a higher velocity gradient in the shear layer, as illustrated in Figure 7.15(b). This means that the resistance, i.e. shear stresses acting on the re-entrant jet will become larger, which then suppresses the full development of the re-entrant jet. Compared to Venturi 1, the throat height of Venturi 2 is increased greatly, but meanwhile another critical parameter, i.e. the contraction ratio of entrance to throat height, is reduced from 1.5 to 1.1. This results in a decrease of adverse pressure gradient at the cavity closure. Since the driving force gets smaller, the re-entrant jet in Venturi 2 can neither be fully developed as pointed out in the previous chapters. Overall, the re-entrant jets in the both Venturi channels are too weak to pinch off the sheet cavity, thereby making the cavity relatively stable. However, the weak re-entrant jet in Venturi 1 is caused by larger resistance associated with smaller throat height while the weak re-entrant jet in Venturi 2 is due to insufficient driving force associated with decreased contraction ratio.

For the test section (Venturi 3) shown in Figure 7.1, it has an appropriate throat height and contraction ratio. As a consequence, the re-entrant jet can be fully developed and the associated cloud cavitation is observed. This in turn demonstrates the throat height and contraction ratio both play a crucial role to the Venturi cavitation dynamics.

As aforementioned, Venturi 3 experiences periodic cloud shedding driven by re-entrant jet, condensation shock and collapse-induced pressure wave in order with the reduction of cavitation number. For Venturi 1 and Venturi 2, the weak re-entrant jet cannot initiate sheet-to-cloud transition due to scale effect, but it does not mean that cloud cavitation cannot take place. Let us recall the cloud shedding processes occurring in a very small Venturi (the throat height is only 0.25 mm), as shown in Figure 7.11 and Figure 7.12. Due to the restriction of the very small throat height, the re-entrant jet is not observed underneath the cavity. However, the periodic cloud shedding induced by the condensation shock or pressure wave mechanism is indeed identified. This implies that as the cavitation number decreases, sheet-to-cloud transition of partial cavities can skip the re-entrant jet mechanism and be directly induced by condensation shocks. Based on the above analysis, it can be inferred that the periodic cloud cavitation will be observed in Venturi 1 and Venturi 2 if the vapour production rate (associated

with cavitation number) is high enough to initiate a condensation shock at the downstream end of the cavity.

7.5. Chapter summary

To understand mechanisms governing the transition of sheet-to-cloud cavitation is of practical importance, since the quasi-stable sheet cavitation is basically harmless while large cloud shedding and subsequent collapse in the periodic cloud cavitation can cause severe issues like vibration, noise and erosion. In addition to the classically-described re-entrant jet, another mechanism to trigger shedding of large vapour clouds is identified in the literature as an upstream-propagating condensation shock within a partial cavity.

In this chapter, we have observed two types of cloud shedding processes in a Venturi channel through the conventional technique of high speed photography. At higher cavitation numbers, the sheet cavity is relatively short and the cloud shedding is a consequence of a re-entrant jet breaking off the cavity from its leading edge. At lower cavitation numbers, the re-entrant jet becomes less important to cavitation instabilities and the dominant mechanism for cavity detachment is found to be the condensation shock mechanism where a void fraction discontinuity forms at the trailing edge of the cavity and then propagates upstream until collapsing the entire cavity. By comparison of these two shedding mechanisms, noticeable differences can be found although they have propagation velocities of the same order of magnitude ($0.3 u_{th}$). The re-entrant jet is generally regarded as a thin physical liquid layer moving upstream beneath the cavity without significant phase change whereas the condensation shock appears as an upstream-propagating discontinuity nearly spanning the complete cavity height with intense condensation at the shock front. Moreover, the detached cloud in re-entrant jet cases is originated from the previous sheet cavity while in condensation shock cases the observed cloud comes from newly-generated vapours due to shear layer cavitation behind the shock front.

In addition to the above two mechanisms, a third mechanism, i.e. the collapse-induced pressure wave mechanism is identified responsible for cavity shedding based on a set of X-ray images of cavitation. When the shed cloud is transported to the downstream high pressure region, it would collapse violently and emit pressure waves that travel in all directions. This mechanism is usually combined with the condensation shock mechanism in the literature because the collapse-induced pressure wave is considered as the trigger of condensation shock

when it impinges on the rear of the cavity. However, in the present experiments we have indeed observed the onset of a condensation front in the absence of cloud collapse, which implies that collapse-induced pressure wave is not the necessary condition for initiating a condensation shock. Also, the X-ray images reveal the alternate existence of these two mechanisms in the same operating conditions and the pronounced distinctions between them are highlighted: i) pressure rise across the condensation front is very weak (a few kPa) while the amplitude of collapse-induced pressure wave can be as high as hundreds of kPa, ii) The propagation velocity of collapse-induced pressure wave within the cavity is an order of magnitude faster than condensation shock, and iii) the propagation of pressure wave front does not result in an obvious discontinuity in void fraction as is the case for the condensation shock.

Regarding the scale effect, the throat height and contraction ratio of entrance to throat height are found to both play a crucial role to the Venturi cavitation dynamics. A smaller throat height causes a larger resistance acting on the re-entrant jet and a smaller contraction ratio results in a weaker driving force. Both of them would suppress the full development of the re-entrant jet and thus tend to stabilize the cavity. However, as the cavitation number decreases to a certain point, sheet-to-cloud transition of partial cavities can skip the re-entrant jet mechanism and be directly induced by condensation shocks.

7.5. Résumé du chapitre

Comprendre les mécanismes régissant la transition de la cavitation feuille à nuage est d'une importance pratique, car la cavitation de feuille quasi-stable est fondamentalement inoffensive tandis que l'effondrement important des nuages et l'effondrement ultérieur dans la cavitation périodique des nuages peuvent causer de graves problèmes tels que les vibrations, le bruit et l'érosion. . En plus du jet rentrant décrit de manière classique, un autre mécanisme pour déclencher la dissipation de gros nuages de vapeur est identifié dans la littérature comme un choc de condensation se propageant en amont dans une cavité partielle.

Dans ce chapitre, nous avons observé deux types de processus d'effacement des nuages dans un canal Venturi grâce à la technique conventionnelle de photographie à grande vitesse. À des nombres de cavitation plus élevés, la cavité de la feuille est relativement courte et la dispersion des nuages est une conséquence d'un jet rentrant rompant la cavité de son bord d'attaque. À des nombres de cavitation inférieurs, le jet rentrant devient moins important pour les instabilités de cavitation et le mécanisme dominant pour le détachement de la cavité s'avère

être le mécanisme de choc de condensation où une discontinuité de la fraction de vide se forme au bord de fuite de la cavité puis se propage en amont jusqu'à l'effondrement. toute la cavité. En comparant ces deux mécanismes de délestage, des différences notables peuvent être trouvées bien qu'ils aient des vitesses de propagation du même ordre de grandeur ($0,3 u_{th}$). Le jet rentrant est généralement considéré comme une fine couche de liquide physique se déplaçant vers l'amont sous la cavité sans changement de phase significatif alors que le choc de condensation apparaît comme une discontinuité se propageant en amont couvrant presque toute la hauteur de la cavité avec une condensation intense au front de choc. De plus, le nuage détaché dans les cas de jets rentrants provient de la cavité de feuille précédente tandis que dans les cas de choc de condensation, le nuage observé provient de vapeurs nouvellement générées en raison de la cavitation de la couche de cisaillement derrière le front de choc.

En plus des deux mécanismes ci-dessus, un troisième mécanisme, c'est-à-dire le mécanisme d'onde de pression induite par l'effondrement, est identifié comme responsable de l'effondrement de la cavité sur la base d'un ensemble d'images radiographiques de cavitation. Lorsque le nuage de jet est transporté vers la région de haute pression en aval, il s'effondrerait violemment et émettrait des ondes de pression qui se déplacent dans toutes les directions. Ce mécanisme est généralement combiné avec le mécanisme de choc de condensation dans la littérature car l'onde de pression induite par l'effondrement est considérée comme le déclencheur du choc de condensation lorsqu'elle frappe l'arrière de la cavité. Cependant, dans les présentes expériences, nous avons bien observé l'apparition d'un front de condensation en l'absence d'effondrement des nuages, ce qui implique qu'une onde de pression induite par l'effondrement n'est pas la condition nécessaire pour déclencher un choc de condensation. Aussi, les images radiographiques révèlent l'existence alternée de ces deux mécanismes dans les mêmes conditions de fonctionnement et les distinctions prononcées entre eux sont mises en évidence: i) la montée en pression à travers le front de condensation est très faible (quelques kPa) tandis que l'amplitude de l'effondrement - l'onde de pression induite peut atteindre des centaines de kPa, ii) la vitesse de propagation de l'onde de pression induite par l'effondrement dans la cavité est d'un ordre de grandeur plus rapide que le choc de condensation, et iii) la propagation du front d'onde de pression n'entraîne pas une discontinuité évidente dans la fraction de vide comme c'est le cas pour le choc de condensation.

En ce qui concerne l'effet d'échelle, la hauteur de la gorge et le rapport de contraction de l'entrée à la hauteur de la gorge jouent tous deux un rôle crucial dans la dynamique de cavitation

du Venturi. Une hauteur de col plus petite entraîne une plus grande résistance agissant sur le jet rentrant et un rapport de contraction plus petit entraîne une force d'entraînement plus faible. Les deux supprimeraient le développement complet du jet rentrant et tentaient ainsi de stabiliser la cavité. Cependant, à mesure que le nombre de cavitation diminue jusqu'à un certain point, la transition feuille à nuage des cavités partielles peut sauter le mécanisme de jet rentrant et être directement induite par des chocs de condensation.

Chapter 8

Overall summary and perspectives

This thesis focuses on the investigation of the internal structures and the dynamics of partial cavitation developed in two-dimensional convergent-divergent (Venturi) channels, through several experimental techniques including the state-of-the-art synchrotron X-ray imaging. In general, partial cavitation takes two forms of appearance: sheet cavitation and cloud cavitation. The former is often stated as stable in the literature due to slight variation of the observed cavity length and location, while the latter undergoes strong instabilities associated with periodic shedding of large vapour clouds when the cavity length exceeds a certain extent. The mechanisms governing transition from stable to shedding cavities are also discussed in the present work.

8.1. The application of X-ray imaging technique to cavitating flows

An accurate description of cavitation physics strongly relies on the visualization of two-phase morphology and the measurements of characteristic quantities (e.g. velocity and void fraction) inside cavitating areas. The use of conventional optical techniques has been unsuccessful to provide this information, due to the opacity of the liquid/vapour mixture. Motivated by solving this problem, an ultra-fast synchrotron X-ray imaging technique was developed in consideration of X-rays high penetrability and weak interaction with matter. Small silver-coated hollow particles ($\sim 10 \mu\text{m}$) were injected into cavitating flows as the liquid phase tracers for PIV. Thanks to the high-flux coherent X-ray beam provided by the APS synchrotron facility and the purposed-made test section with extremely thin Plexiglas side walls, we obtained high-quality images containing diphasic structures and tracer particles with an unprecedented spatial resolution, under the combined effects of X-ray phase contrast and absorption contrast. A wavelet-decomposition-based image processing method was developed

originally and applied to separate the seeding particles from the vapour structures, which enabled the simultaneous acquisition of time-resolved velocity and void fraction fields in the cavitating flow.

8.2. Internal two-phase flow structures and dynamics of quasi-stable sheet cavitation

Sheet cavitation was generated in the throat region of a convergent-divergent channel with a small contraction ratio, where the quasi-stable cavity can be sustained in a wide range of cavitation numbers. The global behavior of sheet cavitation was studied through the conventional high speed photography. It was observed that the main part of the sheet cavity attached to the solid surface steadily while small vapour structures were rolled up and shed continuously from the closure region in an irregular manner. So far, the mainstream explanation to quasi-stable sheet cavitation is that no re-entrant jet exists underneath the cavity or the re-entrant jet only exists near the cavity closure region, thereby producing a relatively stable fore part with a turbulent frothy closure. However, this conjecture was challenged by the detailed X-ray imaging measurements.

According to the X-ray measurement results, we classify quasi-stable sheet cavitation into three representative stages based on the status of re-entrant flow: (i) at the early stage ($\sigma = 9.13$), the incipient cavity is short and no reverse flow is observed; (ii) at the intermediate stage ($\sigma = 8.0$), an intermittent re-entrant jet is identified underneath the sheet cavity; (iii) at the developed stage ($\sigma = 7.54$), the re-entrant jet becomes continuous and it can almost penetrate the entire cavity. It is clear that the sheet cavity beyond inception level can still remain quasi-stable under the influence of a re-entrant jet.

For the developed sheet cavitation, 6 characteristic parts are identified: (1) very upstream part of the cavity, (2) shear layer, (3) cavity closure, (4) cavity wake, (5) reverse flow region, and (6) main flow region outside the cavity. An attached vapour pocket is sustained in the upstream part (1) due to intense vaporization, but it oscillates quasi-periodically under the influence of re-entrant jet. The main part of the re-entrant jet (5) exists persistently along the wall with a relatively constant thickness and velocity. When the attached vapour pocket interacts with the front of the re-entrant jet, it detaches from the wall transforming into a low-void-ratio bubbly mixture. The whole re-entrant jet can be regarded as a thin liquid film moving upstream underneath the cavity. The dispersed bubbles entrained by the reverse flow tend to be of spherical shape due to small velocity gradient. The strong velocity shear layer (2) is

formed steadily between the re-entrant jet (5) and the main flow (6). In this region, the bubbly mixtures originated from the upstream vapour pocket are convected downstream without significant morphological and phase changes as their collapse might be limited by low pressure in the cores of coherent vortical structures. In the cavity closure region (3), small-scale vapour structures are shed continuously from the main cavity under the entrainment of the main flow and/or the action of horseshoe vortices. In the cavity wake region (4), the shed vapour structures collapse into a large number of small bubbles.

Differing from cloud cavitation, the presence of re-entrant jet in sheet cavitation does not cause a large cavity detachment from the leading edge although the jet can pierce the entire cavity. This might be attributed to the re-entrant jet having a propagation speed one order of magnitude smaller than that in cloud cavitation. The weak re-entrant jet does not have sufficient momentum to break off the cavity when it impinges on the cavity interface, thereby leading sheet cavitation to remain in a quasi-stable state. On the other side, the experimental results suggest that besides capturing the presence of re-entrant jet it is also essential to predict the re-entrant flow velocity correctly in numerical simulations in order to accurately simulate the transition of sheet-to-cloud cavitation.

8.3. Effect of cavitation on turbulence

It is impossible to generally conclude that cavitation promotes or depresses turbulence, and therefore the discussion is focused on several more specific points.

(1) Normal Reynolds stresses ($\overline{u'u'}$ and $\overline{v'v'}$)

On one hand, the occurrence of cavitation alters velocity field significantly, which affects turbulent velocity fluctuations indirectly due to the strong positive correlation between velocity gradient and turbulence intensity. On the other hand, the presence of vapour phase due to cavitation is observed to greatly suppress turbulent fluctuations, which could be related to two mechanisms: (i) the presence of vapor phase modifies the vortex-stretching process, and (ii) the cavitation compressibility damps out the turbulent fluctuations. As the shed vapour structures are transported to the high-pressure region, the collapse happening there would cause the augmentation of velocity fluctuations. However, this influence is not apparent in sheet cavitation since small vapour structures implode progressively.

(2) Reynolds shear stress ($\overline{u'v'}$)

Unlike the streamwise and cross-stream velocity fluctuations, the shear stress appears to

be weakly correlated with the velocity gradient. The collapse of vapour phase was found to be the main cause of the largest shear stress in the cavity wake. The phase change of vaporization at the upstream interface of the cavity was also found to increase the shear stress noticeably. The lowest shear stress was identified in the shear layer where vapour bubbles are convected without significant phase change.

(3) The ratio of Reynolds shear stress to turbulent kinetic energy (τ/k)

The Bradshaw hypothesis states that the Reynolds shear stress τ in a boundary layer is proportional to the turbulent kinetic energy k . It is well applied to single-phase flows. However, when cavitation takes place, the linear relationship between them is no longer satisfied due to the effect of two-phase mixtures compressibility, as suggested by the Reboud empirical correction. The X-ray experimental data in the present work show that the Reboud correction with $n=10$ describes the ratio of τ/k in cavitating areas much better than the Bradshaw hypothesis.

8.4. Cavitating flows in a Venturi-type test section with side gaps

A new test section was designed to investigate the structure and dynamics of cloud cavitation. The existence of the side gaps was not on purpose, and they resulted from large assembly errors between the 3D-printed plastic parts and the machined glass inserts. Individual bubbles tracking analysis showed that most of the re-entrant jet was directed into the gaps instead of moving towards the cavity leading edge along the wall. As a consequence, the anticipated large cloud shedding was not observed. On the negative side, this unexpected result delayed our plan to perform fast X-ray imaging measurements in cloud cavitating flows. On the positive side, the gaps changing the propagation path of the re-entrant jet could be a passive control of transition to the destructive cloud cavitation.

Although the desired cloud cavitation was not observed in the new test section, the conventional measurements were still carried out. The time-resolved PIV-LIF measurements revealed that the collapse of vapour clouds resulted in a rise of turbulence level while the presence of the attached cavity suppressed the streamwise and cross-stream velocity fluctuations, which were consistent with the measurement results in sheet cavitation by fast X-ray imaging. Based on the pressure measurement results, the intensity of pressure fluctuations at the inlet was found to present a trend of decrease with the reduction of cavitation number, suggesting that the pressure fluctuations upstream of the cavity were suppressed due to the presence of the two-phase cavitation structures.

8.5. Three mechanisms to initiate cloud cavitation

The conventional high speed images of cavitation combined with a set of X-ray phase contrast images from our collaborative team at University of Ljubljana reveal the presence of three different types of mechanisms responsible for large cloud shedding: re-entrant jet mechanism, condensation shock wave mechanism, and collapse-induced pressure wave mechanism. At higher cavitation numbers, the sheet cavity is relatively short and the cavity detachment is a consequence of a re-entrant jet pinching off the cavity from its leading edge. At lower cavitation numbers, the re-entrant jet plays a smaller role in the cavitation instabilities and the primary reason for periodic cloud shedding is found to be the condensation shock mechanism where a void fraction discontinuity forms at the trailing edge of the cavity and then propagates upstream until collapsing the entire cavity. In addition, if the amount of shed vapour cloud reaches a certain extent, the collapse will emit a pressure wave strong enough to disturb the growing cavity, and subsequently make it detached from the wall. This is the third mechanism observed in the experiments. In the present work, we point out the inappropriate classification of combining condensation shock and collapse-induced pressure wave mechanisms, since we identify pronounced differences between them: (i) the pressure increase across the condensation front is very weak (a few kPa) while the amplitude of collapse-induced pressure wave can be as high as hundreds of kPa, (ii) the travelling velocity of collapse-induced pressure wave within the cavity is an order of magnitude faster than the condensation shock, and (iii) the collapse-induced pressure wave does not result in an obvious discontinuity in void fraction when it propagates through the cavity, in contrary of the case of the condensation shock.

8.6. Geometry scale effect on the Venturi cavitating flow

The re-entrant jet induced cloud cavitation is highly affected by Venturi geometrical parameters, especially the throat height and the contraction ratio from the entrance to the throat. A smaller throat height would cause a larger drag force acting on the re-entrant jet, and a smaller contraction ratio would result in a weaker driving force, i.e. adverse pressure gradient. Both of them would suppress the full development of the re-entrant jet and hence lead the sheet cavity to remain relatively stable. Just like the aforementioned gaps altering the propagation path of the re-entrant jet, the transition from sheet-to-cloud cavitation could also be postponed by adjusting Venturi geometrical parameters. This may guide the design of hydraulic machines that are expected to operate without unsteady shedding of large clouds. Note that cloud

cavitation can still take place even in the absence of re-entrant jet as it can be directly initiated by the other two mechanisms.

8.7. Perspectives

In order to optimize the application of synchrotron X-ray imaging to cavitating flows and improve the physical understanding of sheet/cloud cavitation, a few further plans can be proposed:

- The acquisition of velocity fields from X-ray images relies on the extraction of tracer particles seeded into the cavitating flow. Although the wavelet-transform-based image processing method developed in this thesis improves the particle detection rate compared to the previous algorithms, the loss of particle information due to overlapped particles in clusters and varying background noises still needs to be considered. In recent years, machine learning has become a prevailing technique for pattern recognition. The work of Li et al. (2020) also shows the advantages of a machine-learning-based method for analyzing particle shadow images, especially for recognizing incomplete or highly superimposed particles. The burgeoning machine learning technique provides us a promising tool for more accurate extraction of particles from X-ray images and thereby improving velocity field measurements inside cavitating regions.
- The synchrotron X-ray imaging technique will be employed to investigate structures and dynamics of cloud cavitation once a new test section eliminating the side gaps is manufactured. The new data will provide an opportunity to compare the two cases of shedding/no-shedding and provide insights about the transition from stable sheet cavitation to unsteady cloud cavitation with large-scale shedding.
- A new test section equipped with a certain number of aligned pressure sensors along the Venturi divergent wall will be designed, in which we expect to observe cloud shedding induced by re-entrant jet, condensation shock and collapse-induced pressure wave mechanisms in order with the reduction of cavitation number. The pressure rise associated with these three mechanisms will be recorded and analyzed.
- The APS X-ray source emits X-ray pulses successively at a frequency of 271 696 Hz. However, in the present X-ray imaging experiments, the camera recording rate was set at 12 070 Hz which was achieved through the fast chopper shutter blocking most of the X-ray pulses. The purpose of this is to increase the field of view since the increase of

camera frame rate would reduce the spatial resolution drastically. In the future, if a camera can operate at 271 696 Hz with its full spatial resolution, we will remove the fast shutter in the beamline and thus be able to take advantage of every X-ray pulse for imaging. In this way, the much greater temporal resolution will provide significant insights into the two-phase morphology and dynamics of cavitation. In addition, the removal of the fast shutter will simplify the synchronization scheme, thereby reducing the measurement error of vapour volume fraction.

Résumé général et perspectives

Cette thèse se concentre sur l'investigation des structures internes et la dynamique de la cavitation partielle développées dans des canaux bidimensionnels convergents-divergents (Venturi), à travers plusieurs techniques expérimentales dont l'imagerie par rayons X synchrotron de pointe. En général, la cavitation partielle prend deux formes d'apparence: la cavitation en feuille et la cavitation nuageuse. Le premier est souvent déclaré stable dans la littérature en raison de la légère variation de la longueur et de l'emplacement de la cavité observée, tandis que le second subit de fortes instabilités associées à la perte périodique de gros nuages de vapeur lorsque la longueur de la cavité dépasse une certaine étendue. Les mécanismes qui régissent la transition des cavités stables aux cavités délestantes sont également discutés dans le présent travail.

8.1. L'application de la technique d'imagerie par rayons X aux écoulements de cavitation

Une description précise de la physique de la cavitation repose fortement sur la visualisation de la morphologie à deux phases et les mesures de grandeurs caractéristiques (par exemple la vitesse et la fraction de vide) à l'intérieur des zones de cavitation. L'utilisation de techniques optiques conventionnelles n'a pas réussi à fournir ces informations, en raison de l'opacité du mélange liquide/vapeur. Motivée par la résolution de ce problème, une technique d'imagerie par rayons X synchrotron ultra-rapide a été développée en tenant compte de la haute pénétrabilité des rayons X et de la faible interaction avec la matière. De petites particules creuses recouvertes d'argent ($\sim 10 \mu\text{m}$) ont été injectées dans des écoulements de cavitation comme traceurs de phase liquide pour PIV. Grâce au faisceau de rayons X cohérent à haut flux

fourni par le synchrotron APS et à la section de test spécialement conçue avec des parois latérales en plexiglas extrêmement minces, nous avons obtenu des images de haute qualité contenant des structures diphasiques et des particules traceurs avec une résolution spatiale sans précédent, sous les effets combinés du contraste de phase des rayons X et du contraste d'absorption. Une méthode de traitement d'image basée sur la décomposition en ondelettes a été développée à l'origine et appliquée pour séparer les particules d'ensemencement des structures de vapeur, ce qui a permis l'acquisition simultanée de champs de vitesse et de fraction de vide résolus dans le temps dans l'écoulement de cavitation.

8.2. Structures d'écoulement à deux phases internes et dynamique de la cavitation de feuille quasi stable

La cavitation de la feuille a été générée dans la région de la gorge d'un canal convergent-divergent avec un faible rapport de contraction, où la cavité quasi-stable peut être maintenue dans une large gamme de nombres de cavitation. Le comportement global de la cavitation des feuilles a été étudié grâce à la photographie conventionnelle à grande vitesse. On a observé que la partie principale de la cavité de la feuille était attachée à la surface solide de manière constante tandis que de petites structures de vapeur étaient enroulées et s'échappaient en continu de la région de fermeture de manière irrégulière. Jusqu'à présent, l'explication principale de la cavitation de feuille quasi-stable est qu'aucun jet rentrant n'existe sous la cavité ou que le jet rentrant n'existe que près de la région de fermeture de la cavité, produisant ainsi une partie antérieure relativement stable avec une fermeture écumeuse turbulente. Cependant, cette conjecture a été contestée par les mesures détaillées d'imagerie aux rayons X.

Selon les résultats de la mesure aux rayons X, nous classons la cavitation de feuille quasi-stable en trois étapes représentatives en fonction de l'état du flux rentrant: (i) au stade précoce ($\sigma = 9,13$), la cavité naissante est courte et non un flux inversé est observé; (II) au stade intermédiaire ($\sigma = 8,0$), un jet rentrant intermittent est identifié sous la cavité de la feuille; (III) au stade développé ($\sigma = 7,54$), le jet rentrant devient continu et il peut presque pénétrer dans toute la cavité. Il est clair que la cavité de la feuille au-delà du niveau de départ peut encore rester quasi-stable sous l'influence d'un jet rentrant.

Pour la cavitation de feuille développée, 6 parties caractéristiques sont identifiées: (1) partie très en amont de la cavité, (2) couche de cisaillement, (3) fermeture de cavité, (4) sillage de cavité, (5) région d'écoulement inverse, et (6) région d'écoulement principale à l'extérieur

de la cavité. Une poche de vapeur attachée est entretenue dans la partie amont (1) du fait d'une vaporisation intense, mais elle oscille quasi-périodiquement sous l'influence du jet rentrant. La partie principale du jet rentrant (5) existe en permanence le long de la paroi avec une épaisseur et une vitesse relativement constantes. Lorsque la poche de vapeur attachée interagit avec l'avant du jet rentrant, elle se détache de la paroi et se transforme en un mélange bouillonnant à faible taux de vide. L'ensemble du jet rentrant peut être considéré comme un mince film liquide se déplaçant en amont sous la cavité. Les bulles dispersées entraînées par l'écoulement inverse ont tendance à être de forme sphérique en raison du faible gradient de vitesse. La couche de cisaillement à forte vitesse (2) est formée de manière régulière entre le jet rentrant (5) et le flux principal (6). Dans cette région, les mélanges bouillonnants issus de la poche de vapeur amont sont convectés en aval sans changements morphologiques et de phase significatifs car leur effondrement pourrait être limité par une basse pression dans les noyaux de structures vorticales cohérentes. Dans la région de fermeture de cavité (3), des structures de vapeur à petite échelle sont évacuées en continu de la cavité principale sous l'entraînement du flux principal et/ou l'action de tourbillons en fer à cheval. Dans la région de sillage de cavité (4), les structures de vapeur évacuées s'effondrent en un grand nombre de petites bulles.

A la différence de la cavitation nuageuse, la présence de jet rentrant dans la cavitation de la feuille n'entraîne pas un décollement important de la cavité du bord d'attaque bien que le jet puisse percer toute la cavité. Cela pourrait être attribué au jet rentrant ayant une vitesse de propagation d'un ordre de grandeur inférieure à celle de la cavitation des nuages. Le jet rentrant faible n'a pas une impulsion suffisante pour rompre la cavité lorsqu'il heurte l'interface de la cavité, conduisant ainsi la cavitation de la feuille à rester dans un état quasi-stable. D'un autre côté, les résultats expérimentaux suggèrent qu'en plus de capturer la présence d'un jet rentrant, il est également essentiel de prédire correctement la vitesse d'écoulement rentrant dans des simulations numériques afin de simuler avec précision la transition de la cavitation feuille à nuage.

8.3. Effet de la cavitation sur la turbulence

Il est impossible de conclure de manière générale que la cavitation favorise ou diminue la turbulence, et par conséquent la discussion se concentre sur plusieurs points plus spécifiques.

(1) Contraintes de Reynolds normales ($\overline{u'u'}$ et $\overline{v'v'}$)

D'une part, l'apparition de cavitation modifie considérablement le champ de vitesse, ce qui affecte indirectement les fluctuations de vitesse turbulentes en raison de la forte corrélation positive entre le gradient de vitesse et l'intensité de la turbulence. D'un autre côté, on observe que la présence de phase vapeur due à la cavitation supprime fortement les fluctuations turbulentes, qui pourraient être liées à deux mécanismes: (i) la présence de phase vapeur modifie le processus d'étirement du vortex, et (ii) la cavitation la compressibilité amortit les fluctuations turbulentes. Lorsque les structures de vapeur de rejet sont transportées vers la région à haute pression, l'effondrement qui s'y produit provoquerait une augmentation des fluctuations de vitesse. Cependant, cette influence n'est pas apparente dans la cavitation des plaques car de petites structures de vapeur implosent progressivement.

(2) Contrainte de cisaillement de Reynolds ($\overline{u'v'}$)

Contrairement aux fluctuations de vitesse dans le sens des courants et transversaux, la contrainte de cisaillement semble être faiblement corrélée avec le gradient de vitesse. L'effondrement de la phase vapeur est la principale cause de la plus grande contrainte de cisaillement dans le sillage de la cavité. Le changement de phase de vaporisation à l'interface amont de la cavité s'est également avéré augmenter sensiblement la contrainte de cisaillement. La contrainte de cisaillement la plus faible a été identifiée dans la couche de cisaillement où les bulles de vapeur sont convectées sans changement de phase significatif.

(3) Le rapport de la contrainte de cisaillement de Reynolds à l'énergie cinétique turbulente (τ/k)

L'hypothèse de Bradshaw stipule que la contrainte de cisaillement de Reynolds τ dans une couche limite est proportionnelle à l'énergie cinétique turbulente k . Il est bien appliqué aux écoulements monophasés. Cependant, lorsque la cavitation a lieu, la relation linéaire entre eux n'est plus satisfaite en raison de l'effet de compressibilité des mélanges biphasés, comme suggéré par la correction empirique de Reboud. Les données expérimentales aux rayons X dans le présent travail montrent que la correction Reboud avec $n = 10$ décrit le rapport de τ/k dans les zones de cavitation bien mieux que l'hypothèse de Bradshaw.

8.4. Circuits de cavitation dans une section d'essai de type Venturi avec fentes latérales

Une nouvelle section d'essai a été conçue pour étudier la structure et la dynamique de la cavitation des nuages. L'existence des espaces latéraux n'était pas exprès, et ils résultaient d'erreurs d'assemblage importantes entre les pièces en plastique imprimées en 3D et les inserts

en verre usinés. L'analyse de suivi des bulles individuelles a montré que la majeure partie du jet rentrant était dirigée dans les espaces au lieu de se déplacer vers le bord avant de la cavité le long de la paroi. En conséquence, le grand dégagement de nuages prévu n'a pas été observé. Sur le plan négatif, ce résultat inattendu a retardé notre projet de réaliser des mesures d'imagerie par rayons X rapides dans des flux de cavitation dans les nuages. Du côté positif, les intervalles modifiant le chemin de propagation du jet rentrant pourraient être un contrôle passif de la transition vers la cavitation destructrice des nuages.

Bien que la cavitation des nuages souhaitée n'ait pas été observée dans la nouvelle section d'essai, les mesures conventionnelles ont toujours été effectuées. Les mesures PIV-LIF résolues en temps ont révélé que l'effondrement des nuages de vapeur entraînait une augmentation du niveau de turbulence tandis que la présence de la cavité attachée supprimait les fluctuations de vitesse dans le sens du courant et transversal, qui étaient cohérentes avec les résultats de mesure dans la cavitation de la feuille par imagerie par rayons X rapide. Sur la base des résultats de la mesure de la pression, l'intensité des fluctuations de pression à l'entrée s'est avérée présenter une tendance à la diminution avec la réduction du nombre de cavitation, ce qui suggère que les fluctuations de pression en amont de la cavité ont été supprimées en raison de la présence du biphase. structures de cavitation.

8.5. Trois mécanismes pour initier la cavitation des nuages

Les images conventionnelles à haute vitesse de cavitation combinées à un ensemble d'images à contraste de phase aux rayons X de notre équipe collaborative de l'Université de Ljubljana révèlent la présence de trois types différents de mécanismes responsables de la dispersion des grands nuages: mécanisme de jet rentrant, onde de choc de condensation mécanisme et mécanisme d'onde de pression induit par l'effondrement. A des nombres de cavitation plus élevés, la cavité de la feuille est relativement courte et le détachement de la cavité est une conséquence d'un jet rentrant pincant la cavité de son bord d'attaque. À des nombres de cavitation inférieurs, le jet rentrant joue un rôle plus petit dans les instabilités de cavitation et la principale raison de l'effacement périodique des nuages est le mécanisme de choc de condensation où une discontinuité de la fraction de vide se forme au bord de fuite de la cavité puis se propage. en amont jusqu'à effondrement de toute la cavité. De plus, si la quantité de nuage de vapeur répandu atteint un certain degré, l'effondrement émettra une onde de pression suffisamment forte pour perturber la cavité en croissance, et par la suite la détacher

de la paroi. C'est le troisième mécanisme observé dans les expériences. Dans le présent travail, nous soulignons la classification inappropriée de la combinaison des mécanismes de choc de condensation et d'onde de pression induite par l'effondrement, car nous identifions des différences prononcées entre eux: (i) l'augmentation de pression à travers le front de condensation est très faible (quelques kPa) tandis que l'amplitude de l'onde de pression induite par l'effondrement peut atteindre des centaines de kPa, (ii) la vitesse de déplacement de l'onde de pression induite par l'effondrement dans la cavité est d'un ordre de grandeur plus rapide que le choc de condensation, et (iii) l'effondrement- l'onde de pression induite n'entraîne pas une discontinuité évidente de la fraction de vide lorsqu'elle se propage à travers la cavité, contrairement au cas du choc de condensation.

8.6. Effet d'échelle de géométrie sur l'écoulement de cavitation du Venturi

La cavitation nuageuse induite par le jet rentrant est fortement affectée par les paramètres géométriques du Venturi, en particulier la hauteur de la gorge et le rapport de contraction de l'entrée à la gorge. Une hauteur de col plus petite entraînerait une force de traînée plus grande agissant sur le jet rentrant, et un rapport de contraction plus petit entraînerait une force d'entraînement plus faible, c'est-à-dire un gradient de pression défavorable. Les deux supprimeraient le développement complet du jet rentrant et conduiraient donc la cavité de la feuille à rester relativement stable. Tout comme les interstices précités modifiant le trajet de propagation du jet rentrant, le passage de la cavitation nappe à nuage pourrait également être reporté en ajustant les paramètres géométriques du Venturi. Cela peut guider la conception de machines hydrauliques qui devraient fonctionner sans effusion instable de gros nuages. A noter que la cavitation des nuages peut encore avoir lieu même en l'absence de jet rentrant car elle peut être directement initiée par les deux autres mécanismes.

8.7. Points de vue

Afin d'optimiser l'application de l'imagerie par rayons X synchrotron aux écoulements de cavitation et d'améliorer la compréhension physique de la cavitation nappe / nuage, quelques plans supplémentaires peuvent être proposés:

- L'acquisition des champs de vitesse à partir d'images radiographiques repose sur l'extraction de particules traceurs ensemencées dans le flux de cavitation. Bien que la méthode de traitement d'image basée sur la transformée en ondelettes développée dans

cette thèse améliore le taux de détection des particules par rapport aux algorithmes précédents, la perte d'informations sur les particules due à des particules superposées en grappes et à des bruits de fond variables doit encore être prise en compte. Ces dernières années, l'apprentissage automatique est devenu une technique dominante pour la reconnaissance de formes. Les travaux de Li et al. (2020) montre également les avantages d'une méthode basée sur l'apprentissage automatique pour analyser les images d'ombre de particules, en particulier pour reconnaître des particules incomplètes ou fortement superposées. La technique d'apprentissage automatique en plein essor nous fournit un outil prometteur pour une extraction plus précise des particules à partir d'images radiographiques et ainsi améliorer les mesures de champ de vitesse à l'intérieur des régions de cavitation.

- La technique d'imagerie par rayons X synchrotron sera utilisée pour étudier les structures et la dynamique de la cavitation des nuages une fois qu'une nouvelle section d'essai éliminant les espaces latéraux sera fabriquée. Les nouvelles données fourniront l'occasion de comparer les deux cas de délestage/non-effusion et fourniront des informations sur la transition d'une cavitation de feuille stable à une cavitation nuageuse instable avec effusion à grande échelle.
- Une nouvelle section de test équipée d'un certain nombre de capteurs de pression alignés le long de la paroi divergente du Venturi sera conçue, dans laquelle on s'attend à observer l'effondrement des nuages induit par les mécanismes de jet rentrant, de choc de condensation et d'onde de pression induite par l'effondrement dans l'ordre avec la réduction du nombre de cavitation. La montée en pression associée à ces trois mécanismes sera enregistrée et analysée.
- La source de rayons X APS émet successivement des impulsions de rayons X à une fréquence de 271 696 Hz. Cependant, dans les présentes expériences d'imagerie aux rayons X, la fréquence d'enregistrement de la caméra a été fixée à 12 070 Hz, ce qui a été obtenu grâce à l'obturateur hacheur rapide bloquant la plupart des impulsions de rayons X. Le but de ceci est d'augmenter le champ de vision car l'augmentation de la fréquence d'images de la caméra réduirait considérablement la résolution spatiale. À l'avenir, si une caméra peut fonctionner à 271 696 Hz avec sa pleine résolution spatiale, nous supprimerons l'obturateur rapide de la ligne de lumière et pourrons ainsi profiter de chaque impulsion de rayons X pour l'imagerie. De cette façon, la résolution temporelle beaucoup plus grande fournira des

informations significatives sur la morphologie à deux phases et la dynamique de la cavitation. De plus, la suppression de l'obturateur rapide simplifiera le schéma de synchronisation, réduisant ainsi l'erreur de mesure de la fraction volumique de vapeur.

REFERENCES

1. Aeschlimann, V., Barre, S., & Legoupil, S. (2011a). X-ray attenuation measurements in a cavitating mixing layer for instantaneous two-dimensional void ratio determination. *Physics of Fluids*, 23(5), 055101.
2. Aeschlimann, V., Barre, S., & Djeridi, H. (2011b). Velocity field analysis in an experimental cavitating mixing layer. *Physics of Fluids*, 23(5), 055105.
3. Aeschlimann, V., Prothin, S., Barre, S., & Djeridi, H. (2012). High speed visualizations of the cavitating vortices of 2D mixing layer. *European Journal of Mechanics B/fluids*, 31, 171-180.
4. Barre, S., Quine, C., & Dussauge, J. P. (1994). Compressibility effects on the structure of supersonic mixing layers: experimental results. *Journal of Fluid Mechanics*, 259, 47-78.
5. Barre, S., Rolland, J., Boitel, G., Goncalves, E., & Patella, R. F. (2009). Experiments and modeling of cavitating flows in venturi: attached sheet cavitation. *European Journal of Mechanics - B/Fluids*, 28(3), 444–464.
6. Brennen, C. E. (1995). *Cavitation and Bubble Dynamics*. Oxford University Press
7. Bauer, D., Barthel, F., & Hampel, U. (2018). High-speed X-ray CT imaging of a strongly cavitating nozzle flow. *Journal of Physics Communications*, 2(7), 075009.
8. Budich, B., Schmidt, S. J., & Adams, N. A. (2018). Numerical simulation and analysis of condensation shocks in cavitating flow. *Journal of Fluid Mechanics*, 838, 759–813.
9. Bhatt, M., & Mahesh, K. (2020). Numerical investigation of partial cavitation regimes over a wedge using large eddy simulation. *International Journal of Multiphase Flow*, 103155.
10. Canny, J. (1986). A computational approach to edge detection. *IEEE Transactions on pattern analysis and machine intelligence*, (6), 679-698.
11. Ceccio, S. L., & Brennen, C. E. (1991). Observations of the dynamics and acoustics of

- travelling bubble cavitation. *Journal of Fluid Mechanics*, 233(1), 633.
12. Callenaere, M., Franc, J. P., Michel, J. M., & Riondet, M. (2001). The cavitation instability induced by the development of a re-entrant jet. *Journal of Fluid Mechanics*, 444, 223-256.
 13. Coutier-Delgosha, O., Fortes-Patella, R., & Reboud, J. L. (2003). Evaluation of the turbulence model influence on the numerical simulations of unsteady cavitation. *Journal of Fluids Engineering*, 125(1), 38-45.
 14. Coutier-Delgosha, O., Devillers, J. F., Pichon, T., Vabre, A., Woo, R., & Legoupil, S. (2006). Internal structure and dynamics of sheet cavitation. *Physics of Fluids*, 18(1), 017103.
 15. Coutier-Delgosha, O., Stutz, B., Vabre, A., & Legoupil, S. (2007). Analysis of cavitating flow structure by experimental and numerical investigations. *Journal of Fluid Mechanics*, 578, 171-222.
 16. Coutier-Delgosha, O., Vabre, A., Hocevar, M., Delion, R., Dazin, A., Lazaro, D., & Lee, W. K. (2009). Local measurements in cavitating flow by ultra-fast X-ray imaging. In *ASME 2009 Fluids Engineering Division Summer Meeting* (pp. 371-379).
 17. Dittakavi, N., Chunekar, A., & Frankel, S. (2010). Large eddy simulation of turbulent-cavitation interactions in a Venturi nozzle. *Journal of Fluids Engineering*, 132(12), 121301.
 18. Dular M, Bachert B, Stoffel B, Širok B (2004). Relationship between cavitation structures and cavitation damage. *Wear* 257:1176–1184.
 19. Dular, M., Bachert, R., Stoffel, B., & Širok, B. (2005). Experimental evaluation of numerical simulation of cavitating flow around hydrofoil. *European Journal of Mechanics - B/Fluids*, 24(4), 522–538.
 20. Dular, M., Khelifa, I., Fuzier, S., Adama Maiga, M., & Coutier-Delgosha, O. (2012). Scale effect on unsteady cloud cavitation. *Experiments in Fluids*, 53(5), 1233–1250.
 21. Dular, M. & Petkovšek, M. (2015). On the mechanisms of cavitation erosion—Coupling high speed videos to damage patterns. *Experimental Thermal and Fluid Science*, 68, 359–370.
 22. Danlos A, Mehal J E, Ravelet F, Coutier-Delgosha O, Bakir F (2014). Study of the cavitating instability on a grooved Venturi profile. *Journal of Fluids Engineering*, 136(10), 101302.

23. Furness, R. A., & Hutton, S. P. (1975). Experimental and theoretical studies of two-dimensional fixed-type cavities. *Journal of Fluids Engineering*, 97(4), 515.
24. Franc, J. P. & Michel, J.M. (2005). *Fundamentals of Cavitation*. Springer Science & Business Media.
25. Foeth, E. J., Van Doorne, C. W. H., Van Terwisga, T., & Wieneke, B. (2006). Time resolved PIV and flow visualization of 3D sheet cavitation. *Experiments in Fluids*, 40(4), 503-513.
26. Foeth, E.J., van Terwisga, T., & van Doorne, C. (2008a). On the Collapse Structure of an Attached Cavity on a Three-Dimensional Hydrofoil. *Journal of Fluids Engineering*, 130(7), 071303.
27. Foeth, E. J. (2008b). The structure of three-dimensional sheet cavitation. PhD thesis, Delft University of Technology.
28. Gopalan, S., & Katz, J. (2000). Flow structure and modeling issues in the closure region of attached cavitation. *Physics of fluids*, 12(4), 895-911.
29. Gembicky, M., Oss, D., Fuchs, R., & Coppens, P. (2005). A fast mechanical shutter for submicrosecond time-resolved synchrotron experiments. *Journal of Synchrotron radiation*, 12(5), 665-669.
30. Ganesh, H. (2015). Bubbly shock propagation as a cause of sheet to cloud transition of partial cavitation and stationary cavitation bubbles forming on a delta wing vortex. PhD thesis, University of Michigan.
31. Ganesh, H., Mäkiharju, S. A., & Ceccio, S. L. (2016). Bubbly shock propagation as a mechanism for sheet-to-cloud transition of partial cavities. *Journal of Fluid Mechanics*, 802, 37-78.
32. Ganesh, H., Mäkiharju, S. A., & Ceccio, S. L. (2017). Bubbly shock propagation as a mechanism of shedding in separated cavitating flows. *Journal of Hydrodynamics, Ser. B*, 29(6), 907-916.
33. Gnanaskandan, A., & Mahesh, K. (2016). Large eddy simulation of the transition from sheet to cloud cavitation over a wedge. *International Journal of Multiphase Flow*, 83, 86-102.
34. Heindel, T. J. (2011). A review of X-ray flow visualization with applications to multiphase

- flows. *Journal of Fluids Engineering*, 133(7), 074001.
35. Iyer, C. O., & Ceccio, S. L. (2002). The influence of developed cavitation on the flow of a turbulent shear layer. *Physics of Fluids*, 14(10), 3414-3431.
36. Im, K. S., Fezzaa, K., Wang, Y. J., Liu, X., Wang, J., & Lai, M. C. (2007). Particle tracking velocimetry using fast x-ray phase-contrast imaging. *Applied Physics Letters*, 90(9), 091919.
37. Jakobsen, J. K. (1964). On the mechanism of head breakdown in cavitating inducers. *Journal of Basic Engineering*, 86(2), 291.
38. Jahangir, S., Hogendoorn, W., & Poelma, C. (2018). Dynamics of partial cavitation in an axisymmetric converging-diverging nozzle. *International Journal of Multiphase Flow*, 106, 34-45.
39. Jahangir, S., Wagner, E. C., Mudde, R. F., & Poelma, C. (2019). Void fraction measurements in partial cavitation regimes by X-ray computed tomography. *International Journal of Multiphase Flow*, 120, 103085.
40. Knapp, R.T. (1955). Recent investigations of the mechanics of cavitation and cavitation damage. *Trans. ASME* 77, 1045–1054.
41. Kawanami, Y., Kato, H., Yamaguchi, H., Tanimura, M., & Tagaya, Y. (1997). Mechanism and control of cloud cavitation. *Journal of Fluids Engineering*, 119(4), 788-794.
42. Kastengren, A., & Powell, C. F. (2014). Synchrotron X-ray techniques for fluid dynamics. *Experiments in Fluids*, 55(3).
43. Kravtsova, A. Y., Markovich, D. M., Pervunin, K. S., Timoshevskiy, M. V., & Hanjalić, K. (2014). High-speed visualization and PIV measurements of cavitating flows around a semi-circular leading-edge flat plate and NACA0015 hydrofoil. *International Journal of Multiphase Flow*, 60, 119-134.
44. Khlifa, I. (2014). *Imagerie rapide par rayons X des écoulements diphasiques: Application aux écoulements cavitants*. PhD thesis, ENSAM.
45. Khlifa, I., Vabre, A., Marko Hočevár, Fezzaa, K., Fuzier, S., Roussette, O., & Coutier-Delgosha, O. (2017). Fast x-ray imaging of cavitating flows. *Experiments in Fluids*, 58(11), 157.

46. Karathanassis, I. K., Koukouvinis, P., Kontolatis, E., Lee, Z., Wang, J., Mitroglou, N., & Gavaises, M. (2018). High-speed visualization of vortical cavitation using synchrotron radiation. *Journal of Fluid Mechanics*, 838, 148–164.
47. Le, Q., Franc, J., & Michel, J. (1993). Partial cavities: global behavior and mean pressure distribution. *Journal of Fluids Engineering*, 115, 243–248.
48. Laberteaux, K. R., & Ceccio, S. L. (2001a). Partial cavity flows. Part 1. Cavities forming on models without spanwise variation. *Journal of Fluid Mechanics*, 431, 1-41.
49. Laberteaux, K. R., & Ceccio, S. L. (2001b). Partial cavity flows. Part 2. Cavities forming on test objects with spanwise variation. *Journal of Fluid Mechanics*, 431, 43–63.
50. Lee, S. J., & Kim, G. B. (2003). X-ray particle image velocimetry for measuring quantitative flow information inside opaque objects. *Journal of Applied Physics*, 94(5), 3620-3623.
51. Leroux, J. B., Jacques André Astolfi, & Billard, J. Y. (2004). An experimental study of unsteady partial cavitation. *Journal of Fluids Engineering*, 126(1), 94-101.
52. Leroux, J.-B., Coutier-Delgosha, O., & Astolfi, J. A. (2005). A joint experimental and numerical study of mechanisms associated to instability of partial cavitation on two-dimensional hydrofoil. *Physics of Fluids*, 17(5), 052101.
53. Lee, S. J., Kim, G. B., Yim, D. H., & Jung, S. Y. (2009). Development of a compact x-ray particle image velocimetry for measuring opaque flows. *Review of Scientific Instruments*, 80(3), 033706.
54. Long, X., Zhang, J., Wang, J., Xu, M., & Ji, B. (2016). Experimental investigation of the global cavitation dynamic behavior in a venturi tube with special emphasis on the cavity length variation. *International Journal of Multiphase Flow*, 89, 290-298.
55. Li, J., Shao, S., & Hong, J. (2020). Machine learning shadowgraph for particle size and shape characterization. *Measurement Science and Technology*, accepted manuscript online. DOI: 10.1088/1361-6501/abae90.
56. Menter, F. R. (1994). Two-equation eddy-viscosity turbulence models for engineering applications. *AIAA journal*, 32(8), 1598-1605.
57. Moon, S. (2016). Novel insights into the dynamic structure of biodiesel and conventional

- fuel sprays from high-pressure diesel injectors. *Energy*, 115, 615–625.
58. Pham, T. M., Larrarte, F., & Fruman, D. H. (1999). Investigation of unsteady sheet cavitation and cloud cavitation mechanisms. *Journal of Fluids Engineering*, 121(2), 289-296.
59. Prothin, S., Billard, J.Y., & Djeridi, H. (2016). Image processing using proper orthogonal and dynamic mode decompositions for the study of cavitation developing on a NACA0015 foil. *Experiments in Fluids*, 57(10).
60. Pelz, P. F., Keil, T., & Groß, T. F. (2017). The transition from sheet to cloud cavitation. *Journal of Fluid Mechanics*, 817, 439-454.
61. Petkovšek, M., Hočevár, M., & Dular, M. (2020). Visualization and measurements of shock waves in cavitating flow. *Experimental Thermal and Fluid Science*, 110215.
62. Reboud, J. L., Stutz, B., & Coutier, O. (1998). Two-phase flow structure of cavitation: experiment and modeling of unsteady effects, 3rd Int. Symp. on Cavitation, Grenoble, France.
63. Reisman, G. E., Wang, Y.-C., & Brennen, C. E. (1998). Observations of shock waves in cloud cavitation. *Journal of Fluid Mechanics*, 355, 255–283.
64. Raffel, M., Willert, C. E., & Kompenhans, J. (2007). Particle image velocimetry: a practical guide. Springer Science & Business Media.
65. Stutz, B., & Reboud, J. L. (1997a). Experiments on unsteady cavitation. *Experiments in Fluids*, 22(3), 191-198.
66. Stutz, B., & Reboud, J. L. (1997b). Two-phase flow structure of sheet cavitation. *Physics of Fluids*, 9(12), 3678-3686.
67. Stutz, B., & Reboud, J. L. (2000). Measurements within unsteady cavitation. *Experiments in Fluids*, 29(6), 545-552.
68. Stutz, B., & Legoupil, S. (2003). X-ray measurements within unsteady cavitation. *Experiments in Fluids*, 35(2), 130-138.
69. Shamsborhan, H., Coutier-Delgosha, O., Caignaert, G., & Nour, F. A. (2010). Experimental determination of the speed of sound in cavitating flows. *Experiments in Fluids*, 49(6), 1359-1373.

70. Stanley, C., Barber, T., & Rosengarten, G. (2014). Re-entrant jet mechanism for periodic cavitation shedding in a cylindrical orifice. *International Journal of Heat and Fluid Flow*, 50, 169–176.
71. Trummler, T., Schmidt, S. J., & Adams, N. A. (2020). Investigation of condensation shocks and re-entrant jet dynamics in a cavitating nozzle flow by Large-Eddy Simulation. *International Journal of Multiphase Flow*, 103215.
72. Wang, Y., Liu, X., Im, K. S., Lee, W. K., Wang, J., Fezzaa, K., & Winkelman, J. R. (2008). Ultrafast X-ray study of dense-liquid-jet flow dynamics using structure-tracking velocimetry. *Nature Physics*, 4(4), 305.
73. Wang, C., Huang, B., Wang, G., Zhang, M., & Ding, N. (2017). Unsteady pressure fluctuation characteristics in the process of breakup and shedding of sheet/cloud cavitation. *International Journal of Heat and Mass Transfer*, 114, 769–785.
74. Wu, X., Maheux, E., & Chahine, G. L. (2017). An experimental study of sheet to cloud cavitation. *Experimental Thermal and Fluid Science*, 83, 129-140.
75. Wu, J., Ganesh, H., & Ceccio, S. (2019). Multimodal partial cavity shedding on a two-dimensional hydrofoil and its relation to the presence of bubbly shocks. *Experiments in Fluids*, 60(4), 66.
76. Xing, T., Li, Z., & Frankel, S. H. (2005). Numerical simulation of vortex cavitation in a three-dimensional submerged transitional jet. *Journal of Fluids Engineering*, 127(4), 714-725.
77. Zhang, H., Zuo, Z., Mørch, K. A. & Liu, S. (2019). Thermodynamic effects on Venturi cavitation characteristics. *Physics of Fluids*, 31(9), 097107.

List of Figures

Figure 2.1. (a) Sheet cavitation on the suction side of a hydrofoil from Foeth (2008b); (b) sheet cavitation on the divergent wall of a Venturi channel from Barre et al. (2009).....	8
Figure 2.2. (a) Cloud cavitation on the suction side of a hydrofoil from Foeth (2008b); (b) cloud cavitation on the divergent wall of a Venturi channel from Stutz & Reboud (1997a).	8
Figure 2.3. Typical unsteady behavior of a partial cavity with the development of a re-entrant jet and the periodic shedding of cavitation clouds from Franc & Michel (2005).....	9
Figure 2.4. Instantaneous void fraction fields illustrating the condensation shock mechanism to cause sheet-to-cloud cavitation from Ganesh et al. (2016).....	10
Figure 3.1. Schematic of the cavitation tunnel.....	18
Figure 3.2. (a) Profile of Venturi-type test section; the convergent-divergent channel is formed by the lower insert part (2) with the confinement of the top wall (3); flow direction is from left to right, (b) detailed dimensions of the convergent-divergent section (in mm).....	18
Figure 3.3. (a) Schematic of in-line X-ray imaging system; R_1 and R_2 are the source to object distance and object to detector distance, respectively. (b) Simple model for absorption contrast of X-ray imaging; the resulting image recorded at the exit-surface $z = 0$ is a two dimensional distribution of intensity. (c) Simple model for free-space propagation-based phase contrast of X-ray imaging; the resulting image recorded at a certain distance downstream $z = R_2$ is a two dimensional distribution of intensity.	20
Figure 3.4. (a) Diagram showing light path of X-ray imaging system at the APS (from Khelifa et al. 2017). (b) Synchronization of the shutters, the X-ray pulses and the camera frames to acquire image pairs for PIV analysis.	21
Figure 3.5. (a) Schematic of X-ray beam scanning positions; position 1 corresponds to the beginning of the cavity. The test section was moved to different positions enabling X-ray beam to scan the complete flow field of interest. (b) A representative raw X-ray image of cavitation recorded at the scanning window 2.....	22
Figure 3.6. Result of image processing for separation of two phases. (a) Raw X-ray image of cavitation; (b) particle image for measurements of liquid phase velocities; (c) vapour structure image for measurements of gaseous phase velocities.....	24

Figure 3.7. Measurements of vapour volume fractions, (a) calibration image of air; (b) calibration image of water; (c) processed image for computation of void fraction; (d) vapour volume fraction field.....25

Figure 3.8. Instantaneous velocity vector field evaluated from an image pair, (a) liquid phase; (b) vapour phase.....26

Figure 3.9. Comparison of mean streamwise velocity (\bar{u}) profiles at two locations measured by the standard PIV and the X-ray PIV in the non-cavitating condition, (a) x=8 mm; (b) x=14 mm.28

Figure 3.10. Discrete wavelet transform. (a) A binary tree of 4-level discrete wavelet transform; (b) raw X-ray image and the enlarged part; (c) wavelet decomposition results corresponding to the binary tree of 4-level discrete wavelet transform.....30

Figure 3.11. Particle detection based on the phase contrast imaging mechanism, (a) reconstructed approximation component; (b) reconstructed detail component; (c) preliminary particle detection by Canny edge detector; (d) removed objects by prescribed criteria; (e) remaining particles; (f) removed region shown in grey level mode; (g) hidden particles in the removed regions; (h) final result of the first identification of particles.31

Figure 3.12. Particle detection based on the absorption contrast imaging mechanism, (a) reconstructed approximation component; (b) reconstructed detail component; (c) background suppression; (d) binary image of identified particles with the presence of vapour structures; (e) final result of the second identification of particles.32

Figure 3.13. (a) Combination of particles identified by the two methods; (b) particle gray level restoration; (c) vapour structures after filtering particles out.33

Figure 3.14. Three actual synchronization schemes, (a) Image 1 exposed to one primary pulse and one secondary pulse, Image 2 exposed to one primary pulse and two secondary pulses; (b) both Image 1 and Image 2 exposed to one primary pulse and one secondary pulse; (c) Image 1 exposed to one primary pulse and two secondary pulses, Image 2 exposed to one primary pulse and one secondary pulse. The image row-averaged intensity is plotted for a quantitative comparison between Image 1 and Image 2 in the same pair.34

Figure 3.15. Variation of global intensity of air reference images in a packet of 144 image pairs. (a) Intensity variations of the first image and the second image; the green solid line denotes the mean intensity of the first image of each pair; the blue solid line denotes the mean intensity of the second image of each pair; the red dashed line signifies the average intensity of all images in the packet; (b) variation of the average intensity of the two images belonging to the same pair (the blue solid line) relative to the packet average value (the red dashed line). 35

Figure 3.16. Variation of global intensity of water reference images in a packet of 144 image pairs. (a) Intensity variations of the first image and the second image; the green solid line denotes the mean intensity of the first image of each pair; the blue solid line denotes the mean intensity of the second image of each pair; the red dashed line signifies the average intensity of

all images in the packet; (b) variation of the average intensity of the two images belonging to the same pair (the blue solid line) relative to the packet average value (the red dashed line). 35

Figure 3.17. Mean vapour volume fraction error estimated from pure air images.36

Figure 3.18. Comparison between the air calibration image (left) and the averaged image of a typical air image pair (middle); their row-averaged intensity is plotted for a quantitative comparison (right).....37

Figure 3.19. Smooth the band edges to reduce vapour volume fraction errors within the transition zone. (a) An original X-ray image of air with sharp intensity change at the middle band edges; (b) separated detail component of band edges; (c) smoothing the intensity change at the band edges; (d) reconstructed air image with smooth intensity change at the band edges; (e) mean vapour volume fraction error estimated from processed air images, compared to the mean error estimated from air images without band edge intensity correction.38

Figure 3.20. Image processing for vapour volume fraction measurements, (a) unprocessed X-ray image of cavitation; (b) detail component of wavelet decomposition; (c) detail component processed by averaging filter; (d) first processed image in a pair; (e) second processed image in a pair; (f) pair averaged image for estimating vapour volume fraction.39

Figure 4.1. Time series of high-speed photographs for the cavitating case of $\sigma = 7.54$, (a) back-lighting mode; (b) top-lighting mode; (c) time-space (t-x) diagram derived from 1000 consecutive cavitation snapshots in top-lighting mode.43

Figure 4.2. (a) Mean gray level values of 2000 high speed images; (b) standard deviations of gray levels; (c) time evolution of gray level in the probing window (indicated by the red frame in (a)) and its FFT result.44

Figure 4.3. (a) Distribution of the mean void fraction $\bar{\alpha}$; (b) mean void fraction profiles overlaid on the mean cavity shape; (c) evolution of the mean void fraction $\bar{\alpha}$ and the standard deviation of void fraction α' along the streamwise direction.....46

Figure 4.4. (a) Distribution of the time-averaged longitudinal velocity normalized by the reference velocity, \bar{u}/u_{ref} . The white dashed line denotes the contour line of $\bar{\alpha} = 0.1$. (b) Mean void fraction field on which the contour lines of $\bar{u}/u_{ref} = 0$ and 1 are overlaid to indicate the mean reverse flow and the external main flow.48

Figure 4.5. Comparison of the mean void fraction profiles (red dashed line) and the mean longitudinal velocity profiles (black solid line) at different distances from the throat.....49

Figure 4.6. Time-varying streamwise velocities at four positions along the line of $y = 0.1$ mm. The percentage represents the probability of re-entrant jet occurrence. The red dashed line denotes the averaged velocity. The vertical blue dashed lines separates different packets.50

Figure 4.7. Evolution of the probability of re-entrant jet occurrence (red line with squares) and the time-averaged longitudinal velocity (black line) along the horizontal line of $y = 0.1$ mm.51

Figure 4.8. Examination of void fraction in the X-ray scanning position 1, (a) time-varying void fraction in the first probe location indicated by the red dashed frame in (c); (b) average of all the spectra of 13 packets; (c) X-ray images at five typical time instants.	53
Figure 4.9. Examination of void fraction in the X-ray scanning position 2, (a) time-varying void fraction in the second probe location indicated by the red dashed frame in (c); (b) average of all the spectra of 13 packets; (c) X-ray images at five typical time instants.	53
Figure 4.10. Examination of void fraction in the X-ray scanning position 107, (a) time-varying void fraction in the third probe location indicated by the red dashed frame in (c); (b) average of all the spectra of 13 packets; (c) X-ray images at five typical time instants.	54
Figure 4.11. Two-phase flow structures inside sheet cavity, (a) a reconstructed image from 22 scanning positions showing the internal structures of sheet cavity. The arrows indicate the mean flow directions in each sub-regions; the image is equally split into 3 sections which are zoomed and shown in (b-d).	56
Figure 4.12. (a) Distribution of streamwise velocity fluctuations $\overline{u'u'}/u_{ref}^2$, (b) distribution of transversal velocity fluctuations $\overline{v'v'}/u_{ref}^2$, (c) distribution of shear stress $ \overline{u'v'} /u_{ref}^2$, (d) evolution of velocity gradient $\partial\overline{u}/\partial y$ along the flow direction. The two dashed lines indicate the shear area between the re-entrant jet and the main flow.	59
Figure 4.13. Profiles of streamwise velocity fluctuations $\sqrt{\overline{u'u'}}/u_{ref}$ (black line), transversal velocity fluctuations $\sqrt{\overline{v'v'}}/u_{ref}$ (red line), and shear stress $\sqrt{ \overline{u'v'} }/u_{ref}$ (blue line) with mean streamwise velocity \overline{u}/u_{ref} (pink line) at different streamwise locations.	60
Figure 4.14. Comparison between the experimental data and the Reboud empirical modification with $n=1, 3$ and 10 ($n=1$ is the Bradshaw hypothesis).	62
Figure 5.1. Distribution of the mean void fraction α at different cavitation numbers. The mean cavity length L_{cav} and thickness T_{cav} (in mm) are obtained based on the contour line of $\overline{\alpha} = 0.1$	67
Figure 5.2. Evolution of the mean void fraction (maximum value in the y direction) along the flow direction.	68
Figure 5.3. Comparison of mean void fraction profiles at different streamwise locations.	69
Figure 5.4. Contours of the time-averaged longitudinal velocity normalized by the reference velocity \overline{u}/u_{ref} at different cavitation numbers. The white dotted line depicts the mean cavity profile.	70
Figure 5.5. Evolution of the time-averaged longitudinal velocity \overline{u}/u_{ref} along the horizontal line of $y=0.1$ mm (adjacent to the Venturi wall).	71

Figure 5.6. Comparison of mean longitudinal velocity profiles at different streamwise locations. 72

Figure 5.7. Reconstructed X-ray image from the first four positions showing the characteristic structures of the cavity in the upstream region. The mean velocity vectors are overlaid on the corresponding area. The red dashed line indicates the boundary of the mean reverse flow.... 73

Figure 5.8. Evolution of the standard deviation of void fraction α' along the streamwise direction. 74

Figure 5.9. Evolution of the occurrence probability of negative velocity along the line of $y = 0.1$ mm. 74

Figure 5.10. The mean longitudinal velocity profile at station of $x=2$ mm for $\sigma = 9.13$. The error bars denote the standard deviation of the velocity. 74

Figure 5.11. (a) The location and size of the probe window chosen to examine the void fraction variation for three cases; (b) PDF of void fraction $P(\alpha)$ within the selected probe window. 76

Figure 5.12. (a) Time-varying void fraction in a representative packet corresponding to a duration of 0.024 s; (b-d) FFT of the time-varying void fraction for three cavitation numbers. 78

Figure 5.13. Average of 13 packets of spectra for three cavitation numbers. 78

Figure 5.14. Brightness fluctuations when the test section is empty (full of air) and the corresponding spectrum. 79

Figure 5.15. (a) Distributions of normalized longitudinal velocity fluctuations $\overline{u'u'}/u_{ref}^2$ at four different cavitation numbers. The white dashed line depicts the mean cavity profile. (b) Mean streamwise velocity field in the non-cavitating case. 81

Figure 5.16. Comparison of mean streamwise velocity \overline{u}/u_{ref} profiles between the non-cavitating case $\sigma = 10.72$ and the cavitating case $\sigma = 7.54$ 81

Figure 5.17. Profiles of (a) longitudinal velocity fluctuations $\overline{u'u'}/u_{ref}^2$, (b) mean velocity gradient $\partial\overline{u}/\partial y$ and (c) mean void fraction $\overline{\alpha}$ at $x=2$ mm..... 82

Figure 5.18. Distributions of normalized Reynolds shear stress $|\overline{u'v'}|/u_{ref}^2$ at four different cavitation numbers. The white dashed line depicts the mean cavity profile. 84

Figure 6.1. Test section - flow direction from left to right, (a) side view of the overall test section; (b) the zoomed convergent-divergent section, dimensions in mm; (c) side wall insert; (d) hollow side wall insert for X-ray imaging; (e) top view of the convergent-divergent section. 90

Figure 6.2. An example of pressure signals recorded by the inlet and outlet sensors ($\sigma=2.08$, $u_{in}=10$ m/s)..... 91

Figure 6.3. Calibration plate with regular distribution of marks. The dot diameter is 0.33 mm and the distance between dots is 1 mm. The coordinate system used is also defined.	92
Figure 6.4. An example of evaluating the instantaneous velocity field in the cavitating flow ($\sigma=2.49$, $u_{in}=8.75$ m/s), flow direction from left to right. (a) Raw PIV image; (b) processed image with a high-pass Gaussian filter; (c) instantaneous velocity vector field (every second vector is displayed in the horizontal direction for clarity).....	93
Figure 6.5. A sequence of high speed images showing a typical cavitation regime obtained in the new test section ($\sigma=2.34$, $u_{in}=10$ m/s). The time interval between two images is 0.5 ms.	94
Figure 6.6. High speed images in back-lighting mode showing the flow paths in the gap between the bottom insert and the side wall insert ($\sigma=2.08$, $u_{in}=10$ m/s).	95
Figure 6.7. Comparison of mean streamwise velocity profiles in two test sections: one with a gap and the other without a gap.	96
Figure 6.8. Cloud cavitation regime on the smooth divergent wall (left) versus sheet cavity without large cloud shedding on the grooved wall (right) from Danlos et al. (2014).	97
Figure 6.9. The pressure loss as a function of the cavitation number σ , (a) absolute pressure loss P_l ; (b) pressure loss coefficient $P_{l,c}$; (c) outlet-to-inlet pressure ratio P_r	98
Figure 6.10. Convergence test of the mean value and the standard deviation of gray levels ($\sigma=2.23$, $u_{in}=10$ m/s).....	99
Figure 6.11. The nondimensional mean cavity length as a function of the cavitation number. The curve fits through the measurement points.	99
Figure 6.12. (a) Profiles of u'^* , v'^* and $u'v'^*$ for the different cavitation numbers at $x=3$ mm; (b) profiles of u'^* , v'^* and $u'v'^*$ for the different cavitation numbers at $x=12$ mm.	101
Figure 6.13. Nondimensional pressure fluctuation intensity with respect to the cavitation number, (a) P'_{in} at the Venturi inlet; (b) P'_{out} at the Venturi outlet.....	102
Figure 7.1. Schematic of the Venturi section with dimensions in mm, flow from right to left.	105
Figure 7.2. T-x diagram obtained by stacking 1000 successive high speed images of cavitation (inlet cavitation number $\sigma =5.76$, bulk flow velocity at the throat $u_{th}=11.17$ m/s). These flow conditions produce the transitional cavitation regime.	106
Figure 7.3. Spectral analysis of the transitional cavity shedding for $\sigma =5.76$ and $u_{th}=11.17$ m/s. (a) Distribution of the standard deviation of gray level. The probe window for tracing gray level variation is located at the maximum standard deviation. (b) Time-varying spatially averaged gray level within the probe window and the corresponding FFT result.	106

Figure 7.4. High speed photography images showing the main and secondary cloud sheddings of a transitional cavity for $\sigma = 5.76$ and $u_{th} = 11.17$ m/s. The numbers 1-3 denote the secondary clouds, and 4 denotes the main cloud. The corresponding time instants are indicated in the above t-x diagram that is a small portion of the one in Figure 7.2. 107

Figure 7.5. T-x diagram obtained by stacking 1000 successive high speed images of re-entrant jet induced cloud cavitation ($\sigma = 4.95$, $u_{th} = 14.6$ m/s). The yellow solid line depicts the cavity growth process. The red solid line denotes the progression of the re-entrant jet, and the blue dashed lines indicate the shed cloud. 109

Figure 7.6. Spectral analysis of re-entrant jet induced cloud cavitation for $\sigma = 4.95$ and $u_{th} = 14.6$ m/s. (a) Distribution of the standard deviation of gray level. The probe window for tracing gray level variation is located at the maximum standard deviation. (b) Time-varying spatially averaged gray level within the probe window and the corresponding FFT result. . 109

Figure 7.7. High speed photography images showing re-entrant jet induced cloud shedding for $\sigma = 4.95$ and $u_{th} = 14.6$ m/s. The corresponding time instants are indicated in the above t-x diagram that is a portion of the one in Figure 7.5. 111

Figure 7.8. (a) Temporal evolution of the cloud shedding processes mainly induced by condensation shocks for $\sigma = 4.31$ and $u_{th} = 20.83$ m/s. (b) Time-varying gray level signal and the corresponding FFT result probed at the cavity closure. 113

Figure 7.9. High speed photography images showing processes of a small cloud shedding induced by re-entrant jet and a large cloud shedding induced by condensation shock for $\sigma = 4.31$ and $u_{th} = 20.83$ m/s. The corresponding time instants are indicated in the above t-x diagram that is a portion of the one in Figure 7.8(a). 114

Figure 7.10. High speed images at three representative time instants showing the cavity collapse caused by condensation shock for $\sigma = 4.31$ and $u_{th} = 20.83$ m/s. The corresponding time instants are indicated in the t-x diagram of Figure 7.9. 115

Figure 7.11. A sequence of X-ray images showing the upstream progression of the condensation shock through the attached sheet cavity. 117

Figure 7.12. A sequence of X-ray images showing a cavity shedding cycle induced by pressure wave emitted from cloud collapse. 118

Figure 7.13. Schematic illustration of cloud shedding processes initiated by re-entrant jet. 120

Figure 7.14. Schematic illustration of cloud shedding processes initiated by condensation shock (a) and collapse-induced pressure wave (b). 121

Figure 7.15. (a) Main dimensions (in mm) of two Venturi-type test section. (b) Schematic showing the effect of throat height on shear velocity gradient. 124

Etude expérimentale de la structure et de la dynamique des écoulements cavitants

Résumé

La cavitation est un phénomène complexe impliquant un transfert de masse entre la phase liquide et vapeur à des températures presque constantes. Les processus physiques qui contrôlent les instabilités dans les écoulements cavitants ne sont pas encore compris, principalement en raison du manque de données expérimentales quantitatives sur les structures diphasiques et la dynamique à l'intérieur des zones de cavitation opaques. Dans cette thèse, la cavitation partielle développée dans de petits canaux convergents-divergents (Venturi) a été étudiée expérimentalement en détail pour élucider ces mécanismes. Ceci a été réalisé en combinant une technique d'imagerie par rayons X ultra-rapide, la visualisation conventionnelle à haute fréquence et la vélocimétrie par images de particules. Les principales contributions de la présente étude portent sur les quatre aspects suivants: (1) une description détaillée des structures d'écoulement diphasique au sein des poches de cavitation quasi stables, qui se caractérisent par un écoulement rentrant à faible vitesse existant en continu sous la cavité; (2) analyse de l'effet complexe de la cavitation sur les fluctuations de vitesses turbulentes; (3) identification et discussion de trois mécanismes distincts responsables de la transition vers un comportement instable périodique; (4) analyse de l'effet d'échelle sur les comportements cavitants, dans le cas des profils Venturi étudiés.

Mots clés: poche de cavitation, instabilités, Imagerie par rayons X, Structure diphasique

Résumé en anglais

Cavitation is a complex phenomenon involving mass transfer between liquid and vapour phase at nearly constant temperature. Advances in the understanding of the physical processes of cavitating flows are challenging, mainly due to the lack of quantitative experimental data on the two-phase structures and dynamics inside the opaque cavitation areas. In this thesis, partial cavitation developed in small convergent-divergent (Venturi) channels was studied experimentally in detail for a better knowledge of the physical mechanisms governing the cavitation instabilities. This was achieved by using an ultra-fast synchrotron X-ray imaging technique aided with conventional high speed photography and Particle Image Velocimetry. The main contributions of the present study can be summarized as follows: (1) detailed description of the two-phase flow structures in quasi-stable sheet cavitation, which is characterized by a low-speed re-entrant flow existing continuously underneath the cavity; (2) analysis of the complex effect of cavitation on turbulent velocity fluctuations; (3) identification of three distinct mechanisms responsible for the transition of sheet-to-cloud cavitation, with a discussion of the differences between them; (4) analysis of the scale effect on cavitation in the studied Venturi flows.

Key words: Sheet/cloud cavitation, X-ray imaging, Two-phase structure